ACOUSTIC PERFORMANCE OF BIAS FLOW LINERS IN GAS TURBINE COMBUSTORS

CLAUS LAHIRI

DISSERTATION

ACOUSTIC PERFORMANCE OF BIAS FLOW LINERS IN GAS TURBINE COMBUSTORS

vorgelegt von
Dipl.-Ing. Claus Lahiri
geb. in Bergisch Gladbach

von der Fakultät V - Verkehrs- und Maschinensysteme
der Technischen Universität Berlin
zur Erlangung des akademischen Grades

Doktor der Ingenieurwissenschaften
– Dr.-Ing. –

genehmigte Dissertation

Berlin 2014

Promotionsausschuss:

Vorsitzender:	Prof. Dr.-Ing. Dieter Peitsch
Gutachter:	Prof. Dr. rer. nat. Lars Enghardt
Gutachter:	Prof. Dr. Tech. Hans Bodén

Tag der wissenschaftlichen Aussprache: 25. November 2014

ABSTRACT

Thermoacoustic instabilities prevent the implementation of modern combustion concepts in gas turbines, which are essential for higher efficiency and lower emissions. Bias flow liners are able to suppress these instabilities by increasing the acoustic losses of the system. However, it is an open question under which conditions their full potential can be retrieved.

This thesis collects the available information concerning the acoustic properties of bias flow liners and puts it into perspective for the application in a gas turbine combustor. The review includes a rigorous assessment of the existing models. The models and previous findings are evaluated by comparing them to the results of a comprehensive experimental study regarding the relevant acoustic, geometric, thermodynamic, and flow parameters. This includes for the first time the influence of pressure and temperature.

The results reveal that there is a resonance dominated regime at low bias flow Mach numbers with rather complex parameter dependencies and a bias flow dominated regime which is mainly dependent on three parameters only: the bias flow, the porosity, and a resonance parameter.

ZUSAMMENFASSUNG

Der Einsatz moderner Verbrennungskonzepte zur Effizienzsteigerung und Schadstoffreduktion bei Gasturbinen wird oft durch thermo-akustische Instabilitäten verhindert. Durchströmte Brennkammerliner können die akustische Dämpfung des Systems erhöhen und die Instabilitäten unterdrücken. Eine wesentliche Frage ist, bei welchen Parametereinstellungen eine optimale Dämpfungswirkung erzielt werden kann.

Diese Arbeit liefert eine umfassende Übersicht der bisherigen Forschung. In einer experimentellen Studie werden akustische, geometrische, thermodynamische und strömungsmechanische Parameter untersucht. Zum ersten Mal wird hier auch der Einfluss von Druck und Temperatur durch eine Messung abgebildet. Diese weitreichende Datenbasis ermöglicht eine detaillierte Bewertung der einzelnen Parameter und der Qualität der Modelle.

Die Ergebnisse zeigen einen Betriebsbereich bei langsamen Geschwindigkeiten der von Resonanzen dominiert ist und komplizierte Parameterabhängigkeiten aufweist. Bei höheren Geschwindigkeiten dominiert die Durchströmung und die Schallabsorption ist im Wesentlichen von nur drei Parametern abhängig: Porosität, Durchströmungsgeschwindigkeit und einem Resonanzparameter.

CONTENTS

LIST OF SYMBOLS

LATIN SYMBOLS

A	Amplitude
A	Cross-section area
A_{open}	Liner total open area
A_{rel}	Relative error
a	Attenuation rate
$\hat{B}$	Complex stagnation enthalpy amplitude
B'	Fluctuating stagnation enthalpy
C	Acoustic compliance
C	Circumference
C_c	Contraction coefficient
C_d	Discharge coefficient
C_r	Resistance coefficient
C_v	Velocity coefficient
c	Speed of sound
c_p	Specific heat capacity at constant pressure
c_{ph}	Phase velocity
c_v	Specific heat capacity at constant volume
D	Duct diameter
D	Energy dissipation coefficient
D_c	Cavity diameter
D_h	Hydraulic diameter
d	Orifice diameter
d_c	Cavity depth
e	Exponential function
err	Fit error
$\overline{err}$	Average fit error over all microphones
f	Darcy friction factor
f	Frequency
$f_{c,mn}$	Cut-on frequency of mode m:n

f_r	Resonance frequency
$f_{r,i}$	Vibrational relaxation frequency of constituent i
G_{xx}	One-sided auto-spectral density
G_{xy}	One-sided cross-spectral density
He	Helmholtz number
H_m	Hankel function of order m
h	Humidity as molar concentration of water vapor
$\mathrm{Im}\{z\}$	Imaginary part of complex number z
I_m	Modified Bessel function of the first kind of order m
i	Imaginary unit
J_m	Bessel function of the first kind of order m
j_{mn}	Eigenvalue of J_m
K_m	Modified Bessel function of the second kind of order m
K_R	Rayleigh conductivity
k	Wave number
$k^{\pm}$	Convective wave number
k_0	Free field wave number
$k_{r,mn}$	Radial wave number of mode m:n
k_s	Stokes wave number
k'_s	Effective Stokes wave number
$k_{x,mn}$	Axial wave number of mode m:n
L	Length
L	Perforation length
L_c	Cavity length
L_{eff}	Effective perforation length
l	Orifice length
l'	Length end correction
l_{eff}	Effective orifice length
M	Acoustic inertance
M	Mach number
M_B	Bias flow Mach number
$M_{\bar{B}}$	Mean orifice bias flow Mach number
M_G	Grazing flow Mach number
m	Circumferential mode order
$\dot{m}$	Mass flow rate

$\dot{m}_B$	Bias flow mass flow rate
$\dot{m}_G$	Grazing flow mass flow rate
n	Radial mode order
P	Acoustic power
P	Acoustic energy flux
P	Perimeter
p	Pressure
p_o	Mean pressure
p^*	Critical pressure
p'	Acoustic pressure
$\hat{p}$	Complex pressure amplitude
p_c	Pressure at the critical point of water
$\hat{p}_{mn}$	Complex amplitude of mode m:n
p_{ref}	Reference pressure
p_{ws}	Saturation water vapor pressure
Pr	Prandtl number
Pr_t	Turbulence Prandtl number
Q	Resonance parameter
Q'	Heat release fluctuation
Q_{mn}	Hard-wall Eigenvalue of Y_m
q	Acoustic volume velocity
$\hat{q}$	Complex volume velocity amplitude
R	Acoustic resistance
R	Duct radius
R	Energy reflection coefficient
R	Specific gas constant
R	Radius
R_c	Cavity radius
$Re\{z\}$	Real part of complex number z
Re	Reynolds number
Re_c	Critical Reynolds number for pipe flow
RH	Relative humidity
r	Orifice radius
r	Radial coordinate
r	Specific acoustic resistance

r	Amplitude reflection coefficient
r_e	Amplitude end-reflection coefficient
r_h	Hydraulic radius
$\mathbf{S}$	Scattering matrix
S_{xy}	Scattering matrix element
Sh	Shear number
St	Strouhal number
s	Entropy
s	Spacing between microphones
s	Spacing between orifices
s'	Entropy fluctuations
s_θ	Spacing between orifices in circumferential direction
s_x	Spacing between orifices in axial direction
T	Energy transmission coefficient
T'	Fluctuating temperature
T	Temperature
$\mathbf{T}$	Transfer matrix
T_a	Constant, see Tab. A.1
T_b	Constant, see Tab. A.1
T_c	Temperature at the critical point of water
T_d	Temperature at dew point
T_{ref}	Reference temperature
T_s	Sutherland constant
T_{xy}	Transfer matrix element
t	Time
t	Wall thickness
t	Amplitude transmission coefficient
TL	Transmission loss
U	Mean flow velocity
U_B	Bias flow velocity
$U_{\overline{B}}$	Mean orifice bias flow velocity
U_G	Grazing flow velocity
V	Cavity volume
v	Velocity
v_*	Friction velocity

v_o	Mean velocity
v'	Acoustic particle velocity
$\hat{v}$	Complex velocity amplitude
ν	Acoustic mass velocity
$\hat{\nu}$	Complex mass velocity amplitude
w	Window function
X	Acoustic reactance
X_i	Mole fraction of constituent i
x	Specific acoustic reactance
x	Axial coordinate
Y	Wall shear layer admittance
Y_m	Bessel function of the second kind of order m
y	Transverse coordinate
Z	Acoustic impedance based on the mass velocity
Z	Acoustic impedance
Z_o	Characteristic acoustic impedance of a lumped element
Z_{rot}	Rotational collision number
z	Specific acoustic impedance
z_o	Characteristic acoustic impedance

GREEK SYMBOLS

α	Orifice pitch angle
α	Absorption coefficient
α	Attenuation coefficient
$\alpha^{\pm}$	Convective attenuation coefficient
$\overline{\alpha}$	Average convective attenuation coefficient
β	Coefficient of thermal expansion
χ	Normalized specific acoustic reactance
χ	Thermal diffusivity
δ	Imaginary part of the Rayleigh conductivity
δ	Boundary layer thickness
δ_τ	Thickness of the viscous sublayer of turbulent flow
δ_ν	Thickness of the viscous acoustic boundary layer
δ_χ	Thickness of the thermal acoustic boundary layer
δ_{ij}	Kronecker delta

Δc_{ph}	Change of phase velocity
ΔP	Bias flow pressure drop
ΔP_T	Bias flow total pressure drop in a double-skin configuration
η	Compliance
η	Hub-to-tip ratio in an annular duct
Γ	Propagation constant
γ_{xy}	Coherence
γ	Heat capacity ratio
γ	Real part of the Rayleigh conductivity
κ	Kármán constant
κ	Thermal conductivity
λ	Ratio of bias flow to grazing flow
λ	Second viscosity coefficient
λ	Wavelength
μ	Dynamic viscosity
μ_B	Bulk viscosity (also called volume viscosity)
ν	Kinematic viscosity
ν'	Effective kinematic viscosity including thermal conductivity losses
π	Mathematical constant
Φ	Acoustic losses
φ	Phase angle
ϕ	Viscous dissipation rate
θ	Circumferential coordinate
θ	Normalized specific acoustic resistance
θ_i	Characteristic vibrational temperature of constituent i
ρ	Density
ρ'	Fluctuating density
ρ_o	Mean density
σ	Perforation porosity
τ_{ij}	Viscous stress tensor
ω	Angular frequency
ψ	Fok function
ζ	Normalized specific acoustic impedance

SUPERSCRIPTS

$+$	in positive x-direction, in flow direction
$-$	in negative x-direction, against flow direction

SUBSCRIPTS

1	Section 1
2	Section 2
a	Excitation A
ac	regarding the acoustic mode
b	Excitation B
cl	regarding classical, i. e. viscothermal, losses within the fluid
cr	regarding classical and rotational relaxation losses within the fluid
ent	regarding the entropy mode
fluid	regarding losses within the fluid
rot	regarding rotational relaxation losses within the fluid
total	regarding total losses
turb	regarding viscothermal and turbulence losses at the wall
vib	regarding vibrational relaxation losses within the fluid
vor	regarding the vorticity mode
wall	regarding viscothermal losses at the wall

ACRONYMS

DDOF	Double-Degree-of-Freedom (also: 2DOF)
DLR	Deutsches Zentrum für Luft- und Raumfahrt
DUCT-C	Duct Acoustic Test Rig - Circular Cross-Section
EDM	Eldredge and Dowling Method
HAT	Hot Acoustic Test Rig
ISA	International Standard Atmosphere
ICAO	International Civil Aviation Organization
ISO	International Organization for Standardization
SDOF	Single-Degree-of-Freedom
SNR	Signal-to-noise ratio
SPL	Sound Pressure Level
TMM	Transfer Matrix Method

1

INTRODUCTION

Gas turbines convert the chemical energy inherent in a gaseous or liquid fuel into mechanical energy. Depending on their application they are designed to deliver shaft power or thrust, for example to generate electricity in a power plant or as aircraft propulsion, respectively.

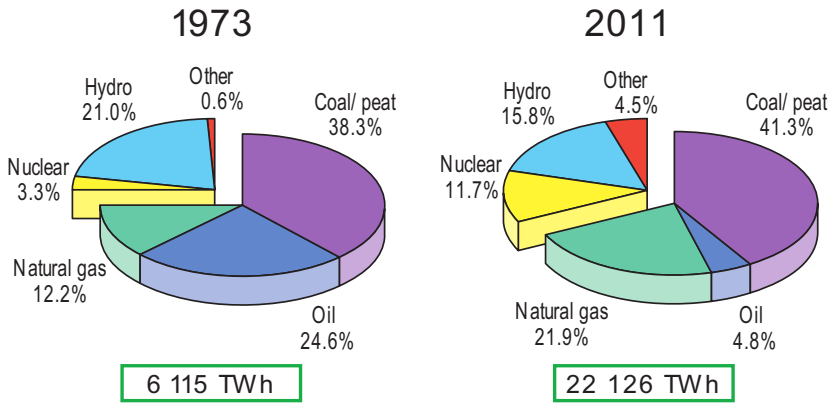

Figure 1.1: 1973 and 2011 fuel shares of electricity generation. (Key World Energy Statistics © OECD/IEA, 2013 [231])

The energy industry relies heavily on gas turbines for electricity production. The global electricity consumption has more than tripled from 439 Mtoe[1] in 1973 to 1582 Mtoe in 2011 [231]. Fig-

1 Million tonnes of oil equivalent, 1 Mtoe = 11630 GWh [231].

ure 1.1 illustrates the fuel shares involved in the electricity generation. With a collective share of 68 % in 2011, fossil fuels (coal, oil, and natural gas) remain the largest supplier of primary energy for electricity generation. While gas turbines can run on a variety of fuels, natural gas is the most common for power generation. The contribution of natural gas has nearly doubled from 1973 to 2011, indicating the growing dominance of gas turbines in that field. Today, gas turbines are one of the most widely-used power generating machines with industry leading efficiencies of around 40 % in simple cycle and up to 60 % in combined cycle[2] operation [331, 439].

Many countries are working on the Energiewende[3], that is increasing the use of renewable energy as an alternative to fossil and nuclear fuels. The gas turbine is essential to support this transition. Due to its short start-up time, compared to other means of power generation, the power supply can be balanced flexibly at peak times or when there is a temporary shortage of wind or solar power, for example. Gas turbines will remain a dominant technology for power generation and business analysts predict a stable growth for the gas turbine industry [163].

The first flight of a gas turbine powered aircraft took place on 27th of August 1939 in Rostock, Germany [80]. Light weight[4], compact size[4], and reliable operation have quickly made the gas turbine the engine of choice throughout the aviation industry. As of December 2013 there are a total of 44836 jet engines in service on active commercial aircraft in operation with airlines [159]. This number is expected to grow quickly, with predictions of 31 % rise in passenger demand by 2017 compared to 2012 [230].

2 A combined cycle gas turbine (CCGT) power plant reuses the hot exhaust gas of the gas turbine to additionally drive a steam turbine.

3 Due to the lack of an appropriate equivalent in the English language (see the discussion in [499]), the German term Energiewende has been adopted here.

4 Compared to traditional reciprocating engines of the same power rating.

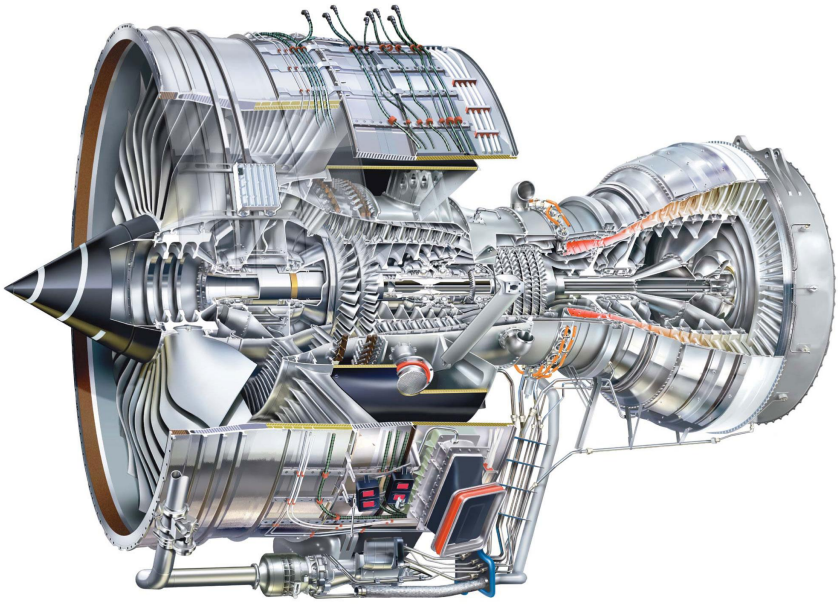

Figure 1.2: Rolls-Royce Trent 900, a modern high-bypass turbofan engine powering the Airbus A380. (Courtesy of Rolls-Royce plc © Rolls-Royce plc, 2012.)

A modern high-bypass turbofan engine is shown in Figure 1.2. The Rolls-Royce Trent 900 is one of the most powerful jet engines in operation, delivering a maximum thrust of 334–374 kN with a fan diameter of 2.95 m and a length of 5.478 m [151].

The increased environmental awareness has made the reduction of pollutant emissions from the combustion process one of the key challenges for modern gas turbines [292]. The global[5] aircraft engine emission standards are set by the Committee on Aviation Environmental Protection (CAEP) of the International Civil Aviation Organization (ICAO) and are published in the current edition of

5 The emissions of power plant gas turbines are regulated regionally, so that a wide diversity exists. An overview is given in [306].

Annex 16, Volume 2. The Advisory Council for Aviation Research and Innovation in Europe (ACARE) has formulated future goals for the emissions of carbon dioxide CO_2 and nitrogen oxide[6] NO_x in their Vision 2020 [4] and Flightpath 2050 [5] reports. It should be aimed for a reduction in CO_2 of 50 % and 75 % and NO_x of 80 % and 90 % until 2020 and 2050[7], respectively. The amount of CO_2 in the exhaust gases is directly related to the combustion efficiency [292], so that the levels have been reduced continuously, in line with the optimization for low fuel consumption. The prime factor in reducing NO_x is to lower the flame temperature[8], which adversely affects the efficiency and the CO_2 production. Thus, the reduction of NO_x is a major concern throughout the gas turbine industry, including both aviation and power.

This problem is addressed by modern combustion concepts, which operate in the lean regime. The lean combustion increases the air-fuel-ratio beyond the stoichiometric mixture[9], i. e. more air, relative to the fuel, is taking part in the combustion. As a result, the flame temperature is lowered and NO_x production is reduced. Particularly rewarding is the lean pre-mixed/pre-vaporized combustion (LPP) [292].

However, the implementation of this concept is often prevented by its tendency to promote combustion instabilities. Combustion instabilities are pressure pulsations resulting from a thermoacoustic feedback between the heat release of the flame and acoustic pressure oscillations. The instabilities lead to excessive wearing or even cracking of exposed components within or adjacent to the combustor. High amplitude instabilities can result in a flame blow-off or in the immediate and fatal damage of components, po-

6 This collectively includes nitrogen monoxide NO and nitrogen dioxide NO_2.

7 These values are relative to the capabilities of a typical new aircraft in the year 2000.

8 Two additional factors are a uniform temperature distribution and a short residence time.

9 A stoichiometric mixture contains sufficient oxygen for a complete combustion of the available fuel.

tentially releasing detached pieces into the turbine downstream. Low amplitude instabilities require an increased downtime of gas turbines for inspections and repairs if necessary. The maintenance costs that can be directly associated with damages due to combustion instabilities exceed $1 billion annually [305]. Furthermore, combustion instabilities are not limited to gas turbines, but are a widespread problem in combustion systems, e. g. liquid and solid propellant rocket engines [102, 190, 497], ramjet engines [102, 440], afterburners of turbojet engines [67, 102], and domestic or industrial furnaces [375].

The process leading up to an instability is not yet fully understood. Thus, it is not possible to predict the occurrence of instability or avoid it in the first place. Lieuwen and Yang [305] give an overview of the recent situation and mitigation strategies in the gas turbine industry. Commonly, thermoacoustic instabilities occur at one dominant frequency, which is mainly dependent on the combustor geometry and the operating condition. The general mechanism can be described as follows: The oscillating heat release of the flame produces sound, which is reflected at the combustor boundary, feeding back to the heat release oscillation. This feedback loop in itself does not necessarily lead to instability, the combustion becomes unstable only when the heat release fluctuation and the acoustic pressure oscillations are in phase ([388, 390]). This necessary condition is referred to as Rayleigh criterion[10]. In mathematical terms, instability does occur when [376][11]

$$\int_T p'(t)\, Q'(t)\, dt > \Phi, \tag{1.1}$$

where T is the period of one oscillation, p' is the acoustic pressure fluctuation, Q' is the heat release fluctuation, and Φ describes the

10 Named after John William Strutt, Lord Rayleigh (1842-1919, English physicist).

11 The original derivation by Putnam and Dennis [376] neglects the acoustic losses, so that $\Phi = 0$. The expression including the acoustic losses can be found in [238, 506], for example.

acoustic losses of the system. Equation (1.1) suggests two possibilities to control the instabilities:

1. Adjusting the phase relationship for a destructive interaction between the heat release fluctuation and the acoustic pressure (active control).

2. Increasing the acoustic losses of the system (passive control).

Active control measures mostly act on the modulation of the fuel flow. Even though it has been successfully demonstrated in laboratory setups, several barriers to implementation in full-scale gas turbine combustors still exist [98, 333], so that the industry is relying heavily on passive control concepts to suppress combustion instabilities. Traditionally, that means adding Helmholtz resonators or quarter-wave resonators to the combustor system [42, 85, 137, 189, 284, 395]. Unfortunately, the damping abilities of these resonators are limited to a rather small frequency range, so that several resonators of different sizes would be required to cover various operating conditions. Generally, a broadband damping characteristic would be preferred. Furthermore, at low frequencies the resonators grow to a considerable size and are certainly difficult to integrate into the engine. At the same time the increasing weight prevents their installation in an aero-engine.

An alternative approach is to use the acoustic absorption capabilities of the perforated combustor liner [131]. It is a well known fact, that perforations or orifices in general can be applied to damp acoustic pulsations. For example, Putnam [375] humorously quotes an anonymous author[12]: "To stop pulsation, drill one hole [...]; if that doesn't work, drill two holes!" One particular feature of the holes in a combustor liner is, that they are always purged with a cooling flow. This bias flow through the orifices has been found to have a substantial effect on the absorption characteristics of the liner. Bechert [38] has shown that the absorption mechanism is dominated by the transfer of acoustic energy into the shedding

12 Anonymous: "To reduce pulsations", *Fuel-Oil Journal*, Vol. 18, p. 16, 1940

vorticity when a bias flow is present. In order to distinguish such a configuration from a perforated liner without flow, it is commonly referred to as *bias flow liner*. The main advantages over Helmholtz and quarter-wave resonators are, that the bias flow liner is able to provide a broadband damping and that the actual components are already available in a combustor.

While an acoustically well designed combustor liner could decide over the stability of the combustion, its acoustic properties are rarely considered in the design of a new combustor. Throughout the industry overview given in [305], it is only Dowling and Stow [131] who address the acoustic properties of the combustor liner in their modeling. While a considerable amount of research is available, the industry is clearly hesitant to rely on the existing models.

1.1 MOTIVATION

The high potential of bias flow liners as dampers in a gas turbine combustor is well-known. However, it still seems to be an open question, under which circumstances this potential can be retrieved. One obvious complexity is due to the multitude of parameters that are involved. The amount of literature that deals with acoustic properties of orifices or perforations in general is overwhelming, so that all the parameters considered here have been addressed in the literature in some way. However, most geometries or operating conditions are very far from what is encountered in a gas turbine combustor. In particular, the presence of the bias flow is often not considered, while it is a key parameter for the combustor application. On the other hand, there exist plenty of studies aimed at the combustor application and many important conclusions could be drawn. Commonly, these studies are focused on one parameter, which additionally might be limited in its range, so a generalization of conclusions can only be assumed.

It seems to be necessary to take a step back and look at the broader picture. The scattered fragments of information need to be collected and put into perspective. However, the available experimental data varies immensely in setup, experimental method, and describing quantities, so that an independent set of data, based on one foundation, is required for the evaluation of the information.

The goal of this holistic approach is to identify and determine the influence of the significant parameters. Furthermore, a comprehensive assessment of the existing models can be provided, so that possible improvements can be suggested if necessary.

1.2 OUTLINE

Chapter 2 begins with a detailed overview of the liner setup and the operating conditions within a gas turbine combustor. The relevant geometric, thermodynamic, acoustic, and flow parameters are defined with respect to the experiments performed here and put into perspective with the definitions found in the literature. The parameter in focus is the bias flow, so that its definition is complemented by a review of the available research involving bias flow liners in Chapter 3. The various modeling approaches that are available to predict the acoustic performance of bias flow liners are illustrated in Chapter 4, concluding the review part of the thesis.

The second part focuses on the experimental parameter study. Chapter 5 collects the essential theoretical background, which is needed to understand the acoustic phenomena occurring within a duct. Special attention is put on the various loss mechanisms, that a sound wave experiences when propagating through a hard-walled duct. As will be shown later, these effects become more significant at elevated pressure and temperature.
Chapter 6 discloses all the details about the realization and the analysis of the measurements. This includes a detailed description

of the features and properties of the Duct Acoustic Test Rig and the Hot Acoustic Test Rig, which have both provided their services in the parameter study. The results of the study are presented in Chapter 7. The influence of each parameter is discussed separately, regarding the current findings as well as previous results from other studies. When applicable, the models are compared to the experimental results.

2

BIAS FLOW LINERS

This chapter takes a detailed look at the setup of typical gas turbine combustors and their operating conditions. The parameters that are relevant for the acoustic performance of a perforated liner are collected and discussed individually. The discussion includes a brief review of the presence and definition of each parameter in the literature, not limited to combustor liners but for orifices in general. Due to the essential nature of the bias flow in this work, the literature review regarding the bias flow effect receives its own dedicated chapter (see Chapter 3).

2.1 COMBUSTOR LINER

Until today, the layout of the holes in a combustor wall has been determined by combustion and cooling requirements and not by acoustic demands. Figure 2.1 illustrates the setup of a conventional combustion chamber. Traditionally, the openings in the liner serve the following purposes: 1. Introducing additional air to the combustion process (secondary air holes in Figure 2.1), 2. cooling down the hot gas before it enters the turbine (dilution air holes in Figure 2.1), and 3. cooling of the combustor wall (corrugated joint in Figure 2.1). The amount of air taking part in the combustion process, that is the primary air injected through the swirler and the secondary air injected through the walls, yields only 40 %

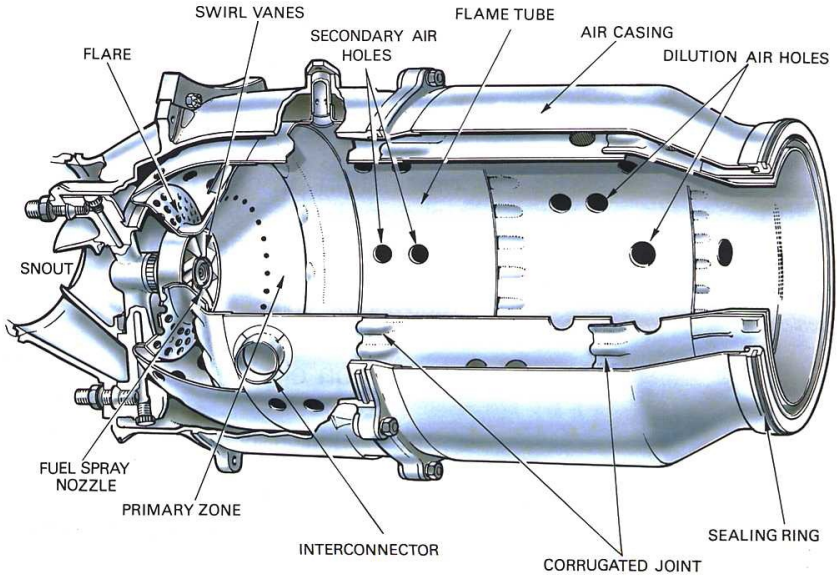

Figure 2.1: Setup of a conventional combustion chamber. (From [408], courtesy of Rolls-Royce plc.)

of the total airflow. The remaining 60 % are required for dilution (20 %) and wall cooling (40 %) [408].

The flow distribution has drastically changed in modern combustors. Lean combustion demands more air to take part in the combustion process. As a consequence, a reduction of cooling air became necessary. With novel materials being available and optimized cooling techniques, the wall cooling air could be reduced by half to 20 % for combustors that are now in service [292].

The arrangements of two modern combustors, designed for low emissions and high efficiency, are shown in Figures 2.2 and 2.3. Both examples employ angled effusion cooling of the walls. According to Lefebvre and Ballal [292], this is the most promising advancement in cooling methods regarding its potential for further significant reductions in cooling air requirements. The walls are perforated by a large number of small holes, where a shallow

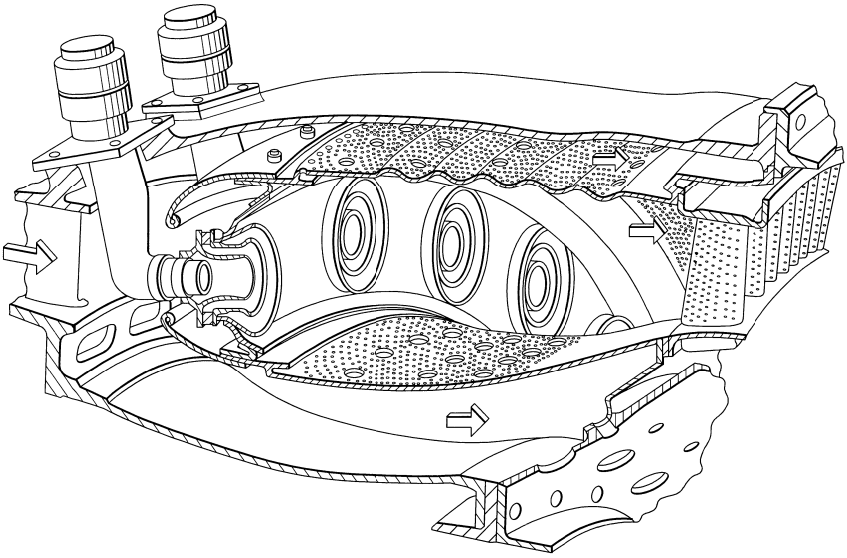

Figure 2.2: The GE twin annular premixing swirler (TAPS) combustor with effusion cooling, designed for low emissions and high efficiency. (From [157], courtesy of General Electric Company.)

angle in combustor mean flow direction provides two advantages for the cooling [292]: A larger surface area within the hole for increased heat removal and the establishment of a cooling film along the surface of the wall.

Typical orifice inclination angles are between $20° - 60°$. The orientation of the cooling orifices might be additionally skewed in the circumferential direction [92, 253]. The hole diameters range between 0.64-8.82 mm [88]. The cooling efficiency can be further increased by using shaped holes, i. e. holes with an enlarged exit area where the velocity is reduced and the lateral spreading of the cooling air is improved [178, 183]. A typical wall thickness is in the range of 0.5-1.5 mm [351].

Generally, the combustor operates at high pressure, high temperature, and with a relatively low flow velocity within the chamber. Aero-engines are designed to deliver much higher pressure

Figure 2.3: View into the annular combustor of the Rolls-Royce E3E Core 3/2 technology demonstrator, optimized for lean burn combustion and NOx reduction. (Courtesy of Rolls-Royce plc.)

ratios than stationary gas turbines. Current engine configurations achieve an overall pressure ratio[1] between 30 and 52. For example, the pressure ratio of the Rolls-Royce Trent 900 shown in Figure 1.2 is 39. Stationary gas turbines typically operate at pressure ratios between 10 and 25.

A characteristic temperature of a gas turbine is the turbine inlet temperature, that is the temperature of the flow leaving the combustor and entering the turbine. While a high turbine inlet temperature is desirable from an efficiency point of view, the maximum temperature is limited by the material properties of the turbine blades and the applied cooling. Currently, temperatures of nearly 1900 K can be achieved [331], while typical values are between 1300-1700 K [80]. However, the flame temperature within the com-

1 The overall pressure ratio is defined as p_3/p_1, where p_1 is the pressure at the inlet and p_3 the pressure delivered to the combustor [408].

buster can be as high as 2200-2600 K [80], with lean burn temperatures usually below 2000 K [292]. The cooling air provided by the compressor is typically between 500-800 K [408].

In pre-mixed flames, the flow velocity is restricted by the flashback and blowoff limits. Flashback occurs at low flow velocities, when the flame starts propagating upstream into the supply passages, i. e. when the flow velocity is slower than the flame speed. In order to stabilize the flame, the flow velocity exceeds the flame speed in any real combustor. The upper limit of the flow velocity is given by the blowoff condition, where the flame cannot be stabilized and is convected downstream by the flow [304]. Due to the latter restriction the mean Mach number in the combustor is fairly low and commonly around 0.05 [305].

The velocity of the bias flow through the perforated wall is determined by the pressure drop across the wall. Typical operating conditions correspond to a 3 % pressure drop [417].

Combustion instabilities are a tonal phenomenon, so that they are observed as a narrow peak in a frequency spectrum of the combustor. Several types of instabilities do exist, depending on various coupling mechanisms (see [301, 305] for an overview and classification). Thermoacoustic instabilities in gas turbine combustors are typically observed at frequencies in the range of 100-1000 Hz [272, 333]. The actual frequency is depending mainly on the combustor geometry and the operating condition, thus the frequency is not fixed but might change during operation.

2.1.1 *Parameter Overview*

The setup within a gas turbine combustor reveals a multitude of parameters that might be relevant for the acoustic performance of the liner. Table 2.1 gives an overview of these parameters, grouped into four categories based on their physical origin.

Some of these parameters are fixed by the operating condition and are not available for modification. Thus, an additional classifi-

Table 2.1: Overview of parameters relevant to the acoustic performance of gas turbine combustor liners. The independent parameters are available for modification to improve the acoustic performance.

GEOMETRY PARAMETERS	THERMODYNAMIC PARAMETERS
Orifice Geometry*	Pressure
Perforation Geometry*	Temperature
Cavity Geometry*	
ACOUSTIC PARAMETERS	**FLOW PARAMETERS**
Frequency	Bias Flow*
Amplitude	Grazing Flow

* independent parameter

cation into *dependent* and *independent* parameters makes sense. The dependent parameters cannot be used as a design tool to improve the acoustic performance. They are determined by the operational requirements of the gas turbine combustor. Nonetheless, their impact on the performance is of great importance. The independent parameters can be adjusted within certain restrictions to optimize the damping. The independent parameters are indicated by a star in Table 2.1.

2.2 GEOMETRY PARAMETERS

As seen in Figures 2.2 and 2.3, the geometry of a combustion chamber is rather complex. Putting the focus on the perforated liner, the geometric features can be abstracted and simplified. A simplified geometry that resembles the characteristic features, i. e. the circular shape and the grazing sound incidence, is illustrated in Figure 2.4. This configuration is generally referred to as a cylindrical perforated liner and will be used in the parameter study in Chapter 7. A similar setup was used in [16, 17, 142, 198, 279, 294, 310, 501], for example.

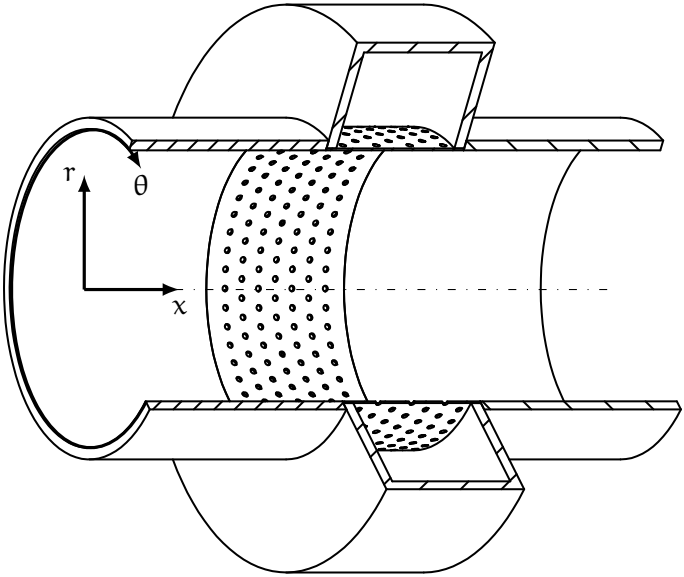

Figure 2.4: Simplified geometry of a combustor liner for acoustic studies: a cylindrical perforated liner.

2.2.1 *Orifice Geometry*

The orifice geometry is composed of three main features: the orifice cross-section shape, the orifice edge, and the orifice profile.

The *orifice cross-section shape* is given by a cut through a plane normal to the direction of the orifice. Figure 2.5 gives an overview of the orifice shapes that have been studied in the literature regarding their acoustic properties: circle, ellipse [336, 385], square [7, 89, 169, 181], rectangle [89, 129, 225, 336, 389], oblong [410], triangle [7, 169, 181], cross [89, 282], star [7, 169], crown [181], eye[2] [7, 169], and trapezoid [213].

A single rectangular orifice with a high aspect ratio, i. e. a long and thin slit, is often used for its two-dimensional characteristics

2 The eye-shape is obtained by sliding a perforation consisting of circular orifices over another identical perforation, as indicated in Figure 2.5j.

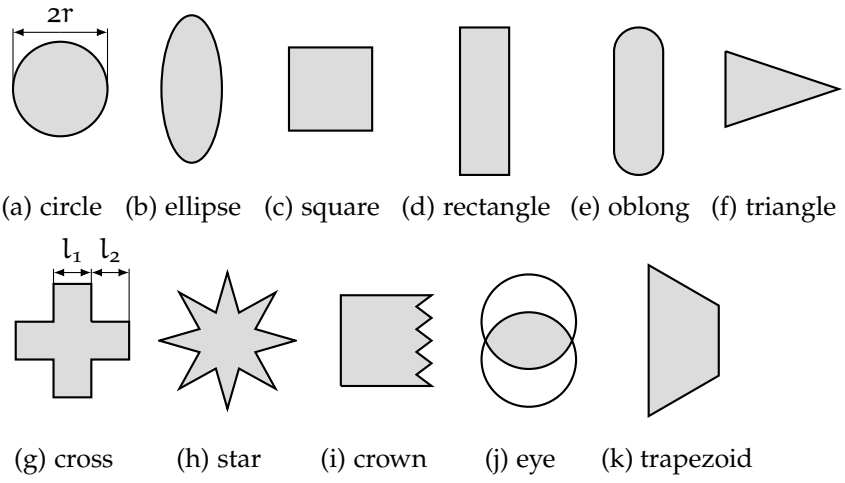

(a) circle (b) ellipse (c) square (d) rectangle (e) oblong (f) triangle

(g) cross (h) star (i) crown (j) eye (k) trapezoid

Figure 2.5: Overview of orifice cross-section shapes, that have been studied in the literature regarding their acoustic properties.

[10, 138, 168, 203, 204, 267, 332, 468, 469, 478]. The circular orifice (Figure 2.5a) is the standard orifice that serves as a status quo in all[3] the references given above. The majority of the literature treats circular orifices only, so that a circular shape is assumed if not stated otherwise.

Introducing sharp corners and breaking up straight edges, the different cross-section shapes can be compared by the *orifice cross-section area* A and the length of the orifice edge, i. e. the *orifice perimeter* P. For a circular orifice the area and perimeter are given by $A = \pi r^2$ and $P = 2\pi r$, respectively, where r is the orifice radius. The *hydraulic diameter* relates the cross-section area to the perimeter $D_h = 4A/P$. In fluid dynamics the hydraulic diameter defines the diameter of an equivalent circular geometry for a non-circular shape.

3 Except Howe [213], who compares the trapezoid to a square.

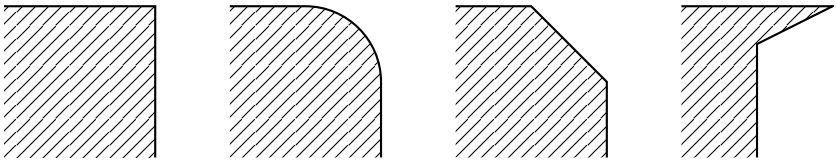

(a) square (b) round (c) bevel (d) wedge

Figure 2.6: Overview of orifice edge shapes, that have been studied in the literature regarding their acoustic properties.

Several *orifice edge shapes*, that are found in the literature, are illustrated in Figure 2.6: square, round [258, 282, 284, 480], bevel [360, 412], and wedge [269, 284, 478]. The square edge is the most common geometry and treated in most studies.

Looking at a cut through the wall material reveals the *orifice profile shape*. Figure 2.7 compiles some geometries that have been treated in the literature: straight, inclined [16, 17, 55, 141, 142, 286, 332, 478], conical [286], and sharp. Generally, the straight orifice is the most common. A circular, straight orifice is defined by its diameter $d = 2r$ and the *wall thickness* t. In this case, the *orifice length* l is identical to the wall thickness. A characteristic dimensionless quantity is the *orifice aspect ratio* l/d.
As shown in the previous section, inclined orifices are very common for cooling the combustor wall. The *orifice inclination angle* α increases the orifice length at constant wall thickness, as demonstrated in Figure 2.7b. The orifice length is then given by

$$l = t/\sin\alpha. \tag{2.1}$$

The sharp orifice, shown in Figure 2.7d, is a standardized geometry employed in flow measurements with orifice plates. The dimensions are specified in ISO 5167-2:2003 [234]. Generally, a sharp orifice is a straight orifice with square edges and $l/d < 0.02$. However, for structural reasons the wall thickness is often larger than l, so that the downstream edge needs to be beveled to maintain

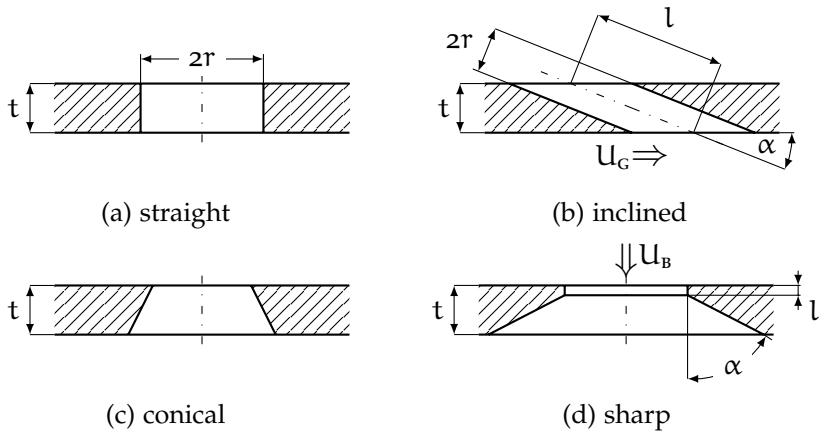

Figure 2.7: Overview of orifice profile shapes, that have been studied in the literature regarding their acoustic properties.

the sharp edge characteristics. According to the ISO standard, the bevel angle needs to be within 30° – 60°.

2.2.2 *Perforation Geometry*

Owing to their simplicity, single orifices are often employed in scientific studies. While many parameters can be investigated with a single orifice, the arrangement of a multitude of orifices in a liner adds some more degrees of freedom and complexity. Figure 2.8 illustrates different *perforation patterns*.

The most simple pattern is the *square perforation pattern* presented in Figure 2.8a. Shown is the plan view of a segment of a cylindrical liner with the coordinates x in axial direction and θ in circumferential direction. Any curvature effects are neglected for now, so that the liner is considered to be flat. The orifices are arranged in straight rows in axial and circumferential direction. The *perforation spacing* s is identical in both directions, forming a square grid. Based on the perforation spacing, an *orifice unit area* $s_x \times s_\theta$ can be assigned to each orifice (in the case of the square

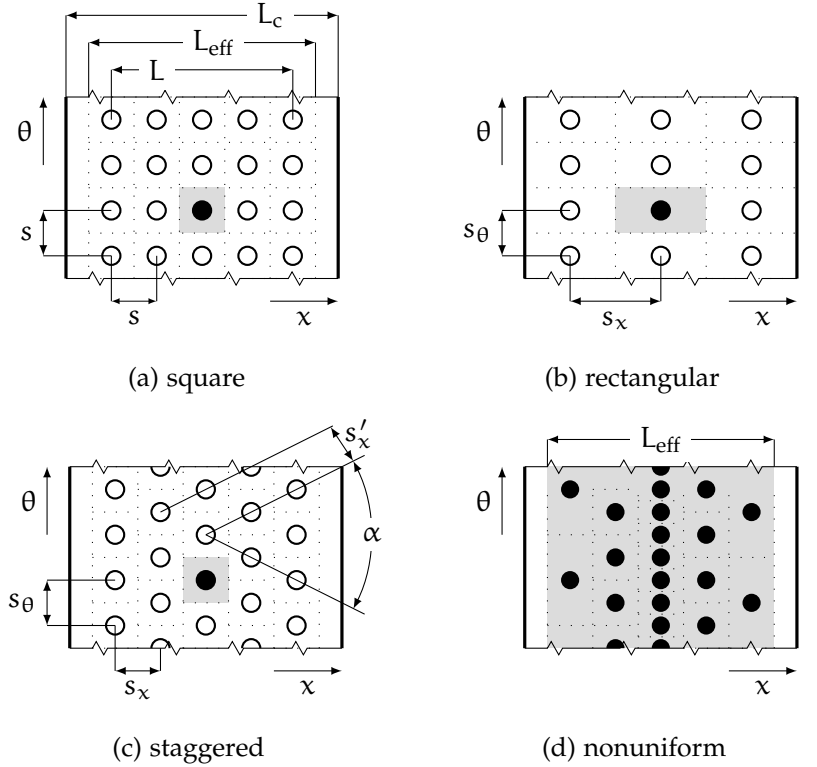

Figure 2.8: Overview of perforation patterns that have been studied in the literature regarding their acoustic properties.

pattern that is s^2). This is indicated by the dashed grid lines in Figure 2.8. For a uniform perforation pattern the *porosity* σ is defined as the ratio of the open-area of one orifice to its unit area[4] $\sigma = A/(s_x s_\theta)$. For a circular orifice in a square perforation pattern that yields $\sigma = \pi r^2/s^2$. This is illustrated by the filled black orifice and the gray area around it. For a specified surface area the same

4 In the literature this ratio is often called open-area-ratio. Here, the term open-area-ratio is reserved for the ratio of the open areas of two liners in a double-skin configuration (see Section 2.2.3).

porosity can be realized by applying many small orifices or fewer large ones.

The maximum axial distance between two orifices defines the *perforation length* L. An *effective perforation length* L_{eff} of the perforation can be specified according to the unit areas of all orifices. Finally, the *cavity length* L_c is defined by the dimensions of the cavity behind the liner. In a theoretically constructed setup the effective perforation length and the cavity length would most probably be identical (as they are in Figure 2.8b). In Figure 2.8a, the effective perforation length is shorter than the cavity length, resulting in some margins on both sides. It is as well possible, that the effective perforation length becomes longer than the cavity length, producing a 'negative' margin. In other cases the perforation only covers a fraction of the available length, resulting in large margins of hard wall. Then, the *perforation placement* could be shifted along the axial coordinate. The default position is at the center with equal margins on both sides.

An important parameter regarding the efficiency of a bias flow liner is the *total open area*, which is the open area of all orifices combined. The larger the open area, the more mass flow is needed to achieve a certain bias flow velocity.

The *rectangular perforation pattern* in Figure 2.8b is similar to the square pattern described above. The only difference is that the orifice spacing is not identical in axial and circumferential direction. This can happen easily when designing a cylindrical liner of a certain porosity. The selection of circumferential spacing is not continuous, but dependent on the circular pitch resulting from the number of orifices around the circumference. The axial spacing has to be adapted accordingly to obtain the desired porosity. The rectangular pattern is defined by the *perforation aspect ratio* s_x/s_θ. The influence of the aspect ratio on the acoustic performance was studied in [17, 288, 289].

The *staggered perforation pattern* in Figure 2.8c is the most widespread in technical applications. The structural strength of the ma-

terial is enhanced compared to a rectangular or square pattern. Common *perforation stagger angles* α are 60° (sometimes called triangular pattern) and 45° (sometimes called diagonal pattern). At 60° the distances between any neighboring orifices are equal $s_\theta = s'_x$. Thus, the sheet material retains the most strength while offering the largest possible open area. The pattern presented here has a stagger angle of 53.1°. This value might seem odd at first, but it can be easily obtained by just turning every second row of the square pattern about half the orifice circumferential spacing. By doing so, the porosity remains constant compared to the square pattern, as in both cases $s_\theta = s_x$. In order to obtain a 60° stagger angle the axial distance between the rows has to be reduced, so that the porosity would be increased in relation to the square pattern.
Another effect of the circumferential stagger is, that a potential interaction of two adjacent orifices in grazing flow direction is reduced as their distance is doubled (the orifice in-between is moved sideways).

Figure 2.8d demonstrates an example of a *nonuniform perforation pattern*. The term nonuniform is used for patterns where the porosity is not constant, either in axial direction (as shown), circumferential direction, or both. Still, the pattern is not completely random and shows some sort of regularity. In the example, the 'local' porosity increases towards the center of the liner. For nonuniform patterns the porosity is given by the ratio of the total open-area to the area defined by the active length, as indicated in Figure 2.8d. This gives an overall or average porosity. The significance of this value might be questionable, but it provides a comparative value between uniform and nonuniform patterns. The influence of nonuniform patterns is studied in [116, 259, 282] with very different configurations.

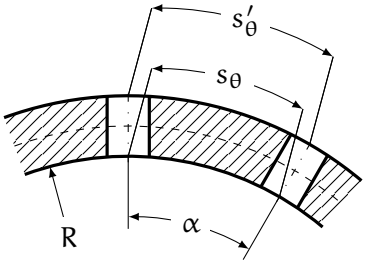

Figure 2.9: Effect of the curvature on the definition of the circumferential perforation spacing.

Curvature

Any effects of curvature on the geometric specifications above were neglected. However, the curvature requires a more detailed look at the specifications of the circumferential perforation spacing. Figure 2.9 illustrates the curvature effect. For a cylindrical liner s_θ is given as the arc length between the centers of two neighboring orifices. Due to the curvature it makes a difference if the inner arc length s_θ or the outer arc length s'_θ (or the center arc length) is used. Here, the inner arc length ($s_\theta = \pi R\,\alpha/180°$ for α in degree) will be used as the sound is incident from that side. The difference is very small for the geometries studied here, but might become more substantial for smaller duct radii and/or larger wall thickness.

2.2.3 *Cavity Geometry*

The volume behind a cylindrical liner forms an annular cavity (see Figure 2.4). Figure 2.10 gives examples of a single-skin, double-skin, and partitioned configuration. Shown is the top half of a cut through the axisymmetric cavity. The liner has the same radius as the duct and it forms the inner wall of the cavity.

Figure 2.10a illustrates a standard *single-skin* configuration. All boundaries of the cavity, except the liner, are acoustically hard.

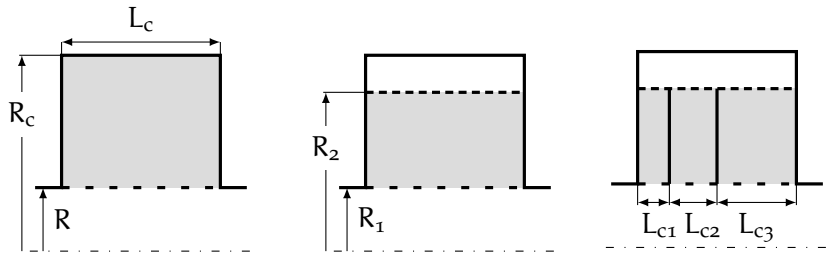

(a) single-skin (b) double-skin (c) partitioned

Figure 2.10: Overview of common variations in cavity geometry.

The *cavity length* L_c corresponds to the axial dimension of the cavity. The liner radius R and the cavity radius R_c are indicated in the drawing. The annular *cavity volume* can be calculated from $V = \pi(R_c^2 - (R + t)^2)L_c$. Variations of the cavity volume have been presented for plane liner configurations with normal sound incidence in [219, 241, 417, 423, 429, 434, 481].

The *double-skin* configuration in Figure 2.10b introduces a second liner in-between the existing liner and the cavity wall. The second liner is introduced to match the required pressure drop in a combustor, when a lower pressure drop is desired for the inner liner[5]. The velocities through the orifices of the two liners are related via the *open-area-ratio* between the two liners. According to their functions, the inner liner is called damping liner and the outer liner metering liner. Double-skin configurations are used in [142, 282, 310, 417], for example.

A variation of the cavity geometry can be obtained by partitioning the cavity into several smaller cavities. Such a *partitioned cavity* is illustrated in Figure 2.10c by introducing two solid partition walls in axial direction. Partition walls might be necessary for structural reasons.

5 Such a configuration can already be found in a combustor with an impingement cooling setup, for example.

2.3 THERMODYNAMIC PARAMETERS

A combustor operates at extreme pressure and temperature conditions. Many fluid properties change considerably when these two parameters are changing. Appendix A.3 gives an overview of the behavior of some properties of air with variation of pressure and temperature.

2.3.1 *Temperature*

The temperature within the combustor is around 2000 K and the cooling flow is provided at temperatures between 500-800 K. Most laboratory test rigs for liner measurements operate at ambient temperature, i. e. the temperature of the grazing flow and the bias flow is around 288 K. Some results are reported for tests including combustion [55, 294, 310, 357, 481, 484]. In that case, the temperature is much higher, but it is fixed at that level so that the influence of varying temperature on the absorption cannot be determined. Only a few studies exist where the temperature was controlled, e. g. involving perforated liners [381], a single orifice with cavity [144], or porous materials [93, 174, 355, 379, 381, 403, 462]. Measurements of porous materials at reduced temperature (172 K) are presented in [9]. None of the references above include a bias flow. The only configuration where temperature effects have been studied including a bias flow is a duct termination issuing a hot jet [104, 166, 251, 346, 370, 382].

Here, measurements are presented from the Hot Acoustic Test Rig (see Section 6.6). It provides an acoustically defined environment where the temperature of the grazing flow can be adjusted between ambient and 823 K. The bias flow is provided at a constant temperature of 288 K. The mean temperature of the grazing flow entering the lined section will serve as a reference temperature.

2.3.2 *Pressure*

The combustor operates at very high static pressure levels. Commonly, this is not accounted for when testing perforated liners. Even the measurements that involve combustion are typically at atmospheric conditions [55, 310, 481]. The Hot Acoustic Test Rig allows to increase the static pressure in the duct from ambient up to 1100 kPa (see Section 6.6), so that the influence of the static pressure on the absorption can be determined.

2.4 ACOUSTIC PARAMETERS

2.4.1 *Frequency*

A combustion instability is a discrete frequency phenomena. However, the exact frequency where the instability occurs cannot be predicted and it changes with the operating condition of the combustor. Therefore, the frequency characteristic of the liner is one of its most important features.

Commonly, the performance of a liner is measured over a range of frequencies. In order to obtain such a performance spectrum, various test signals can be applied, e. g. single-sine [52, 162, 247], multi-sine[82, 282], swept-sine [87], or broadband [90].

Closely related to the frequency, or more precisely the wave length, is the spatial structure of the sound field. Due to the low frequency (< 1 kHz) nature of the combustion instabilities, it is often the plane wave mode[6] that is dominant [305]. Thus, most studies are limited to plane waves. Some theoretical studies are available that describe the interaction of higher order modes with an acoustic liner, e. g. [140, 393].

6 That means, the acoustic field quantities are a function of the axial coordinate only (see Section 5.3).

2.4.2 *Amplitude / Sound Pressure Level*

The influence of the amplitude on the acoustic properties of an orifice has been the subject of many studies, e. g. [26, 58, 61, 72, 105, 123, 225, 227, 228, 243, 327, 361, 441, 473, 474, 505]. Depending on the amplitude, a linear or a nonlinear behavior is observed. The definition of a linear system is given by Bendat and Piersol [47]: The response characteristics are additive[7] and homogeneous[8]. At high amplitudes the behavior of the orifice is not homogeneous anymore, i. e. the response depends on the excitation amplitude. As a conclusion, the knowledge of the exact amplitude is rather unimportant in the linear regime, while it becomes relevant in the nonlinear regime.

Unfortunately, the definition of the amplitude is not quite consistent in the literature. Actually, often no clear definition is given. Authors refer to: the particle velocity amplitude in the orifice [227, 441], the pressure amplitude at the liner surface [41, 158, 161, 243], the amplitude of the incident wave [8, 415, 425], the amplitude at a fixed reference location in the hard-walled duct section in front of the liner [82, 142, 199, 247], the peak amplitude of the standing wave field in the hard-wall duct section [327], the amplitude in the loudspeaker mounting [7], or the amplitude in the cavity behind the perforation [227, 481].

It is generally assumed that the physical quantity relevant to the nonlinear behavior is the particle velocity in the orifice. However, in most cases it would take a great effort to measure the particle velocity in the orifice, so that the amplitude is often given in terms of sound pressure level (SPL). Now, the three most common approaches are discussed and evaluated for their comparability and practicality.

---

7 Additive means, that the output to a sum of inputs is equal to the sum of the outputs produced by each input individually: $f(x_1 + x_2) = f(x1) + f(x_2)$ [47].

8 Homogeneous means, that the output produced by a constant times the input is equal to the constant times the output produced by the input alone: $f(cx) = cf(x)$ [47].

In a setup with normal (perpendicular) sound incidence it is common to specify the *SPL at the liner surface*. It is either measured directly with a microphone installed at the liner surface [158, 161, 243][9], or determined from a wave decomposition based on microphone measurements in the hard-walled duct section [41]. The direct measurement has the advantage of being very straightforward and fast, while it requires a microphone within (or at least very close to) the liner surface. The wave decomposition method enables to extrapolate the sound field from microphones placed along the hard-walled duct onto the liner surface. However, the wave decomposition is not performed in real time with the measurements, so that typically several iterations (preliminary measurements) are necessary to set the desired SPL. The amplitude at the liner surface is dependent on the reflection coefficient of the liner, so that for keeping a constant SPL the loudspeaker output needs to be adjusted when modifying any parameters that change the liner properties, e.g. frequency, geometry, flow condition.

Another approach considers the *SPL of the incident wave* only [8, 105, 415, 425]. Normally[10], the incident wave amplitude cannot be measured directly, so that a wave decomposition is necessary. The advantage over the previous approach is that the incident wave amplitude is independent of the axial position within the hard-walled duct[11]. Furthermore, the incident wave amplitude is independent of the liner properties. The desired output of the source needs to be determined once for each frequency and SPL and can then be applied to different liner configurations and flow settings. Again, this requires an iterative measurement procedure.

9 The reference location in [161] and [243] is chosen to be very close to the liner surface, so that for low frequencies the amplitude value can be considered identical to the amplitude at the liner surface.

10 The incident wave amplitude can be measured directly when there is no reflected wave, i. e. when there is no liner installed and the duct is terminated anechoically.

11 When disregarding any losses within the hard-walled duct.

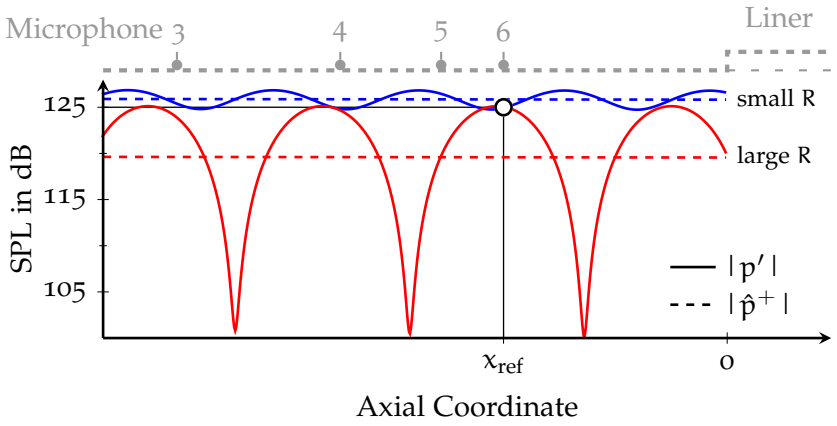

Figure 2.11: Illustration of the sound field at a nominal amplitude of 125 dB measured at position x_{ref} for a liner configuration with a small and large reflection coefficient R. Plotted is the amplitude of the sound field including the reflected wave $|p'|$ and the amplitude of the incident wave alone $|\hat{p}^+|$.

The most straightforward approach defines the *SPL at a fixed reference location* in the hard-walled duct section in front of the liner [82, 142, 199, 248]. However, Figure 2.11 demonstrates that the results can be quite misleading. Plotted is the sound pressure level over the axial coordinate obtained from a wave decomposition in the hard-walled duct section upstream of the liner for a configuration with a small and a large reflection coefficient R. The loudspeaker output is adjusted, so that the amplitude $|p'|$ at the reference position x_{ref} is 125 dB for both configurations. However, the amplitude at the liner location at $x = 0$ would be very different when choosing another axial position as reference or when the reflection coefficient changes.

The amplitude at the liner surface is independent of the test rig and thus serves well as a reference quantity when comparing different measurements. However, in a setup with grazing sound incidence the liner extends in axial direction, so that the amplitude changes along the liner (due to the presence of a standing wave

content in the sound field and due to the absorption of the liner). In this case, it is difficult to choose the 'correct' reference plane, so this approach is not applicable in a grazing incidence setup. The incident wave amplitude should be the preferred quantity in a grazing incidence setup.

Multi-Sine Signals

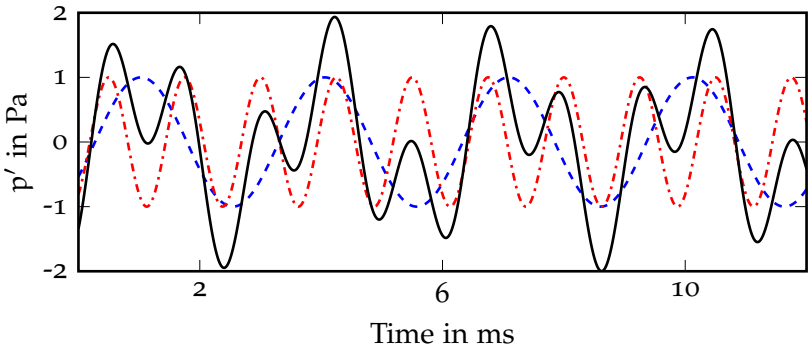

Figure 2.12: Superposition of two single-sine signals (- - - 330 Hz and -·- 800 Hz) to one multi-sine (—— 330 + 800 Hz) signal in the time domain.

Using multi-sine signals[12] can reduce the measurement time dramatically. However, multi-sine signals should be used with special care when studying high amplitude effects. Figure 2.12 illustrates the superposition of two frequency components to one multi-sine signal in the time domain. While the single-tone signals have a constant peak amplitude, the multi-sine signal shows events of varying amplitudes. Analyzing the data in the frequency domain disregards these events which are a product of the superposition. However, the orifice ´sees' these events and might behave nonlinear, when the amplitude of an event is high enough. That means, when specifying the amplitude of a multi-sine signal the

12 A multi-sine signal is synthesized by combining multiple single-sine signals.

overall SPL is the more appropriate quantity, and not the SPL of each tonal component separately. In other words, in order to ensure that one acts in the linear domain the overall SPL should be consulted. For a single-sine signal the amplitude of the tone and the overall SPL are identical.

Another characteristic of multi-sine signals in the nonlinear domain is that the different frequency components might influence each other [68, 281].

2.5 FLOW PARAMETERS

The flow paths in a combustor liner were discussed in Section 2.1. The general motion of fluid at the liner is a combination of a flow grazing the liner surface tangentially on the inside of the combustor, referred to as *grazing flow*, and the cooling flow through the orifices of the liner, referred to as *bias flow*.

2.5.1 *Grazing Flow*

The effect of a grazing flow on the acoustic properties of orifices and liners has been studied in many publications, e. g. [21, 24, 56, 81, 83, 106, 122, 145, 153–155, 175, 177, 209, 215, 244, 264–266, 268, 274, 290, 312, 322, 329, 341, 364, 384, 396, 406, 426, 467, 478, 480]. This interest in the grazing flow effect is mostly motivated by the application of liners in aero engine inlets and bypass ducts, where grazing flow Mach numbers of 0.5-0.7 are typical. This is in contrast to gas turbine combustors where $M_G = 0.05$ is a common value. So the typical grazing flow Mach number is an order of magnitude lower. Most of the references given above study the influence of the flow boundary layer on the acoustic behavior, i. e. the significance of the friction velocity over the mean flow velocity. However, Peat et al. [364] conclude that the mean flow velocity is the adequate parameter when the flow is turbulent and fully developed. The flow in a combustion chamber as well as in the

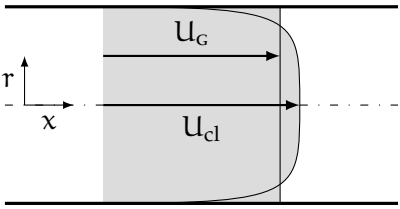

Figure 2.13: Illustration of the relationship between mean grazing flow velocity U_G and maximum velocity at the center-line U_{cl}.

test rigs used here (see Sections 6.5 and 6.6) is fully turbulent[13], so that only the mean grazing flow Mach number is considered.

The mean grazing flow velocity can be computed from the continuity equation $U_G = \dot{m}/(\rho A)$, if the mass flow rate $\dot{m}$ is known. Otherwise, the mean velocity can be determined from velocity profile measurements or, assuming turbulent pipe flow, from the measurement of the center-line velocity only. In turbulent flow the center-line velocity U_{cl} is related to the mean velocity via[14] [496, p. 346]

$$U_G \approx \frac{U_{cl}}{1 + 1.35\sqrt{f}}, \tag{2.2}$$

where f is the Darcy friction factor[15]. For Reynolds numbers in the range $Re = 4000 \ldots 10^8$, it can be approximated by $f = 0.316\sqrt[4]{Re}$ [65, 496]. The relationship between mean and center-line velocity is illustrated in Figure 2.13.

2.5.2 *Bias Flow*

The bias flow in a combustor is driven by a steady pressure difference across the liner. The higher pressure is applied to the cavity,

13 The grazing flow Reynolds number is larger than the critical Reynolds number $Re_c = 4000$ [496].

14 Equation (2.2) assumes that the boundary layer profile is described by the logarithmic law [496].

15 Named after Henry Darcy (1803-1858), French engineer.

so that the fluid discharges from the cavity, through the orifices, into the combustor. Some authors have studied the effect of *negative bias flow* [6, 26, 87, 241, 276, 332][16], that is in the opposite direction as described above. However, such a concept cannot be applied to a combustion chamber. The discharging hot gas would compromise the integrity of the liner and other components downstream. Therefore, this study exclusively treats bias flow directed into the combustor or test duct. The effect of a periodic oscillating, *unsteady bias flow* is studied by Heuwinkel et al. [200] and Lahiri et al. [280, 281] and also, will not be included here.

A steady bias flow can be defined by its mass flow rate, the pressure drop across the wall, or the velocity through the orifices. As these three quantities provide different information and enable different conclusions it is an advantage to have all three available at the same time.

The *bias flow pressure drop*, that is the pressure difference across the liner, is an operational quantity of a gas turbine combustor. A certain operating condition yields a fixed pressure drop. The air flow in the combustor is regulated by the relation of the pressure drops of the different components. Thus, it is very important to match the pressure drop when replacing a liner with a new design. Otherwise the intended air distribution might change. The pressure drop across the liner can be measured with a differential pressure meter via static pressure taps on both sides of the liner, i. e. in the cavity and in the duct. The pressure drop is then given in relation to the absolute pressure in the duct as

$$\Delta P = \frac{p_{\text{cavity}} - p_{\text{duct}}}{p_{\text{duct}}} \times 100\,\%\,. \tag{2.3}$$

In a double-skin configuration (see Section 2.2.3) the pressure drop refers to the total pressure drop across both liners, as this

16 Jing and Sun [241] and von Barthel [26] found that blowing and suction have the same effect. However, when a grazing flow is present the results are substantially different [332], e. g. Tonon et al. [478] report that the acoustic resistance appears to be a factor four lower for a grazing-bias outflow compared to a grazing-bias inflow case.

is the relevant quantity for the operation of the combustor. A typical pressure drop across a combustor wall is about 3 % [417].

The *bias flow mass flow rate* can be a measure of the efficiency of the liner, i. e. a liner achieving the same damping performance at a lower mass flow rate is more efficient. The efficiency is evaluated for the liner as a whole, so that the total mass flow rate, instead of the mass flow rate per orifice, should be compared. Most laboratory experiments use a mass flow controller to adjust the bias flow. Thus, its value is available in most cases.

The *bias flow velocity* is the quantity that is related to the absorption of sound. Typically, the velocity is not measured directly, but estimated from the pressure difference across the liner or the mass flow rate through the liner.

The literature offers two views on a definition of the bias flow velocity. Some authors [8, 17, 142, 210, 214, 219] use the velocity based on the orifice area, usually referred to as *mean orifice velocity*. The mean orifice velocity can be calculated when the mass flow rate and the open area of the liner is known. Howe [210] argues that the vorticity convection velocity is the mean velocity in the plane of the orifice. The second definition is based on the *jet velocity* [41, 55, 282]. The difference between these two velocities can be as large as a factor of 2. For a better understanding of these differences, a closer look at the steady flow field in the vicinity of the orifice is required.

Figure 2.14 illustrates the steady flow through an orifice for three significant geometries. In Figure 2.14a the fluid discharges through a thin orifice with square edges. The streamlines cannot follow the sharp contour of the geometry. They form a smooth path, resulting in a contraction of the emerging jet. The cross-section area of the jet is reduced to a value that is smaller than the actual area of the orifice[17]. The location of maximum contraction

17 Evangelista Torricelli (1608-1647), Italian physicist and mathematician, is accredited with the observation of this phenomenon.

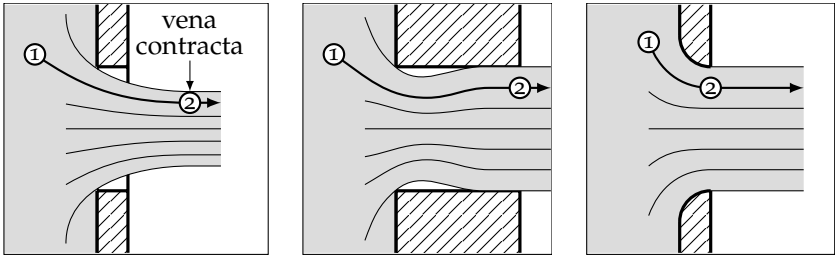

(a) thin orifice (b) thick orifice (c) round edge

Figure 2.14: Illustration of the bias flow through orifices of three significant geometries, demonstration the jet contraction and friction losses.

is named *vena contracta*[18] (latin for "contracted vein"). For a circular, sharp orifice the vena contracta is located approximately half a diameter downstream of the leading edge of the orifice [76, 353]. Here, the streamlines of the jet are parallel, the velocity is at maximum, and the pressure in the jet is equal to the surrounding pressure.

For the thick orifice shown in Figure 2.14b the flow separates at the sharp inlet edge and then reattaches to the wall before it discharges through the outlet. The emerging jet is of the same area as the orifice, but the friction losses increase. The reattachment of the flow occurs for orifice aspect ratios beyond $l/d > 2$ [119, 302]. ISO 5167-2:2003 [234] defines a thin orifice as $l/d < 0.02$. In the transition region, say $0.02 < l/d < 2$, the flow might or might not reattach, so that the flow field is subject to wide variations [320]. Unfortunately, typical liner geometries are often within this transition region.

The round edge orifice in Figure 2.14c guides the flow along the smoothly curved inlet of the orifice. The area of the resulting jet is identical with the orifice area. The friction losses are similar to the thin orifice and are small for both geometries.

18 The term *vena contracta* was introduced by Sir Isaac Newton (1642-1727, English physicist, mathematician, astronomer, natural philosopher, alchemist, and theologian) [353].

Hydraulic coefficients of the orifice

The friction losses and the jet contraction can be accounted for by introducing the hydraulic coefficients of the orifice [25, 91, 456]. The *velocity coefficient* C_v relates the theoretical velocity of an ideal fluid[19] to the actual velocity of a viscous fluid, accounting for the friction losses within the orifice

$$C_v = \frac{u}{u_{ideal}}. \tag{2.4}$$

The velocity coefficients for sharp or round orifices are similar and range from 0.95 to 0.99 [76, 456]. Typically, a value of $C_v = 0.98$ is given [25, 303], so that C_v is often neglected for these geometries. The friction losses increase considerably in a thick orifice ($l/d > 1$), where a typical value is given by $C_v = 0.8$ [25].
In engineering, the friction losses are often expressed by the *resistance coefficient* C_r, which is related to C_v by

$$C_r = 1/C_v^2. \tag{2.5}$$

The *contraction coefficient* C_c relates the area of the jet A_{jet} to the cross-section area of the orifice A. The area of the jet corresponds to location 2 in Figure 2.14 and the contraction coefficient is given by

$$C_c = \frac{A_{jet}}{A}. \tag{2.6}$$

An appreciable contraction is only observed for the thin orifice, where A_{jet} corresponds to the vena contracta. Kirchhoff [262] gives an analytical expression for the contraction of a jet through a circular orifice in a thin and infinitely extending wall as $C_c = \pi/(\pi + 2) \approx 0.611$. Rayleigh [386] derives a theoretical limit of $0.5 \leqslant C_c \leqslant 1$. Measurements with a circular, sharp orifice find a

19 Ideal fluids are free from all dissipative phenomena, e.g. they have zero viscosity and thermal conductivity [338]. The term should not be confused with ideal gas.

Table 2.2: Nominal values of the hydraulic coefficients for three significant orifice geometries corresponding to Figure 2.14 (from [25, p. 3-60]).

Orifice geometry	C_c	C_v	C_d
Thin orifice (see Fig. 2.14a)	0.62	0.98	0.61
Thick orifice (see Fig. 2.14b)	1.00	0.80	0.80
Round edge (see Fig. 2.14c)	1.00	0.98	0.98

contraction coefficient in the range from 0.61 to 0.67 [76]. Typically, $C_c = 0.62$ is used [25].

The *discharge coefficient* C_d is the ratio of the actual to the theoretical flow rate through the orifice. It considers the jet contraction as well as the friction losses and is given by the product of the velocity and contraction coefficients

$$C_d = \frac{\dot{m}}{\dot{m}_{\text{theoretical}}} = C_c \cdot C_v. \tag{2.7}$$

Often, the discharge coefficient and the contraction coefficient are used interchangeably in literature[20]. Indeed, in many cases C_v is close to unity, so that $C_d = C_c$. However, one should keep in mind that this is just an approximation and that the influence of C_v increases with thicker orifices.

For circular, sharp orifices in a straight pipe there exists a large amount of empirical formulas [221] and tabulated values [76, 442, 443]. However, the flow conditions at a liner can include non-uniform inflow conditions, orifice interaction, and maybe grazing flow, so that the standard formulas are not applicable. There is data available for more realistic flow conditions and geometries [84, 124, 125, 184, 185, 254, 407, 478], but in most cases it is more reliable to determine the hydraulic coefficients experimentally.

Nominal values of the hydraulic coefficients for geometries corresponding to Figure 2.14 are summarized in Table 2.2.

20 This was already noted by Ahuja and Gaeta [7].

Determination of the bias flow velocity from the pressure drop

For the steady flow of an ideal, incompressible[21] fluid, the pressure and velocity of any two points along a streamline are related via the Bernoulli equation[22] (Bernoulli [49], or [33, 283])

$$p_1 + \frac{1}{2}\rho U_1^2 = p_2 + \frac{1}{2}\rho U_2^2, \tag{2.8}$$

where gravity is neglected. Equation (2.8) can be applied to the orifices presented in Figure 2.14. For convenience, the location of point 1 is chosen to be far upstream, so that the velocity on the inlet side is assumed to be zero (the flow is driven by the pressure difference only). The pressure at location 2 refers to the pressure within the duct, so that the location of point 2 is at the vena contracta (Figure 2.14a) or the orifice outlet (Figure 2.14b and 2.14c). Viscosity is neglected in Equation (2.8), so that U_2 is the velocity of the jet of an ideal fluid

$$U_2 = U_{B,\text{ideal}} = \sqrt{\frac{2}{\rho}(p_1 - p_2)}. \tag{2.9}$$

The friction losses can be accounted for by the velocity coefficient C_V, see Equation (2.4). Then the bias flow velocity U_B is given by

$$U_B = C_V \sqrt{\frac{2}{\rho}(p_1 - p_2)}. \tag{2.10}$$

The bias flow velocity corresponds to the jet velocity. For thin orifices C_V is close to unity, so that it is often neglected.

Determination of the bias flow velocity from the mass flow rate

The theoretical mass flow rate of an ideal fluid through an orifice is given by the continuity equation:

$$\dot{m}_{\text{theoretical}} = \rho A U_{\overline{B},\text{ideal}}\,. \tag{2.11}$$

21 Air can be considered incompressible for $M < 0.3$ [33].

22 Named after Daniel Bernoulli (1700-1782, Swiss mathematician and physicist).

A is the orifice cross-section area, so that $U_{\overline{B}}$ corresponds to the mean velocity in the plane of the orifice, i. e. it is not taking the jet contraction into account. This is indicated by the bar over the index $\overline{B}$.
The actual mass flow rate includes the jet contraction via the contraction coefficient C_c, as well as friction losses with the velocity coefficient C_v, so that

$$\dot{m} = \rho \cdot C_c A \cdot C_v U_{B,\text{ideal}} \,. \tag{2.12}$$

Here, $U_{B,\text{ideal}}$ represents the jet velocity of an ideal fluid, corresponding to Equation (2.9). The bias flow velocity $U_B = C_v U_{B,\text{ideal}}$ is given by

$$U_B = \frac{\dot{m}}{\rho C_c A} \,. \tag{2.13}$$

U_B corresponds to the jet velocity including viscosity effects, corresponding to Equation (2.10). Unfortunately, C_c is mostly not known a priori and can only be approximated. In that case, the pressure drop and Equation (2.10) should be used to determine U_B.

In a liner with many orifices $\dot{m}$ is the total mass flow rate and the corresponding area is nA, where n is the number of orifices. This approach assumes that the mass flow is divided up evenly through all orifices. In practice, the mass flow through the orifices might vary due to a non-uniform flow distribution on the inlet side and manufacturing differences of the orifices. Then, Equation (2.13) yields the mean velocity of all orifices of the liner.

Measurement of the discharge coefficient

The discharge coefficient can be determined when the pressure difference across the liner and the mass flow rate through the

liner are both available. Combining Equations (2.10) and (2.13), together with (2.7) yields

$$C_d = \frac{\dot{m}}{\rho A \sqrt{\frac{2}{\rho}(p_1 - p_2)}}. \tag{2.14}$$

For sufficiently thin orifices it can be assumed that C_v is close to unity, so that $C_d \approx C_c$.

Here, the bias flow velocity refers to the velocity of the jet as defined in Equations (2.10) and (2.13). A certain mass flow rate or pressure difference is set for the measurement, while both quantities are recorded. Then, the velocity is calculated from the pressure difference with Equation (2.10), where it is assumed that $C_v = 1$. The bias flow velocity is given in dimensionless form as the bias flow Mach number

$$M_B = \frac{u_B}{c} \tag{2.15}$$

Furthermore, C_d is calculated from the mass flow rate and the pressure difference with Equation (2.13).

3

LITERATURE ON BIAS FLOW LINERS

Historically, the damping effect of a bias flow orifice was observed in 1916, when Borth [73] reports on the successful suppression of resonances in the ducts of a piston blower with the help of a bias flow orifice. In fact, he created a constriction by partially closing a throttle valve. His observation was confirmed by Maier and Lutz [311] and Lutz [309], who eliminated resonances by deliberately placing orifice plates into the exhaust ducts of combustion engines and reciprocating engines, respectively.

3.1 BIAS FLOW AS A CONCEPT OF IMPEDANCE CONTROL

The first study of a more fundamental nature was published in 1950 by McAuliffe [319], presenting the results of impedance tube measurements. He demonstrated the dependency of the orifice impedance on a steady bias flow. Increasing the velocity revealed a substantial drop of the orifice reactance and a linear increase of the orifice resistance[1]. When applied to a Helmholtz resonator, the bias flow provokes a shift of the resonance frequency to higher values and a decrease of the Q factor[2] of the resonance. Other au-

1 The resistance and the reactance are, respectively, the real and imaginary part of the acoustic impedance, which will be introduced in Section 4.2.

2 The Q factor, short for quality factor, describes the bandwidth of a resonance. A high Q factor represents a sharp peak, while a resonance with a low Q has a higher bandwidth.

thors reproduced these findings with a wide variety of different setups: The same setup was used by Westervelt [491], the experiments of Barthel [26] were performed with a Helmholtz resonator with normal sound incidence, the theoretical setup of Ingard [226] consisted of a perforated screen, Mechel et al. [326] studied a duct termination, and Mechel et al. [325] employed screens of porous materials. In conclusion of these studies, Utvik et al. [483, p. 3] summarize the general effects of the flow: "Alteration in absorption, which can either increase or decrease the damping effectiveness of the liner configuration; and a shift in resonant frequency, with broadening of the bandwidth characteristics."

In the meantime, technological advancements have produced further applications of the bias flow concept, namely the suppression of combustion instabilities in rocket engines [20, 62, 78, 170, 180, 300, 367, 368, 484]. An early patent describes, "[...] a combustion chamber with a perforated absorption liner having a regulator [...] to control the air flow in the space behind the liner and through the perforations thereof in such a manner so as to compensate for variations in the absorption of the liner with variations in pressure level" (US2941356 [62, p. 1]).

Feder and Dean [158] and Dean and Tester [118] propose the bias flow concept as a method of impedance control to turbofan inlet liners. Dean and Tester [118] see the greatest benefit in the ability to easily tune the impedance of the liner when it is installed in an engine. This helps to overcome the inaccuracies of the available models, thus reducing the need for expensive trial-and-error testing.

The effect of the bias flow is commonly modeled by a resistance that depends linearly on the bias flow velocity. Several authors [118, 171, 227, 326, 459, 491] use this approach with varying empirical constants. While an effect on the reactance has also been reported, this is often not reflected in the models.

The impact of the bias flow on the impedance characteristics is very similar to the behavior observed at high amplitude excita-

tion [26, 58, 61, 72, 105, 123, 225, 227, 228, 243, 327, 361, 441, 473, 474, 505]. Indeed, the high amplitude produces an oscillating flow through the orifice [228, 423, 473], so that the relevant quantity in both cases is the velocity in the orifice. Dean and Tester [118] include the bias flow in their impedance model by simply replacing the acoustic particle velocity v' with the bias flow velocity U_B. However, this can only be correct if $U_B \gg |v'|$.

The impedance model of Bauer [34] is often referred to when perforations with bias flow are involved, e. g. [14, 18, 143]. Actually, Bauer's model includes only a v' term describing the nonlinearity at high amplitudes, but not an explicit bias flow term. However, it seems common practice to replace the acoustic velocity in the nonlinear term with the bias flow velocity, as Dean and Tester [118] demonstrated. The Bauer model is presented in Section 4.6.

After a long break, the bias flow concept was revived in a comprehensive study initiated by the Boeing Company [56, 57]. The work regarding the bias flow involves measurements of various liner geometries as well as impedance modeling [52–54, 161, 162, 276, 373]. The resulting impedance model proposed by Betts [52, 54] is based on the state of the art models used in the industry with the addition of a bias flow resistance term. The bias flow term is integrated in the nonlinear impedance term by using the sum of the acoustic particle velocity and bias flow velocity as proposed by Premo [373]. The impedance model will be referred to as Betts model and is discussed in more detail in Section 4.7.

3.2 SOUND ABSORPTION DUE TO VORTICITY SHEDDING

In the late 1970s Bechert et al. [39, 40] could provide some insight into the interaction of sound with a turbulent jet. In their experiments they observed a substantial attenuation at low frequencies for pure tone sound propagating through a nozzle along a turbulent jet. The conical nozzle issuing the jet was located in an anechoic room, while the acoustic signal was introduced into the

duct upstream of the nozzle. The transmitted sound power from within the duct was compared to the sound power radiated into the far field at various jet velocities between $0 \leqslant M \leqslant 0.7$. While the sound power is conserved without flow, with flow it is attenuated at low frequencies[3]. It was verified that the sound power is neither shifted to other frequencies nor that it contributes to the broadband jet noise amplification. Also, measurements at different sound power levels revealed that the absorption effect is independent of the sound power level, i. e. it has a linear behavior.

These results reveal the existence of a sound absorption phenomenon which has not been considered previously. Bechert et al. emphasize that the characteristics of the new phenomenon, i. e. broadband, low frequency sound absorption, has been a long desired characteristic of an acoustic absorber.

Shortly after his experimental observations, Bechert [37, 38] illustrates the physical mechanisms of the absorption phenomenon and proposes a model to account for the absorption. In his theory, acoustic energy is converted into energy of fluctuating vorticity, which is shed from the nozzle edge and is dissipated into heat further downstream[4]. This is implemented in his model by applying a Kutta condition[5] at the edge to enable the vorticity shedding.

Bechert's observation and his associated theory are regarded as a breakthrough in understanding the physical phenomena of the interaction of flow and sound at an orifice. He could experi-

3 That is below $\mathrm{He} = 0.8$ or 2000 Hz for the geometry in the experiments.

4 The existence of such a phenomenon was already suspected by Gordon and Smith [180, p. 267]: "We believe that this luxuriance of interaction phenomena at low Mach numbers is all to be explained by coupling between sound and fluid flow, particularly vortices, at the sharp edges of the vent. A quantitative explanation has not been attempted."

5 Named after Martin Wilhelm Kutta (1867-1944, German mathematician) [275]. From [338]: The Kutta condition is applied to a sharp trailing edge to simulate the effects of viscosity, in flow models where viscosity is not explicitly included. The Kutta condition requires that all velocities remain finite in the vicinity of the edge.

mentally demonstrate the existence of a new mechanism of sound absorption and was able to give an explanation of the responsible physics.

Howe [208] analytically derives a model based on Powell's vortex sound theory [207, 371] applied to a low Mach number nozzle flow. His approach confirms that the main mechanism of sound absorption, when flow discharges through a nozzle, stems from the transfer of acoustic energy into vorticity.

Inspired by Bechert's experiments, Howe [210, 214] presents a model for the unsteady flow through a circular orifice. He analytically derives an expression of the Rayleigh conductivity for an orifice with bias flow and demonstrates the application of his model to a perforated plate with bias flow. Howe's model has become a quasi-standard when modeling bias flow orifices or perforations [16, 42, 131, 142, 219, 282, 317, 318, 391, 417, 430, 489]. The model itself is discussed in detail in Section 4.3.

Hughes and Dowling [219] and Dowling and Hughes [129] apply Howe's approach to a perforated plate with a solid back wall. Based on the work of Leppington [297] they develop a smooth boundary condition for the perforation in terms of an effective compliance[6,7]. The perforation consists of a uniform array of circular orifices or slits, respectively. They show theoretically and experimentally that it is possible to absorb all the incident sound energy when a solid back wall is provided. The predictions of Howe's model agree well with the experimental data.

One of the shortcomings of Howe's model is the assumption of an infinitesimal thin wall, which does not exist in practice. Jing and Sun [241] introduce a thickness term in Howe's model by physical reasoning. The resulting expression of the Rayleigh conductivity is commonly referred to as modified Howe model. Following the notation here, it will be referred to as Jing model (see Section 4.4).

6 The concept of acoustic compliance is introduced in Section 4.2.1.

7 A recent mathematical discussion on the effective compliance for various orifice geometries is given by Laurens et al. [285].

Later, Jing and Sun [242] include a finite wall thickness and the contraction of the jet in Howe's equations. However, an analytical solution can not be obtained, so that the equations are solved with the boundary element method. This extension yields an improved agreement to their measurements, compared to the modified Howe model.

Luong et al. [308] use the Cummings equation [105, 107] to derive a simplified formula for the Rayleigh conductivity of a circular bias flow orifice in an infinitesimally thin wall and in a wall of finite thickness. This approach is often referred to as simplified Howe model and is labeled Luong model in the notation used here (see Section 4.5).

Eldredge and Dowling [142] apply Howe's model to a cylindrical geometry, as described in Section 4.9.2. The Eldredge and Dowling method solves the acoustic equations in the lined section of a duct, which are coupled to the sound propagation in the cavity via the compliance of the perforation. This approach is, for example, included in a Low-Order Thermo-Acoustic Network model (LOTAN) developed by Stow and Dowling [130, 131, 452–455] and used by Rolls-Royce plc [282].

Howe's model [210], as well as the later adaptations by Jing and Sun [241] and Luong et al. [308], focus exclusively on the bias flow and do not include predictions of an orifice without bias flow. A more comprehensive approach is followed by Bellucci et al. [42]. They present an impedance model which takes into account all the usual effects when there is no flow, e. g. viscosity, mass reactance, end correction, nonlinearity, orifice interaction, and is then modified to include the bias flow effect. In contrast to the other impedance models mentioned in Section 3.1, the bias flow resistance in this model is based on Howe's formulation. This model will be referred to as Bellucci model and is described in Section 4.8.

3.3 RECENT DEVELOPMENTS

Based on publications within the last five years, there are several groups doing active research regarding bias flow orifices.

LOUGHBOROUGH UNIVERSITY / ROLLS-ROYCE (UK)

Rupp and Carrotte [415] present an experimental study regarding high amplitude effects at a single orifice with and without bias flow. The same setup is used to perform Particle Image Velocimetry (PIV) measurements. The results are processed with a Proper Orthogonal Decomposition (POD) technique to identify the coherent structures of the periodic velocity field. In a later paper [419], they are able to compare the energy found in the unsteady flow field to the lost acoustic energy and find a surprisingly good agreement. In [417], Rupp et al. present an experimental study with a model combustor geometry, but without combustion. The airflow through the fuel injector produces a complex flow field at the surface of the liner, which is representative of a realistic combustor situation. The main parameter in the study is the distance between the liners in a double-skin configuration. They are able to find an optimum distance with the help of a simple model.

UNIVERSITY OF FLORENCE / AVIO (ITALY)

Andreini et al. [16, 17, 18, 19] have published a series of papers while building up their expertise regarding bias flow liners. Andreini et al. [16] compare numerical tools for the evaluation of bias flow liners. In particular, these are a 1D network tool based on [142], the FEM solver COMSOL, and large eddy simulations with the OpenFOAM toolbox. Andreini et al. [17] present an experimental study regarding various parameters, including frequency, bias flow velocity, porosity, orifice angle, and perforation aspect ratio. A full annular geometry is analyzed in [18]. Three different models for the perforation are applied, i. e. the Howe model (see Section 4.3), the Jing model (see Section 4.4), and the Bauer model

(see Section 4.6). In their most recent paper Andreini et al. [19] study the cooling effectiveness of the perforation geometries that have been investigated for their acoustic properties in [17].

KTH ROYAL INSTITUTE OF TECHNOLOGY (SWEDEN)

Bodén and Zhou [70] and Zhou and Bodén [504] study the combination of bias flow and high amplitude acoustic excitation. In [70] they make a detailed experimental study of the transition between the dominance of the nonlinear high amplitude effect and the bias flow effect. In [504] they derive an impedance model from a modification of the Cummings equation [105, 107]. They include a new model for the discharge coefficient, which introduces a separate discharge coefficient for the periodic acoustic flow, different from the steady flow discharge coefficient.

EINDHOVEN UNIVERSITY OF TECHNOLOGY (NETHERLANDS)

Moers et al. [332] and Tonon et al. [478] present a comprehensive treatment of the grazing and bias flow interaction. They discuss the different steady flow regimes, i. e. pure grazing flow, low inflow, . . . , pure bias outflow, which were introduced by Baumeister and Rice [35] and Rogers and Hersh [406]. They present an analytical model for the inflow regime and present impedance measurements for various orifice geometries.

ECOLE CENTRALE PARIS / CNRS (FRANCE)

Tran et al. [481] investigates the use of perforated plates backed by a cavity in a combustion chamber. They designed two perforated plates that are tested in an impedance tube as well as in an atmospheric combustion test rig. Scarpato et al. [427] conduct Large Eddy Simulations of an orifice with bias flow at low and high sound levels. Scarpato et al. [428, 429, 430] present a low Strouhal number analysis and find that the optimal bias flow velocity is controlled by the porosity only. Then, the peak absorption frequency can be modified by changing the cavity depth.

They achieve a larger absorption bandwidth in the low Strouhal number regime and claim, that a low Strouhal number design is generally superior compared to previous efforts looking at the Helmholtz regime (e. g. [219]).

CAMBRIDGE UNIVERSITY (UK)

Bhayaraju et al. [55] and Schmidt et al. [434] conduct acoustic measurements in a rectangular model combustor. The acoustic absorption is measured for various perforation geometries and bias flow velocities at ambient conditions with loudspeaker excitation. In combustion tests, they evaluate the influence of the different perforation geometries on the flame.

UNIVERSITY OF DAYTON (USA)

Mazdeh and Kashani [317, 318] present results from an ongoing numerical study. They are using Large Eddy Simulation (LES) and are working on including geometry parameters like the hole size, shape, orientation, and radius to thickness ratio. So far they have presented impedance results while varying the thickness to radius ratio of the orifices. More results are announced to be presented in future publications.

DLR GERMAN AEROSPACE CENTER (GERMANY)

Two optical measurement techniques, Particle Image Velocimetry (PIV) and Laser Doppler Anemometry (LDA), are applied to a bias flow liner in [201]. This work is a joint effort with ONERA who performed the LDA measurements. Both techniques deliver similar results and are able to resolve the acoustic flow structures in the vicinity of the orifice. A third optical technique is used in a cooperation with TU Berlin and TU Dresden. Haufe et al. [191, 192] perform measurements applying Doppler Global Velocimetry with Frequency Modulation (FM-DGV). Schulz et al. [436] investigate the energy transfer with a spectral analysis approach based on FM-DGV data. The results reveal a correlation

between the absorbed energy and the production of additional spectral turbulence fluctuation components.

Heuwinkel et al. [200] and Lahiri et al. [280, 281] study the effect of an oscillating unsteady bias flow. The unsteady bias flow is generated by a high amplitude acoustic excitation within the cavity of the liner. This new concept, the Zero Mass Flow Liner, promises a dramatic reduction of the required mass flow rate while achieving a similar damping performance.

The comprehensive experimental parameter study with cylindrical bias flow liners presented in [277, 279, 282] is the basis of this thesis. All details can be found in the following chapters.

3.4 CHRONOLOGICAL OVERVIEW

Due to the large amount of publications addressing the bias flow effect, the previous sections only present a limited selection. A more comprehensive overview is given in Table 3.1. The table includes not only the perforated liner setup, but various setups where the bias flow effect can be observed: single orifice, Helmholtz resonator, perforated plate, sudden area expansion in a duct, duct termination, single-degree-of-freedom (SDOF) liner, double-degree-of-freedom (DDOF) liner. The nature of the work in the references can be mainly theoretical, experimental studies, and numerical simulations, indicated by the cross in the T (theoretical), E (experimental), and S (simulation) columns, respectively. A 'c' in the experimental column indicates that combustion tests have been performed. For a quick reference, the last columns list some common parameters that are addressed in each publication: frequency f, sound pressure level p', bias flow Mach number M_B, grazing flow Mach number M_G, porosity σ, orifice diameter d, wall thickness t, orifice angle α, cavity volume V, and temperature T.

Table 3.1: Chronological overview of publications concerned with the bias flow effect. The columns T, E, and S indicate if the nature of the work is mainly theoretical, experimental, or numerical simulations, respectively. A 'c' in the experimental column indicates that combustion tests have been performed.

Author	T	E	S	Setup	Parameters					
Borth (1916) [73]			x	orifice		M_B				
Maier (1934) [311]			x	orifice		M_B				
Lutz (1934) [309]		x	x	orifice		M_B				
McAuliffe (1950) [319]			x	orifice		M_B		d		
McAuliffe (1950) [319]			x	Helmholtz res.		M_B	M_G			
Westervelt (1951) [491]			x	orifice	f	M_B		σ	t	
Barthel (1958) [26]			x	Helmholtz res.	f	p′	M_B			
Ingard (1959) [226]		x		perforated plate	f	M_B				
Gordon (1965) [180]			x	orifice		M_B		σ		
Mechel (1965) [326]		x	x	duct termination	f	M_B		d		
Mechel (1965) [325]			x	orifice	f	M_B		d		
Utvik (1965) [483, 484]		x	c	perforated liner	f	M_B	M_G	σ		
Ingard (1967) [227]			x	orifice		p′	M_B			
Ronneberger (1967) [409, 412]			x	duct expansion	f	M_B				
Feder (1969) [158]			x	perforated plate	f	p′	M_B	M_G	σ	
Garrison (1969) [170, 171]			x	perforated liner	f	p′	M_B		σ	
Tonon (1970) [479]		x		Helmholtz res.	f	M_B				
Alfredson (1971) [11]		x	x	duct expansion	f	M_B				
Oberg (1971) [357]			c	perforated liner		M_B		σ		
Cummings (1975) [103]		x		duct expansion		M_B		d		
Dean (1975) [118]		x	x	DDOF liner	f	M_B		σ		
Munt (1977) [346, 347]		x		duct termination	f	M_B				
Bechert (1977) [39, 40]		x	x	duct termination	f	M_B				
Imelmann (1978) [223, 224]			x	duct termination	f	M_B				
Richter (1978) [397, 399, 412]			x	orifice	f	M_B				
Bechert (1979) [37, 38]		x	x	duct termination	f	M_B				
Howe (1979) [208]		x		duct termination	f	M_B				
Howe (1979) [210]		x		orifice	f	M_B		d		
Nilsson (1981) [354]		x		duct expansion	f	M_B				
Rienstra (1981) [400]		x		duct termination	f	M_B				
Salikuddin (1981) [421, 422]			x	duct termination	f	M_B				T
Sullivan (1982) [461]			x	perforate	f	M_B				
Cummings (1983) [109]		x	x	duct termination	f	p′	M_B		σ	

continued on the next page

Table 3.1 – *continued from the previous page*

Author	T	E	S	Setup	Parameters				
Whiffen (1983) [494]			x	duct termination		M_B			
Pallek (1984) [360, 412]			x	orifice	f	M_B			
Pallek (1984) [360, 412]			x	perforated plate	f	M_B			
Pallek (1984) [360, 412]			x	duct expansion	f	M_B			
Peat (1988) [363]	x			duct expansion	f	M_B			
Hughes (1990) [219]			x	perforated liner	f	M_B		σ	V
Salikuddin (1990) [424, 425]			x	perforated liner	f	p′ M_B		σ t	V
Fukumoto (1991) [168]	x			perforated plate	f	M_B			
Dowling (1992) [129]			x	perforated liner	f	M_B			
Keller (1995) [258]		x	x	Helmholtz res.	f	M_B			
Dupere (1998) [133, 134]			x	duct expansion	f	M_B			
Wendoloski (1998) [489]	x			orifice	f	M_B		d	
Ahuja (1999) [6, 87]			x	DDOF liner	f	M_B	M_G		
Jing (1999) [241]			x	perforated liner	f	M_B		σ t	V
Kwan (1999) [276]			x	SDOF liner	f	p′ M_B	M_G		
Premo (1999) [373]		x	x	SDOF liner	f	p′ M_B		σ	
Zhao (1999) [502]			x	perforated liner	f	p′ M_B		σ	
Ahuja (2000) [8]			x	orifice	f	M_B			
Betts (2000) [52, 54, 162]		x	x	perforated liner	f	p′ M_B		σ t	
Jing (2000) [242]		x	x	perforated plate	f	M_B		σ t	
Betts (2001) [53]		x	x	perforated plate	f	M_B		σ	
Dupere (2001) [135]			x	duct expansion	f	M_B			
Durrieu (2001) [138]		x	x	orifice	f	M_B		σ	
Durrieu (2001) [138]		x	x	perforated plate	f	M_B		σ	
Hofmans (2001) [138, 203]		x	x	orifice	f	M_B			
Follett (2001) [161]		x	x	DDOF liner	f	M_B			
Bellucci (2002) [41, 43]		x	x	perforated liner	f	p′ M_B		σ t	
Bielak (2002) [56]			x	DDOF liner	f	p′ M_B	M_G		T
Dupère (2002) [136, 137]		x	x	Helmholtz res.	f	M_B			
Sun (2002) [463]			x	orifice	f	M_B	M_G	σ t	
Sun (2002) [463]			x	perforated plate	f	M_B	M_G	σ t	
Eldredge (2003) [142]		x	x	cylindrical liner	f	M_B	M_G		
Forster (2003) [164]			x	perforated plate	f	M_B		σ	
Forster (2003) [164]			x	cylindrical liner	f	M_B	M_G	d	
Eldredge (2004) [140]	x			cylindrical liner	f	M_B			
Rademaker (2004) [378]			x	3DOF liner	f	p′ M_B	M_G		
Boij (2005) [71]		x	x	duct expansion		M_B			
Luong (2005) [308]	x			orifice	f	M_B		d t	
Heuwinkel (2006) [197, 198]			x	cylindrical liner	f	M_B	M_G	σ	

continued on the next page

Table 3.1 – *continued from the previous page*

Author	T	E	S	Setup	Parameters						
Macquisten (2006) [310]		c		cylindrical liner		M_B	M_G	σ			T
Efraimsson (2007) [139]			x	orifice	f	M_B					
Eldredge (2007) [141]			x	perforated plate	f	M_B	M_G		α		
Lee (2007) [291]	x	x		perforated plate	f	M_B		σ			
Leung (2007) [299]			x	orifice	f	M_B		d			
Dasse (2008) [112, 328]			x	perforated plate	f	M_B					
Gullaud (2008) [187, 188]			x	perforated plate	f	M_B					
Heuwinkel (2008) [199]		x		cylindrical liner	f	p′	M_B	M_G			
Mendez (2009) [328]			x	perforated plate	f	M_B					
Rupp (2009) [415, 418]		x		orifice		p′	M_B				
Tran (2009) [481]		c		perforated plate	f	p′	M_B			V	T
Zhao (2009) [500, 501]		x		cylindrical liner	f	p′	M_B				
Bhayaraju (2010) [55]		c		perforated liner	f	M_B		σ	α		
Heuwinkel (2010) [201]		x		cylindrical liner	f	M_B	M_G				
Lahiri (2010) [202, 282]		x		cylindrical liner	f	M_B	M_G	σ	t	V	
Lei (2010) [294]		c		perforated liner		M_B		σ			T
Rupp (2010) [415, 419]		x		orifice		p′	M_B		t		
Schmidt (2010) [434]		x		perforated liner	f	M_B	M_G	σ	α	V	
Andreini (2011) [16]			x	cylindrical liner	f	M_B	M_G	σ	α		
Mazdeh (2011) [317]			x	orifice	f	M_B					
Rupp (2011) [416, 417]		x		perforated liner	f	M_B				V	
Scarpato (2011) [427]			x	perforated plate		p′	M_B				
Andreini (2012) [17]		x		cylindrical liner	f	M_B		σ	α		
Bodén (2012) [70]		x		orifice	f	p′	M_B				
Jayatunga (2012) [240]		x		perforated liner	f	M_B		σ	t		
Jörg (2012) [252]		x		cylindrical liner	f	M_B				V	
Lahiri (2012) [279]		x		cylindrical liner	f	M_B	M_G			V	T
Mazdeh (2012) [318]			x	orifice	f	M_B		d	t		
Moers (2012) [332]		x		slit	f	M_B	M_G		α		
Scarpato (2012) [428, 430]		x		perforated liner	f	M_B		σ		V	
Zhong (2012) [503]	x			cylindrical liner	f	M_B	M_G				
Andreini (2013) [18]			x	perforated liner	f	M_B					T
Schulz (2013) [436]		x		perforated liner	f	M_B	M_G				
Tonon (2013) [478]		x		slit	f	M_B	M_G		α		
Zhou (2013) [504]		x		orifice	f	M_B			t		
Rupp (2014) [420]		x		Helmholtz res.	f	p′	M_B		t		

4

MODELING OF BIAS FLOW LINERS

4.1 RAYLEIGH CONDUCTIVITY

The first attempt at a theoretical description of the acoustic properties of an orifice was presented by Rayleigh [385, 390] when he was studying Helmholtz resonators. He introduced the concept of acoustic conductivity as an analogy to Ohm's law[1] in electricity. While the electric conductivity of a circuit element is described by the ratio of the electric current to the potential difference, the acoustic conductivity of an orifice is given by the ratio of the volume flow through the orifice to the driving pressure difference. It is commonly referred to as Rayleigh conductivity[2].

Let the fluctuating pressure on both sides of an orifice be a harmonic function of time, so that $p_1' = \mathrm{Re}\{\hat{p}_1 \, e^{i\omega t}\}$ for the fluctuating pressure above and $p_2' = \mathrm{Re}\{\hat{p}_2 \, e^{i\omega t}\}$ for the fluctuating pressure below the orifice. Then, the pressure difference across the orifice $\mathrm{Re}\{(\hat{p}_1 - \hat{p}_2) \, e^{i\omega t}\}$ produces the fluctuating volume velocity $q' = \mathrm{Re}\{\hat{q} \, e^{i\omega t}\}$ through the orifice. When the flow is regarded

1 Named after Georg Simon Ohm (1789-1854, German physicist and mathematician) [358].

2 Named after John William Strutt, Lord Rayleigh (1842-1919, English physicist).

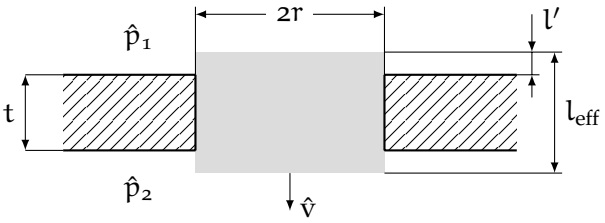

Figure 4.1: Illustration of the quantities determining the Rayleigh conductivity of an orifice.

as incompressible and the orifice is acoustically compact, that is $\lambda \gg r$, then the Rayleigh conductivity is defined as [385, 390][3]

$$K_R = i\omega\rho \frac{\hat{q}}{\hat{p}_1 - \hat{p}_2}, \tag{4.1}$$

where ρ is the mean density. The acoustic volume velocity is defined as $\hat{q} = A\hat{v}$, with the orifice area $A = \pi r^2$ and the acoustic particle velocity $\hat{v}$. This is illustrated in Figure 4.1.

In an ideal fluid the Rayleigh conductivity is determined by the orifice geometry alone. For a circular orifice in a wall of infinitesimal thickness Rayleigh found that [385, 390]

$$K_R = 2r, \tag{4.2}$$

where r is the orifice radius. For an orifice in a wall of finite thickness the Rayleigh conductivity can be expressed as the ratio of the area of the orifice and an effective length [385, 390]

$$K_R = \frac{A}{l_{eff}}. \tag{4.3}$$

The effective length is longer than the physical length of the orifice l. The additional length l' accounts for the additional mass of fluid that takes part in the oscillatory motion outside of the orifice

3 In addition to Rayleigh's original derivation detailed discussions are given by Stewart and Lindsay [447, Ch. 2.4], Morfey [336], and Howe [214, Ch. 5.3].

and is commonly referred to as *end correction*. This is illustrated in Figure 4.1. The effective length is defined as the sum of the physical length of the orifice and the end correction for both ends: $l_{\text{eff}} = l + 2\,l'$.

In continuation, Rayleigh derives an upper and lower limit of the conductivity[4] [385, 390]

$$\frac{\pi r^2}{l + \frac{16}{3\pi} r} < K_R < \frac{\pi r^2}{l + \frac{\pi}{2} r} \tag{4.4}$$

For $l = 0$ the upper limit coincides with Equation (4.2) and the end correction can be determined from Equation (4.4) to be in the range $0.785\,r < l' < 0.849\,r$. In a further analysis Rayleigh [385, 390] suggests $l' \approx 0.82\,r$ as the appropriate value for an orifice in an infinite wall. The exact value of the end correction has been an ongoing topic of discussion. A generally accepted value for one end of an orifice in a wall[5] is [72, 100, 225, 260, 339]

$$l' = \frac{8}{3\pi} r \approx 0.85\,r\,. \tag{4.5}$$

While the end correction can be neglected for $l \gg r$ it contributes substantially when $l \to 0$.

4.2 ACOUSTIC IMPEDANCE

The concept of acoustic impedance is similar[6] to the Rayleigh conductivity, but allows a more comprehensive description of a dynamic system. Originally, the impedance concept was introduced by Heaviside [193] for treating alternating currents of electricity.

4 A recent mathematical discussion of the limits is given by Laurens et al. [286].

5 This configuration is often referred to as flanged pipe, in contrast to an unflanged pipe.

6 It is shown in Appendix B.1, how the Rayleigh conductivity is converted into an impedance.

The electric impedance is defined by the ratio of voltage to current and is measured in Ohm. It describes the opposition of an element to transmit a current when a voltage is applied. Accordingly, the acoustic impedance is defined as the complex ratio of the acoustic pressure to the acoustic volume velocity (Webster [487] or [369])

$$Z = \frac{\hat{p}}{\hat{q}}, \tag{4.6}$$

Another form of impedance is given by the specific impedance

$$z = \frac{\hat{p}}{\hat{v}}. \tag{4.7}$$

The specific impedance is related to the acoustic impedance by $Z = z/A$ and is used to describe the acoustic properties of a medium or material, for example a perforated wall. Then, $\hat{v}$ is the normal component of the acoustic particle velocity directed into the surface. The specific impedance of a fluid is a characteristic quantity of the medium only and is therefore referred to as characteristic impedance z_0. For plane waves $z_0 = \rho c$. A convenient dimensionless quantity is obtained by the ratio of specific and characteristic impedance, i. e. the normalized specific impedance

$$\zeta = z/z_0. \tag{4.8}$$

Mathematically, the impedance is represented by a complex number[7]

$$Z = R + iX, \quad z = r + ix, \quad \text{and} \quad \zeta = \theta + i\chi, \tag{4.9}$$

where the real part is referred to as resistance and the imaginary part as reactance.

7 The notation is for an $e^{i\omega t}$ time dependency. For a negative exponent the imaginary part in Equation (4.9) changes sign.

4.2.1 *Impedance Modeling of Perforations*

When the dimensions of an acoustic element, e. g. orifice, Helmholtz resonator, etc., are much smaller than the relevant acoustic wavelength, its characteristic behavior can be described by three parameters: the resistance R, the inertance M, and the compliance C. The acoustic impedance can be written as the sum of these three quantities [260]

$$Z = R + i\left[\omega M - 1/(\omega C)\right]. \tag{4.10}$$

The three parameters R, M, and C are commonly referred to as lumped parameters and an element that complies with the acoustic compact assumption is a lumped element.

In a mechanical system the resistance represents a linear, massless, viscous damper, the inertance corresponds to a lumped mass, and the compliance describes the reciprocal of the stiffness of a lumped, linear, massless spring [156]. Generally, the resistance describes the energy dissipation, while the reactive elements store energy, either in the form of potential energy in a spring-like element or kinetic energy in a mass-like element [338].

Now, the process of building up an impedance model of a perforate is demonstrated. Similar, but more detailed derivation can be found in [271, 327].

Internal Impedance

First, the impedance within an orifice is considered, without any end effects. The normalized specific impedance for a unit length l of an infinite tube filled with a viscous fluid is given by (Crandall [100] or [327])

$$\zeta = \frac{1}{\sigma}\frac{ikl}{F(k_s' r)}. \tag{4.11}$$

The division by the porosity σ converts the impedance of a single orifice into the impedance of an array of orifices in a perforation[8]. ikl is the inviscid impedance of an infinite tube. It describes the inertia of the oscillating mass of air. The function F introduces the viscous effects. Based on the theories given by Stokes [451], Helmholtz [195], and Kirchhoff [261], which are presented in Section 5.4.1, Crandall [100, Appx. A] derives

$$F(x) = 1 - \frac{2\,J_1(x)}{x\,J_0(x)}\,, \tag{4.12}$$

where J_0 and J_1 are Bessel functions[9] of the first kind. The effective Stokes wave number[10] k_s' considers the viscosity as well as thermal conductivity losses near a highly conducting wall. In order to include both effects an effective kinematic viscosity $\nu' = 2.179\nu$ is used, so that $k_s' = \sqrt{-i\omega/\nu'}$. Sometimes the heat conduction is neglected entirely, then ν' is replaced by ν.

The Bessel functions with a complex argument produces a complex result, so that the impedance consists of a reactive and resistive part. Unfortunately, more physical insight is not provided by Equation (4.11). However, two approximations do exist, which are more physically revealing. Depending on the shear number $Sh = r\sqrt{\omega/\nu}$ they yield [100, 327]:

$$\zeta \approx \frac{8\nu l}{c\sigma r^2} + i\frac{k}{\sigma}\left(l + \frac{1}{3}l\right) \qquad \text{for } Sh < 2 \tag{4.13}$$

$$\zeta \approx \frac{\sqrt{2\omega\nu}\,l}{c\sigma r} + i\left(\frac{kl}{\sigma} + \frac{\sqrt{2\omega\nu}\,l}{c\sigma r}\right) \qquad \text{for } Sh > 10 \tag{4.14}$$

8 Often, the impedance is divided also by the discharge coefficient, e. g. [271]. However, this was not done traditionally, e. g. [100, 327].

9 Named after Friedrich Wilhelm Bessel (1784-1846, German mathematician and astronomer). Bessel functions are the solutions to the Bessel differential equation [51]. They are a standard mathematical tool when dealing with cylindrical geometries, e.g. [3, 77].

10 Named after Sir George Gabriel Stokes (1819-1903, Irish mathematician and physicist.

The resistance terms in Equations (4.13) and (4.14) represent the well known Poiseuille- and Helmholtz-type losses within a tube (e. g. [260]), respectively. Besides the obvious introduction of a resistance term, the viscosity also affects the mass reactance, which is increased from its inviscid value.

Mass End Correction (Radiation Reactance)

It was already discussed in Section 4.1, that the effective length which needs to be accounted for in the inertance is longer than the actual length of the orifice. This additional length is defined by the reactive part of the radiation impedance of a circular piston of air in an infinite baffle. A typical value considering both ends is $2l' = 16r/(3\pi)$, e. g. [260].

Resistance End Correction

In the idealization of the effective length the orifice is virtually extended, keeping the same cylindrical shape. In reality the air is drawn from the radial direction as well. This is considered by Ingard [225] and he introduces an additional resistive end correction to account for the friction losses on the wall surrounding the orifice. A very similar term is presented by Sivian [441], but he justifies the additional resistance with friction losses in the shear layer of the emerging jet. Following the discussion of Melling [327], Sivian's expression will be used here. Similar to the mass end correction, the additional resistance is included by extending the length of the orifice (now in the resistance term). Sivian finds good agreement with experiments when using the same additional length as for the reactance. Applying both end corrections to Equation (4.11) yields [327, 441]

$$\zeta = \frac{ik}{\sigma}\left(\frac{l}{F(k_s' r)} + \frac{16r/(3\pi)}{F(k_s r)}\right), \tag{4.15}$$

Please note, that the Stokes wave number external to the orifice considers the viscosity only, i. e. $k_s = \sqrt{-i\omega/\nu}$.

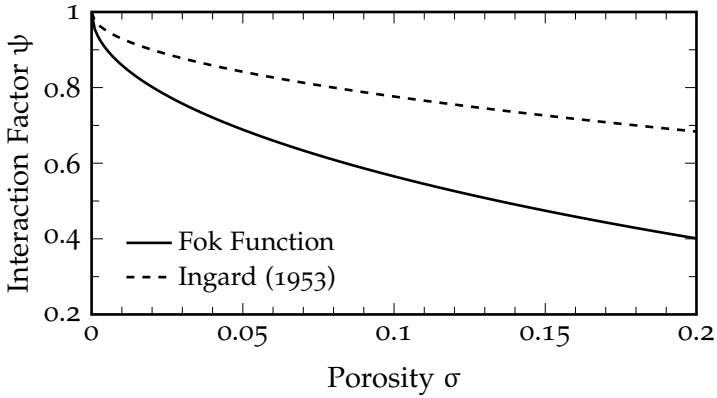

Figure 4.2: Orifice interaction factor ψ plotted over the porosity according to Ingard (Equation (4.16)) and Fok (Equation (4.17)).

Orifice Interaction

Ingard [225] studied the interaction effect of two adjacent orifices and introduces a correction factor for the end correction

$$\psi(\sigma) = 1 - \sqrt{\frac{\sigma}{2}}\,. \tag{4.16}$$

The correction factor $\psi(\sigma)$ reduces the end correction with increasing porosity, i. e. with decreasing orifice distance. The term above was used by Guess [186] and Bellucci et al. [41], for example. Melling [327] presents a comprehensive discussion on the topic and refers to a solution that was found by Fok [160]

$$\psi(\sigma) = \sum_{n=0}^{8} a_n \left(\sqrt{\sigma}\right)^n \text{, with} \tag{4.17}$$

$$\begin{aligned} a_0 &= 1\,, & a_1 &= -1.4092\,, & a_2 &= 0\,, \\ a_3 &= 0.33818\,, & a_4 &= 0\,, & a_5 &= 0.06793\,, \\ a_6 &= -0.02287\,, & a_7 &= 0.03015\,, & a_8 &= -0.01614\,. \end{aligned}$$

Figure 4.2 plots Equations (4.16) and (4.17) over the porosity. The Fok function predicts a stronger influence of the interaction than Ingard's approach and will be used here. Melling [327] states that the interaction effects can be neglected for porosities $< 4\,\%$.
Applying the correction for orifice interaction to Equation (4.15) yields [327, Eq. 18][11]

$$\zeta_{\text{Melling}} = \frac{ik}{\sigma}\left(\frac{l}{F(Sh')} + \frac{16r/(3\pi)}{F(Sh)}\psi\right), \tag{4.18}$$

Equation (4.18) will be referred to as Melling model.

Nonlinear Resistance

At high amplitudes the acoustic behavior of the orifice becomes nonlinear [327, 441], i. e. the impedance depends on the amplitude of the oscillation. Various approaches have been followed to include this effect in the impedance formulation [72, 225, 227, 228, 327, 441, 479, 505, 507]. For example, Melling [327] derives a resistance term that depends on the velocity within the orifice, describing the nonlinear behavior[12]:

$$\theta_{\text{nl}} = \frac{1.2}{2c}\frac{1-\sigma^2}{(\sigma C_d)^2} v'_{\text{rms}}, \tag{4.19}$$

11 Please note, that there is a mismatch in the handling of the Fok function in Melling's paper [327]. Melling defines the Fok function as in Equation (4.17), but divides the end correction by ψ, instead of multiplying it as shown in Equation (4.18). This is clearly not correct. As shown in Figure 4.2, the Fok function is smaller than unity and thus needs to be multiplied to achieve the desired effect. However, it seems that Melling uses the Fok function as it would be defined as the reciprocal of Equation (4.17). For example, in Fig. 6 of [327], Melling plots $1/\psi$, but labels it with ψ. Unfortunately, Melling's erroneous formula had been reproduced by others, e. g. [52, 54, 271, 288, 472] (though Kraft et al. [271] seem to use it correctly). The correct notation was used by Randeberg [383] and the mismatch was also pointed out by Elnady [143].

12 Generally, the nonlinearity will affect the reactance as well [143, 186], which was neglected by Melling.

where v'_{rms} is the root-mean-square value of the acoustic velocity within the orifice. The difficulty is, that the impedance now depends on the acoustic particle velocity. So it is not possible to directly calculate the impedance when the acoustic pressure is known. The acoustic particle velocity can be determined iteratively from $|v'| = |p'|/(\rho c\sqrt{\theta^2 + \chi^2})$ [143]. However, a first approximation of the acoustic particle velocity can be given from the applied sound pressure level SPL by [54]

$$v'_{rms} = \frac{1}{2c\sigma C_d} \frac{p_{ref} 10^{SPL/20}}{\rho c}. \tag{4.20}$$

Including the nonlinear resistance term in Equation (4.18) yields the nonlinear Melling model

$$\zeta_{Melling,nl} = \frac{ik}{\sigma}\left(\frac{l}{F(Sh')} + \frac{16r/(3\pi)}{F(Sh)}\psi\right) + \frac{1.2}{2c}\frac{1-\sigma^2}{(\sigma C_d)^2} v'_{rms}. \tag{4.21}$$

Radiation Resistance

Another contribution that was neglected by Melling is given by the resistive part of the radiation impedance[13]. It accounts for the acoustic losses by radiation into the surrounding medium. The radiation resistance for an array of circular orifices is (Morse and Ingard [340, p. 384] or [271])

$$\theta_{rad} = \frac{1}{\sigma}\left(1 - \frac{J_1(2kr)}{kr}\right). \tag{4.22}$$

For small kr Equation (4.22) can be approximated by [271]

$$\theta_{rad} \approx \frac{(kr)^2}{2\sigma} \tag{4.23}$$

Equation (4.22) or (4.23) can be simply added to the impedance, similarly to θ_{nl} above.

13 The reactive part of the radiation impedance is already included by the mass end correction as discussed above.

4.2.2 *Grazing Flow Impedance*

The effect of grazing flow on the impedance is often accounted for by a simple contribution to the resistance [34, 186, 194, 392][14]

$$\theta_G = \frac{0.3\, M_G}{\sigma} \tag{4.24}$$

More sophisticated models are available, e. g. [106, 181, 209, 244, 266, 290]. Especially the importance of the friction velocity, rather than the mean flow velocity, has been studied [175, 194]. However, Peat et al. [364] conclude that the influence of the friction velocity is of no significance when the boundary layer is turbulent and fully developed. That is the case for the measurements presented here, so that the use of the mean velocity is adequate and the simple model of Equation (4.24) is sufficient. It should be noted, that Equation (4.24) neglects the reduction of the attached mass by the grazing flow.

4.2.3 *Bias Flow Impedance*

Traditionally, there are two alternatives to include the influence of a steady bias flow on the impedance of an orifice or perforation. In the first approach the acoustic particle velocity in a nonlinear model is replaced by the bias flow velocity [34, 118, 171, 227, 326, 459, 505]. This replacement is only reasonable if the bias flow velocity is assumed to be much greater than the acoustic particle velocity. For a simple linear relationship of resistance and bias flow Mach number given by Sivian [441] this yields

$$\theta_B = \frac{C \cdot M_B}{\sigma} \tag{4.25}$$

and is very similar to the grazing flow resistance introduced in Equation (4.24). C is a constant that is based on empiricism and

14 The factor of 0.3 is most common. However, some variations can be found in the literature, for example Rice [392] suggests 0.5.

is in the range $1 - 1.5$, typically 1.15 [34][15]. For a steady bias flow Cummings and Eversman [109] derive $C = (1 - \sigma^2 C_c^2)/C_c^2$ from the linearized Bernoulli equation, where C_c is the contraction coefficient of the jet.

The second approach combines the effects of the acoustic particle velocity and the steady bias flow velocity in one resistance term. For example, Premo [373] suggests a combined velocity term of $\sqrt{(1.15\, v'_{rms})^2 + (2\, U_B)^2}$. Betts [52, 54] finds the similar expression $|1.2\, v'_{rms} + 2\, U_B|$. Adding this to Equation (4.19) yields

$$\theta_B = \frac{1}{2c} \frac{1 - \sigma^2}{(\sigma C_d)^2} |1.2\, v'_{rms} + 2\, U_B| \tag{4.26}$$

Both approaches are mostly based on empiricism and lack the influence of the bias flow on the reactance.

More advanced approaches are presented by Jing and Sun [242] and Lee et al. [291]. However, both need to be solved numerically, so that they do not provide a simple parametric description of the impedance. Jing and Sun [242] solve Howe's [210] governing equations with a boundary element method. Howe himself obtains an analytical solution when assuming infinitesimal thickness and a cylindrical vortex sheet (see Section 4.3 below). Jing and Sun [242] include a finite thickness and allow a contraction of the vortex sheet, which requires a numerical solution of the equations. Lee et al. [291] determine the impedance of a perforated plate by solving the incompressible Euler equation. In particular, they consider the interaction effect.

4.3 HOWE RAYLEIGH CONDUCTIVITY MODEL

Howe [210, 214] analytically derives a formulation of the Rayleigh conductivity for an orifice with a bias flow and includes the ab-

15 This value is often accredited to Bauer [34]. However, Bauer himself references Zinn [505]. Both, Zinn [505] and Bauer [34], use this term to describe high amplitude effects, not a steady bias flow. See as well the discussion in Section 4.6.

sorption caused by vorticity shedding. He treats a single, circular orifice in a wall of infinitesimal thickness. On the inlet side the flow field resembles that of a potential sink at the center of the orifice and on the outlet side that of an axisymmetric jet flow with a potential core and shear layer. Viscosity is neglected except at the rims of the orifice, where the acoustic perturbations trigger the periodical shedding of vortex rings. The convection velocity of the vortex rings is taken to be the mean velocity within the orifice. The radius of the vortex rings coincides with the orifice radius and remains constant when traveling downstream, forming a cylindrical vortex sheet. The assumptions can be summarized:

1. The frequency of the sound is low, so that the wavelength is much larger than the orifice radius (the orifice is acoustically compact)[16]: $\lambda \gg r$
2. The Mach number of the bias flow is low, so that the fluid can be considered incompressible[17]: $M_B \ll 1$
3. The Reynolds number of the bias flow is high, so that viscosity is only considered at the rims of the orifice[18]: $U_B\, r/\nu \gg 1$
4. The wall is infinitely thin: $t = 0$

After a lengthy derivation Howe arrives at [210, 214][19]

$$K_R = 2r(\gamma + i\delta) \tag{4.27}$$

16 For the largest orifice dimension treated in the parameter study here ($r = 1.25\,\mathrm{mm}$), this yields a frequency limit of $f \ll 272360\,\mathrm{Hz}$ at standard temperature and pressure conditions. Higher temperatures and smaller radii increases the limit further.

17 Typically, $M_B < 0.3$.

18 The highest limit is given at high temperature, low pressure, and small radius. The extreme values of the parameter study here ($T = 823.15\,\mathrm{K}$, $p = 101.325\,\mathrm{kPa}$, $r = 0.5\,\mathrm{mm}$) restrict the applicability of Howe's model to $M_{\overline{B}} \gg 0.0003$.

19 Here, the sign is adjusted to the $e^{i\omega t}$ convention.

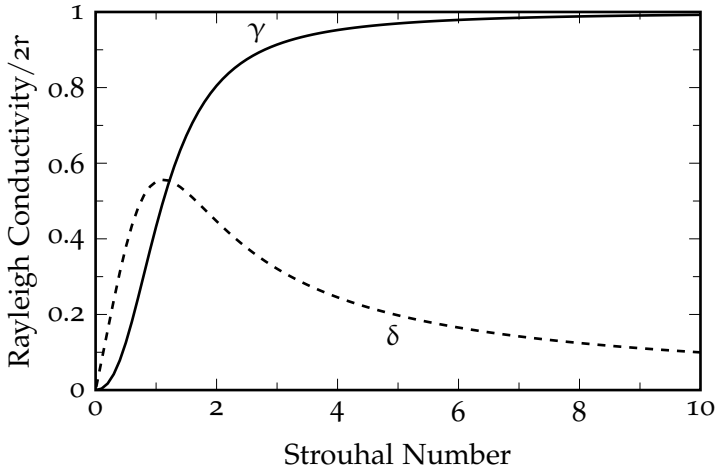

Figure 4.3: Real part γ and imaginary part δ of the normalized Rayleigh conductivity plotted over the Strouhal number.

with

$$\gamma + i\delta = 1 + \frac{\frac{\pi}{2} I_1(St)\, e^{-St} + iK_1(St)\, \sinh(St)}{St\left[\frac{\pi}{2} I_1(St)\, e^{-St} - iK_1(St)\, \cosh(St)\right]}, \tag{4.28}$$

where St is the Strouhal number, and I_m and K_m are the modified Bessel functions of order m of first and second kind, respectively. Equation (4.28) is a function of the Strouhal number only. The Strouhal number is based on the vorticity convection velocity, which is, according to Howe [210], assumed identical to the mean velocity within the orifice $U_{\overline{B}}$, and the orifice radius $St = \omega r / U_{\overline{B}}$.

Figure 4.3 plots the real and imaginary part of Equation 4.28 over the Strouhal number. γ represents the inertia of the orifice, while δ is a resistance term responsible for the acoustic absorption. At very high Strouhal numbers $\delta \to 0$, i. e. the vorticity shedding has a negligible influence and δ reverts to its value in the absence of the flow. The maximum of the imaginary part is found at a Strouhal number just beyond unity.

Howe's model has become a quasi-standard describing the bias flow effect at an orifice [16, 42, 131, 142, 219, 282, 317, 318, 391, 417, 430, 489]. However, Howe's model assumes an infinitely thin wall. This assumption does not hold for any practical application. A modified Howe model that includes a finite thickness is proposed by Jing and Sun [241] (see below). Most references listed above resort to the modified version to include the thickness.

4.4 JING MODEL (MODIFIED HOWE MODEL)

Jing and Sun [241] propose a way to include the wall thickness in Howe's model. Their argumentation is expressed in terms of impedance. The relation between the normalized specific impedance ζ and the Rayleigh conductivity is given by[20]

$$\zeta = \frac{ikA}{K_R}. \tag{4.29}$$

For a circular orifice $A = \pi r^2$ with bias flow $K_R = 2r(\gamma + i\delta)$ and after splitting the real and imaginary parts by multiplication with $(\gamma - i\delta)/(\gamma - i\delta)$ this results in

$$\zeta = \frac{k\pi r\delta}{2\left(\gamma^2 + \delta^2\right)} + i\frac{k\pi r\gamma}{2\left(\gamma^2 + \delta^2\right)}. \tag{4.30}$$

The thickness adds a mass inertance to the system so that the impedance for a circular orifice of finite thickness and with bias flow yields [241]

$$\zeta_{\text{Jing}} = \frac{k\pi r\delta}{2\left(\gamma^2 + \delta^2\right)} + i\left(\frac{k\pi r\gamma}{2\left(\gamma^2 + \delta^2\right)} + kt\right), \tag{4.31}$$

where viscosity effects have been neglected. The δ term represents the acoustic resistance due to the bias flow, the γ term describes the end correction when a bias flow is present, and the t term adds the mass inertance of the fluid within the orifice. The thickness

20 This relation is derived in Appendix B.1.

Table 4.1: Parameter range of experimental data that has been compared to the modified Howe model.

		Jing [241, 242]	Eldredge [142]	Andreini [17]	Scarpato [428, 430]
f	Hz	300-1400	100-700	200-1500	100-2000
SPL	dB	90-125	90-120	N/A	100
M_B	–	0.004-0.07	0.005-0.045	0.03-0.13	0.005-0.0.045
M_G	–	N/A	0-0.057	0.02	N/A
σ	%	1.13-2.54	4	1.16	1-15.3
d	mm	2-5	0.75	0.8	0.6-1
t	mm	0.2-3	3	2.5	1
α	deg	90	45	30-90	90

term was simply added to the impedance. The conductivities need to be added reciprocally $1/K_R = 1/K_1 + 1/K_2$, so that the Rayleigh conductivity for a circular orifice of finite thickness with bias flow yields

$$K_R = 2r \left(\frac{1}{\gamma + i\delta} + \frac{2t}{\pi r} \right)^{-1}. \tag{4.32}$$

The outcome of Equation (4.32) has been compared to experimental data by several authors. Table 4.1 gives an overview of the parameter ranges from these measurements. Jing and Scarpato study a perforated screen with normal sound incidence, while the measurements of Eldredge and Andreini include a cylindrical liner. Generally, the modified Howe model agrees well with the experimental data. The data from Lahiri et al. [282] is presented in Chapter 7, so that these parameters are not listed in the table. Another comparison is presented by Macquisten et al. [310] for measurements in a combustion test rig. While the data is a valuable contribution to demonstrate the behavior at combustion conditions, it exhibits large scatter which makes a comparison difficult.

4.5 LUONG MODEL (SIMPLIFIED HOWE MODEL)

Luong et al. [308] use the Cummings equation [105, 107] to derive a simplified formula for the Rayleigh conductivity of a circular bias flow orifice. They modify the Cummings equation using the assumption that the steady pressure drop across the orifice is much larger than the acoustic pressure, in particular a reversal of the flow within the orifice against bias flow direction is excluded. Luong et al. derive the Rayleigh conductivity for an infinitesimal thin wall[21]. Including a finite thickness they arrive at

$$K_R = \frac{A}{l_{eff}} \left(\frac{\omega l_{eff}/U_{\overline{B}}}{\omega l_{eff}/U_{\overline{B}} + \frac{i}{C_c^2}} \right) \tag{4.33}$$

where A/l_{eff} is the Rayleigh conductivity without flow (see Equation (4.3)) and $U_{\overline{B}}$ is the mean velocity in the plane of the orifice. From comparison with experiments, Cummings [107] recommends a contraction coefficient of $C_c \approx 0.75$. Luong et al. [308] find that the agreement between Howe's linear theory [210] and their approach is best for this particular choice of C_c. This is demonstrated in Figure 4.4, where both results are compared. Luong et al. state that Equation (4.33) is a good approximation for the linear and nonlinear regime, when flow reversal does not occur. The principal effect of nonlinearity is expressed in a small reduction of the steady bias flow velocity.

4.6 BAUER IMPEDANCE MODEL

Bauer [34] presents an impedance model that includes the effect of bias[22] and grazing flow. He compiles a resistance expression from

21 For an infinitesimal thin wall l_{eff} represents the end correction only, in that case l_{eff} can be replaced by $\pi r/2$ in Equation (4.33).

22 Originally, the bias flow term was included to describe nonlinear effects at high amplitudes. However, it has become common practice to use this term for the steady bias flow and negelect nonlinear effects, cf. [12, 14, 18, 143, 363]

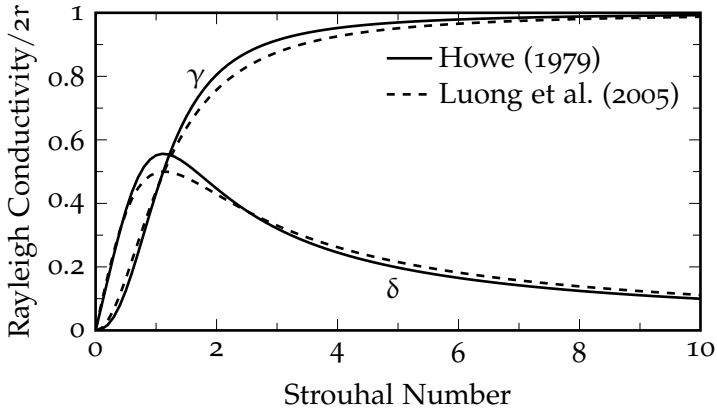

Figure 4.4: Comparison of the Rayleigh conductivity derived by Howe [210] and Luong et al. [308] for an infinitesimal thin wall and $C_c = 0.75$.

the viscous term of Ingard [225], an empirical grazing flow term from Dean [117], an empirical bias flow term given by Zinn [505], and an expression for the reactance proposed by Rice [394] and Dean [117] based on experimental data. The resulting normalized specific impedance yields

$$\zeta_{\text{Bauer}} = \frac{\sqrt{8\mu\rho\omega}}{\rho c\sigma}\left(1+\frac{t}{d}\right) + \frac{0.3\,M_G}{\sigma} + \frac{1.15\,M_B}{\sigma} + i\frac{k\,(t+0.25\,d)}{\sigma}. \tag{4.34}$$

The factor of 0.25 in the reactance term was found to match well when a grazing flow is present, but seems to be somewhat higher without grazing flow [34, 117]. However, Bauer [34] does not give any guidance on the actual value without grazing flow, so that 0.25 is used even without grazing flow.

The bias flow term is originally derived by Zinn [505]. The factor 1.15 results from $4/(3\pi C_d^2) = 1.1406$ where $C_d = 0.61$. Zinn actually gives 1.16 as result. The differences in the second digit after the decimal point are probably due to rounding errors. Commonly

1.15 is used. More importantly, the dependency on the discharge coefficient is already included in this value, so that it does not need to be divided by C_d as was done in [14, 18, 143, 290].
Bauer [34] divides the bias flow term by σ^2 instead of σ as in Equation (4.34). However, dividing by the square of the porosity produces unreasonable results, so that the division is done with σ only, as was done by others [14, 18, 143, 290].

4.7 BETTS IMPEDANCE MODEL

The impedance model proposed by Betts [52, 54] is based on Equation (4.18) with the extension for nonlinear effects proposed by Melling [327], i. e. Equation (4.19). Then, Betts modifies the nonlinear term to include the bias flow as shown in Equation (4.26). However, he does not use the exact solution of Equation (4.18), but a combination of the low and high shear number approximations. The approximations are combined in order to obtain an intuitive impedance formulation without Bessel functions that 'works' for all frequencies. As a result half the Poiseuille viscous term is added to the Helmholtz approximation, so that[23,24]

$$\begin{aligned}\zeta_{\text{Betts}} = &\frac{4\nu l}{c\sigma C_d r^2} + \frac{\sqrt{2\omega\nu}l}{c\sigma C_d r} + \frac{1-\sigma^2}{\sigma C_d}\left|M_B^{\text{eff}}\right| \\ &+ i\left(\frac{kl}{\sigma C_d} + \frac{\sqrt{2\omega\nu}l}{c\sigma C_d r} + \frac{16}{3\pi}\frac{r}{\psi}\right),\end{aligned} \tag{4.35}$$

23 While Melling [327] still includes the thermal conductivity losses inside the orifice with an effective viscosity (see discussion on page 62), Betts [52, 54] and as well Kraft et al. [271] only consider the regular viscosity when they present the approximations. If this modification was made intentionally or unconsciously remains unclear. However, Melling's notation might be misleading as he refers to the regular viscosity as μ' and the effective viscosity as μ. For consistency with [52, 54] the regular viscosity is used here as well.

24 Please note that the use of ψ is not correct in Equation (4.35). The end correction needs to be multiplied by ψ, not divided by ψ (please see footnote [11] on page 65). The error is kept for consistency with [52, 54]. Anyhow, the differences are small for the porosities considered here.

Table 4.2: Parameter range of experimental data from Betts [52, 54] that has been compared to the Betts impedance model.

f	Hz	$1000 - 3000$
SPL	dB	$120 - 140$
M_B	–	$0 - 0.0175$
σ	%	$0.9 - 16.5$
d	mm	$0.24 - 1.48$
t	mm	$0.51 - 1.02$
d_c	mm	272

where M_B^{eff} is the effective bias flow Mach number considering the acoustically induced flow as well as the steady bias flow [54]

$$M_B^{eff} = \frac{1}{2c\sigma C_d}\left(\frac{p'_{ref}10^{SPL/20}\sqrt{2}}{\rho c}\right) + M_B \tag{4.36}$$

Betts calls this model the Perforate Bias Flow Intermediate Frequency (PBFIF) model. He compares the model to impedance measurements of a perforated plate with normal sound incidence. The parameters of the study are listed in Table 4.2. The impedance model and the measured data show a generally good agreement for these parameters.

4.8 BELLUCCI IMPEDANCE MODEL

The impedance model of Bellucci et al. [41, 43] is based on Crandall's impedance model given in Equation (4.11). However, they do not consider the thermal conductivity losses, so that the nor-

malized specific impedance of a perforation without end corrections and without flow yields[25]

$$\zeta = \frac{1}{\sigma}\frac{\mathrm{ikl}}{F(k_s r)}\,, \tag{4.37}$$

where the function F is defined in Equation (4.12). Bellucci et al. use the common approximation of Equation (4.37) for large shear numbers

$$\zeta = \frac{1}{\sigma}\mathrm{ikl}\Gamma \quad \text{with} \quad \Gamma = \left[\left(1+\frac{\sqrt{2}}{\mathrm{Sh}}\right) - \mathrm{i}\left(\frac{\sqrt{2}}{\mathrm{Sh}}\right)\right]. \tag{4.38}$$

Several terms are added to include the effect of the bias flow and the end corrections. They introduce an end correction length, consisting of contributions from the radiation reactance l'_{rad}, the orifice interaction l'_{int}, the bias flow l'_{B}, and nonlinear effects of high amplitudes l'_{nl}. Including both ends this yields

$$l'_{\mathrm{Bellucci}} = l'_{\mathrm{rad}} \cdot l'_{\mathrm{int}} \cdot l'_{\mathrm{B}} \cdot l'_{\mathrm{nl}}\,. \tag{4.39}$$

The individual terms, compiled from various publications, are given by:

$$l'_{\mathrm{rad}} = 2 \cdot 0.8216\, r \left(1 + \frac{(0.77\,\mathrm{He})^2}{1+0.77\,\mathrm{He}}\right)^{-1} \qquad \text{from [356]} \tag{4.40}$$

$$l'_{\mathrm{int}} = 1 - \sqrt{\sigma/2} \qquad \text{from [225]} \tag{4.41}$$

$$l'_{\mathrm{B}} = \frac{0.3(6.0/\mathrm{St}^2)+1}{6.0/\mathrm{St}^2+1} \qquad \text{from [242, 366, 401]} \tag{4.42}$$

$$l'_{\mathrm{nl}} = 1 - 0.3/\mathrm{St}_{\mathrm{ac}}^{0.6} \qquad \text{from [366]} \tag{4.43}$$

The references are the ones given by Bellucci et al. [41]. The Helmholtz and Strouhal numbers are based on the orifice radius, so

25 Please note that there is a spelling mistake in Eq. 18 of reference [41]. It should be $\Gamma = [\ldots]^{-1}$ (see [327]). However, the approximate expression for Γ given in Eq. 19 of reference [41], i. e. Equation (4.38) here, is correct.

that $He = kr$, $St = \omega r / U_B$, and $St_{ac} = \omega r / |\hat{v}|$. The coefficients for l'_B and l'_{nl} have been fitted to their experimental data.

The resistance term of Bellucci et al. [41] regarding the bias flow effect and the nonlinearity due to high amplitudes yields

$$\theta_{Bellucci} = \frac{\xi}{c\sigma} G\left(\frac{U_B}{|\hat{v}|}\right) |\hat{v}|, \tag{4.44}$$

where $G(x)$ is given by Keller and Zauner [258] as

$$G(x) = \begin{cases} \frac{2}{\pi}\left(x \cdot \arcsin(x) + \frac{\sqrt{1-x^2}}{3}(2+x^2)\right) & \text{if } |x| \leqslant 1 \\ |x| & \text{if } |x| > 1 \end{cases} \tag{4.45}$$

The term ξ in Equation (4.44) is evaluated depending on the ratio of bias flow velocity to acoustic particle velocity[26]:

$$\xi = \begin{cases} 1/C_d^2 & \text{if } U_B = 0,\ St_{ac} \leqslant (St_{ac})_{qs} \quad (4.46) \\ 0.5\left(\frac{3\pi}{4}\right) St_{ac}^{1/3} & \text{if } U_B = 0,\ St_{ac} > (St_{ac})_{qs} \quad (4.47) \\ \frac{\pi}{2}\frac{\delta\, St}{\gamma^2+\delta^2} & \text{if } U_B \geqslant |\hat{v}| \quad (4.48) \\ \frac{\xi_0(1-G) + \xi_B\left(G - \frac{4}{3\pi}\right)}{1 - \frac{4}{3\pi}} & \text{if } 0 < U_B < |\hat{v}| \quad (4.49) \end{cases}$$

In Equation 4.49, ξ_0 refers to Equations 4.46 or 4.47, depending on St_{ac}, and ξ_B refers to Equation 4.48. γ and δ are, respectively, the real and imaginary part of Howe's Rayleigh conductivity, defined in Equation (4.28). The limit of the quasi-steady assumption for the acoustic Strouhal number is given by $(St_{ac})_{qs} = 0.61/C_d^6$. Adding Equations (4.39) and (4.44) to (4.37) yields

$$\zeta_{Bellucci} = \frac{\xi}{c\sigma} G\left(\frac{U_B}{|\hat{v}|}\right) |\hat{v}| + \frac{ik}{\sigma}\left(l\Gamma + l'_{Bellucci}\right). \tag{4.50}$$

26 Please note that there is a spelling mistake in Eq. 29 of reference [41]. The radius is already contained in the Strouhal number, so that the additional radius term needs to be dropped. See Equation 4.48.

Table 4.3: Parameter range of experimental data from Bellucci et al. [41] that has been compared to the Bellucci impedance model.

f	Hz	$50 - 600$
SPL	dB	N/A
M_B	–	$0 - 0.023$
σ	%	$1.03 - 2.31$
d	mm	$4 - 13.8$
t	mm	$1.5 - 43$

Equation (4.50) describes the impedance of the perforation only, while Bellucci et al. [41] also included the cavity reactance.

Bellucci et al. [41] determine the acoustic particle velocity $|\hat{v}|$ iteratively with a Newton-Raphson method. Here, the particle velocity is approximated as suggested by Betts et al. [54]

$$|\hat{v}| = \frac{1}{2\sigma C_d} \left(\frac{p'_{ref} 10^{SPL/20} \sqrt{2}}{\rho c} \right) . \tag{4.51}$$

Bellucci et al. [41] present a comparison of the model with experimental data from measurements of the reflection coefficient of a perforated plate with normal sound incidence. The parameters of the study are listed in Table 4.3. The impedance model and the measured data show a good agreement for these parameters.

4.9 APPLICATION TO A CYLINDRICAL GEOMETRY

It is straightforward to calculate the plane wave reflection and absorption coefficients of a perforated liner with normal sound incidence when its impedance is given (see [260], for example). However, when the same liner with an unpartitioned cavity is mounted as a sidewall, i. e. with grazing sound incidence, the sound propagation within the cavity needs to be considered. These type of liners are commonly called liners with extended reaction or non-locally-reacting liners. That is in contrast to a locally-reacting sur-

face, where the acoustic particle velocity at one point depends on the acoustic pressure at only the same point [369]. For a non-locally-reacting liner the acoustic field inside the duct and the acoustic field inside the cavity need to be modeled, while they are coupled via the impedance boundary of the perforated liner in-between. Two methods are presented that follow this approach for a cylindrical geometry.

4.9.1 *Transfer Matrix Method*

The transfer matrix method is a convenient approach for modeling one-dimensional, linear dynamic systems. With its origins in electrical circuit theory, it has become a standard tool in acoustics (Igarashi and Toyama [222] or [323, 343]). It is especially popular in muffler modeling [343] and as well widely used for the modeling of thermoacoustic effects in gas turbine combustors [44, 362, 452, 455].

A transfer matrix $\mathbf{T}$ relates the input and output state variables, commonly the acoustic pressure $\hat{p}$ and the acoustic volume velocity $\hat{q}$. For a two-port system [343]:

$$\begin{bmatrix} \hat{p}_1 \\ \hat{q}_1 \end{bmatrix} = \mathbf{T} \begin{bmatrix} \hat{p}_2 \\ \hat{q}_2 \end{bmatrix} \quad \text{with} \quad \mathbf{T} = \begin{bmatrix} T_{11} & T_{12} \\ T_{21} & T_{22} \end{bmatrix} \tag{4.52}$$

The individual terms are [343]:

$$T_{11} = \left.\frac{\hat{p}_1}{\hat{p}_2}\right|_{\hat{q}_2=0} \quad T_{12} = \left.\frac{\hat{p}_1}{\hat{q}_2}\right|_{\hat{p}_2=0} \quad T_{21} = \left.\frac{\hat{q}_1}{\hat{p}_2}\right|_{\hat{q}_2=0} \quad T_{22} = \left.\frac{\hat{q}_1}{\hat{q}_2}\right|_{\hat{p}_2=0}$$

The transfer matrix of a network of elements is obtained by multiplication of the individual transfer matrices of all the elements of the network. For example, the transfer matrix $\mathbf{T}$ of a network of n elements, each represented by a transfer matrix $\mathbf{T}_n$, is given by

$$\mathbf{T} = \mathbf{T}_1 \cdot \mathbf{T}_2 \cdot \ldots \cdot \mathbf{T}_n \,. \tag{4.53}$$

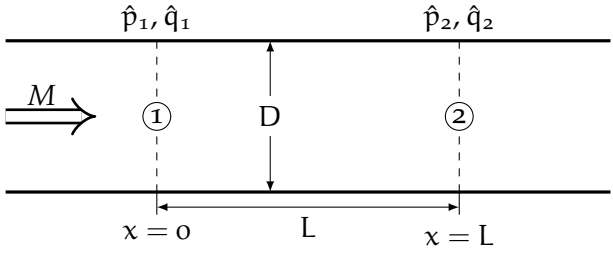

Figure 4.5: Transfer matrix representation of a uniform tube.

The literature provides transfer matrices for many common duct elements, e. g. uniform tube, sudden area change, orifice, Helmholtz resonator [323, 342].

Uniform Tube

The transfer matrix method is demonstrated with a simple uniform tube. The uniform tube setup is illustrated in Figure 4.5. The transfer matrix from position 1, where $x = 0$, to position 2, where $x = L$, along the uniform tube with constant flow Mach number M is given by the elements [323, 343]

$$\begin{aligned} T_{11} &= \cos(kL)\, e^{-iMkL} \\ T_{12} &= iZ_0 \sin(kL)\, e^{-iMkL} \\ T_{21} &= (i/Z_0) \sin(kL)\, e^{-iMkL} \\ T_{22} &= \cos(kL)\, e^{-iMkL} \end{aligned} \tag{4.54}$$

with the convective wave number $k = k_0/(1 - M^2)$. Z_0 is the characteristic acoustic impedance of a duct element. For plane waves

$$Z_0 = \frac{\hat{p}}{\hat{q}} = \frac{\hat{p}}{A\hat{v}} = \frac{\rho c}{A}\,. \tag{4.55}$$

Concentric-Tube Resonator

A description of the transfer matrix for a cylindrical perforated liner, or in muffler terminology called concentric-tube resonator, was presented by Sullivan and Crocker [460] and Sullivan [458, 459]. The sound field in the duct and in the annular cavity are described by their respective differential equation. However, the equations are coupled by the connection of the duct and the cavity through the perforated wall. Sullivan used a segmentation approach by dividing the geometry into many small control volumes. According to Peat [363] this approach is very flexible in the representation of different geometries, but it requires relatively high computing effort and might lead to numerical instabilities at high porosities. A decoupling approach that yields a closed form solution of the coupled differential equations was presented by Jayaraman and Yam [239]. This approach overcomes the necessity of forming small control volumes, so that the solution is much more compact. Unfortunately, the decoupling requires for the grazing flow Mach number within the duct and the cavity to be equal. A condition which is unlikely in most applications. These shortcoming have been solved in the formulations by Munjal et al. [345] and Peat [363], where Peat claims that his solution is more stable numerically. The state of the art approach is described in [323, 343] and will be summarized here.

The set of coupled differential equations for the setup illustrated in Figure 4.6a can be described by the 4×4 transfer matrix relation

$$\begin{bmatrix} \hat{p}_1(0) \\ \hat{p}_2(0) \\ \hat{q}_1(0) \\ \hat{q}_2(0) \end{bmatrix} = \mathbf{T} \begin{bmatrix} \hat{p}_1(L) \\ \hat{p}_2(L) \\ \hat{q}_1(L) \\ \hat{q}_2(L) \end{bmatrix} \quad \text{with } \mathbf{T} = \begin{bmatrix} T_{11} & T_{12} & T_{13} & T_{14} \\ T_{21} & T_{22} & T_{23} & T_{24} \\ T_{31} & T_{32} & T_{33} & T_{34} \\ T_{41} & T_{42} & T_{43} & T_{44} \end{bmatrix}, \tag{4.56}$$

where the indexes 1 and 2 refer to the inner and outer tube, respectively. The transfer matrix is given by

$$\mathbf{T} = \mathbf{A}(x = 0)\, \mathbf{A}^{-1}(x = L). \tag{4.57}$$

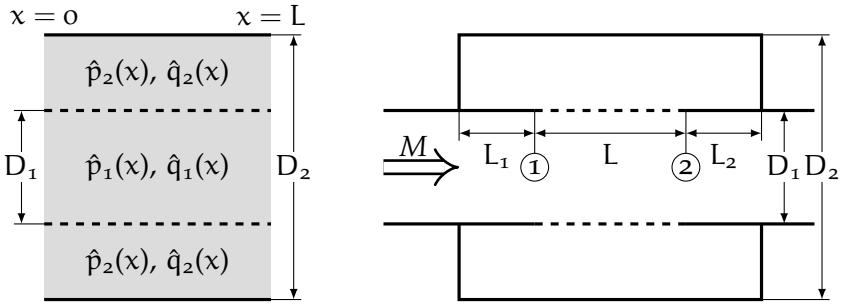

(a) Two concentric tubes coupled via a perforation.

(b) Concentric-tube resonator.

Figure 4.6: Transfer matrix representation of a concentric-tube resonator.

The elements of matrix $\mathbf{A}(x)$ are

$$\begin{aligned} A_{1,n} &= \psi_{3,n} e^{\beta_n x}, & A_{2,n} &= \psi_{4,n} e^{\beta_n x}, \\ A_{3,n} &= -\frac{e^{\beta_n x}}{ik_0 + M_1\beta_n}, \text{ and} & A_{4,n} &= -\frac{\psi_{2,n} e^{\beta_n x}}{ik_0 + M_2\beta_n}. \end{aligned} \tag{4.58}$$

with $n = 1, 2, 3, 4$. ψ and β are respectively the eigenmatrix and eigenvector of the matrix

$$\begin{bmatrix} -\alpha_1 & -\alpha_3 & -\alpha_2 & -\alpha_4 \\ -\alpha_5 & -\alpha_7 & -\alpha_6 & -\alpha_8 \\ 1 & 0 & 0 & 0 \\ 0 & 1 & 0 & 0 \end{bmatrix}, \tag{4.59}$$

where

$$\begin{aligned} &\alpha_1 = -\frac{iM_1}{1-M_1^2}\left(\frac{k_a^2 + k_0^2}{k_0}\right), \alpha_2 = \frac{k_a^2}{1-M_1^2}, \alpha_3 = \frac{iM_1}{1-M_1^2}\left(\frac{k_a^2 - k_0^2}{k_0}\right), \\ &\alpha_4 = -\left(\frac{k_a^2 - k_0^2}{1-M_1^2}\right), \ \alpha_5 = \frac{iM_2}{1-M_2^2}\left(\frac{k_b^2 - k_0^2}{k_0}\right), \ \alpha_6 = -\left(\frac{k_b^2 - k_0^2}{1-M_2^2}\right), \\ &\alpha_7 = \frac{iM_2}{1-M_2^2}\left(\frac{k_b^2 + k_0^2}{k_0}\right), \ \alpha_8 = \frac{k_b^2}{1-M_2^2} \end{aligned} \tag{4.60}$$

with

$$k_0 = \frac{\omega}{c}, \quad k_a^2 = k_0^2 - \frac{4ik_0}{D_1\zeta}, \quad k_b^2 = k_0^2 - \frac{4ik_0 D_1}{(D_2^2 - D_1^2)\,\zeta}. \tag{4.61}$$

and ζ is the normalized specific impedance of the perforation. All elements of the transfer matrix in Equation (4.56) can be calculated from Equations (4.58) to (4.61). The setup of a concentric-tube resonator, as illustrated in Figure 4.6b, introduces hard-wall boundary conditions at both ends of the cavity, so that it can be represented by the 2×2 transfer matrix[27]

$$\begin{bmatrix} \hat{p}_1(0) \\ \hat{v}_1(0) \end{bmatrix} = \mathbf{T} \begin{bmatrix} \hat{p}_2(L) \\ \hat{v}_2(L) \end{bmatrix} \quad \text{with} \quad \mathbf{T} = \begin{bmatrix} T_a & T_b \\ T_c & T_d \end{bmatrix} \tag{4.62}$$

with

$$\begin{aligned} T_a &= T_{12} + A_1 A_2\,, & T_b &= \left(T_{14} + B_1 A_2\right) Z_0 \\ T_c &= \left(T_{32} + A_1 B_2\right)/Z_0\,, \text{ and} & T_d &= T_{34} + B_1 B_2\,, \end{aligned} \tag{4.63}$$

where T_{12}, T_{14}, T_{32}, and T_{34} are elements of the matrix in Equation (4.56). The remaining quantities are given by

$$\begin{aligned} A_1 &= \left(X_1 T_{22} - T_{42}\right)/F\,, & B_1 &= \left(X_1 T_{24} - T_{44}\right)/F\,, \\ A_2 &= T_{11} + X_2 T_{13}\,, & B_2 &= T_{31} + X_2 T_{33}\,, \\ X_1 &= -i\tan\left(k_0 L_1\right)\,, & X_2 &= i\tan\left(k_0 L_2\right)\,, \text{ and} \\ F &= T_{41} + X_2 T_{43} - X_1\left(T_{21} + X_2 T_{23}\right). \end{aligned}$$

The transfer matrix in Equation (4.62) describes the relation of acoustic pressure and velocity when a sound wave is traveling from position 1 to 2 in Figure 4.6b. The equations above include the convective effect of a grazing flow. Commonly, there is no grazing flow within the cavity, so that $M_2 = 0$. The acoustic behavior of the perforation is represented by the impedance term ζ in Equation (4.61).

27 To avoid confusion between the elements of the matrices in Equations (4.56) and (4.62), an a,b,c,d indexing scheme has been used.

Acoustic Performance Criteria

Traditionally, the performance of a muffler is evaluated by its transmission loss, level difference, or insertion loss. For example, the transmission loss[28] can be calculated directly from the transfer matrix elements as [323]

$$\mathrm{TL} = 20\ \lg\left(\sqrt{\frac{Z_n}{Z_1}}\frac{1+M_1}{1+M_n}\left|\frac{T_{11}+\frac{T_{12}}{Z_n}+T_{21}Z_1+T_{22}\frac{Z_1}{Z_n}}{2}\right|\right), \qquad (4.64)$$

where the index 1 refers to the first and the index n to the last element of the network and the terminations are assumed anechoic.

Here, the acoustic performance is evaluated with the dissipation coefficient. Therefore, the transfer matrix is converted into a scattering matrix. This is demonstrated in Appendix B.2. Then, the dissipation coefficient can be calculated from the reflection and transmission coefficients given by the scattering matrix according to Section 6.4.

This method will be referred to as Transfer Matrix Method, short TMM. The acoustic properties of the liner are included in Equation (4.61) and can be represented by an impedance model of choice. This will be indicated, for example, by TMM:Bauer, where the Transfer Matrix Method is used in combination with the Bauer impedance model.

4.9.2 *Eldredge & Dowling Method*

Eldredge and Dowling [142] develop equations for the stagnation enthalpy[29] and the acoustic particle velocity in the lined section

28 The transmission loss describes the difference between the incident power and transmitted power in dB, that is $\mathrm{TL} = 10\ \lg(P_i/P_t)$.

29 The fluctuating stagnation enthalpy is defined by [142, 214] $B' = p'/\overline{\rho} + \overline{v}v'$. For a plane wave, where the acoustic pressure and velocity are related via the impedance $\rho c = \hat{p}/\hat{v}$, the fluctuating stagnation enthalpy yields $\hat{B}^{\pm} = \frac{\hat{p}}{\rho}(1 \pm M)$.

of a duct by applying a mass and momentum balance to a defined control volume. An analytic solution does exist for the hard-walled duct sections upstream and downstream, so that the stagnation enthalpy and acoustic particle velocity need to match at the respective boundaries. For convenience, they introduce the characteristic quantities

$$\psi^+ = \frac{1}{2}(1+U_G)\left[\hat{B} + (1-U_G)\,\hat{v}_x\right], \text{ and} \tag{4.65}$$

$$\psi^- = \frac{1}{2}(1-U_G)\left[\hat{B} - (1+U_G)\,\hat{v}_x\right], \tag{4.66}$$

where U_G is the grazing flow velocity and $\hat{v}_x$ is the complex amplitude of the particle velocity in axial direction within the duct. Then, the equations for the lined duct are given by

$$\frac{d\psi^+}{dx} = -\frac{ikL_{eff}}{1+U_G(x)}\psi^+ + \frac{1}{2}\frac{C_1 L_{eff}}{A}\hat{v}_1 \quad \text{and} \tag{4.67}$$

$$\frac{d\psi^-}{dx} = \frac{ikL_{eff}}{1-U_G(x)}\psi^- - \frac{1}{2}\frac{C_1 L_{eff}}{A}\hat{v}_1, \tag{4.68}$$

with the two boundary conditions

$$\psi^+(0) = 1 \quad \text{and} \quad \psi^-(1)e^{-ik^- L_{eff}} - \psi^+(1) r_e e^{ik^+ L_{eff}} = 0, \tag{4.69}$$

the liner circumference C_1, the effective perforation length[30] L_{eff}, the duct cross-section area A, and the acoustic particle velocity through the perforation $\hat{v}_1$ specified below. Please note, that the grazing flow velocity increases with x over the length of the liner

$$U_G = M_G + \frac{C_1 L_{eff}}{A} M_B x. \tag{4.70}$$

Eldredge and Dowling consider three configurations: 1. Open exterior, 2. Annular cavity enclosed by a rigid wall, and 3. Annular cavity enclosed by a second liner. Only the last two are of importance here.

30 The effective perforation length yields best agreement with the experimental data (see the discussion in Section 4.10.2).

The equations within the annular cavity enclosed by a rigid wall yield

$$\frac{d\hat{B}_1}{dx} = -ikL_{eff}\hat{v}_{x,1} \quad \text{and} \tag{4.71}$$

$$\frac{d\hat{v}_{x,1}}{dx} = -ikL_{eff}\hat{B}_1 - \frac{C_1 L_{eff}}{A_C}\hat{v}_1 \,. \tag{4.72}$$

$\hat{v}_{x,1}$ is the axial particle velocity in the cavity with the rigid wall boundary conditions

$$\hat{v}_{x,1}(0) = 0 \quad \text{and} \quad \hat{v}_{x,1}(1) = 0 \,. \tag{4.73}$$

The particle velocity through the liner is given by

$$\hat{v}_1 = \frac{\eta_1}{ikL_{eff}} \left(\hat{B}_1(x) - \psi^+(x) - \psi^-(x)\right) . \tag{4.74}$$

When a second liner is present Equation (4.72) is modified to

$$\frac{d\hat{v}_{x,1}}{dx} = -ikL_{eff}\hat{B}_1 - \frac{C_1 L_{eff}}{A_C}\hat{v}_1 + \frac{C_2 L_{eff}}{A_C}\hat{v}_2 \,, \tag{4.75}$$

with

$$\hat{v}_2 = \frac{\eta_2}{ikL} \left(\hat{B}_2(x) - \hat{B}_1(x)\right) . \tag{4.76}$$

For the rigid wall case, the four differential equations (4.67), (4.68), (4.71) and (4.72) form a closed system for the four unknowns ψ^+, ψ^-, $\hat{B}_1$, and $\hat{v}_{x,1}$. The liner velocity $\hat{v}_B$ is given in Equation (4.74) and the four boundary conditions by Equations (4.69) and (4.73). The boundary value problem is solved using the shooting method, for example in Matlab with the function `bvp4c`. This can be done accordingly for the case with a second liner with equations (4.67), (4.68), (4.71) and (4.75). When the surrounding enclosure is sufficiently large, the stagnation enthalpy fluctuation external to the second liner can be assumed negligible, i. e. $\hat{B}_2 = 0$.

The damping liner is represented by the compliance[31] η_1 in Equation (4.74). It is defined as

$$\frac{1}{\eta_1} = \frac{\pi r^2}{\sigma L_{\text{eff}}^2} \frac{1}{K_R} + \frac{l}{\sigma L_{\text{eff}}} . \tag{4.77}$$

The compliance of the second liner η_2 is given accordingly, when needed. As was done with the impedance in Section 4.2.1, the compliance delivers a homogeneous boundary condition for the perforation by dividing the single orifice value by the porosity. The acoustic properties of the bias flow orifice are given by the Howe Rayleigh conductivity model, i. e. that is Equation (4.27). Here, the compliance includes a thickness term, following the argumentation given by Jing and Sun [241], see Section 4.4.

Eldredge and Dowling [142] define an absorption coefficient as the net energy absorbed by the liner, scaled by the energy incident upon the lined section, thus

$$\alpha = 1 - \frac{\left|\hat{B}_2^+\right|^2 + \left|\hat{B}_1^-\right|^2}{\left|\hat{B}_1^+\right|^2 + \left|\hat{B}_2^-\right|^2} , \tag{4.78}$$

where the index 1 and 2 refers to the upstream and downstream hard-walled duct section adjacent to the liner. Equation (4.78) can be expressed in terms of ψ^+ and ψ^- as

$$\alpha = \frac{1 + \left(|r_e|^2 - 1\right) |\psi^+(1)|^2 - |\psi^-(0)|^2}{1 + |r_e|^2 |\psi^+(1)|^2} . \tag{4.79}$$

Eldredge and Dowling [142] give several expressions to calculate the end reflection coefficient r_e, with and without flow. Here, the duct end is assumed to be anechoic, so that $r_e = 0$. Then, the absorption coefficient and the average dissipation coefficient are identical and can be compared directly, as shown in Section 6.4.3.

31 This term was introduced by Hughes and Dowling [219] to describe the homogeneous boundary condition of an acoustically 'soft' wall. It should not be mixed up with the acoustic compliance that was introduced in Equation (4.10).

This approach will be referred to as Eldredge and Dowling Method, short EDM, and EDM:Jing when including the description of the liner according to Equation (4.77).

4.10 SOME COMPARISONS

4.10.1 *Impedance Models*

The first comparison is done for a configuration without any flow. The linear acoustic behavior of a perforation without flow is fairly well understood, so that the models should predict a similar behavior. The Howe model and its derivatives are only valid when a bias flow is present, so that they are excluded from this comparison.

Figure 4.7 plots a) the resistance, b) the reactance, and c) the dissipation over the frequency. The liner geometry corresponds to configuration DC006 of the parameter study. The specifications are given in Table 7.1. Even without flow the impedance prediction of the models varies slightly. The effect of these variations on the absorption are revealed in Figure 4.7c. The theoretical dissipation is calculated with the transfer matrix method and compared to the experimental results. Surprisingly, the oldest model, i. e. the linear Melling model, shows the best agreement with the experiments. The other models do not include some effects that are considered in the Melling model, i. e. thermal conductivity losses within the orifice are neglected or approximations of the Bessel functions are used, for example. The prediction quality for the no flow case would have benefited from including these effects. The peak frequency predicted by the Bauer model is significantly higher than the other models. This results from the empirical correction factor in the reactance, which is strictly valid only when a grazing flow is present (see discussion in Section 4.6).

The impedance of the same setup as above, but including a bias flow of $M_B = 0.03$ is plotted in Figure 4.8. The Melling model does

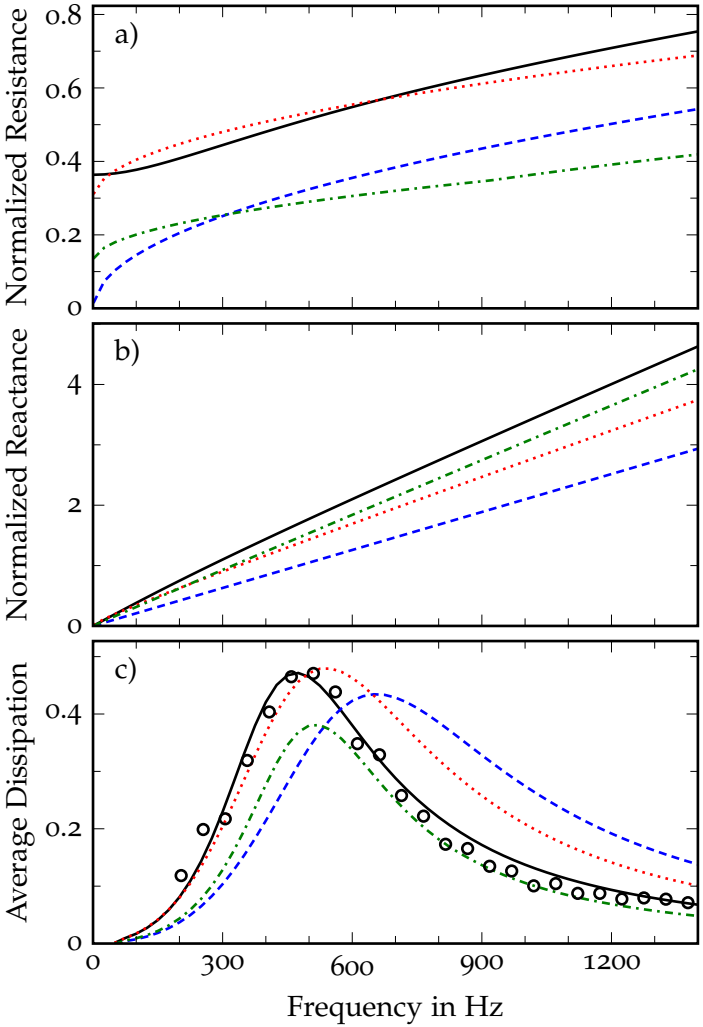

Figure 4.7: Comparison of the impedance and the dissipation predicted by various models plotted over the frequency for DC006 without flow: a) normalized specific resitance, b) normalized specific reactance, c) average dissipation coefficient. Legend: —— Melling; - - - Bauer; ····· Betts; -·-·- Bellucci; o Experiment.

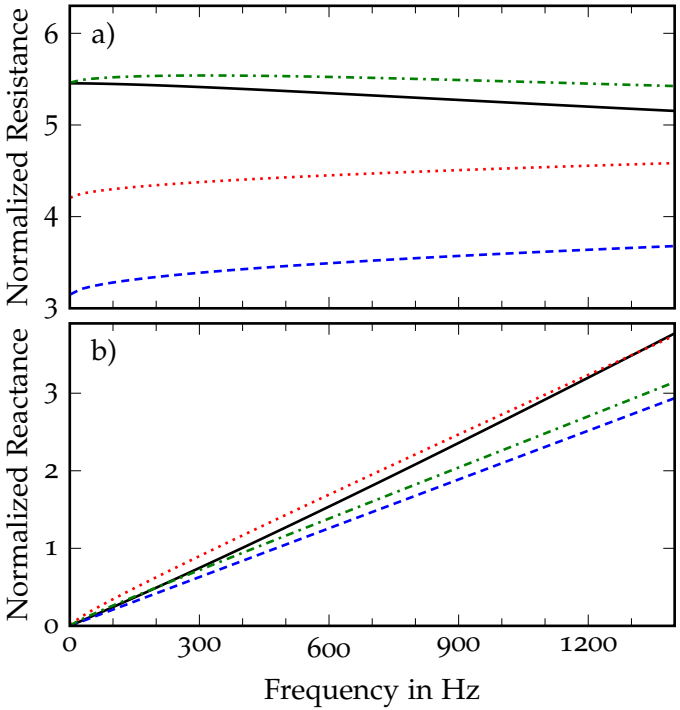

Figure 4.8: Comparison of the impedance models plotted over the frequency for DC006 with $M_B = 0.03$. —— Jing; - - - Bauer; ····· Betts; -·-·- Bellucci.

not consider bias flow, so that it would remain unchanged from Figure 4.7 and has been omitted here. Instead, the Jing model is plotted.

All models predict a significant increase of the resistance due to the bias flow. The resistance terms of Jing and Bellucci are both based on the Howe model (with an addition contribution from viscous losses in the Bellucci model), so that they give similar results. The resistance predicted by Betts and Bauer is much lower. The Betts and Bauer models neglect any influence of the bias flow on the reactance, so that the reactance is identical to the config-

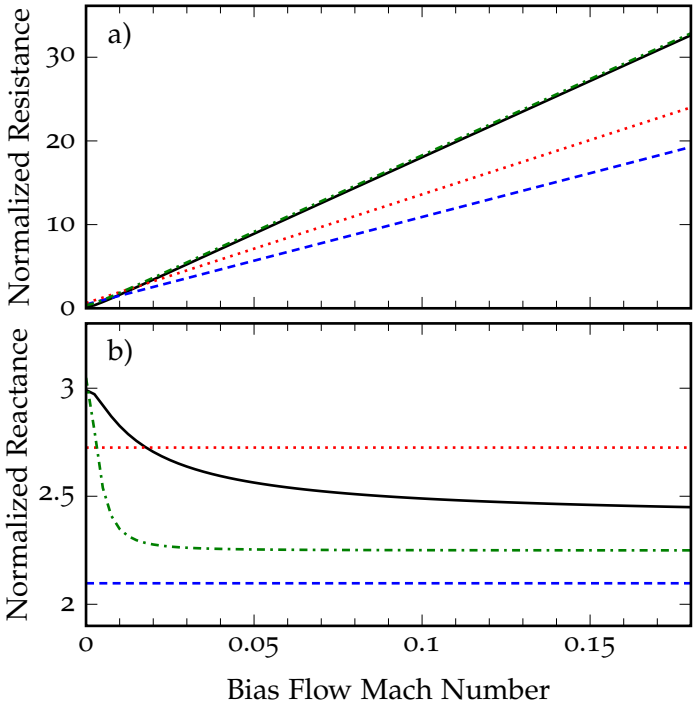

Figure 4.9: Comparison of the impedance models plotted over the bias flow Mach number for DC006 with $f = 1000\,\text{Hz}$. —— Jing; - - - Bauer; ····· Betts; -·-· Bellucci.

uration without flow in Figure 4.7. The reactance of Bellucci is significantly reduced compared to the no flow configuration.

Figure 4.9 plots the impedance over the bias flow Mach number for a fixed frequency. All models predict a mainly linear increase of the resistance with the bias flow Mach number. As discussed above, the reactance is constant for the Betts and Bauer models. On the other hand, Jing and Bellucci predict a decreasing reactance, when increasing the bias flow. In that case, the reactance is rapidly reduced at low bias flow Mach numbers and approaching a constant value at high bias flow Mach numbers. The effect is much stronger in the Bellucci model. The more complex models

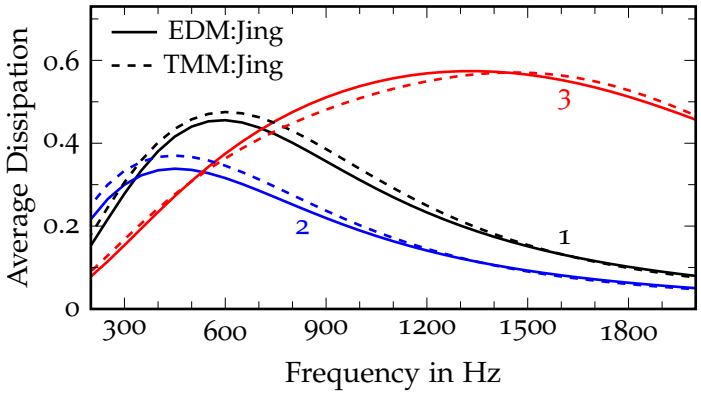

Figure 4.10: Comparison of the Eldredge and Dowling method and the transfer matrix method for three configurations: 1. DC006 with $M_B = 0.015$; 2. DC007 with $M_B = 0.029$; 3. DC008 with $M_B = 0.049$.

of Jing and Sun [242] and Lee et al. [291], which require a numerical solution and are not plotted here, predict a similar effect (not shown here).

4.10.2 *Transfer Matrix Method vs. Eldredge & Dowling Method*

Theoretically, the Eldredge and Dowling Method (EDM) and the Transfer Matrix Method (TMM) should give identical results when the same model for the perforation is used. The remaining differences are due to the two methods. This will be demonstrated for three configurations, varying liner geometry as well as bias flow Mach number, applying the Jing model. The liner geometries correspond to configurations DC006, DC007, and DC008 of the parameter study. The specifications can be found in Table 7.1.

A first comparison is given in Figure 4.10. Both methods predict similar results, but they are not identical. While both methods predict a similar level of dissipation for setup 3, TMM yields slightly higher dissipation levels for setups 1 and 2. However, the predicted peak frequencies agree for setups 1 and 2, while they are

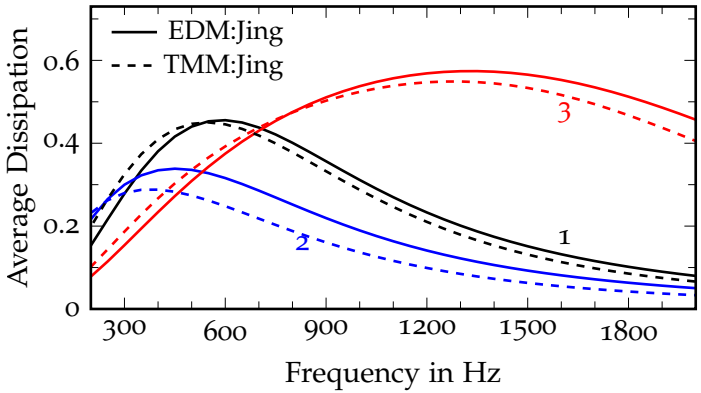

Figure 4.11: Comparison of EDM using the effective perforation length and TMM using the perforation length plus additional hard-wall sections for three configurations: 1. DC006 with $M_B = 0.015$; 2. DC007 with $M_B = 0.029$; 3. DC008 with $M_B = 0.049$.

slightly different for setup 3. The origin of these differences is not obvious and no general trend can be observed (e. g. one method always predicts higher values than the other).

It was found that the axial length is a crucial parameter. It is not entirely clear which length should be used here, that is either the perforation length L, the effective perforation length L_{eff}, or the cavity length L_c as defined in Figure 2.8. Additionally, TMM can account for hard-walled sections at either end of the perforation, see Figure 4.6b. For the theoretical comparison of the two methods in Figure 4.10, the effective perforation length was used in both methods and any additional hard-wall sections were neglected in TMM.

When comparing the models to measurement data, it will be made use of the feature of TMM which takes the hard-walled sections into account. In that case, the perforation length is used and the length of the hard-walled sections is treated separately. However, due to the lack of this feature in EDM, it will continue to use the effective perforation length. The comparison between

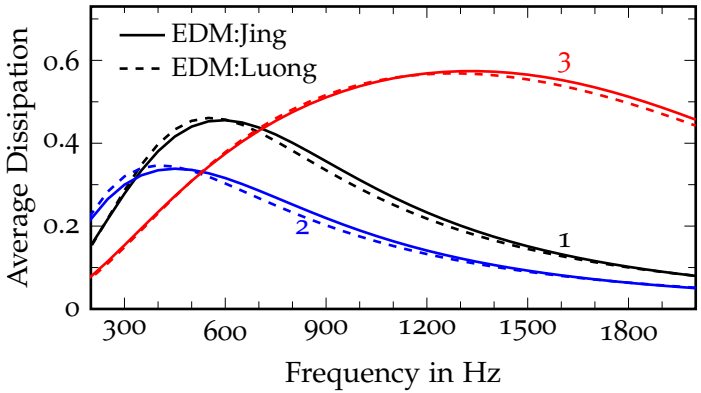

Figure 4.12: Comparison of the Howe model and the Luong model for three configurations: 1. DC006 with $M_B = 0.015$; 2. DC007 with $M_B = 0.029$; 3. DC008 with $M_B = 0.049$.

the two methods looks slightly different when they are based on different characteristic lengths. This is shown in Figure 4.11. Various length combinations have been applied to the models and were compared to the experimental data. There was no clear best match of any one length. Using the effective perforation length with EDM and the perforation length plus additional hard-wall sections with TMM yielded the best overall agreement. Thus, this setup is applied throughout this work.

4.10.3 *Howe vs. Luong*

Figure 4.12 compares the results when using the Jing model or the Luong model to represent the perforation. Both cases are calculated with the Eldredge and Dowling method, setting $C_c = 0.75$ for EDM:Luong. The Luong model for zero thickness is used with the thickness term applied by EDM. The three configurations are the same as in the previous section.

The results from the two models are very similar. However, EDM:Luong predicts a slightly lower peak frequency in all three

cases. Due to their similar results, only EDM:Jing will be compared with the experimental data in Chapter 7.

5

DUCT ACOUSTICS

5.1 ACOUSTIC WAVE EQUATION

Fundamental Equations of Fluid Dynamics

The motion of fluid is governed by the conservation laws for mass, momentum, and energy. The conservation of mass in the absence of any sources is described by the partial differential equation[1] (Euler [148], or [33, 369])

$$\frac{\partial \rho}{\partial t} + \nabla \cdot (\rho \mathbf{v}) = 0 \,. \tag{5.1}$$

It is commonly known as the continuity equation. It relates the velocity of the fluid to its density and is valid without any restrictions, except that the fluid and its properties must be continuous[2]. An alternative formulation is given by replacing the local time derivative $\partial/\partial t$ with the substantial derivative (Stokes [449], or [33, 59])

$$\frac{D}{Dt} = \frac{\partial}{\partial t} + \mathbf{v}\nabla \,. \tag{5.2}$$

1 This and the following equations are given in Gibbs notation (Gibbs and Wilson [173], or [59]). The Nabla operator ∇ is used as a convenient mathematical notation for either the gradient $\operatorname{grad} f = \nabla f$, the divergence $\operatorname{div} f = \nabla \cdot f$, or rotation (or curl) $\operatorname{rot} f = \nabla \times f$ [77].

2 The continuum hypothesis disregards the discrete molecular nature of a fluid and assumes, that its macroscopic behavior is the same as if it were perfectly continuous in structure [33].

The substantial time derivative follows the motion of the fluid, thus it reveals the convective effect of the mean flow. It follows from Equation (5.1) that [33]

$$\frac{D\rho}{Dt} + \rho\,(\nabla \cdot \mathbf{v}) = 0\,. \tag{5.3a}$$

The conservation of momentum for an ideal fluid is given by (Euler [148] or [33, 369])

$$\rho \frac{D\mathbf{v}}{Dt} = -\nabla p\,, \tag{5.3b}$$

where gravity is neglected. This equation is also called equation of motion, while this special case for an ideal fluid is commonly known as the Euler equation[3]. It relates the pressure to the velocity of the fluid.

The conservation of energy is expressed by the equation of state, which for an ideal gas[4] is given by (Clapeyron [97], or [33])

$$p = \rho R T\,.$$

This equation is also called ideal gas law. The acoustic motion is considered to be isentropic[5], so that the thermodynamic relation between the density and the pressure can be given by [33, 369]

$$\left(\frac{\partial p}{\partial \rho}\right)_s = c^2 \quad \text{with} \quad \frac{Ds}{Dt} = 0\,. \tag{5.3c}$$

This system of three Equations (5.3) is commonly referred to as Euler equations[6]. They describe the motion of a compressible, ideal fluid.

3 Named after Leonhard Euler (1707-1783), Swiss mathematician and physicist.

4 An ideal gas is an idealization where the molecular interaction is neglected. Air of normal atmospheric temperature and pressure can be considered to behave ideal.

5 Morfey [338]: "In an isentropic change of thermodynamic state the entropy remains constant. An adiabatic process is isentropic provided it is reversible."

6 Even though only the first two originate from Euler.

Equations of Linear Acoustics

The field quantities (pressure, velocity, and density) that are used in the previous section can be written as the sum of their mean and fluctuating (acoustic) values:

$$\begin{aligned} p &= p_0 + p' \\ v &= v_0 + v' \\ \rho &= \rho_0 + \rho' \end{aligned} \tag{5.4}$$

A linearization of Equations (5.3) is possible by assuming that the acoustic quantities are much smaller than the mean quantities

$$\frac{p'}{p_0} \ll 1 \qquad \frac{v'}{v_0} \ll 1 \qquad \frac{\rho'}{\rho_0} \ll 1\,, \tag{5.5}$$

which is fulfilled in most applications. This assumption allows to disregard higher order terms in Equations (5.3), so that the approximate acoustic equations are given by [176, 369]

$$\frac{D\rho'}{Dt} + \rho_0 \left(\nabla \cdot \mathbf{v}'\right) = 0\,, \tag{5.6a}$$

$$\rho_0 \frac{D\mathbf{v}'}{Dt} + \nabla p' = 0\,, \text{and} \tag{5.6b}$$

$$p' = c^2 \rho'\,. \tag{5.6c}$$

Acoustic Wave Equation

The acoustic wave equation can be obtained from Equation (5.6) in a few simple steps: Substitute the fluctuating density ρ' in Equation (5.6a) with (5.6c). Then, taking the time derivative of Equation (5.6a) and replacing its second term with Equation (5.6b) yields the acoustic wave equation

$$\nabla^2 p' - \frac{1}{c^2} \frac{D^2 p'}{Dt^2} = 0\,. \tag{5.7}$$

where ∇^2 is the Laplace operator[7]. This general notation including the material derivative, see Equation (5.2), can be applied to stationary or moving medium. The assumptions that have been introduced are:

- homogeneous medium[8]
- ideal fluid
- linear acoustics[9]
- isentropic relation between pressure and density
- uniform flow[10] or stationary medium

Expanding the material derivative in Equation (5.7) results in the commonly used form of the convected wave equation (Howe [207, 214], or [340, 343])

$$\nabla^2 p' - \frac{1}{c^2}\left(\frac{\partial}{\partial t} + \mathbf{v}_0\nabla\right)^2 p' = 0\,. \tag{5.8}$$

In stationary medium, $\mathbf{v}_0 = 0$, the material derivative can be replaced by the local time derivative and Equation (5.7) and ((5.8)) reduce to the well known form of the classical acoustic wave equation (d'Alembert [111] and Euler [149, 150], or [369])

$$\nabla^2 p' - \frac{1}{c^2}\frac{\partial^2 p'}{\partial t^2} = 0\,. \tag{5.9}$$

7 The Laplace operator ∇^2, or sometimes denoted as Δ, is named after Pierre-Simon de Laplace (1749–1827, French mathematician). It prescribes the summation of the second partial derivatives of a function f with respect to a given coordinate system. In general: $\nabla^2 f = \nabla \cdot (\nabla f) = \mathrm{div}(\mathrm{grad}\, f)$ [77]

8 Morfey [338]: "A homogeneous medium is a medium whose properties are spatially uniform, i.e. independent of position."

9 Morfey [338]: "Linear acoustics is limited to small amplitude signals or oscillations, so that the relation between any two oscillatory quantities is independent of amplitude. Linear sound waves propagate independently of one another, without interaction."

10 In uniform flow the magnitude and direction of the velocity is spatially uniform.

The wave equations above are expressed for the acoustic pressure. However, since all coefficients are constant they apply to all acoustic variables, e.g. pressure, velocity, density, and potential [86].

5.2 THREE-DIMENSIONAL WAVES

For the description of the wave propagation in a circular duct the wave equation (5.7) can be expressed in cylindrical coordinates with the axial coordinate x, the radial coordinate r, and the circumferential coordinate θ. The Laplace operator in cylindrical coordinates is given by (e. g. [77])

$$\nabla^2 p' = \frac{\partial^2 p'}{\partial x^2} + \frac{1}{r}\frac{\partial}{\partial r}\left(r\frac{\partial p'}{\partial r}\right) + \frac{1}{r^2}\frac{\partial^2 p'}{\partial \theta^2}\,, \tag{5.10}$$

so that the three-dimensional wave equation in cylindrical coordinates yields

$$\frac{\partial^2 p'}{\partial x^2} + \frac{1}{r}\frac{\partial}{\partial r}\left(r\frac{\partial p'}{\partial r}\right) + \frac{1}{r^2}\frac{\partial^2 p'}{\partial \theta^2} - \frac{1}{c^2}\frac{D^2 p'}{Dt^2} = 0\,. \tag{5.11}$$

This is a linear second-order partial differential equation which can be solved by the separation of variables[11]. A general solution for a circular duct is given by (e. g. [206, 352, 444])[12]

$$\begin{aligned} \hat{p}_{mn}(x, r, \theta, t) = \quad & \hat{p}^{+}_{mn}\, e^{-ik_{x,mn}x} + \hat{p}^{-}_{mn}\, e^{ik_{x,mn}x} \\ & \times J_m\left(k_{r,mn}r\right) \quad + Q_{mn}\, Y_m\left(k_{r,mn}r\right) \\ & \times e^{im\theta} \\ & \times e^{i\omega t}, \end{aligned} \tag{5.12}$$

11 The separation of variables introduces a substitution in the form $p'(x, r, \theta, t) = f_x(x) \cdot f_r(r) \cdot f_\theta(\theta) \cdot f_t(t)$ and reduces the partial differential equation into a set of ordinary differential equations (Bernoulli [50] or [77]).

12 The original derivation of the modal character of a sound field goes back to Duhamel [132] and Rayleigh [387]. Detailed discussion are given by Tyler and Sofrin [482], Morfey [335], or Morse and Ingard [340], for example.

where the axial and radial wave numbers are related by

$$\left(\frac{\omega}{c}\right)^2 = k_{x,mn}^2 + k_{r,mn}^2. \tag{5.13}$$

The four rows in Equation (5.12) describe the spatial (axial, radial, and circumferential) and temporal shape of the mode, respectively. While the spatial patterns in axial and circumferential direction are sinusoidal (as well as the temporal development), the radial pattern is defined by Bessel functions. J_m is the Bessel function of the first kind, commonly only called Bessel function, Y_m is the Bessel function of the second kind, often called Weber[13] or Neumann[14] function, and Q_{mn} is the n-th Eigenvalue of Y_m.

Equation (5.12) represents the so called modal solution. The actual sound pressure of a time harmonic wave is given by the real part of the superposition of an infinite number of modes[15]

$$p'(x, r, \theta, t) = \sum_m \sum_n \hat{p}_{mn}(x, r, \theta, t)\,, \tag{5.14}$$

where $m \in \{\ldots, -2, -1, 0, 1, 2, \ldots\}$ and $n \in \{0, 1, 2, \ldots\}$. Each mode is characterized by its circumferential mode order m and its radial mode order n. The integers m and n describe the number of nodal lines in circumferential and radial direction, respectively. For $m = 0$ and $n = 0$ there are no nodal lines in transverse direction, so that the sound field is one-dimensional with variations in x-direction only. This special case is called fundamental mode or plane wave and will be discussed separately in Section 5.3. All other modes are referred to as higher order modes.

In a cylindrical duct, without any central hub, Q_{mn} in Equation (5.12) becomes zero, so that the solution for a time harmonic

13 Named after Heinrich Martin Weber (1842-1913, German mathematician).

14 Named after Carl Gottfried Neumann (1832-1925, German mathematician).

15 Morfey [338]: "A mode is a spatial pattern of vibration, whose shape remains invariant as the vibration propagates spatially."

Table 5.1: Eigenvalues of the hard-wall solution for a cylindrical duct, sorted in ascending order of j_{mn}. (From [3, p. 411])

m:n	0:0	1:0	2:0	0:1	3:0	4:0	1:1
j_{mn}	0	1.8412	3.0542	3.8317	4.2012	5.3176	5.3314

wave propagating in a cylindrical duct with hard walls and uniform mean flow yields (e. g. [315, 330, 337, 343, 444])

$$\hat{p}_{mn} = \left(\hat{p}^{+}_{mn} e^{-ik^{+}_{x,mn}x} + \hat{p}^{-}_{mn} e^{-ik^{-}_{x,mn}x}\right) J_m\left(k_{r,mn} r\right) e^{im\theta} e^{i\omega t}, \tag{5.15}$$

with the axial wave number

$$k^{\pm}_{x,mn} = \frac{k}{1-M^2}\left(-M \pm \sqrt{1-(1-M^2)\left(\frac{j_{mn}}{kR}\right)^2}\right). \tag{5.16}$$

The hard-wall boundary condition[16] requires that the derivative of J_m vanishes at the wall, so that for $r = R$

$$J'_m\left(k_{r,mn} R\right) = 0\,, \tag{5.17}$$

with the radial wave number

$$k_{r,mn} = \frac{j_{mn}}{R}\,. \tag{5.18}$$

j_{mn} is the n-th root of J'_m or the n-th Eigenvalue of J_m for the hard-wall boundary condition. Some values of j_{mn} are given in Table 5.1. More extensive tables can be found in mathematical references, e. g. Abramowitz and Stegun [3].

The mathematical description of the acoustic pressure in a cylindrical duct is demonstrated graphically in Figure 5.1. The spatial distribution of the acoustic pressure is plotted for the four modal

16 The hard-wall boundary condition demands that the radial velocity vanishes at the wall. From Equation (5.6b) follows the boundary condition for the acoustic pressure: $\frac{\partial p'}{\partial r} = 0$ at $r = R$.

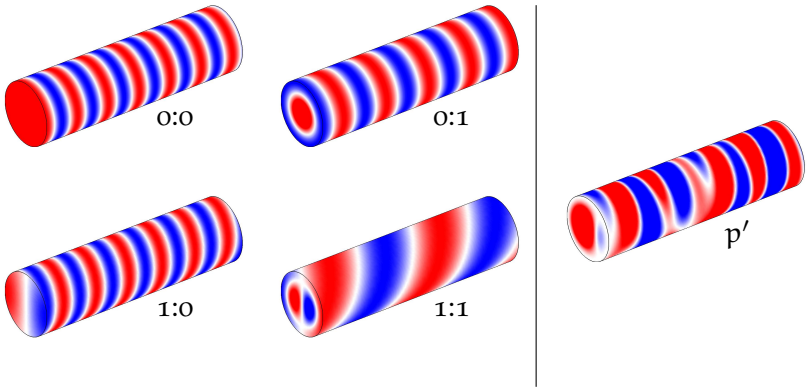

Figure 5.1: Illustration of the acoustic pressure in a cylindrical duct for four modal components (m:n) 0:0, 1:0, 0:1, and 1:1 and the resulting sound field p' at a single frequency.

components (m:n) 0:0, 1:0, 0:1, and 1:1 and the resulting sound field $p' = p'_{0:0} + p'_{1:0} + p'_{0:1} + p'_{1:1}$. The nodal lines of the circumferential and radial patterns are visible in the duct cross-section. Another characteristic feature of modes of higher circumferential order $m > 0$ is that their transversal pattern is rotating around the x-axis. A behavior which has coined the term spinning mode [482]. While the images are snapshots of the instantaneous acoustic pressure at $t = 0$, the spinning modes produce the spiral pattern of the acoustic pressure at the duct surface.

5.2.1 *Cut-On Frequency*

The axial wave number $k^{\pm}_{x,mn}$ defines the propagation of a mode in x-direction. Equation (5.16) allows for two fundamentally different propagation characteristics depending on the evaluation of the square root in the equation:

1. $1 - (1 - M^2)\left(\frac{j_{mn}}{kR}\right)^2 \geqslant 0 \quad \rightarrow \quad k^{\pm}_{x,mn} \in \mathbb{R}$

2. $1-(1-M^2)\left(\frac{j_{mn}}{kR}\right)^2 < 0 \quad \rightarrow \quad k^{\pm}_{x,mn} \in \mathbb{C}$

In the first case $k^{\pm}_{x,mn}$ is a real quantity. The mode propagates along the duct unattenuated (considering ideal fluid). In the second case $k^{\pm}_{x,mn}$ is complex and its imaginary part serves as an attenuation coefficient. The amplitude of the mode decays exponentially with axial distance from the source, i. e. the mode is not able to propagate. A characteristic frequency can be defined as the frequency where a mode becomes 'cut-on', i. e. the mode starts propagating. At this cut-on frequency the term under the square root in Equation (5.16) vanishes, so that

$$f_{c,mn} = \frac{j_{mn}}{2\pi R} c\sqrt{1-M^2}\,. \tag{5.19}$$

The cut-on frequency is dependent on the duct radius, the mean flow Mach number, the speed of sound, and the Eigenvalue of the associated mode. The Eigenvalue j_{mn} of the fundamental mode 0:0 is zero and it follows that the cut-on frequency is also zero, i. e. the fundamental mode is able to propagate at all frequencies.

The cut-on behavior of the higher order modes introduces a major advantage. Only a limited number of higher order modes are able to propagate at a given frequency, so that the remaining non-propagating modes can be neglected (in most cases). The cut-on frequency of the first[17] higher order mode defines the transition between one-dimensional and three-dimensional sound propagation.

5.2.2 *Evanescent Modes*

A mode that is excited below its cut-on frequency is not able to propagate. These modes are referred to as evanescent modes or

17 The 'first' higher order mode refers to the higher order mode with the lowest cut-on frequency. For a fixed setup (R, M, c = constant) the numerical order of the cut-on frequencies is given by the numerical order of the values of j_{mn} (as they are given in Table 5.1).

cut-off modes. Their amplitude decays exponentially with axial distance from their source. The decay is determined by the imaginary part of the axial wave number $k^{\pm}_{x,mn}$ in Equation (5.16), so that the evanescent mode attenuation coefficient is given by[18]

$$\alpha_{mn} = \left|\mathrm{Im}\left\{k^{\pm}_{x,mn}\right\}\right| = \frac{2\pi}{c\,(1-M^2)}\sqrt{\left|f^2 - f^2_{c,mn}\right|}\,. \tag{5.20}$$

The unit of the attenuation coefficient is Np/m, i. e. Neper[19] per meter. It can be converted to the attenuation rate a_{mn} in dB/m by applying

$$a_{mn} = 20 \cdot \lg\left(e^{\alpha_{mn}}\right) \approx 8.69\,\alpha_{mn}\,. \tag{5.21}$$

The attenuation decreases when increasing the frequency towards the cut-on frequency of a mode.

At a certain frequency only a limited number of modes are able to propagate and it is reasonable to neglect all evanescent modes. However, evanescent modes might become important if the frequency of interest is close to the cut-on frequency and the location of interest is in the vicinity of the source, e. g. a microphone which is located near a loudspeaker (see Section 6.5.4).

Figure 5.2 concludes the discussion of cut-on frequency and evanescent modes by demonstrating the phenomena visually. The acoustic pressure of the plane wave $p'_{0:0}$, the first higher order mode $p'_{1:0}$, and the resulting sound field $p' = p'_{0:0} + p'_{1:0}$ is plotted for three distinct frequencies:

1. The frequency is below the cut-on frequency,
2. the frequency is equal to the cut-on frequency, and
3. the frequency is above the cut-on frequency.

18 This notation is according to Tyler and Sofrin [482], where it was given for a stationary fluid.

19 Similar to the decibel, the Neper is a logarithmic scaled ratio of field or power quantities. While the Neper uses the natural logarithm ln, the decibel uses the decadic logarithm lg.

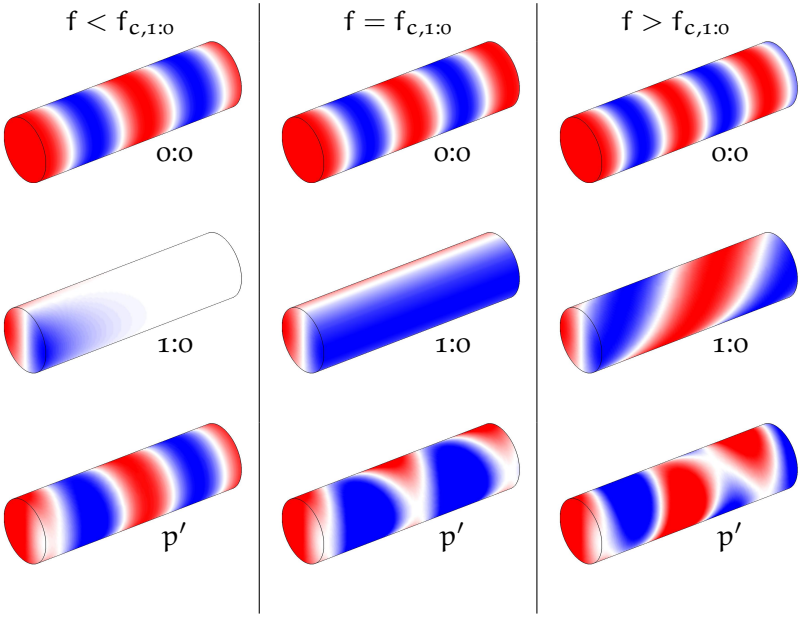

Figure 5.2: Illustration of the cut-on phenomena of higher order modes and the influence on the resulting sound field for mode 1:0.

The source of the circumferential mode is located at $x = 0$, that is the visible cross-section. The amplitude of the circumferential mode is chosen, so that the maximum acoustic pressure at the duct wall corresponds to the maximum acoustic pressure of the plane wave.
In the first case, the circumferential mode is excited at a frequency below its cut-on frequency. The mode is not able to propagate and becomes insignificant within a short axial distance. The resulting sound field, shown at the bottom, reflects the influence of the higher order mode close to its source, while it blends into the one-dimensional plane wave further along the duct. In the middle column the frequency is equal to the cut-on frequency, so that the circumferential mode is able to propagate along the duct. The resulting sound field is three-dimensional throughout the pictured

Table 5.2: Eigenvalues of the hard-wall solution for an annular duct according to Equations (5.22) and (5.23) with $\eta = 0.59$ and sorted in ascending order of j_{mn}.

m:n	0:0	1:0	2:0	3:0	4:0	5:0	6:0	0:1	1:1
j_{mn}	0	1.269	2.529	3.772	4.990	6.179	7.338	7.772	7.887
Q_{mn}	0	-0.320	-0.298	-0.239	-0.178	-0.126	-0.084	0.935	-0.745

duct segment and beyond. Even though the circumferential mode starts spinning at its cut-on frequency, the spinning motion can be observed much better at higher frequencies (as shown in the right column).

5.2.3 *Resonances in an Annular Cavity*

Starting from Equation (5.12), a resonance condition for a hard-walled annular cavity can be derived. The annular cavity is confined by two concentric cylinders with axial boundaries in both directions. The solution in radial direction is now dependent on the radius-ratio of the inner and outer wall, the so called hub-to-tip ratio $\eta = R_{hub}/R$. j_{mn} and Q_{mn} are determined by solving the equations (e. g. [255])

$$J'_m(j_{mn})Y'_m(\eta j_{mn}) - J'_m(\eta j_{mn})Y'_m(j_{mn}) = 0 \tag{5.22}$$

$$Q_{mn} = -\frac{J'_m(j_{mn})}{Y'_m(j_{mn})} \tag{5.23}$$

Equation (5.22) needs to be solved numerically. Some values of j_{mn} and Q_{mn} for a hub-to-tip ratio $\eta = 0.59$ are listed in Table 5.2. The radial wave number is still defined by Equation (5.18), with the appropriate values of j_{mn} for the annular geometry.

The hard-wall boundary conditions in axial direction require that $\hat{p}^+_{mn} = \hat{p}^-_{mn}$ at $x = 0$ and that $\sin(k_{x,mn}L_c) = 0$ at $x = L_c$, where L_c is the length of the cavity. The latter one is fulfilled for

any integer multiples of π, so that the axial wave number for the annular cavity is given by

$$k_x = \frac{\pi l}{L_c} \quad \text{with} \quad l \in \{1, 2, \dots\}. \tag{5.24}$$

Inserting Equations (5.18) and (5.24) into (5.13) yields the resonance condition[20]

$$f_{lmn} = \frac{c}{2\pi}\sqrt{\left(\frac{\pi l}{L_c}\right)^2 + \left(\frac{j_{mn}}{R}\right)^2}. \tag{5.25}$$

Equation (5.25) defines the resonance frequencies in a hard-walled annular cavity for resonances in axial, radial, and circumferential directions.

5.3 PLANE WAVES

At low[21] frequencies the sound field in a duct is one-dimensional. The acoustic field quantities of a wave traveling in x-direction vary with time and x, but are constant in any plane normal to the direction of wave propagation, i.e. in the duct cross-section. Such one-dimensional waves are called plane waves. For plane waves the acoustic wave equation (5.7) reduces to (e. g. [369])

$$\frac{\partial^2 p'}{\partial x^2} - \frac{1}{c^2}\frac{D^2 p'}{Dt^2} = 0. \tag{5.26}$$

A general solution regarding stationary medium ($v_0 = 0$) is given by (d'Alembert [111] and Euler [149], or [343, 369])

$$p'(x,t) = f_1\left(t - \frac{x}{c}\right) + f_2\left(t + \frac{x}{c}\right), \tag{5.27}$$

20 This equation is equally valid in a cylindrical geometry, with the appropriate value for j_{mn} (e. g. [284]).

21 The frequency limit is given by the cut-on frequency of the first higher order mode, as discussed in Section 5.2.1.

where f_1 and f_2 are arbitrary functions, with the only limitation that they have continuous derivatives of first and second order. The equation describes the superposition of two plane waves traveling in opposite direction with the propagation speed c. The acoustic fluctuations are assumed to be sinusoidal, so that f_1 and f_2 can be approximated by a Fourier series[22]. In complex exponential notation the Fourier series is expressed as (Fourier [165] or [369])

$$f(t) = \sum_{\omega} \hat{p}_{\omega} \, e^{i\omega t}. \tag{5.28}$$

The coefficient $\hat{p} = A \, e^{i\varphi}$ is a complex quantity with amplitude $A = |\hat{p}|$ and phase $\varphi = \arg \hat{p}$, commonly called complex pressure amplitude. Applying (5.28) to (5.27) yields (e. g. [48])

$$p'(x,t) = \sum_{\omega} \mathrm{Re} \left\{ \hat{p}^{+}_{\omega} e^{i\omega\left(t-\frac{x}{c}\right)} + \hat{p}^{-}_{\omega} e^{i\omega\left(t+\frac{x}{c}\right)} \right\} . \tag{5.29}$$

where $\hat{p}^{+}_{\omega}$ is the complex pressure amplitude of the wave traveling in positive x-direction and $\hat{p}^{-}_{\omega}$ for the wave in opposite direction. The use of the complex exponential notation is convenient mathematically. However, the relevant physical quantity is only the real part. This fact is indicated above by taking the real part $\mathrm{Re}\{z\}$ of the expression. It is common practice to omit this explicit notation, while still taking the real part. This reduced notation will be adopted here.

The acoustic pressure is given by the sum over all frequency components. Typically, the solution is given for one frequency component or a single frequency wave only, so that the summation of the frequencies can be dropped.

Applying these simplifications and introducing the wave number $k = \omega/c$ yields the familiar notation (e. g. [260, 343])

$$p'(x,t) = \left(\hat{p}^{+} e^{-ikx} + \hat{p}^{-} e^{ikx} \right) e^{i\omega t}. \tag{5.30}$$

22 Named after Jean Baptiste Joseph Fourier (1768-1830, French mathematician and physicist).

Equation (5.30) describes the temporal development and spatial distribution of the acoustic pressure of a one-dimensional, single frequency sound wave in a stationary medium. The behavior is illustrated in Figure 5.3 for three distinct cases depending on the values of $\hat{p}^{\pm}$:

1. Traveling wave: $|\hat{p}^{-}| = 0$
2. Standing wave: $|\hat{p}^{+}| = |\hat{p}^{-}|$
3. Mixed wave: $|\hat{p}^{+}| \neq |\hat{p}^{-}|$

Introducing a uniform mean flow in x-direction affects the propagation speed of the wave. In flow direction the propagation speed c is increased by the mean flow velocity, while it is decreased against flow direction, i.e. $c \pm v_0$ respectively. The convective effect of the mean flow is included in the wave number

$$k^{\pm} = \frac{\omega/c}{1 \pm M}. \tag{5.31}$$

where the superscript $\pm$ denotes in and against flow direction, respectively. Equation (5.30) changes to (e. g. [340, 343])

$$p'(x,t) = \left(\hat{p}^{+} e^{-ik^{+}x} + \hat{p}^{-} e^{ik^{-}x}\right) e^{i\omega t}. \tag{5.32}$$

5.4 ATTENUATION OF SOUND

Until now all dissipative effects have been neglected. In many applications the dissipative effects can be considered small and neglecting them reproduces the physical behavior adequately. However, certain conditions require their inclusion to describe the physics accurately.

The absorption of sound results in an attenuation of the wave amplitude with propagation distance and a change in propagation speed, i. e. phase velocity. Both can be expressed by adjusting the wave number. Disregarding all absorption phenomena the wave

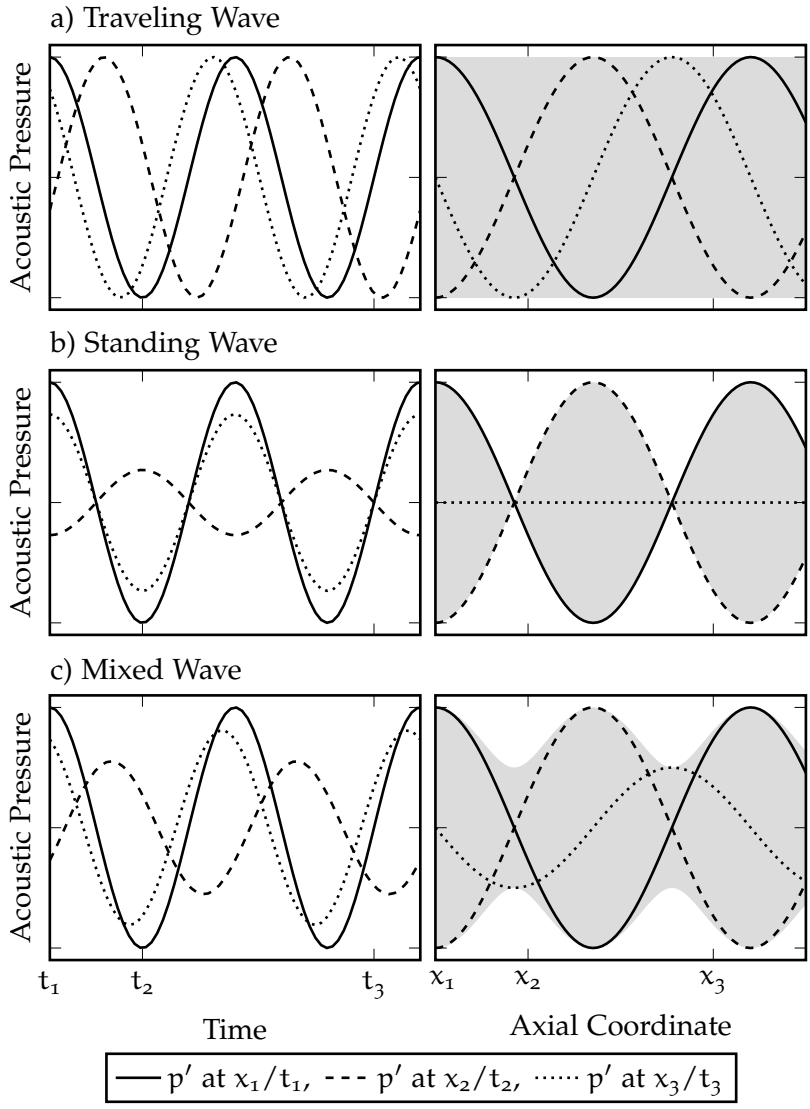

Figure 5.3: Illustration of the temporal development (on the left) and spatial distribution (on the right) of the acoustic pressure for three characteristic plane wave sound fields: a) Traveling Wave, b) Standing Wave, c) Mixed Wave.

number is real and given by $k_0 = \omega/c$ (in a stationary medium). Including absorption the wave number becomes a complex quantity, while Equation (5.30) remains unchanged

$$p'(x,t) = \left(\hat{p}^+ e^{-ikx} + \hat{p}^- e^{ikx}\right) e^{i\omega t} \quad \text{with} \quad k = \frac{\omega}{c_{ph}} - i\alpha\,, \tag{5.33}$$

where $\alpha = -\mathrm{Im}\{k\}$ is the attenuation coefficient in Np/m and $c_{ph} = \omega/\mathrm{Re}\{k\}$ is the phase velocity in m/s.
The attenuation coefficient accounts for the amplitude attenuation. Without any absorption $\alpha = 0$. The attenuation rate a in units dB/m can be computed according to Equation (5.21). The phase velocity reflects a possible change in propagation speed. When c_{ph} is a function of the frequency, the propagation is dispersive, i. e. waves of different frequencies propagate at different speeds. Disregarding any absorption $c_{ph} = c$ and the propagation is non-dispersive.

Some authors prefer the formulation with the propagation constant Γ instead of the wave number. Confusingly, there are some slightly different notations in use. Defined in ISO 80000-8:2007 [235] the propagation constant is related to the wave number by $\Gamma = ik$, so that (e. g. [257, 492, 508])

$$p' = \left(\hat{p}^+ e^{-\Gamma x} + \hat{p}^- e^{\Gamma x}\right) e^{i\omega t} \quad \text{with} \quad \Gamma = \alpha + i\frac{\omega}{c_{ph}}\,, \tag{5.34}$$

where $\alpha = \mathrm{Re}\{\Gamma\}$, $c_{ph} = \omega/\mathrm{Im}\{\Gamma\}$, and $k = \Gamma/i$. However, another common notation seems to be (e. g. [359, 405, 475, 498])

$$p' = \left(\hat{p}^+ e^{-k_0\Gamma x} + \hat{p}^- e^{k_0\Gamma x}\right) e^{i\omega t} \quad \text{with} \quad \Gamma = \frac{\alpha}{k_0} + i\frac{c}{c_{ph}}\,, \tag{5.35}$$

where $\alpha = k_0\mathrm{Re}\{\Gamma\}$, $c_{ph} = c/\mathrm{Im}\{\Gamma\}$, and $k = k_0\Gamma/i$. Yet another notation can be found in [126–128][23]

$$p' = \left(\hat{p}^+ e^{-ik_0\Gamma x} + \hat{p}^- e^{ik_0\Gamma x}\right) e^{i\omega t} \quad \text{with} \quad \Gamma = \frac{c}{c_{ph}} - i\frac{\alpha}{k_0}\,, \tag{5.36}$$

23 Unlike here, the references include the sign of the exponent $ik_0\Gamma$ in the propagation constant Γ.

where $\alpha = -k_o \mathrm{Im}\{\Gamma\}$, $c_{ph} = c/\mathrm{Re}\{\Gamma\}$, and $k = k_o\Gamma$. These differences should be kept in mind when browsing the literature. Here, the wave number notation as in Equation (5.33) will be used.

5.4.1 *Losses at the Wall*

Historically, the effect of viscosity on sound propagation has been studied by Stokes [451] and von Helmholtz [195]. Inspired by the experiments of Kundt [273], Kirchhoff [261] included the thermal conductivity losses and presented a theoretical description of the sound propagation including viscosity and thermal conductivity. His result is still the state of the art used today.

Navier-Stokes-Fourier Model

The equation of continuity 5.3a is generally valid, ideal fluid or otherwise, and is repeated here for convenience

$$\frac{\partial \rho}{\partial t} + \nabla \cdot (\rho \mathbf{v}) = 0\,. \tag{5.37a}$$

The equation of motion for a viscous fluid is given by the Navier-Stokes equation[24]. When neglecting all body forces[25], applying the Stokes hypothesis[26], and assuming Newtonian fluid[27] it is given by (Navier [348] and Stokes [449], or [33, 283, 495])

$$\rho \frac{D\mathbf{v}}{Dt} = -\nabla p + \nabla \cdot \tau_{ij}\,, \tag{5.37b}$$

24 Named after Claude Louis Marie Henri Navier (1785-1836, French engineer and physicist) and Sir George Gabriel Stokes (1819-1903, Irish mathematician, physicist, politician, and theologian).

25 That is in particular gravity.

26 The Stokes hypothesis (Stokes [449], or [495]) neglects the bulk viscosity $\mu_B = \lambda + \frac{2}{3}\mu = 0$, where λ is the second viscosity coefficient. The bulk viscosity will be introduced in Section 5.4.3

27 Named after Sir Isaac Newton (1642-1727, English physicist and mathematician). In Newtonian fluids, e.g. air and water, the viscous stresses are linearly related to the rate of strain [33, 495].

with the viscous, or deviatoric, stress tensor

$$\tau_{ij} = \mu \left(\frac{\partial v_i}{\partial x_j} + \frac{\partial v_j}{\partial x_i} - \frac{2}{3} \frac{\partial v_k}{\partial x_k} \delta_{ij} \right) ,$$

where δ_{ij} is the Kronecker delta[28]. The energy equation is given by the Kirchhoff-Fourier equation[29] (Kirchhoff [261] and Fourier [165], or [33, 283, 495])

$$\rho T \frac{Ds}{Dt} = \nabla \cdot (\kappa \nabla T) + \phi \, , \tag{5.37c}$$

where the viscous dissipation rate is specified as

$$\phi = \tau_{ij} \frac{\partial v_i}{\partial x_j} \, .$$

This system of partial differential equations 5.37a to 5.37c describes the motion of fluid in a compressible, viscous, and heat conducting fluid. It is commonly referred to as Navier-Stokes-Fourier model.

Acoustic, Vorticity, and Entropy Modes

After applying the typical acoustic linearization (corresponding to Equation (5.5)) a solution to Equations 5.37 can be obtained by assuming that the sound field is a superposition of vorticity, entropy, and acoustic modes. Wave equations for the three component modes are derived by Cremer [101] and Kovasznay [270], or in [369]. The fluctuating pressure of the acoustic mode yields

$$\nabla^2 p'_{ac} = \frac{1}{c^2} \frac{\partial^2 p'_{ac}}{\partial t^2} \, . \tag{5.38a}$$

28 Named after Leopold Kronecker (1823-1891, German mathematician). The Kronecker delta, or unit tensor, is such that for $i = j \rightarrow \delta_{ij} = 1$ and for $i \neq= j \rightarrow \delta_{ij} = 0$ [77].

29 Named after Gustav Robert Kirchhoff (1824-1887, German physicist) and Jean Baptiste Joseph Fourier (1768-1830, French mathematician and physicist).

All dissipative effects *within* the fluid are neglected, so that Equation (5.38a) is identical with (5.9). The fluctuating velocity of the vorticity mode is expressed as

$$\nabla^2 v'_{vor} = \frac{\rho}{\mu} \frac{\partial v'_{vor}}{\partial t} . \tag{5.38b}$$

Finally, the entropy mode is described by

$$\nabla^2 s'_{ent} = \frac{\rho c_p}{\kappa} \frac{\partial s'_{ent}}{\partial t} . \tag{5.38c}$$

The subscript at the field variables indicates the associated mode, 'ac' for the acoustic mode, 'vor' for the vorticity mode, and 'ent' for the entropy mode.

In a viscous and heat conducting fluid the boundary conditions at the stationary wall are vanishing velocity (no slip) and constant temperature (isothermal wall), respectively. The first boundary condition is generally valid for any combination of fluid and solid wall material. The second one requires that the heat capacity of the wall material is much larger than the heat capacity of the fluid, a condition which is generally met when the fluid in the duct is air. However, these boundary conditions can not be satisfied by the acoustic mode alone, but only by superposition with the vorticity and entropy mode.

This will be illustrated for the acoustic temperature fluctuations[30]. The fluctuating temperature field, which is a solution to Equations 5.37, is given by

$$T' = T'_{ac} + T'_{vor} + T'_{ent} . \tag{5.39}$$

The temperature fluctuations are related to the field quantities used in Equations 5.38 by (e. g. [369])

$$T'_{ac} \approx \left(\frac{T\beta}{\rho c_p} \right)_o p'_{ac} , \quad T'_{vor} = 0 , \quad T'_{ent} \approx \left(\frac{T}{c_p} \right)_o s'_{ent} , \tag{5.40}$$

30 The discussion applies to the acoustic particle velocity in a similar manner (as shown in [369]).

where the subscript '0' indicates that the approximation is of zeroth order. The vorticity mode does not contribute to the temperature fluctuations. Assuming the acoustic mode to be a lossless plane wave, where the excess temperature is a function of the axial coordinate x and the time t only. The entropy mode introduces a secondary wave which is dependent on time, as well as the distance from the wall y, for a cylindrical geometry $y = R - r$. The boundary condition is satisfied if $T'_{ac} + T'_{ent} = 0$ for $y = 0$. Furthermore, T'_{ent} must vanish for $y \to \infty$. The characteristic lengths after which the secondary waves become insignificant are

$$\delta_\nu = \sqrt{\frac{2\mu}{\omega\rho}} = \sqrt{\frac{2\nu}{\omega}} \quad \text{and} \quad \delta_\chi = \sqrt{\frac{2\kappa}{\omega\rho c_p}} = \sqrt{\frac{2\chi}{\omega}} \tag{5.41}$$

for the vorticity wave and the entropy wave, respectively. They are related via the Prandtl number $\delta_\nu/\delta_\chi = \sqrt{Pr}$.

These characteristic lengths can be regarded as a boundary-layer thickness. The fluid dynamic boundary-layer concept[31] was adopted to an *acoustic boundary-layer* by Cremer [101][32]. The idea is that dissipative effects only need to be considered in a thin layer very close to the wall, while the remaining fluid can be regarded as ideal where the acoustic wave is not affected.

The thickness of the viscous and the thermal acoustic boundary-layers are of the same order of magnitude, with the latter one being slightly thicker. They are thin at high frequencies, but tend to infinity as $f \to 0$. The numerical values at 1 kHz and standard

31 The boundary-layer concept was introduced by Prandtl [372] in 1904 and is considered one of the most important advances in fluid dynamics [15]. Schlichting and Gersten [432] give detailed discussions on all aspects of the subject.

32 Blackstock [64]: "Notice that the acoustic boundary-layer is qualitatively different from the ordinary viscous boundary-layer that develops in a pipe when the flow through the pipe is steady (unidirectional). The thickness of the steady flow boundary layer grows with the distance, eventually filling the entire cross-section of the pipe. The acoustic boundary layer, on the other hand, cannot grow very much because the fluid never flows in one direction for more than half a period."

conditions are $\delta_\nu = 0.068\,\text{mm}$ and $\delta_\chi = 0.081\,\text{mm}$, which is generally small compared to the wavelength (at the same conditions $\lambda = 340.5\,\text{mm}$).

Equation (5.38c) together with (5.40) yields an entropy wave expressed by the fluctuating temperature of the form [101, 340, 369]

$$T'_{ent} = \text{Re}\left\{-T'_{ac} e^{-(1+i)y/\delta_\chi} e^{i\omega t}\right\} . \tag{5.42}$$

The temperature field close to the wall resulting from the superposition of the acoustic mode with the entropy mode is then given by [214][33]

$$T' = \text{Re}\left\{T'_{ac}\left(1 - e^{-(1+i)y/\delta_\chi}\right) e^{i\omega t}\right\} . \tag{5.43}$$

The temperature profiles of the entropy mode alone and of the superposition according to Equations (5.42) and (5.43), respectively, are plotted in Figure 5.4 over a complete oscillation cycle in steps of $\pi/4$. As required, the superposition shows that the temperature fluctuations vanish at the wall and fade into the acoustic mode away from the wall. At the distance given by the boundary-layer thickness δ_χ the magnitude of the combined wave $|T'|$ is within 86 % of $|T'_{ac}|$.

Kirchhoff's Solution

Kirchhoff [261] was seeking a solution of Equations 5.37 in order to quantify the absorption of sound. With some mathematical

33 The notation in the reference is slightly different. The conversion can be done with the help of the relation $\sqrt{i} = (1+i)/\sqrt{2}$ [101]. Please also note the $e^{-i\omega t}$ time-dependency in the reference.

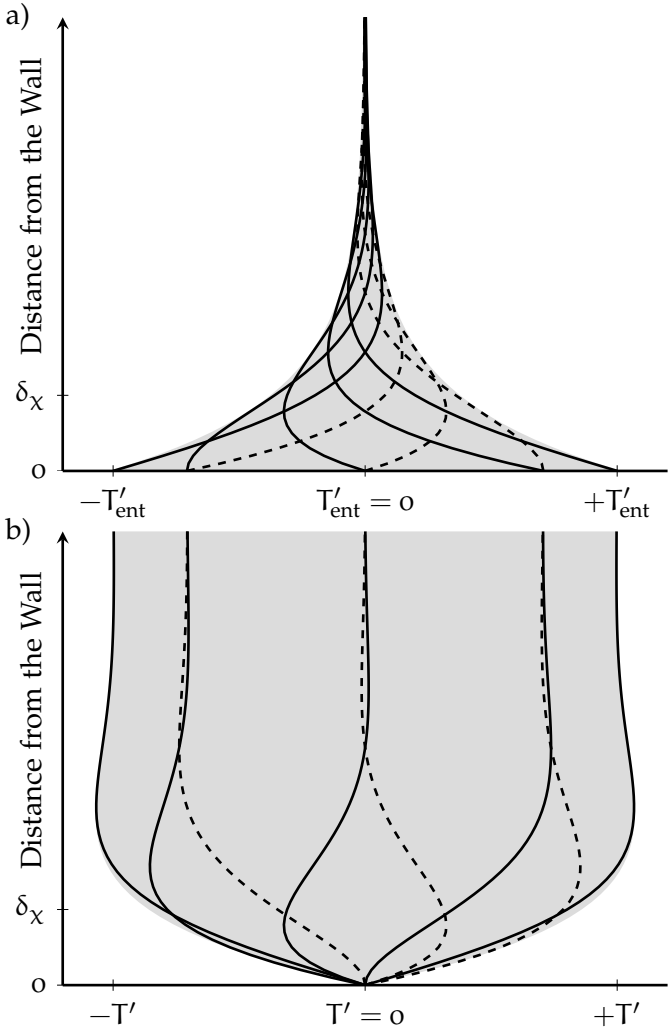

Figure 5.4: Illustration of the entropy mode and the resulting fluctuating temperature field at a wall. a) Temperature fluctuations of the entropy mode. b) Fluctuating temperature field $T' = T'_{ac} + T'_{ent}$. The temperature profiles follow a complete oscillation period in $\pi/4$ steps.

effort he derived a complicated transcendental equation for the propagation constant[34] Γ (Kirchhoff [261] or [390, 475]):

$$\begin{aligned} &i\Gamma^2\left(\Gamma^2 - i\frac{Sh^2}{He^2}\right)^{-\frac{1}{2}}\left(\frac{1}{x_1}-\frac{1}{x_2}\right)\frac{J_1(a_1)}{J_0(a_1)} \\ &+\left(\frac{\gamma\,He^2}{Pr\,Sh^2}-i\frac{1}{x_1}\right)(\Gamma^2-x_1)^{\frac{1}{2}}\;\frac{J_1(a_2)}{J_0(a_2)} \\ &-\left(\frac{\gamma\,He^2}{Pr\,Sh^2}-i\frac{1}{x_2}\right)(\Gamma^2-x_2)^{\frac{1}{2}}\;\frac{J_1(a_3)}{J_0(a_3)} = 0\,, \end{aligned} \tag{5.44}$$

with

$$a_1 = He\sqrt{\Gamma^2 - i\frac{Sh^2}{He^2}},\quad a_2 = He\sqrt{\Gamma^2-x_1},\quad a_3 = He\sqrt{\Gamma^2-x_2},$$

and x_1 and x_2 are the small and large roots of

$$1 + x\left[1 + i\frac{He^2}{Sh^2}\left(\frac{4}{3}+\frac{\gamma}{Pr}\right)\right] + i\frac{\gamma\,He^2}{Pr\,Sh^2}\left(\frac{1}{\gamma}+i\frac{4}{3}\frac{He^2}{Sh^2}\right)x^2 = 0\,.$$

The notation that is used here was introduced by Tijdeman [475], where $He = kR$ is the Helmholtz number (or reduced frequency), $Sh = R\sqrt{\omega/\nu}$ is the shear number (square root of the Stokes number), $Pr = c_p\mu/\kappa$ is the Prandtl number, and J_0 and J_1 are Bessel functions of the first kind of zeroth and first order, respectively. Equation (5.44) is subject to the following assumptions (Kirchhoff [261], or [475, 492]):

1. Homogeneous medium[35],
2. linear acoustics (small amplitude, sinusoidal perturbations),
3. semi-infinite tube, so that end-effects can be neglected,
4. radial velocity is zero at tube axis,

34 The propagation constant is defined as in Equation (5.35).

35 The wave length and the tube radius must be large in comparison with the mean free path. For air of normal atmospheric temperature and pressure the limits are $f < 10^8$ and $R > 10^{-4}$ mm [475].

5. velocity vanishes at the wall (no-slip boundary condition),
6. isothermal walls (const. temperature boundary condition),
7. cylindrical geometry[36],
8. plane waves[37], and
9. stationary medium.

The importance of Equation (5.44) is given by the fact that it is exact[38], and thus has served as a starting point for several further studies [257, 261, 390, 448, 492]. Unfortunately, it fails an analytic solution. In his original paper Kirchhoff [261] presents an approximate solution by restricting himself to a

10. wide tube[39].

That means, the influence of the wall affects only a small layer of fluid which is an insignificant fraction of the whole of the contents. Ultimately, that is the same assumption that Cremer [101] treated rigorously about 80 years later, so that the wide tube case is limited to $\delta_\nu, \delta_\chi \ll R$ [369]. The wide tube assumption yields the following expression for the propagation constant (Kirchhoff [261], or [369, 475])

$$\Gamma = i + \frac{(1+i)}{\sqrt{2}\,\mathrm{Sh}} \left(1 + \frac{\gamma - 1}{\sqrt{\mathrm{Pr}}}\right). \tag{5.45}$$

The notation is again that of Tijdeman [475] with the quantities specified above and the propagation constant is defined as in

36 For non-cylindrical geometries Davies [113] suggest to replace the radius with the hydraulic radius $r_h = 2A/P$. More detailed (and more complicated) treatments are given in [108, 448].

37 A discussion including the effect on higher order modes can be found in [36, 79].

38 It is an exact solution of the linearized Navier-Stokes-Fourier model (linearization of Equations 5.37), which are an approximation to first order.

39 A survey of models for various tube dimensions is given in [475].

Equation (5.35). Written in terms of attenuation coefficient, phase velocity, and wave number this yields

$$\alpha_{\text{wall}} = \frac{\omega}{c}\frac{1}{\sqrt{2}\,\text{Sh}}\left(1+\frac{\gamma-1}{\sqrt{\text{Pr}}}\right) = \underbrace{\frac{1}{R\,c}\sqrt{\frac{\nu\omega}{2}}}_{\alpha_{\text{wall},\nu}} + \underbrace{\frac{\gamma-1}{R\,c}\sqrt{\frac{\chi\omega}{2}}}_{\alpha_{\text{wall},\chi}} \tag{5.46a}$$

$$c_{\text{ph,wall}} = c\left[1+\frac{1}{\sqrt{2}\,\text{Sh}}\left(1+\frac{\gamma-1}{\sqrt{\text{Pr}}}\right)\right]^{-1} \tag{5.46b}$$

$$k_{\text{wall}} = \frac{\omega}{c_{\text{ph,wall}}} - i\alpha_{\text{wall}} = \frac{\omega}{c} + (1-i)\alpha_{\text{wall}} \tag{5.46c}$$

where $\alpha_{\text{wall},\nu}$ and $\alpha_{\text{wall},\chi}$ are the separate attenuation coefficients due to viscosity and thermal conductivity, respectively.

The attenuation is proportional to the square root of the frequency $\alpha_{\text{wall}} \propto \sqrt{f}$ and also dependent on the duct radius and the properties of the fluid. As a numeric example, the wall attenuation coefficient at 1 kHz and ISA conditions[40] is $\alpha_{\text{wall}} = 0.0266\,\text{Np/m}$, corresponding to an attenuation rate $a = 0.23\,\text{dB/m}$. The effect on the phase velocity is rather small.[41] At 1 kHz and standard conditions the phase velocity is reduced from 340.45 m/s to 339.96 m/s. This corresponds to a change of 0.14 %.

Ronneberger [411] used the low reduced frequency solution of [475, 508] to derive a corrected attenuation coefficient[42]

$$\alpha_{\text{wall}} = \frac{\omega}{c}\left[\frac{1}{\sqrt{2}\,\text{Sh}}\left(1+\frac{\gamma-1}{\sqrt{\text{Pr}}}\right) + \frac{1}{\text{Sh}^2}\left(1+\frac{\gamma-1}{\sqrt{\text{Pr}}} - \frac{1}{2}\gamma\frac{\gamma-1}{\text{Pr}}\right)\right]. \tag{5.47}$$

The first term in Equation (5.47) is identical to the attenuation coefficient found by Kirchhoff and the second term adds a constant

40 The International Standard Atmosphere [220] defines the temperature and pressure at sea level as 288.15 K and 101.325 kPa, respectively.

41 Some authors, e. g. [113, 115], suggest to neglect the change of phase velocity, so that the wave number yields $k = \omega/c - i\alpha_{\text{wall}}$.

42 See as well the discussion by Peters et al. [366].

value which is independent of frequency. Its relative contribution to the total losses is larger at low frequencies and small duct radii, where the first term becomes smaller.

Convective Effect of a Mean Flow

The assumptions listed above require a stationary medium. Now, the convective effect of a mean flow will be discussed. A more profound approach including the additional absorption due to a turbulent flow boundary-layer is treated in the succeeding section.

Without any dissipative effects the convective wave number is given by Equation (5.31), where the mean flow introduces a distinction between the wave number in and against flow direction. Following this definition, but without any further explanation, Davies et al. [115][43] suggest that the appropriate wave numbers including viscothermal losses at the wall are given by

$$k^{\pm}_{\text{wall,Davies}} = \frac{\omega/c}{1 \pm M} + (1 - i)\frac{\alpha_{\text{wall}}}{1 \pm M} \tag{5.48}$$

Dokumaci [126, 127] presents an asymptotic solution of the convective acoustic equations for large shear numbers $Sh \gg 1$ following the simplifications given by Zwikker and Kosten [508]. His result is different from Equation (5.48) and reads

$$k^{\pm}_{\text{wall,Dokumaci}} = \frac{\omega}{c}\frac{\Gamma}{1 \pm \Gamma M} = \frac{\omega/c}{1 \pm \Gamma M} + (1 - i)\frac{\alpha_{\text{wall}}}{1 \pm \Gamma M} \tag{5.49}$$

where Γ is the propagation constant that corresponds to the Kirchhoff solution, but given in the notation of Equation (5.36)

$$\Gamma = 1 + \frac{(1 - i)}{\sqrt{2}Sh}\left(1 + \frac{\gamma - 1}{\sqrt{Pr}}\right) = 1 + (1 - i)\frac{c}{\omega}\alpha_{\text{wall}}\,. \tag{5.50}$$

The earliest and probably most rigorous derivation is given by Ronneberger [411, 413]. He presents a quasi-laminar theory that,

43 Please note that Equation (3) in the reference is erroneous, as is discussed in [114].

according to Peters et al. [366], describes the damping of acoustic waves quite accurately, when the acoustic boundary-layer thickness is small compared to the thickness of the viscous sublayer of the flow. To first order and with $1 - 0.18\,M^2 \approx 1$ (for small Mach numbers) Ronneberger results at [411]

$$k^{\pm}_{\text{wall,Ronneberger}} = \frac{\omega/c}{1 \pm M} + (1 - i)\left(\frac{\alpha_{\text{wall},\nu}}{(1 \pm M)^3} + \frac{\alpha_{\text{wall},\chi}}{(1 \pm M)}\right), \quad (5.51)$$

where $\alpha_{\text{wall},\nu}$ and $\alpha_{\text{wall},\chi}$ are the attenuation coefficients due to viscosity and thermal conductivity losses at the wall given in Equation (5.46a), respectively.

The corresponding attenuation coefficients $\alpha^{\pm}{}_{\text{wall}} = -\text{Im}\{k^{\pm}\}$ are plotted in Figure 5.5. While the attenuation is reduced in flow direction, it increases against the flow, compared to the stationary case α_{wall}. The approach of Davies shows the smallest effect. The values of Dokumaci's and Ronneberger's model are very close, but Ronneberger predicts a slightly stronger influence of the flow. The influence of convection on the phase velocity is visualized in Figure 5.5b. Here, $\Delta c^{\pm}_{\text{ph,wall}}$ shows only the additional contribution that is introduced by the losses, so that for Davies and Ronneberger the change is given by $\Delta c^{\pm}_{\text{ph,wall}} = c^{\pm}_{\text{ph,wall}} - c\,(1 \pm M)$ and for Dokumaci $\Delta c^{\pm}_{\text{ph,wall}} = c^{\pm}_{\text{ph,wall}} - c\,(1 \pm \text{Re}\{\Gamma\}M)$. While the change of phase velocity in a stationary medium is small already, the convection introduces an even smaller variation around that value. The results of Davies' and Dokumaci's models are identical. They express a reduction of phase velocity in flow direction and an increase against the flow. Ronneberger's model predicts the opposite and a generally smaller effect.

Comparison to experimental data has shown [366] that Ronneberger's model includes the physical effects most accurately. However, browsing in recent literature it seems that Dokumaci's approach is the most accepted [13, 147, 205]. In the end, the small differences in the result of these two models (Dokumaci vs. Ronneberger) can be neglected in most practical applications.

The limit that the acoustic boundary-layer thickness needs to be

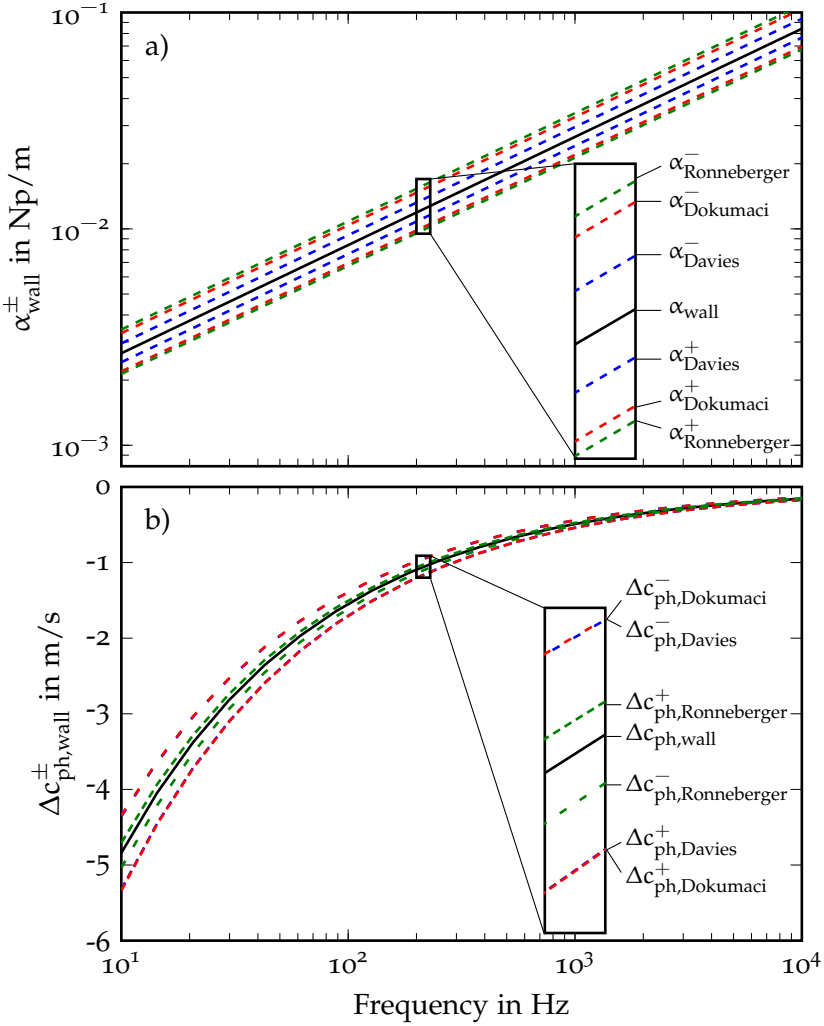

Figure 5.5: Convective effect of a mean flow on the wall attenuation coefficient for $M = 0.1$ and $R = 0.035\,\text{m}$ at ISA conditions.

smaller than the thickness of the viscous sublayer of the turbulent flow $\delta_\nu, \delta_\chi < \delta_\tau$ holds for all three models and is generally fulfilled for the parameters studied here, except for low frequencies at high static pressures. When $\delta_\nu, \delta_\chi > \delta_\tau$, then the additional losses due to the interaction with the turbulent flow boundary-layer need to be considered. This is discussed in the next section.

5.4.2 *Losses due to Turbulent Flow*

The absorption of sound in a duct is increased by the presence of a turbulent flow boundary-layer. This fact has been studied experimentally (e. g. [229, 366, 413]) and theoretically (e. g. [211, 212, 229, 263, 366, 413, 490]). The additional absorption is due to the transfer of acoustic energy to the turbulent stresses, a phenomenon which occurs when the acoustic boundary-layer thickness is larger than the viscous sublayer of the turbulent flow. Allam and Åbom [13] presented a comparison of the available models and concluded that the model by Howe [212, 214] is the most complete model developed so far[44].
Howe [212, 214] derives the following expression for the wave number, including the attenuation due to turbulent flow:

$$k^{\pm}_{\text{turb}} = \frac{\omega/c}{1 \pm M} + \frac{2i\rho c}{(1 \pm M)\, D_h}\, Y, \tag{5.52}$$

where Y is the wall shear layer admittance

$$\begin{aligned} Y = \frac{e^{-\frac{i\pi}{4}}}{\rho\omega^{3/2}} \Bigg[\left(\frac{\omega/c}{1 \pm M}\right)^2 \sqrt{\nu}\, F_A\left(\sqrt{\frac{i\omega\nu}{\kappa^2 v_*^2}}, \delta_\nu \sqrt{\frac{i\omega}{\nu}}\right) \\ + \frac{\beta\omega^2}{c_p} \sqrt{\chi}\, F_A\left(Pr_t \sqrt{\frac{i\omega\chi}{\kappa^2 v_*^2}}, \delta_\nu \sqrt{\frac{i\omega}{\chi}}\right) \Bigg] . \end{aligned} \tag{5.53}$$

44 Since then, some extensions have been proposed in [263, 490], which are not included here.

$D_h = 4A/P$ is the hydraulic diameter of the duct (with the duct cross-section area A and the duct perimeter P), κ is the Kármán constant[45] (please note that the same symbol was used to represent thermal conductivity before), v_* is the friction velocity, δ_ν is the thickness of the viscous acoustic boundary layer, β is the coefficient of expansion at constant pressure[46], c_p is the specific heat capacity at constant pressure per unit of mass, Pr_t is the turbulence Prandtl number[47], and

$$F_A(a,b) = \frac{i\left[H_1^{(1)}(a)\cos(b) - H_0^{(1)}(a)\sin(b)\right]}{H_0^{(1)}(a)\cos(b) + H_1^{(1)}(a)\sin(b)} \tag{5.54}$$

with the Hankel functions[48] $H_m^{(1)}$ and $H_m^{(2)}$. The friction velocity v_* can be computed from the empirical pipe flow formula [212, 432]

$$\frac{U(y)}{v_*} = \frac{1}{\kappa}\ln\left(\frac{v_* y}{\nu}\right) + C\,, \tag{5.55}$$

where $U(y)$ is the flow velocity at a specified distance from the wall y, κ is again the Kármán constant, and C is an empirical constant, usually specified as $C = 5$ [212, 432]. $U(y)$ can be replaced by the mean flow velocity U, when setting $y = R$ and $C = 2$ in the above equation, where the adjustment of C accounts for the difference between the mean flow velocity and the maximum flow velocity at the centerline ($y = R$) of the duct [212, 432].

The thickness of the viscous acoustic boundary layer δ_ν is calculated from [212, 214]

$$\frac{\delta_\nu v_*}{\nu} = 6.5\left(1 + \frac{\sigma(\omega/\omega_*)^3}{1+(\omega/\omega_*)^3}\right)\,, \tag{5.56}$$

45 Named after Theodore von Kármán (1881-1963, Hungarian-American mathematician, aerospace engineer, and physicist) [256]. The Kármán constant is a universal constant for turbulent boundary layers. Its empirical value is $\kappa = 0.41$ [214, 432].

46 For an ideal gas $\beta = 1/T$, so that $\beta c^2/c_p = \gamma - 1$ [212]

47 Schlichting and Gersten [432] state that $Pr_t = 0.87$, while Howe [212, 214] gives a value of $Pr_t = 0.7$, which will be used here

48 Named after Hermann Hankel (1839-1873, German mathematician). Also known as Bessel functions of the third kind.

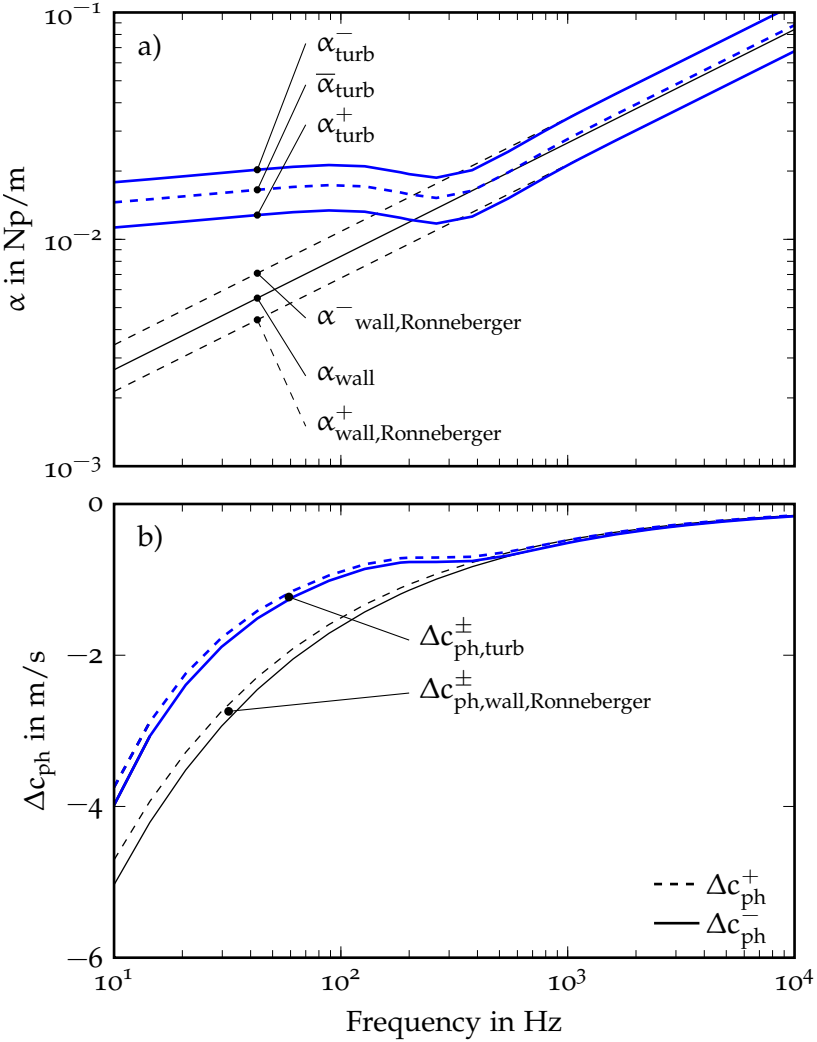

Figure 5.6: Losses at the duct wall including the effect of a turbulent flow boundary-layer for $M = 0.1$ and $R = 0.035\,m$ at ISA conditions in comparison to the stationary and Ronneberger's convective attenuation coefficient: a) attenuation coefficient, b) change of phase velocity.

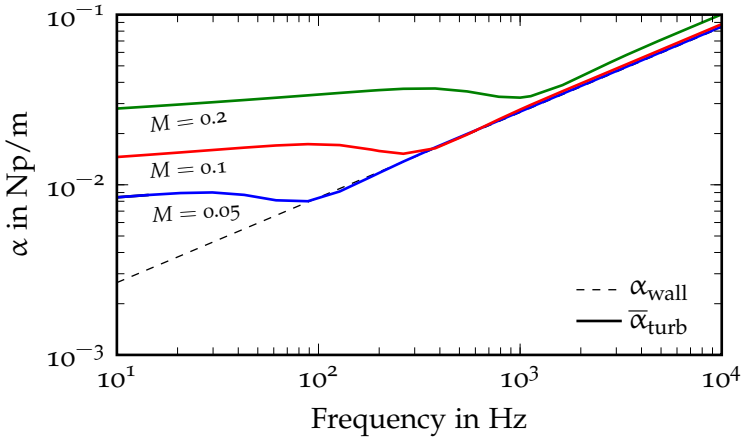

Figure 5.7: Average attenuation coefficient due to losses within the turbulent flow boundary-layer at various Mach numbers and $R = 0.035\,m$.

where the critical frequency ω_* can be roughly estimated by [212, 214] $\omega_* \nu / v_*^2 \approx 0.01$, and $\sigma = 1.7$ yields best agreement with experimental results [212, 214]. At low frequencies, when $\omega \to 0$, Equation (5.56) estimates the thickness of the viscous acoustic boundary layer with $\delta_\nu v_* / \nu = 6.5$, which yields better agreement with experiments [212] than the commonly used value of 7. This value increases at higher frequencies to account for viscous diffusion and for the reduced efficiency of turbulent diffusion.

The turbulence attenuation coefficient is plotted in Figure 5.6a, where it is compared to Ronneberger's convective attenuation coefficient. The wall attenuation coefficient for a stationary medium α_{wall} is given as reference and the average turbulence attenuation coefficient $\overline{\alpha}_{turb} = (\alpha^+_{turb} + \alpha^-_{turb})/2$ is introduced. The additional absorption due to the interaction with the turbulent boundary-layer occurs at low frequencies only. At high frequencies, $\alpha^\pm_{turb}$ becomes identical with $\alpha^\pm_{wall,Ronneberger}$. The same behavior is observed for the phase velocity in Figure 5.6b.

The dependency on the Mach number is illustrated in Figure 5.7 for the average attenuation coefficient and the Mach numbers 0.05,

0.1, and 0.2. Generally, the losses due to the turbulent flow increase at higher Mach numbers, so that higher frequencies are affected.

5.4.3 *Losses Within the Fluid*

At normal atmospheric temperature and pressure conditions, the losses within the fluid become significant at high frequencies (beyond the audible range) or when sound travels long distances. Such conditions are met when dealing with waves propagating through the atmosphere, for example. In duct acoustics, these effects are commonly neglected as they are two orders of magnitude smaller than the losses at the duct walls. While this generally holds for air at normal atmospheric temperature and pressure, it will be shown in Section 6.6.5 that the losses within the fluid might become important at elevated pressure and temperature.

This section will be limited to a collection of the necessary formulas. A detailed historical review of the subject is presented by Delany [120] and an in-depth discussion of the physics is given by Bass et al. [30]. Furthermore, the subject is treated extensively in the book of Pierce [369]. Today's state of the art models that describe the sound absorption within the fluid have been established in a series of publications by Evans et al. [152] and Bass et al. [29, 31, 32], which ultimately led to the international standard ISO 9613-1:1993 [236]. Bass [28] discussed the validity of the available models under high temperature conditions and came to the conclusion that they are accurate within 10 % for low water vapor concentrations (less than 10 %).

The loss mechanisms within the fluid can be grouped into classical absorption mechanisms, resulting from the fundamental transport properties of a fluid, and the losses based on the movement of the molecules, referred to as molecular relaxation losses.

Viscothermal Losses

The classical absorption is associated with the transfer of kinetic energy of molecules into heat. The responsible fluid properties are viscosity, thermal conductivity, diffusion, and radiation. However, the contribution of diffusion[49] and radiation[50] to the total losses is very small, so that only the first two are considered here. Therefore, the classical absorption is also referred to as viscothermal absorption.

The effect of viscosity on sound propagation has been treated by Stokes [449, 451], and the dependency on thermal conductivity has been introduced by Kirchhoff [261]. Both effects are additive, so that the classical attenuation coefficient due to viscothermal absorption within the fluid is given as (Stokes [451] and Kirchhoff [261], or [30, 369])

$$\alpha_{cl} = \underbrace{\frac{\omega^2}{2\rho c^3}\,\frac{4}{3}\mu}_{\text{viscosity}} + \underbrace{\frac{\omega^2}{2\rho c^3}\,\frac{(\gamma-1)\kappa}{c_p}}_{\text{thermal conductivity}} = \frac{\omega^2\mu}{2\rho c^3}\left(\frac{4}{3}+\frac{\gamma-1}{Pr}\right). \quad (5.57)$$

The classical attenuation coefficient is proportional to the square of the frequency: $\alpha_{cl} \propto f^2$. It accurately describes the sound attenuation in a monoatomic gas. In polyatomic gases, for example nitrogen and oxygen (the main constituents of air), the degrees of freedom within the molecules generate additional energy losses, so that the classical absorption underestimates the attenuation.

49 The effect of diffusion is known to be small, mainly because the two major constituents of air, nitrogen and oxygen, are of such similar molecular weights; as Rocard [404] and Herzfeld and Litovitz [196] have shown, this process typically contributes only 0.3 % to the total classical absorption at audio frequencies. (from [120])

50 The effect of radiation is very small (Stokes [450]). Radiation absorption plays little role in gases, except possibly at very low pressures or very high temperatures (Markham et al. [314]). Radiation losses are significant only at very low frequencies (Evans et al. [152]).

Molecular Relaxation Losses

The molecular relaxation losses consider the transfer of energy from various states of molecular motion into rotational and vibrational movements. The time that is necessary for energy to be transferred between the states of motion is called relaxation time. The losses are maximized if the associated relaxation frequency corresponds to the acoustic frequency. Each relaxation process has its own characteristic relaxation frequency. For frequencies below the relaxation frequency, the absorption is proportional to f^2 (a behavior already found for the classical absorption). However, above the relaxation frequency the absorption approaches a constant value.

The relaxation frequency of rotational relaxation is much higher than any frequency of interest[51], so that the associated attenuation is proportional to f^2 over the whole audible range and beyond [120, 369]. The attenuation coefficient due to rotational relaxation is given as [30]

$$\alpha_{\text{rot}} = \frac{\omega^2}{2\rho c^3} \frac{\gamma(\gamma-1)R}{1.25\, c_p} \mu\, Z_{\text{rot}}\,, \tag{5.58}$$

where R is the specific gas constant and the rotational collision number is given by

$$Z_{\text{rot}} = 61.6\, e^{-16.8\, T^{-1/3}}.$$

A simplified approach accounts for the rotational relaxation losses with a bulk viscosity μ_B [29, 369]

$$\alpha_{\text{rot}} = \frac{\omega^2}{2\rho c^3} \mu_B\,. \tag{5.59}$$

The bulk viscosity is related to the dynamic viscosity by $\mu_B = 0.6\,\mu$ [29, 182, 369]. While Equations (5.58) and (5.59) give nearly identical results at normal atmospheric temperature and pressure,

51 In the order of 10^8 Hz [120].

Equation (5.59) underestimates the attenuation at higher temperatures, so that Equation (5.58) will be used.

The relaxation frequencies of the vibrational movements can be much lower than the one for rotation and must be treated for each species separately. The resulting attenuation coefficient is the sum over all species, while for air only the two main constituents, nitrogen N and oxygen O, are considered:

$$\alpha_{vib} = \sum_i \alpha_{vib,i} = \alpha_{vib,O} + \alpha_{vib,N} \tag{5.60}$$

The attenuation coefficient due to vibrational relaxation for one particular constituent is given by [30, 236]

$$\alpha_{vib,i} = \frac{2f}{c}(\alpha\lambda)_{max,i} \frac{f/f_{r,i}}{1 + (f/f_{r,i})^2}\,. \tag{5.61}$$

with the maximum attenuation over a distance of one wavelength given in Np/m

$$(\alpha\lambda)_{max,i} = \frac{2\pi}{35} X_i \left(\frac{\theta_i}{T}\right)^2 e^{-\theta_i/T}, \tag{5.62}$$

where X_i is the mole fraction, θ_i is the characteristic vibrational temperature, and $f_{r,i}$ is the vibrational relaxation frequency of constituent i. For oxygen O and nitrogen N [32, 236, 414]:

$\theta_O = 2239.1\,K, \quad \theta_N = 3352.0\,K, \quad X_O = 0.209, \quad X_N = 0.781,$

$$f_{r,O} = \frac{p}{p_{ref}} \left(24 + 4.04 \cdot 10^4 h \frac{0.02 + h}{0.391 + h}\right), \text{ and}$$

$$f_{r,N} = \frac{p}{p_{ref}} \left(\frac{T}{T_{ref}}\right)^{-\frac{1}{2}} \left(9 + 280\, h \exp\left\{-4.170 \left[\left(\frac{T}{T_o}\right)^{-\frac{1}{3}} - 1\right]\right\}\right).$$

p and T are the ambient pressure in kPa and the ambient temperature in K, respectively, while $p_{ref} = 101.325\,kPa$ and $T_{ref} = 293.15\,K$ are atmospheric reference values. h is the molar concentration of water vapor in % (fraction of air molecules that are wa-

ter). It can be calculated from the relative humidity RH (also in %) via the saturation water vapor pressure p_{ws} [236, 369]

$$h = RH \frac{p_{ws}}{p} . \tag{5.63}$$

While ISO 9613-1:1993 [236] presents a simplified calculation for p_{ws}, the state of the art formula is given by [485, 486]

$$\ln\left(\frac{p_{ws}}{p_c}\right) = \frac{T_c}{T}\left(a_1\vartheta + a_2\vartheta^{1.5} + a_3\vartheta^3 + a_4\vartheta^{3.5} + a_5\vartheta^4 + a_6\vartheta^{7.5}\right) \tag{5.64}$$

with

$$\begin{aligned} a_1 &= -7.85951783 & a_4 &= 22.6807411 & T_c &= 647.096\,\mathrm{K} \\ a_2 &= 1.84408259 & a_5 &= -15.9618719 & p_c &= 22.064 \times 10^6\,\mathrm{Pa} \\ a_3 &= -11.7866497 & a_6 &= 1.80122502 & \vartheta &= 1 - T/T_c \end{aligned}$$

The saturation water vapor pressure is a function of temperature and is defined for temperatures up to the critical point of water at T_c, where the properties of the gas and liquid phase converge.

Combined Losses Within the Fluid

The losses within the fluid are additive[52], so that they are given by the sum

$$\alpha_{fluid} = \alpha_{cl} + \alpha_{rot} + \alpha_{vib,O} + \alpha_{vib,N} \tag{5.65}$$

The classical and rotational relaxation losses are functions of pressure, temperature and frequency only. Often they are combined in one expression $\alpha_{cr} = \alpha_{cl} + \alpha_{rot}$. The vibrational relaxation attenuation depends on the particular atmospheric constituent and the mole fraction of water vapor, as well as pressure, temperature, and frequency.

52 Bass et al. [30] states that this is valid for frequencies up to 10 MHz.

The characteristics of the attenuation within air at normal conditions is illustrated in Figure 5.8a, where the different contributions according to Equation (5.65) are plotted. The relaxation frequencies of oxygen $f_{r,O}$ and nitrogen $f_{r,N}$ are indicated with arrows. The combined losses within the fluid (the sum of all contributions) is given by the solid black line. The attenuation rate of the total losses at 1 kHz is $a_{fluid} = 8.174 \times 10^{-3}\,\mathrm{dB/m}$.

The wave number regarding the attenuation within the fluid is given by [369, 414][53]

$$k_{fluid} = \frac{\omega}{c} - i\alpha_{cl} - i\alpha_{rot} - \frac{2f}{c}\sum_i (\alpha\lambda)_{max,i}\frac{i\,f/f_{r,i}}{1 + i\,f/f_{r,i}}\,. \qquad (5.66)$$

The phase velocity is only affected by the vibrational relaxation losses, while it remains unchanged and identical to c by the classical and rotational relaxation losses alone [414]. Around the relaxation frequency of each constituent, the phase velocity increases by $c_{ph,max,i} = c/\pi(\alpha\lambda)_{max,i}$. This is illustrated in Figure 5.8b. The corresponding increments of oxygen and nitrogen at 288 K are $c_{ph,max,O} = 0.104\,\mathrm{m/s}$ and $c_{ph,max,N} = 0.018\,\mathrm{m/s}$, respectively. The effect of the losses within the fluid on the phase velocity is even smaller than the wall influence (at the specified radius). Furthermore, it should be noted that the attenuation at the wall reduces the phase velocity, while it is increased due to the losses within the fluid.

Figure 5.9 shows the dependency of the attenuation on the relative humidity. At high frequencies, depending on the relative humidity, the total losses within the fluid are given by α_{cr} alone.

53 Please note that the references use a $e^{-i\omega t}$ time dependency.

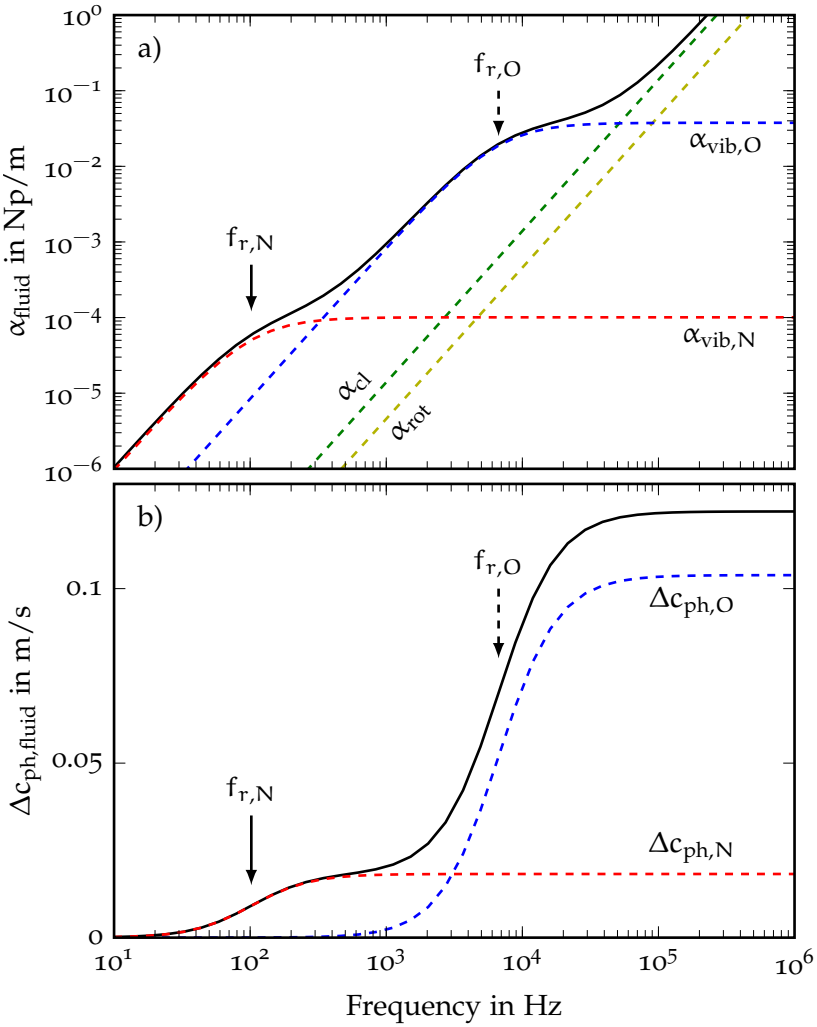

Figure 5.8: Losses within air and its different contributions at ISA conditions and RH = 20 % (h = 0.337 %): a) attenuation coefficient, b) change of phase velocity. The relaxation frequencies are $f_{r,O} = 6691\,\text{Hz}$ and $f_{r,N} = 102\,\text{Hz}$.

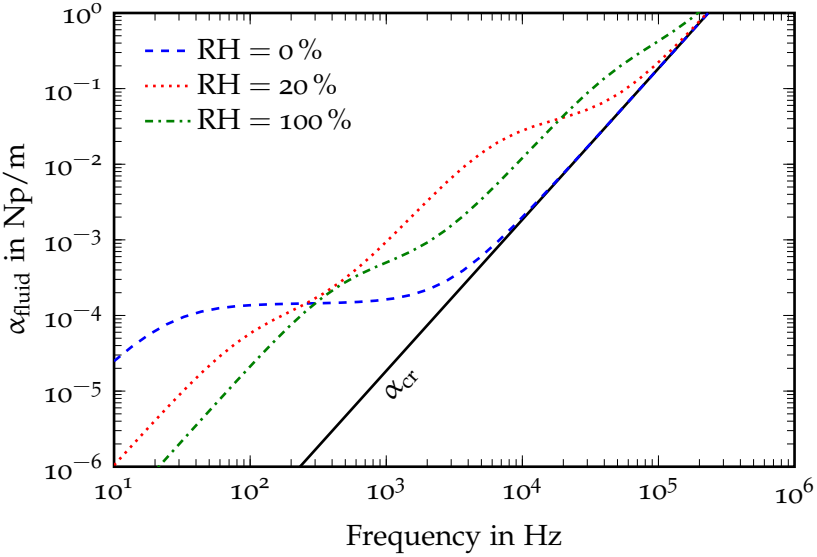

Figure 5.9: Influence of humidity on the combined losses within air at ISA conditions.

6

EXPERIMENTAL METHOD & ANALYSIS

The general methodology of the measurements is based on an approach proposed by Ronneberger [411], which was developed further by Ronneberger and his students [74, 146, 360, 397–399, 412][1]. The same methodology, in principle, is commonly referred to as *two-source scattering matrix method* [1]. This method was used for liner or orifice characterization in [17, 83, 138, 198, 399], for example.

For the evaluation of its acoustic performance, the lined duct section is regarded as a black box and only the input and output quantities are considered, i. e. the lined duct section is represented by an acoustical two-port[2]. The reflection and transmission coefficients of a two-port can be determined from the incoming and outgoing wave amplitudes based on two linearly independent measurements.

The liner is inserted in between two hard-walled duct sections, within which the acoustic pressure is measured at a minimum of two axial locations. Two acoustic measurements are performed, one with acoustic excitation from a loudspeaker located beyond

1 Unfortunately, most of these publications are hard-to-come-by reports, theses, or conference papers.

2 An acoustical two-port is a linear, physical system with one input and one output port. The state at the input and output is fully defined by two state variables, i. e. two independent physical quantities. Based on its origin from electrical network theory, sometimes the term four-pole is used instead of two-port. [1]

the microphones in the first duct section and another one with a second loudspeaker located beyond the microphones in the second duct section. Such a measurement pair is repeated for each frequency of interest.

6.1 SPECTRAL ANALYSIS

The time series data recorded by the microphones is transformed into the frequency domain following the Welch method[3] [488]. In short, that is the calculation of an averaged spectrum from overlapped, windowed signal segments. Additionally, turbulent noise is rejected by using a coherence function method as proposed by Chung [95].

6.1.1 *Welch Method*

The Welch method is an extension and more generalized form of the Bartlett method [27] for spectral density estimation. The concept of the Bartlett method involves the averaging over several signal segments in order to reduce the variance of the resulting spectrum estimation. In order to reduce the leakage that is produced by calculating the Fourier transformation of non-periodic[4] signals, Welch [488] proposes to apply a window function to each segment. However, using this procedure attenuates the signal at the beginning and end of each segment, so that more averages must be taken to obtain the same statistical accuracy of the estimated spectrum, when compared to not using window functions. This would require a longer measurement time. Welch [488] overcomes this by allowing the segments to overlap. The overlapping re-uses the data attenuated by the window function and provides more seg-

3 Named after Peter D. Welch.

4 For example, the non-periodicity of a harmonic sine signal is introduced by taking time-series data of finite length, where the length does not correspond to multiples of the sine period.

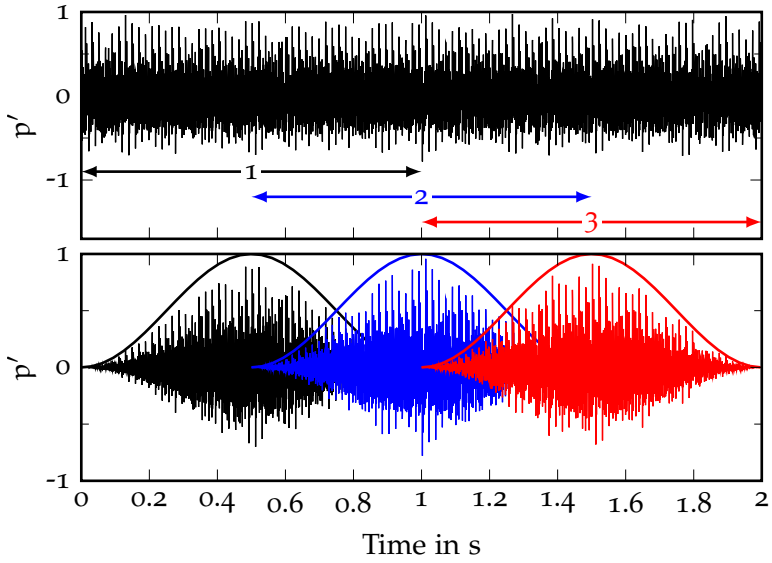

Figure 6.1: Illustration of the Welch method. Top: A two second time series signal is split into several segments of one second length with 50 % overlap. Bottom: Each segment is modified by applying the Hann window function.

ments to the averaging process, keeping the overall length of the signal the same. This procedure is illustrated in Figure 6.1.

Here, the microphone signals are split into segments of one second with 50 % overlap and the Hann[5] window function is used for the modification of the data. For a discrete time series $x(n)$ with N samples the Hann window function is defined as [47]

$$w(n) = \frac{1}{2}\left[1 - \cos\left(\frac{2\pi n}{N}\right)\right] \quad \text{with } n = 0, 1, 2, \ldots, N-1. \quad (6.1)$$

The modified segments are transformed into the frequency domain by Fourier transformation [165]. The discrete Fourier trans-

5 Named after Julius Ferdinand von Hann (1839-1921, Austrian meteorologist). It is often referred to as Hanning window. Originally, the term Hanning was introduced by Blackman and Tukey [63] for the process of applying the Hann window function.

formation $X(k)$ of a discrete time signal $x(n)$ with N samples is given by (e. g. [47])

$$X(k) = \sum_{n=0}^{N-1} x(n) \cdot e^{-i2\pi kn/N} \quad \text{with} \quad k = 0, 1, 2, \ldots, N-1. \tag{6.2}$$

The use of a window function introduces some losses to the magnitude of the Fourier transformed signal. Using the Hann window function $X(k)$ can be corrected by multiplication with $\sqrt{8/3}$.

The one-sided auto-spectral density, or short auto spectrum, is then given by averaging over all segments s and normalizing with the number of samples [47]

$$G_{xx} = \begin{cases} \frac{2}{SN} \sum_{s=1}^{S} |X_s(k)|^2 & \text{for } k = 1, 2, \ldots, (N/2) - 1 \\ \frac{1}{SN} \sum_{s=1}^{S} |X_s(k)|^2 & \text{for } k = 0, (N/2) \end{cases} \tag{6.3}$$

where S is the number of segments. Accordingly the one-sided cross-spectral density, or short cross spectrum, of two signals $x(n)$ and $y(n)$ is given by [47]

$$G_{xy} = \begin{cases} \frac{2}{SN} \sum_{s=1}^{S} [X_s^*(k) \cdot Y_s(k)] & \text{for } k = 1, 2, \ldots, (N/2) - 1 \\ \frac{1}{SN} \sum_{s=1}^{S} [X_s^*(k) \cdot Y_s(k)] & \text{for } k = 0, (N/2) \end{cases} \tag{6.4}$$

where X^* is the complex conjugate[6] of X. In acoustics, the spectrum is commonly scaled to the root-mean-square value by division with $\sqrt{2}$.

6 The complex conjugate of the complex number $z = a + ib$ is given by inverting the sign of the imaginary part, i. e. $z^* = a - ib$ (e. g. [77]).

6.1.2 *Rejection of Flow Noise*

The pressure fluctuations measured with the microphones are a superposition of the sound pressure and flow induced turbulent pressure fluctuations. Chung [95] presents a method to reject the turbulent flow noise using three signals measured at different locations. The basic premise is that the flow noise at these three positions is uncorrelated, while the sound pressure is completely coherent. The coherence between any two signals x and y is calculated from the auto-spectral and cross-spectral densities [47]

$$\gamma_{xy}^2 = \left|G_{xy}\right|^2 / \left(G_{xx} \cdot G_{yy}\right) . \tag{6.5}$$

The 'noise-free' auto-spectral density G'_{xx} yields [95]

$$G'_{11} = G_{11} \left(\gamma_{12} \cdot \gamma_{31}\right) / \gamma_{23} . \tag{6.6}$$

The indexes 1, 2, and 3 refer to the three signals. Here, the signal of two microphones and the input signal of the loudspeaker are used. In that case index 1 refers to the target microphone, index 2 to an arbitrary reference microphone, and index 3 to the speaker input signal.

The result of Equation (6.6) is a real valued auto spectrum with unit Pa^2. However, the plane wave decomposition (see Section 6.2 below) relies on the phase information of each microphone. The phase information is added by using the loudspeaker input signal as an arbitrary, but fixed for all microphones, phase reference. Inserting Equation (6.5) into (6.6) and adding the phase of the cross correlation between the target signal and the loudspeaker signal yields

$$G'_{11} = \frac{|G_{12}| \cdot \left|G_{13}\right|}{\left|G_{23}\right|} e^{i \arg\left(G_{13}\right)} . \tag{6.7}$$

The complex pressure amplitude at the position of the target microphone x_1 is then given by $\hat{p}\left(x_1, f\right) = \sqrt{G'_{11}\left(f\right)}$.

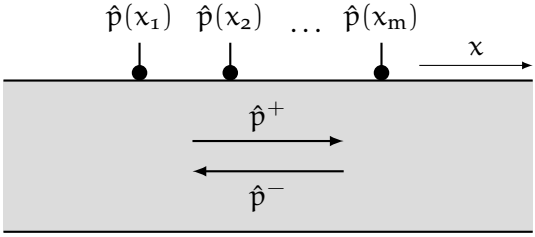

Figure 6.2: Schematic illustration of the plane wave decomposition with wall flush microphones.

6.2 PLANE WAVE DECOMPOSITION

The spectral analysis provides a complex pressure amplitude for each frequency and microphone. From now on, each frequency component will be treated separately and only the tonal components are of interest.

Assuming plane waves, the sound pressure measured by a microphone is a superposition of two waves traveling in opposite direction. Mathematically, this is expressed by Equation (5.32), which is repeated here in terms of complex amplitudes

$$\hat{p}(x) = \hat{p}^+ e^{-ik^+ x} + \hat{p}^- e^{ik^- x}. \tag{6.8}$$

The plane wave decomposition identifies the complex amplitudes $\hat{p}^+$ and $\hat{p}^-$ from the knowledge of $\hat{p}(x)$ at several axial positions $x_1, x_2, \ldots, x_m$, as illustrated in Figure 6.2. This yields the following system of equations:

$$\begin{aligned}
\hat{p}(x_1) &= \hat{p}^+ e^{-ik^+ x_1} + \hat{p}^- e^{ik^- x_1} \\
\hat{p}(x_2) &= \hat{p}^+ e^{-ik^+ x_2} + \hat{p}^- e^{ik^- x_2} \\
&\vdots \\
\hat{p}(x_m) &= \hat{p}^+ e^{-ik^+ x_m} + \hat{p}^- e^{ik^- x_m}
\end{aligned} \tag{6.9}$$

This system of linear equations can be written in matrix form as

$$\underbrace{\begin{bmatrix} e^{-ikx_1} & e^{ikx_1} \\ e^{-ikx_2} & e^{ikx_2} \\ \vdots & \vdots \\ e^{-ikx_m} & e^{ikx_m} \end{bmatrix}}_{\mathbf{A}} \times \underbrace{\begin{bmatrix} \hat{p}^+ \\ \hat{p}^- \end{bmatrix}}_{\mathbf{x}} = \underbrace{\begin{bmatrix} \hat{p}(x_1) \\ \hat{p}(x_2) \\ \vdots \\ \hat{p}(x_m) \end{bmatrix}}_{\mathbf{b}} \tag{6.10}$$

The size of the matrices is defined by the number of unknowns n and the number of available data m. Here, the unknowns are $\hat{p}^+$ and $\hat{p}^-$, so that $n = 2$, and m equals the number of microphones at distinct axial positions. Then, the size of $\mathbf{A}$ is $[m \times 2]$, the size of $\mathbf{x}$ is $[2 \times 1]$, and the size of $\mathbf{b}$ is $[m \times 1]$. A solution to Equation (6.10) can be obtained by solving [110][7]

$$\mathbf{x} = \mathbf{A}^+ \mathbf{b} \tag{6.11}$$

where $\mathbf{A}^+$ is the Moore-Penrose pseudoinverse[8] of matrix $\mathbf{A}$. While an inverse matrix only exists for square matrices, the pseudoinverse is a unique, generalized inverse that exists for matrices of any size. It can be calculated from the singular value decomposition[9] of matrix $\mathbf{A}$. The singular value decomposition is the factorization of the matrix $\mathbf{A}$ into the product of a unitary[10] matrix

7 The reference gives an overview of other solution methods as well.

8 The Moore-Penrose pseudoinverse is named after Eliakim Hastings Moore (1862-1932, American mathematician), [334], and Sir Roger Penrose (born 1931, English mathematical physicist), [365]. Sometimes it is called generalized inverse or just pseudoinverse. More details can be found in [110] or [179], for example.

9 The singular value decomposition originates from the works of E. Beltrami (1835-1899, Italian mathematician) [45], C. Jordan (1838-1921, French mathematician) [249, 250], J.J. Sylvester (1814-1897, English mathematician) [464–466], E. Schmidt (1876-1959, German mathematician) [433], and H. Weyl (1885-1955, German mathematician and theoretical physicist) [493]. Stewart [446] gives an historical overview from where the original references are taken. More details can be found in [110] or [179], for example.

10 A unitary matrix $\mathbf{U}$ is a complex-valued, square matrix, for which $\mathbf{U}^H\mathbf{U} = \mathbf{I}$, where $\mathbf{I}$ is the identity matrix. The real-valued equivalent to the unitary matrix is the orthogonal matrix. [110]

$\mathbf{U}$, a diagonal matrix Σ, and another unitary matrix $\mathbf{V}^H$, so that $\mathbf{A} = \mathbf{U}\Sigma\mathbf{V}^H$, where $\mathbf{V}^H$ is the Hermitian transpose[11] of $\mathbf{V}$ [110]. Then, the pseudoinverse is given by $\mathbf{A}^+ = \mathbf{V}\Sigma^+\mathbf{U}^H$ [110]. This solution method is very universal, as it can be used with matrices of any size and even badly conditioned matrices, e.g. singular or near-singular matrices, can be handled.

A solution to Equation (6.10) exists, if at least two equations are linearly independent. This means, microphones need to be installed at least at two distinct axial positions. Generally, it can be distinguished between two cases, depending on the number of microphones:

1. The number of equations/microphones and the number of unknowns are equal. This is commonly referred to as the two-microphone method.

2. The number of equations/microphones is greater than the number of unknowns. This is commonly referred to as the multi-microphone method.

The two-microphone method is established as a standardized measurement method defined in ISO 10534-2:1998 [232] and ASTM E 1050-12 [22]. It was initially proposed, in slightly varying forms, by Johnston & Schmidt [245], Seybert & Ros [437], and Chung & Blaser [96]. With only two linearly independent equations, the system in Equation (6.10) has one unique solution. The sensitivity to errors has been studied by several authors, in particular [2, 69, 218, 435, 438]. One restriction of the two-microphone method is, that the solution becomes singular when $ks = n\pi$, where s is the spacing between the microphones and $n = \{0, 1, 2, \dots\}$. For $n = 1$ this corresponds to a spacing of half a wave length

$$s = \lambda/2\,. \tag{6.12}$$

11 The Hermitian transpose, or sometimes called conjugate transpose, is defined as $\mathbf{V}^H = (\mathbf{V}^*)^T$, where $\mathbf{V}^T$ denotes the transpose and $\mathbf{V}^*$ denotes the matrix with complex conjugated entries. [110]

The errors increase rapidly in the vicinity of these singularities, so that Åbom and Bodén [2] suggest to limit the two-microphone method to the frequency range

$$0.1\pi < \frac{ks}{1-M^2} < 0.8\pi\,, \tag{6.13}$$

which includes the influence of mean flow in the duct.

The multi-microphone method yields an overdetermined system of equations. The solution given by Equation (6.11) is a best fit in the least-squares[12] sense. Experimental methods that make use of a least-squares fitting procedure over 3+ microphone positions are presented in [167, 246, 411, 412]. Generally, the accuracy of the results can be improved by using more than two microphones [94, 237, 246]. The effect of the number and spacing of the microphones was studied by Jones [246] and Jang and Ih [237]. Both conclude that an equidistant microphone spacing delivers the best results. However, the problem with a singular solution at a certain microphone spacing remains. The influence of the singular solution is reduced to a smaller frequency range when using more microphones.

Brandes [74] investigates the influence of different microphone distributions on the error in the scattering coefficients. He requires accurate measurements over a large frequency range (20-4000 Hz). An exponential distribution, where the spacing increases with a factor of 1.72, fulfills this requirement best. He demonstrates, that the density of the microphones should be higher towards the test object. This reduces errors when extrapolating the result of the wave decomposition from the microphone section to the test object. This approach has been followed at the DUCT-C and HAT facilities (see Section 6.5 and 6.6, respectively). The microphones are distributed exponentially with a factor of 1.62 (DUCT-C) and 1.72 (HAT).

12 The method of least-squares minimizes the sum of squared residuals [60]. This principle was introduced by Legendre [293] and Gauss [172].

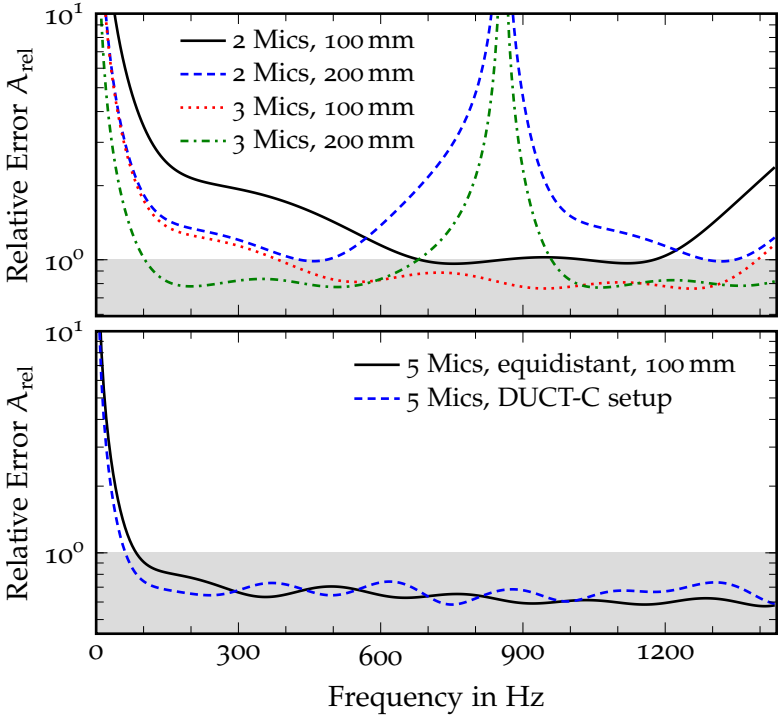

Figure 6.3: Evaluation of different microphone setups. The noise of the input signal is reduced when the relative error is below unity, indicated by the gray background.

Figure 6.3 compares various microphone setups. The relative error A_{rel} describes the influence of errors in the input signal on the result of the wave decomposition, relative to the signal-to-noise ratio (SNR) of the input signal. The procedure of calculating the relative error is explained in [470, 471]. The results can be interpreted as follows: When $A_{rel} < 1$, some noise of the input signal is compensated in the least-squares fit and the SNR of the result is improved compared to the input signal. The SNR remains unchanged when $A_{rel} = 1$ and it is amplified when $A_{rel} > 1$. As

a consequence, a good microphone distribution should achieve $A_{rel} \leqslant 1$ for the relevant frequency range.

The top plot in Figure 6.3 compares microphone setups with two and three microphones, spaced equidistantly by 100 mm and 200 mm. At the long distance, condition (6.12) is fulfilled at 850 Hz, resulting in large errors when using either two or three microphones. This singularity moves to 1700 Hz, just outside the frequency range, when using the tighter spacing. At the same time the error at low frequencies is increasing. The phase difference between two microphones becomes smaller at low frequencies, or rather when the wave length is long. The amount of noise and the distance between the microphones determines the frequency until which the wave decomposition is able to resolve a small phase difference. Using two microphones, yields only a very limited frequency range where A_{rel} is just below unity. Adding a third microphone generally improves the result dramatically. Three microphones should really be the minimum configuration, especially for measurements with flow. The low frequency error is mainly dependent on the maximum distance between two microphones. Thus, the results at $f < 400$ Hz is nearly identical for two microphones spaced at 200 mm or three microphones at 100 mm each.

The plot at the bottom of Figure 6.3 compares a five microphone equidistant distribution to the exponential distribution of the DUCT-C. Both results are very similar. At low frequencies the DUCT-C setup is slightly better than the equidistant setup due to its longer maximum distance between the microphones, i. e. 531 mm compared to 400 mm, respectively. What is not visible here, is that the error of the equidistant setup will of course peak at 1700 Hz, while the DUCT-C setup will not. However, for the frequency range here the dissipation coefficient measured with either microphone distributions would probably be identical.

A typical result of a plane wave decomposition from DUCT-C data is presented in Figure 6.4. $\hat{p}$ is measured at five axial positions x_m in a hard-walled duct section. The solution to Equa-

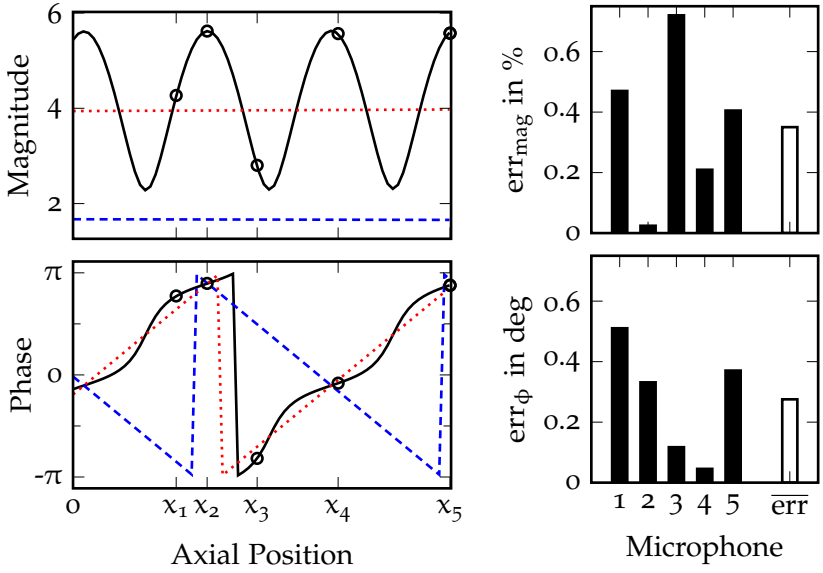

(a) Complex pressure amplitudes: ○ Experiment; —— $\hat{p}$; - - - $\hat{p}^+$; ····· $\hat{p}^-$.

(b) Fit error of each microphone and average value.

Figure 6.4: Typical result of a plane wave decomposition from DUCT-C data at 714 Hz.

tion (6.10) provides the amplitudes of the waves propagating in positive and negative x-direction, $\hat{p}^+$ and $\hat{p}^-$ respectively. Then, the sound field can be reconstructed with Equation (6.8). The deviation regarding magnitude and phase for each microphone between the fitted $\hat{p}$ and the experimental data yields the fit error

$$\mathrm{err}_{\mathrm{mag}}(x_m) = \left| \frac{|\hat{p}_{\mathrm{exp}}(x_m)| - |\hat{p}_{\mathrm{fit}}(x_m)|}{|\hat{p}_{\mathrm{exp}}(x_m)|} \right| \cdot 100\,\% \quad \text{and} \tag{6.14}$$

$$\mathrm{err}_{\phi}(x_m) = \left| \frac{\arg\left(\hat{p}_{\mathrm{exp}}(x_m)\right) - \arg\left(\hat{p}_{\mathrm{fit}}(x_m)\right)}{\arg\left(\hat{p}_{\mathrm{exp}}(x_m)\right)} \right| \cdot \frac{180^\circ}{\pi}, \tag{6.15}$$

respectively. The average fit error of the wave decomposition is given by

$$\overline{\text{err}} = \frac{1}{M} \sum_{m=1}^{M} \text{err}(x_m) \,, \tag{6.16}$$

where M is the total number of microphones contributing to the wave decomposition.

6.3 REFLECTION AND TRANSMISSION COEFFICIENTS

As discussed in the beginning of this chapter, the lined duct section can be represented by an acoustical two-port. The acoustic properties of the two-port are characterized by the reflection and transmission coefficients, which are commonly referred to as scattering coefficients.

The plane wave sound field in the two hard-walled duct sections on both sides of the liner is fully defined by the complex pressure amplitudes of the waves traveling in positive and negative x-direction, $\hat{p}^+$ and $\hat{p}^-$ respectively. They are obtained, separately for both sections 1 and 2, from microphone measurements via a plane wave decomposition as discussed in the previous section. The four waves are related by the scattering coefficients of the liner and the end-reflections of the duct. This is illustrated in Figure 6.5. Now, we want to determine the four scattering coefficients from the measured wave amplitudes.

When the acoustic excitation is introduced by speaker A, it produces the incoming wave $\hat{p}^+_{1a}$, as indicated by the bold arrow in Figure 6.5a. The three remaining wave amplitudes can be expressed in terms of the incoming wave amplitude, the scattering

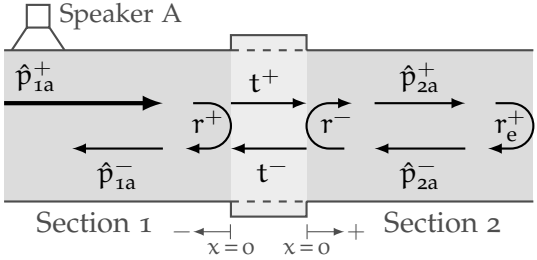

(a) Excitation with speaker A

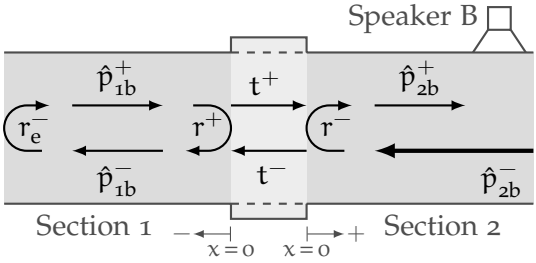

(b) Excitation with speaker B

Figure 6.5: Relation between the complex pressure amplitudes $\hat{p}_1^+$, $\hat{p}_1^-$, $\hat{p}_2^+$, and $\hat{p}_2^-$, the scattering coefficients r^+, r^-, t^+, and t^-, and the end-reflection coefficients r_e^+ and r_e^-.

coefficients, and the end-reflection coefficient. Following the arrows in Figure 6.5a yields

$$\hat{p}_{1a}^{-} = \hat{p}_{1a}^{+} r^{+} + \hat{p}_{1a}^{+} t^{+} r_e^{+} t^{-}, \tag{6.17a}$$

$$\hat{p}_{2a}^{+} = \hat{p}_{1a}^{+} t^{+} + \hat{p}_{1a}^{+} t^{+} r_e^{+} r^{-}, \text{ and} \tag{6.17b}$$

$$\hat{p}_{2a}^{-} = \hat{p}_{1a}^{+} t^{+} r_e^{+}. \tag{6.17c}$$

Equation (6.17c) can be inserted into (6.17a) and (6.17b), which results in two linearly independent equations

$$\hat{p}_{1a}^{-} = \hat{p}_{1a}^{+} r^{+} + \hat{p}_{2a}^{-} t^{-} \text{ and} \tag{6.18a}$$

$$\hat{p}_{2a}^{+} = \hat{p}_{1a}^{+} t^{+} + \hat{p}_{2a}^{-} r^{-}. \tag{6.18b}$$

Please note that Equations (6.18) are not depending on the endreflections anymore. However, to determine the four unknown scattering coefficients, four linear independent equations are necessary. Two additional equations are obtained by a second measurement with excitation from speaker B, as illustrated in Figure 6.5b. The equations are derived accordingly to the excitation with speaker A, so that the two additional equations are given by

$$\hat{p}_{2b}^{+} = \hat{p}_{2b}^{-} r^{-} + \hat{p}_{1b}^{+} t^{+} \text{ and} \tag{6.18c}$$

$$\hat{p}_{1b}^{-} = \hat{p}_{2b}^{-} t^{-} + \hat{p}_{1b}^{+} r^{+}. \tag{6.18d}$$

The four linear independent Equations 6.18 can be solved for the four scattering coefficients r^{+}, r^{-}, t^{+}, and t^{-}. The equivalent matrix notation yields [1]

$$\underbrace{\begin{bmatrix} \hat{p}_{1a}^{-} & \hat{p}_{1b}^{-} \\ \hat{p}_{2a}^{+} & \hat{p}_{2b}^{+} \end{bmatrix}}_{\mathbf{p}_{\text{out}}} = \mathbf{S} \underbrace{\begin{bmatrix} \hat{p}_{1a}^{+} & \hat{p}_{1b}^{+} \\ \hat{p}_{2a}^{-} & \hat{p}_{2b}^{-} \end{bmatrix}}_{\mathbf{p}_{\text{in}}}, \tag{6.19}$$

where $\mathbf{p}_{\text{in}}$ and $\mathbf{p}_{\text{out}}$ are matrices containing the complex pressure amplitudes of the incoming and outgoing waves, respectively. The scattering matrix $\mathbf{S}$ is defined as

$$\mathbf{S} = \begin{bmatrix} \mathbf{S}_{11} & \mathbf{S}_{12} \\ \mathbf{S}_{21} & \mathbf{S}_{22} \end{bmatrix} = \begin{bmatrix} r^{+} & t^{-} \\ t^{+} & r^{-} \end{bmatrix}. \tag{6.20}$$

The scattering coefficients are obtained by solving Equation (6.19) or by basic algebraic transformations of Equations 6.18

$$r^{+} = \frac{\hat{p}_{1a}^{-}\hat{p}_{2b}^{-} - \hat{p}_{1b}^{-}\hat{p}_{2a}^{-}}{\hat{p}_{1a}^{+}\hat{p}_{2b}^{-} - \hat{p}_{1b}^{+}\hat{p}_{2a}^{-}}, \tag{6.21a}$$

$$r^{-} = \frac{\hat{p}_{2b}^{+}\hat{p}_{1a}^{+} - \hat{p}_{2a}^{+}\hat{p}_{1b}^{+}}{\hat{p}_{1a}^{+}\hat{p}_{2b}^{-} - \hat{p}_{1b}^{+}\hat{p}_{2a}^{-}}, \tag{6.21b}$$

$$t^{+} = \frac{\hat{p}_{2a}^{+}\hat{p}_{2b}^{-} - \hat{p}_{2b}^{+}\hat{p}_{2a}^{-}}{\hat{p}_{1a}^{+}\hat{p}_{2b}^{-} - \hat{p}_{1b}^{+}\hat{p}_{2a}^{-}}, \text{ and} \tag{6.21c}$$

$$t^{-} = \frac{\hat{p}_{1a}^{+}\hat{p}_{1b}^{-} - \hat{p}_{1b}^{+}\hat{p}_{1a}^{-}}{\hat{p}_{1a}^{+}\hat{p}_{2b}^{-} - \hat{p}_{1b}^{+}\hat{p}_{2a}^{-}}. \tag{6.21d}$$

With above equations, the reflection and transmission coefficients of the liner can be calculated directly from the incoming and outgoing wave amplitude of two independent measurements. The independence of the measurements is achieved by applying the so-called *two-source location method* [1, 344], where the sound is subsequently incident from either side of the liner.

An alternative approach is the *two-load method* [307, 344, 476, 477], commonly with the source fixed at one end of the duct and varying the load, e. g. the length, at the opposite end. While this method is generally inferior to the two-source location method [344], it could be the only option when the source cannot be moved, e. g. in a combustion test rig with acoustic excitation by the flame.

A variation of the two-source location method is proposed by Enghardt [146], where both speakers are operated simultaneously. Two independent sound fields are produced by keeping the phase of the input signal constant for one speaker, while the phase of the second speaker is shifted by 180° between the measurements. The simultaneous excitation on both sides ensures good signal-to-noise ratios in both duct sections, even when the transmission coefficient of the test object is near zero.

6.4 DISSIPATION COEFFICIENT

An acoustical two-port is characterized by its reflection and transmission coefficients, as defined above. A derived quantity is the energy dissipation coefficient D, which is used here to evaluate the acoustic performance of the liner. In energy terms, the sum of reflection, transmission, and dissipation coefficient is unity

$$R^{\pm} + T^{\pm} + D^{\pm} = 1\,. \tag{6.22}$$

R and T are the *energy* reflection and transmission coefficients, respectively, while r and t have been the *pressure* reflection and transmission coefficients. The energy and pressure quantities are

related by the acoustic energy flux P. For plane waves in a duct with cross-section area A and mean flow Mach number M the energy flux yields [66][13]

$$P^{\pm} = \frac{A}{2\rho c} (1 \pm M)^2 \left|\hat{p}^{\pm}\right|^2 . \tag{6.23}$$

This expression relates the acoustic pressure $\hat{p}$ to the acoustic energy flux P. Accordingly, it can be applied to calculate R and T from r and t, respectively. Combining Equations (6.22) and (6.23), the energy dissipation coefficient is defined as

$$D^{\pm} = 1 - \left(\frac{(1 \mp M_1)^2}{(1 \pm M_1)^2} \cdot \left|r^{\pm}\right|^2 + \frac{\rho_1 c_1}{\rho_2 c_2} \frac{A_2}{A_1} \frac{(1 \pm M_2)^2}{(1 \pm M_1)^2} \cdot \left|t^{\pm}\right|^2 \right) , \tag{6.24}$$

where the indexes 1 and 2 refer to the quantities in section 1 and section 2 as defined in Figure 6.5. When the duct cross-section area and the thermodynamic conditions are the same in both sections, Equation (6.24) reduces to[14]

$$D^{\pm} = 1 - \left(\frac{(1 \mp M_1)^2}{(1 \pm M_1)^2} \cdot \left|r^{\pm}\right|^2 + \frac{(1 \pm M_2)^2}{(1 \pm M_1)^2} \cdot \left|t^{\pm}\right|^2 \right) . \tag{6.25}$$

6.4.1 *Average Dissipation Coefficient*

Averaging the dissipation coefficients in positive and negative x-direction yields the average dissipation

$$\overline{D} = \left(D^{+} + D^{-}\right)/2 . \tag{6.26}$$

The $+$ and $-$ dissipation coefficents are equal when the liner configuration is symmetric and $M_G = 0$. In that case $D^{+} = D^{-} = \overline{D}$

13 See as well the derivations in [374, 412] or the entry in Morfey's dictonary [338] under 'Blokhintsev invariant'.

14 A bias flow liner injects mass flow into the duct in-between the two sections, so that always $M_1 \neq M_2$. However, if $\dot{m}_B \ll \dot{m}_G$ or $M \approx 0$ (when including the additional mass flow), then the difference can be neglected and Equation (6.25) can be reduced further.

and using $\overline{D}$ is merely a reduction of data. An asymmetric configuration or a grazing flow yields $D^+ \neq D^-$. The grazing flow reduces the dissipation in flow direction while increasing it for waves propagating against the flow. Then, a comparison of $\overline{D}$ allows the evaluation of the overall performance of the liner, taking both directions into account.
For example in a combustor, where the main source of sound is the flame, the sound wave travels in flow direction away from the flame and is then reflected at the combuster exit traveling against flow direction towards the flame. In order to suppress the acoustic feedback to the flame D^+ and D^- are equally important, so that the overall performance can be evaluated by their mean value $\overline{D}$.

6.4.2 *Dissipation Error*

The error that is made when measuring the dissipation coefficient can be determined by a reference measurement without liner. The measurement and analysis procedure is the same as if a liner was present. However, without liner the theoretical result is known and yields $R^\pm = 0$, $T^\pm = 1$, and $D^\pm = 0$. The dissipation error is defined as the absolute deviation from this expected value, averaged over both directions and expressed in percent

$$D_{err} = \frac{\left|D^+_{ref}\right| + \left|D^-_{ref}\right|}{2} \cdot 100\,\%. \tag{6.27}$$

The dissipation error is a measure of the accuracy of the results. It is in particular useful when evaluating different setups or changes in the data analysis (see Sections 6.5.2 and 6.5.4).

6.4.3 *Compared to the Absorption Coefficient*

Eldredge and Dowling [142] use the absorption coefficient to evaluate the performance of the liner, see Equation (4.78). The absorption and dissipation coefficients follow the same principle, representing the difference between incoming and outgoing energy.

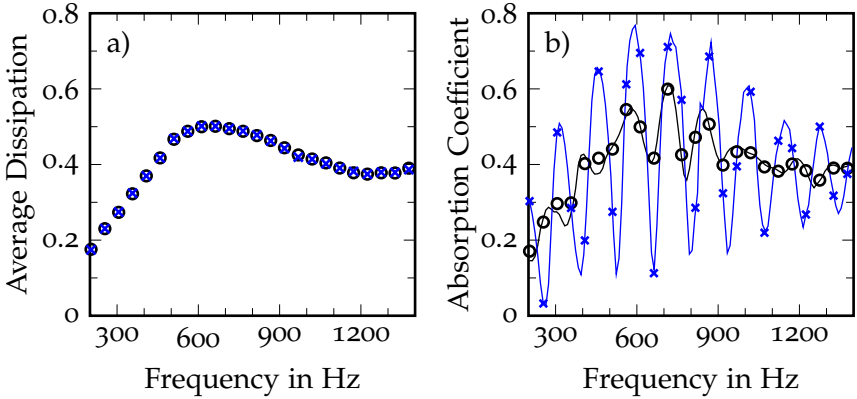

Figure 6.6: Measurements with and without anechoic terminations, comparing the resulting a) average dissipation and b) absorption coefficient. o with anechoic terminations (—— swept-sine excitation), × without anechoic terminations (—— swept-sine excitation).

However, the results can be very different, depending on the endreflections of the test duct. Furthermore, the absorption coefficient does not distinguish between the two directions of wave propagation. In order to be aware of these differences, the term dissipation coefficient is used here[15].

All differences are based on the fact that two measurements are necessary to determine the dissipation coefficient, while only one measurement is performed to obtain the absorption coefficient. The combination of the two measurements eliminates the dependency on the end-reflections, as discussed in Section 6.3. The absorption coefficient is strongly dependent on the end-reflection, and thus on the position of the liner within the duct.

This is demonstrated in Figure 6.6. The average dissipation and the absorption coefficient are presented determined from measurements with and without anechoic terminations. The average

15 However, when referring to the physical phenomenon rather than the numeric quantity, the terms dissipation and absorption are used interchangeably.

dissipation in Figure 6.6a is identical in both cases. It is independent of the end-reflections. The absorption coefficient in Figure 6.6b exhibits large variations due to the end-reflections. Additional measurements with swept-sine excitation reveal the deterministic structure of the variations. They are reduced, but not removed, when the anechoic termination is installed. After all, the anechoic termination only reduces the end-reflections and does not eliminate them completely[16]. However, the plot suggests that the absorption coefficient converges into the average dissipation when the end-reflection becomes zero.

Without end-reflection and with excitation from speaker A the reflection and transmission coefficients are simply given by $r^+ = \hat{p}^-_{1a}/\hat{p}^+_{1a}$ and $t^+ = \hat{p}^+_{2a}/\hat{p}^+_{1a}$ (see Figure 6.5). Inserting these into Equation (6.25) and dropping index a for simplicity yields

$$D^+ = 1 - \left(\frac{(1-M_1)^2 \cdot |\hat{p}^-_1|^2 + (1+M_2)^2 \cdot |\hat{p}^+_2|^2}{(1+M_1)^2 \cdot \left|\hat{p}^+_1\right|^2} \right). \tag{6.28}$$

From Equation (4.78) follows with $\hat{B}^-_2 = 0$ (because $r^+_e = 0$) and $\rho_1 = \rho_2$

$$\alpha = 1 - \left(\frac{(1-M_1)^2 \cdot |\hat{p}^-_1|^2 + (1+M_2)^2 \cdot |\hat{p}^+_2|^2}{(1+M_1)^2 \cdot \left|\hat{p}^+_1\right|^2} \right), \tag{6.29}$$

which is identical to Equation (6.28). Thus, the dissipation coefficient and the absorption coefficient are equivalent when the end-reflection is zero. The result of the Eldredge and Dowling Method, which is the absorption coefficient, can be compared to the dissipation coefficient, which is the result of the measurements and the Transfer Matrix Method, when setting $r_e = 0$ in the Eldredge and Dowling Method.

16 The end-reflection coefficients for the DUCT-C are plotted in Figure 6.10.

6.5 DUCT ACOUSTIC TEST RIG

The Duct Acoustic Test Rig (DUCT) provides three setups with different cross-section geometries of the measurement sections. Here, the circular cross-section (DUCT-C) is used.

6.5.1 *Setup & Instrumentation*

A schematic setup of the DUCT-C is shown in Figure 6.7. The test rig consists of two symmetric measurement sections with the liner module in-between and anechoic terminations[17] at both ends. Each section is made of an 1200 mm long aluminum tube with an inner diameter of 140 mm. Two loudspeakers are installed at the circumference of the duct at $x = \pm 1041$ mm. They are connected to the duct via a conical horn. In order to reduce the interaction between the grazing flow and the opening it is covered by a perforate within the duct. A total of 12 microphones are mounted flush with the duct wall. The microphones are distributed over ten axial positions with a higher density towards the liner. Two microphones are installed at the two outermost positions close to the loudspeakers. The two microphones are mounted opposite each other, canceling out evanescent modes generated by the loudspeaker[18]. The maximum axial distance between the microphones in each section is 531 mm and the minimum distance between the two innermost microphones is 60 mm.

Two liner modules of different lengths are available, so that liners with a length of 60 mm and 280 mm can be studied. The diameter of the liners is identical to the duct diameter. The inner diameter of the cavity of both modules is 240 mm. A second liner can be inserted concentric to the first one at diameters 162, 192, 212 mm in the shorter version and only at 162 mm in the longer version. There are four inlets for the bias flow at the outer cir-

17 The effectiveness of the anechoic termination is demonstrated in Figure 6.10.
18 The influence of evanescent modes is discussed in Section 6.5.4.

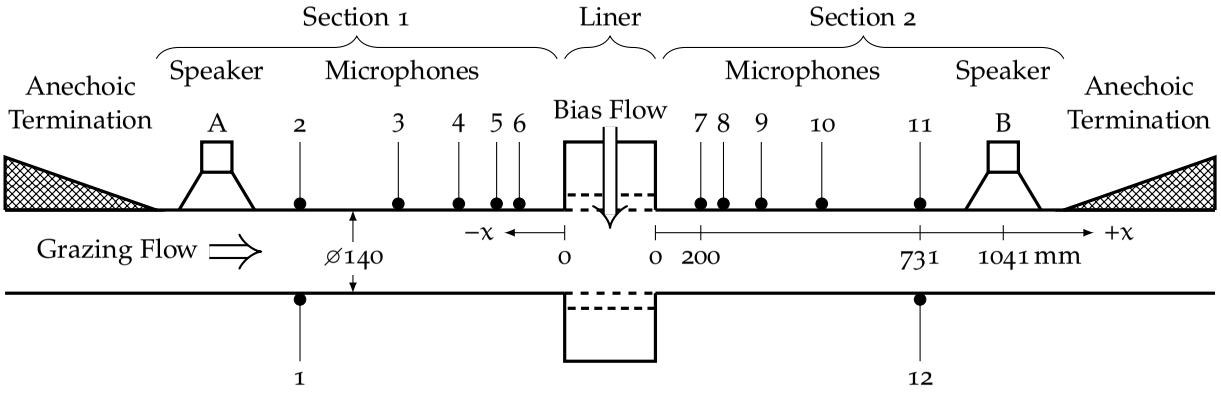

Figure 6.7: Schematic illustration of the Duct Acoustic Test Rig with circular cross-section (DUCT-C) with speakers A and B and microphones 1-12. All dimensions in mm.

cumference, distributed with an even pitch of 90°. In the short module they are centered axially and discharge into the cavity in radial direction through an opening of diameter 17.8 mm. In the longer version, the inlets are at the upstream end of the cavity with tubes extending into the cavity and directing the bias flow in axial direction.

The bias flow is controlled with a Bronkhorst ELFlow mass flow controller with a maximum flow rate of 100 kg/h. At the same time, the pressure difference across the liner is measured with a MKS Baratron differential pressure meter. In the rare case when higher mass flow rates are needed, the controller is excluded and the flow rate is set manually by adjusting the line pressure. However, no mass flow information is available in this approach.

The maximum mean grazing flow Mach number is 0.13. The grazing flow Reynolds number of all velocities studied here is larger than the critical Reynolds number $\mathrm{Re}_c = 4000$ (e. g. [495]), so that the flow can be considered fully turbulent. This was confirmed by velocity profile measurements [197].

The temperature of the flow is measured in section 2 of the test duct with a J-type thermocouple connected directly to an Agilent 34970A data acquisition / data logger switch unit.

The acoustic test signal is a multi-tone sine signal. Three signals have been synthesized containing eight tones each:

SIGNAL 1: 204, 255, 306, 357, 459, 561, 663, 867 Hz

SIGNAL 2: 408, 510, 612, 714, 765, 969, 1071, 1173 Hz

SIGNAL 3: 816, 918, 1020, 1122, 1224, 1275, 1326, 1377 Hz

The frequencies are distributed between the signals, so that no multiples of a frequency are contained in one signal. All three signals together cover a frequency range from 204 to 1377 Hz in steps of 51 Hz. All tonal components are in the plane wave range, i. e. their frequencies are below[19] 1413 Hz. The signal has been

19 Defined by Equation (5.19) for speed of sound at ISA conditions and the maximum grazing flow Mach number.

adjusted in a way that the amplitude of each tonal component inside the duct is about 102 dB. The test signal is generated by an Agilent 33220A function generator. The signals are fed through a KME SPA240E stereo amplifier, which powers two Monacor KU-516 speakers.
The microphones used for the acoustic measurements are 1/4" G.R.A.S. type 40BP condenser microphones in combination with type 26AC pre-amplifiers. Their signals are recorded over a time of 10 s with a 16 track OROS OR36 data acquisition system with a sampling frequency of 8192 Hz. Additionally, the output signal of the function generator is recorded at the same settings as a reference signal for the analysis.

6.5.2 *Microphone Calibration*

The analysis relies on the magnitude and phase relations between the microphones. An in-duct calibration method is applied that provides accurate information about the relative magnitude and phase over the whole frequency range. The method is based on the fact that the plane waves sound field in the duct is one-dimensional, i. e. the acoustic field quantities are constant in any cross-section of the duct and vary only in x-direction. Therefore, microphones installed around the circumference of the duct at the same axial position should measure the same values for amplitude and phase, so that the relative difference between the microphones can be determined. The result of such a calibration measurement is a pair of correction values for magnitude and phase for each microphone, relative to one reference microphone. Typically, correction values are obtained for a whole range of frequencies, so that any frequency dependent behavior is accounted for. The correction values are then applied in the data analysis.

Several measurements are required when the total number of microphones is larger than the available positions around the cir-

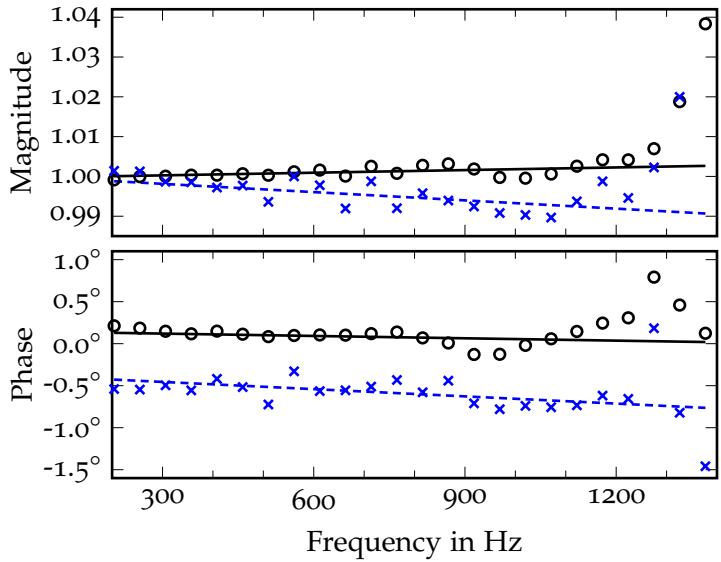

Figure 6.8: Results of an in-duct calibration measurement for two exemplary microphones. Measurement: ○ Microphone 1, × Microphone 2; Linear Fit: —— Microphone 1, - - - - Microphone 2

cumference. In that case it is important, that the same reference microphone is used for all calibration measurements.

Figure 6.8 shows the result of an in-duct calibration measurement for two exemplary microphones. Generally, considering the very detailed scale of the y-axis, the differences between the Microphones are very small. The behavior of the wall-flush microphones is expected to be smooth and linear over the frequency. The plot, however, shows some bumps and a non-linear behavior towards the upper frequency limit. The bumps are certainly measurement errors, as it is unphysical for the microphone response to jump like that between frequencies. The non-linear behavior of magnitude and phase for frequencies beyond 1200 Hz can be attributed to evanescent modes. The sound field can no longer be regarded as one-dimensional when the frequency approaches the cut-on frequency of the first higher order mode.

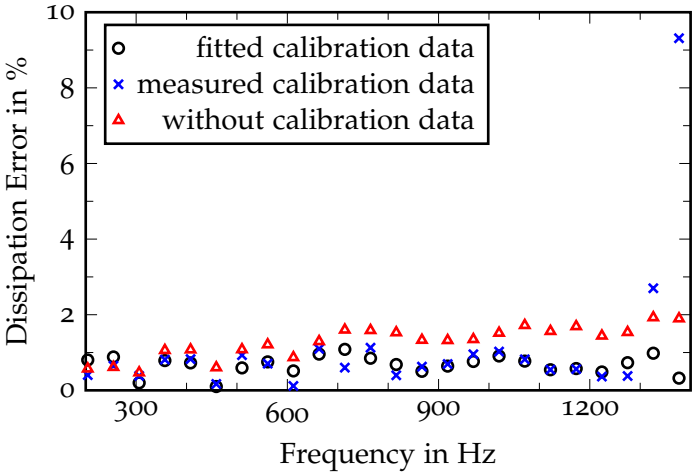

Figure 6.9: Comparison of the influence of the calibration data on the dissipation error in a reference measurement with $M_G = 0.05$.

Both problems are overcome by a linear fit through the measured calibration data, as indicated in Figure 6.8. The fit is limited to frequencies below 1200 Hz, so that the evanescent mode effect is fully excluded. Then, the data for frequencies beyond 1200 Hz is extrapolated from the fit.

The difference between applying the measured calibration data, the fitted calibration data, or no calibration data at all is demonstrated in Figure 6.9. Generally it can be said that the error is already very small without applying any calibration data. Using the measured calibration data reduces the error even more, except at the upper frequency end. Here, the calibration data is tampered by the existence of evanescent modes and cannot be used. Applying the fitted calibration data gives the overall best result. The low error for frequencies below 1300 Hz is maintained, while the falsification at higher frequencies is eliminated. This approach is applied to the measurement data of the DUCT-C facility.

6.5.3 *End-Reflections*

Both ends of the DUCT-C test duct are equipped with anechoic terminations. The anechoic terminations are designed according to ISO 5136:2003 [233, p. 15] in a one-sided configuration with a length of 2.5 m. Figure 6.10 compares the measured reflection coefficients with $M_G = 0$ at the open duct, the anechoic termination, and the DUCT-C setup. As expected, the magnitude of the reflection coefficient at the open end is unity for low frequencies and decreases for higher frequencies.

The anechoic termination reduces the reflection over the whole frequency range. The admissible limit[20] of ISO 5136:2003 is indicated in gray and the anechoic termination complies with this limit.

The setup of the DUCT-C includes a loudspeaker in-between the microphones and the anechoic termination. The sound coming from the active loudspeaker is partly reflected at the opening of the inactive loudspeaker at the other end of the test duct. This reflection cannot be separated from the end-reflection and results in an increased reflection at frequencies from 600 to 900 Hz, as observed in Figure 6.10.

6.5.4 *Influence of Evanescent Modes*

The analysis is limited to frequencies below the cut-on frequency of the first higher order mode, so that the sound field is considered to be one-dimensional. Regardless, some local three-dimensional higher order mode effects might be encountered, that is in particular[21] the existence of evanescent modes in the vicinity of the loudspeaker. The loudspeaker is mounted to the circumfer-

20 ISO 5136:2003 [233] requires the maximum value of the pressure reflection coefficient to be below 0.15 for frequencies > 160 Hz.

21 Another three-dimensional effect is the modal scattering at the leading and trailing edges of the liner [402]. This phenomenon showed no implications on the microphone measurements, so that it will not be considered here.

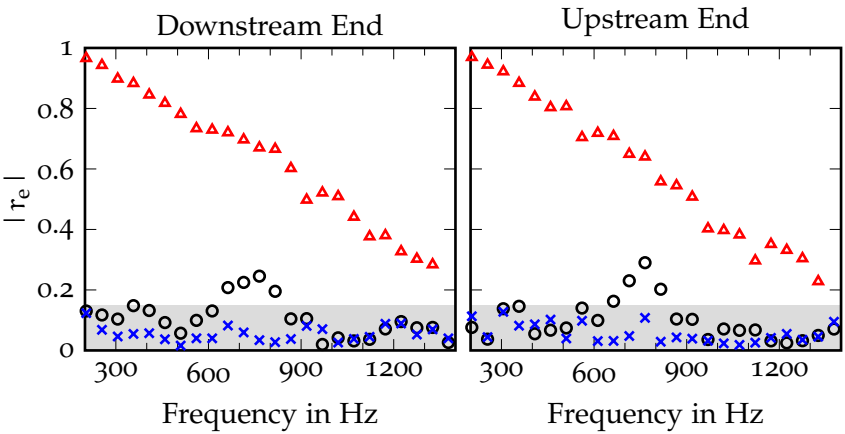

Figure 6.10: Magnitude of the reflection coefficient for △ open end, × anechoic termination, and ○ DUCT-C setup.

ence of the duct, producing a three-dimensional sound field at the point of entry into the duct. The higher order modes are not able to propagate and their amplitudes decay exponentially with the distance from the source. At a sufficient distance only the plane wave prevails.

In order to avoid evanescent mode effects the distance between the loudspeaker and the microphone needs to be large enough, so that the mode has decayed when it reaches the microphone. This is demonstrated for the DUCT-C setup in Figure 6.11. The attenuation rate of mode 1:0 is plotted over the frequency for three distances. The distances coincide with the distances from the loudspeaker to the first, second and third microphone, i. e. loudspeaker A and microphones 2, 3, and 4 in Figure 6.7. The lines are the theoretical predictions of the attenuation according to Equation (5.21). The symbols are obtained from measurements. Eight microphones have been installed uniformly spaced around the circumference of the duct at each respective axial location. A mode analysis[22] based on the data of the eight microphones is per-

22 The mode analysis is conducted with a DLR software tool described in [470].

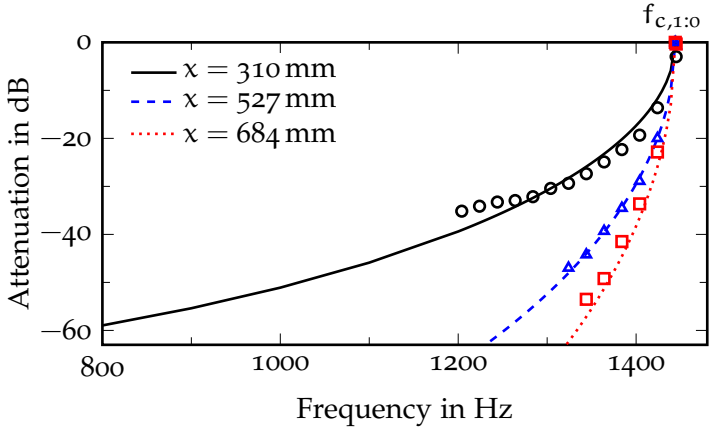

Figure 6.11: Attenuation rate of the evanescent mode 1:0 for three loudspeaker–microphone distances in the DUCT-C setup. Lines: theoretical prediction; Symbols: measurement.

formed in order to identify the amplitude of mode 1:0. In order to obtain the attenuation rate the resulting amplitudes have been normalized with the amplitude at the cut-on frequency:

$$a_{mn} = 20 \cdot \lg \left(\frac{|\hat{p}_{mn}(f)|}{|\hat{p}_{mn}(f_{c,mn})|} \right) \tag{6.30}$$

Figure 6.11 illustrates that the distance between loudspeaker and microphone is crucial for the decay of the mode.

Another approach is to install two microphones opposite each other and taking their average, eliminating the spatial structure of the first higher order mode. The theoretical background to this approach, let's call it double microphone approach, is illustrated in Figure 6.12.

The cross-section of the duct in Figure 6.12a shows the spatial distribution of the acoustic pressure of the mode 1:0. A microphone which moves in θ-direction along the wall observes a sinusoidal pressure distribution, as shown in Figure 6.12b. Taking the mean value of any two locations that are 180° apart (demonstrated

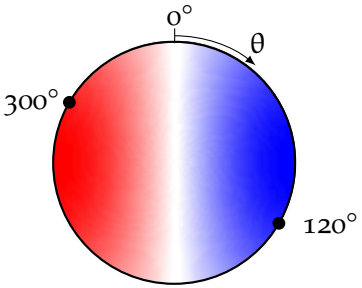

(a) Acoustic pressure distribution in a duct cross-section.

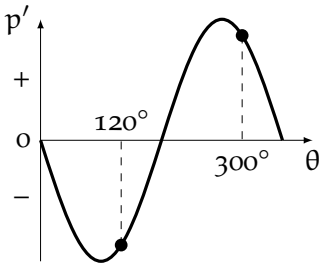

(b) Acoustic pressure distribution around the duct circumference.

Figure 6.12: Illustration of the double microphone approach applied to mode 1:0.

for 120° and 300°) eliminates the contribution of this particular mode.

The effect of the distance and the double microphone approach is demonstrated by studying the following three configurations[23]:

10 MICROPHONES Microphones 2-11 are used. The acoustic pressure is measured at five axial positions in each section. The shortest distance between loudspeaker and microphone is 310 mm. This is the standard configuration with one microphone installed at each axial position.

8 MICROPHONES Microphones 3-10 are used. The acoustic pressure is measured at four axial positions in each section. The smallest distance between loudspeaker and microphone is 527 mm.

12 MICROPHONES Microphone 1-12 are used. The acoustic pressure is measured at five axial positions in each section. The smallest distance between loudspeaker and microphone is 310 mm. This configuration employs the double microphone approach.

23 The numbering of the microphones refers to the labels used in Figure 6.7.

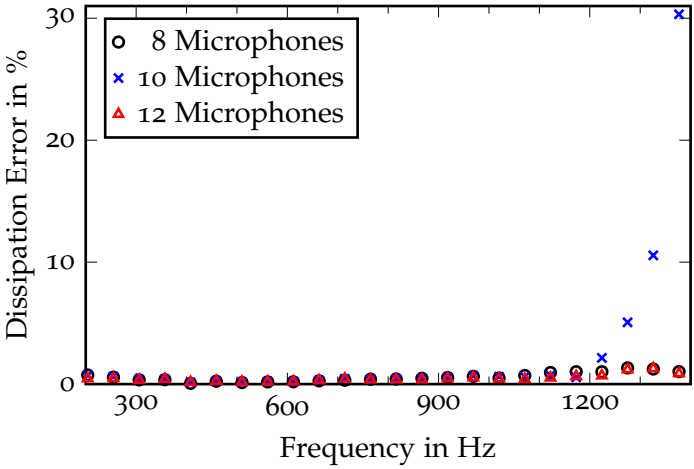

Figure 6.13: Comparison of three reference measurements with different microphone configurations regarding the suppression of evanescent modes.

Figure 6.13 compares the results of these three configurations. The dissipation error for the standard configuration with 10 microphones increases dramatically for frequencies beyond 1200 Hz. This is due to the fact that the sound field contains some relevant three-dimensional components which are not accounted for. In other words, the microphones are too close to the loudspeaker.

Increasing the distance between loudspeaker and microphones is the obvious solution trying to suppress evanescent mode effects. In order to enlarge the distance in the existing test rig, the microphones close to the loudspeakers are excluded from the analysis. Of course the reduction of microphones will create other disadvantages, so that this approach is taken for the sole purpose of demonstrating the influence of the distance. This configuration is referred to as '8 Microphones', based on the total number of microphones that are in use. Looking at the result in Figure 6.13 reveals that the effect of evanescent modes is successfully eliminated, reducing the error at frequencies beyond 1200 Hz.

The double microphone approach achieves the same result at a much shorter distance between loudspeaker and microphones. The influence of the circumferential structure of the first higher order mode is successfully suppressed by averaging over two microphones separated by 180°. This approach is applied here, so that the standard setup of the DUCT-C employs 12 microphones. This gives the benefit of suppressing evanescent mode effects and thus extending the frequency range, without imposing any other limitations.

The double microphone approach is not limited to evanescent modes. The same principle can be applied when the first circumferential mode is propagating through the duct. Then, all microphones need to be installed in a double configuration. The benefit of such a setup would be an extended frequency range. The upper frequency limit would move from the cut-on frequency of the first circumferential mode to the second circumferential mode. For the DUCT-C geometry that would shift the limit for $M_G = 0$ from 1425 Hz to 2364 Hz.

6.5.5 *Accuracy*

The dissipation error, defined in Section 6.4.2, is a measure of the accuracy of the results. It is obtained from a reference measurement without liner, where the theoretical results are known ($D^{\pm} = 0$). Figure 6.14 plots the typical dissipation error of the DUCT-C at three grazing flow Mach numbers. The setup and analysis has been designed for high precision acoustic measurements. At $M_G = 0$, the dissipation error is well below 1 % for most frequencies. The grazing flow increases the error slightly, especially at low frequencies.

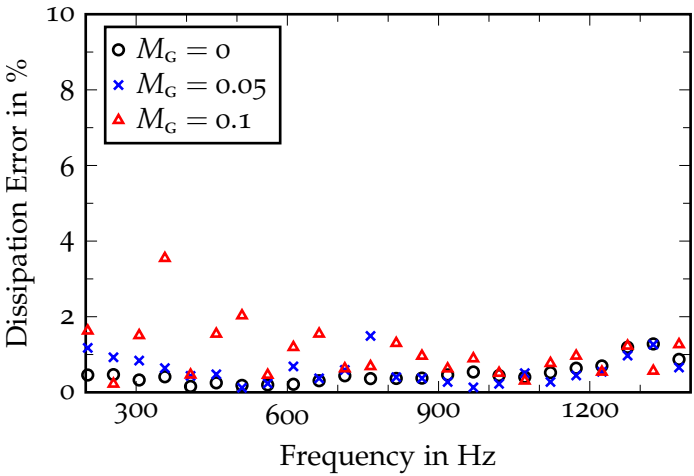

Figure 6.14: Dissipation error of the DUCT-C determined from reference measurements at various grazing flow Mach numbers.

6.6 HOT ACOUSTIC TEST RIG

Perforated liners are commonly studied at normal atmospheric pressure and temperature conditions. These tests can deliver reliable results of high accuracy, so that they are very important for the understanding of the basic parameter relations. On the other hand, measurements including combustion are extremely demanding and costly, while offering a limited accuracy only. So far they have mostly served as a quality check of a given liner design. The Hot Acoustic Test Rig[24] (HAT) fills the gap between fundamental studies and application tests. It enables liner measurements at elevated pressure and temperature in an acoustically well defined environment. The main flow can be heated up to 820 K (550 °C) with an electric air heater and the maximum static pressure is 1100 kPa absolute. Temperature and pressure can

24 The HAT is a joint facility of DLR and TU Berlin, Chair of Aero Engines.

be adjusted independently and continuously from ambient up to their maximum values.

6.6.1 *Setup & Instrumentation*

The layout of the Hot Acoustic Test Rig is based on the successful design of the Duct Acoustic Test Rig. A schematic illustration of the setup and instrumentation is given in Figure 6.15. The test duct is made of a high temperature steel tube with an inner diameter of 70 mm and a total length of about 5.4 m. It consists of two symmetric measurement sections with the liner module in-between and anechoic terminations at both ends. The whole test duct is covered by a custom taylored, two layer insulation, keeping thermal losses at a minimum.

Two loudspeakers are installed at the circumference of the duct at $x = \pm 1415$ mm. They are encased in a pressure proof housing, which is connected to the test duct via a cylindrical shaft with an inner diameter of 50.8 mm. On the side of the test duct the opening is covered with a wiremesh, resembling the geometry of the duct. The speaker housing is flushed with cooling air to ensure a temperature of the speaker below 50 °C at all times. The cooling air discharges into the test duct. Its amount is adjusted, so that the flow velocity within the neck is about 0.2 m/s. This low velocity flow prevents the hot air from entering the speaker housing and ensures a negligible influence when discharged into the hot duct flow.

For the speakers to operate at elevated and changing static pressure it is crucial to allow pressure equalization within the driver. This was accomplished by manually introducing a small gap into the driver's sealing, large enough to enable a balancing flow, but too small to affect the dynamic behavior of the speaker.

Air cooled and pressure proof microphone probes are installed at ten axial positions upstream and downstream of the liner. They are distributed with an increasing density towards the liner. The

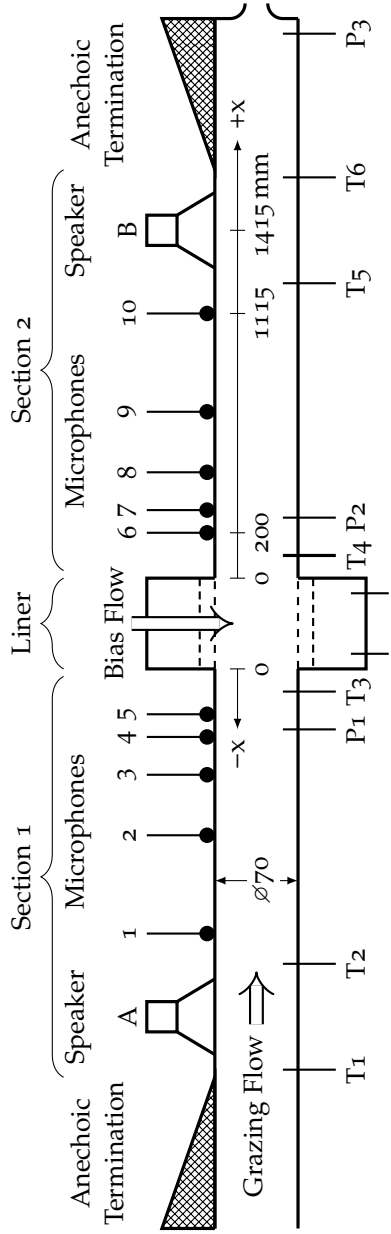

Figure 6.15: Schematic illustration of the Hot Acoustic Test Rig (HAT) with speakers A and B, microphone probes 1-10, temperature probes T1-T7, and pressure taps P1-P4. All dimensions in mm.

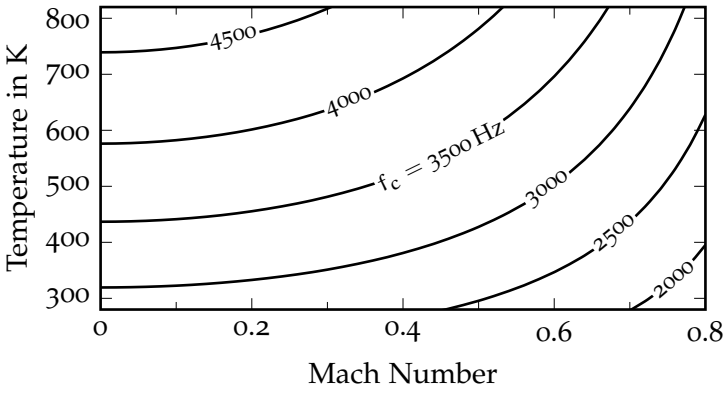

Figure 6.16: Upper limit of the plane wave frequency range in the HAT, depending on Mach number and temperature.

maximum axial distance between the microphone probes in each section is 915 mm and the minimum distance between the two innermost microphone probes is 85 mm.
The operation of the Hot Acoustic Test Rig is controlled with a PC via a LabView interface. Desired values for the temperature and pressure in the duct, as well as the mass flow rates of the cooling and bias flow can be set, while their actual values, as well as temperature and pressure data, are logged at a 0.1 Hz frequency.
The acoustic measurements are controlled with a separate PC. The test signal is a multi-tone sine signal. Three signals have been synthesized:

1: 204, 306, 408, 510, 612, 714, 816, 918, 1020, 1122 Hz

2: 1224, 1326, 1428, 1530, 1632, 1734, 1836, 1938, 2040, 2142 Hz

3: 2244, 2346, 2448, 2550, 2652, 2754 Hz

All three signals together cover a frequency range from 204 to 2754 Hz in steps of 102 Hz. The upper frequency limit for plane wave sound propagation is depending on the temperature and grazing flow Mach number, as illustrated in Figure 6.16. The test

signal is generated by an Agilent 33220A function generator. The signals are fed through a KME SPA240E stereo amplifier, which powers two Monacor KU-516 speakers.

The acoustic pressure is recorded over a time of 30 s with a 16 track OROS OR36 data acquisition system with a sampling frequency of 8192 Hz. Additionally, the output signal of the function generator is recorded at the same settings as a reference signal for the analysis.

Temperature measurements

The temperature of the main flow is measured at six positions along the duct, that is upstream and downstream of each loudspeaker and upstream and downstream of the liner (see T1-T6 in Figure 6.15). The temperature of the bias flow is measured in the cavity of the liner (see T7 in Figure 6.15). Additionally, there is a temperature sensor installed in each speaker housing for health monitoring (not shown in Figure 6.15). The sensors are resistive temperature detectors (RTD) of type PT100 connected in four-wire configuration to a digital multimeter (Agilent AG34972). Their accuracy is specified as ± 0.5°C for the complete temperature range of 280-820 K.

The analysis of the acoustic data requires an accurate knowledge of the temperature, as well as a constant temperature along the measurement sections. The placement of the temperature sensors allows the assessment of temperature changes along the duct. Insufficient insulation would produce a continuous temperature gradient, while the injection of cooling air through the microphone probes, the speaker housing and the liner would cause a sudden change of temperature. Several tests have been made and it can be concluded that the temperature gradient due to insufficient insulation is negligible, as well as the discharge of cooling air through the microphone probes and loudspeaker housings. However, the amount of bias flow can be substantial, so that the temperature in the downstream section can be much lower than the temper-

ature in the upstream section. The actual temperature difference depends on the initial temperature, and the ratio of grazing and bias flow. In extreme cases the temperature difference between section 1 and 2 can be as much as 160 K. The change in temperature is unproblematic as long as the temperatures of both sections are known and considered separately in the acoustic analysis. The temperature of the upstream section serves as the characteristic temperature of a test point.

Static pressure measurements

The static pressure is measured using pressure taps. They are located upstream and downstream of the liner (see P1 and P2 in Figure 6.15), at the nozzle (see P3 in Figure 6.15) and at various positions in the liner cavity (see P4 in Figure 6.15). For redundancy there are two pressure taps at each location. While the average value is used for post-processing, the difference between both values serves as an accuracy indicator. The pressure taps are connected to two modules of PSI (Pressure Systems, Inc.) 9116 pressure scanners. They have separate sensors for absolute and differential pressure measurements and are divided into four blocks of different pressure ranges: 2.5, 5, 69, and 1380 kPa. The accuracy is dependent on the full scale (FS) value of the range and is specified as $\pm 0.05\,\%$ FS for the 2.5 and 5 kPa ranges and $\pm 0.15\,\%$ FS for the larger ranges.

The pressure in the duct is given as absolute value, while the pressure in the liner cavity is given as the differential pressure referring to the absolute pressure in the duct. The pressure in the liner cavity is measured at three different radial positions. This enables the measurement of the pressure drop over each layer of a double skin configuration. In fact, the measured quantities include the pressure drop of the innermost liner and the total pressure drop across both layers. The third pressure tap enables the measurement of the pressure drop in a triple skin configuration. However, until now all measurements dealt with double skin configurations

only, so that the two outermost pressure taps measured the same pressure.

6.6.2 *Air Supply*

The air for the HAT facility is provided by two rotary screw compressors that can deliver a total mass flow rate of 0.78 kg/s. The air is dried (at a dew point of 276 K), filtered, and then delivered into a 2 m^3 pressure reservoir at a temperature of 288 K at 1600 kPa of pressure. The liner bias flow, the microphone cooling flow, and the speaker cooling flow are delivered at these conditions. The supply for each consumer can be set individually via mass flow controllers.

The main duct flow is fed through an electrical air heater before it enters the duct. The air heater can increase the temperature of the flow to any value between ambient and 820 K. It is custom made by DLR and has a maximum power rating of 540 kW.

The flow rate and pressure in the duct is controlled via a pressure valve, a volume flow meter, and a nozzle at the end of the test duct. The pressure in the duct can be adjusted continuously between ambient and 1100 kPa absolute pressure. The resulting flow velocity in the duct is defined by the geometry of the nozzle and can be determined by the laws of gas dynamics. Raising the pressure in the duct increases the flow velocity until a critical pressure is reached. At the critical pressure the velocity in the nozzle equals the speed of sound $M = 1$. For pressures beyond the critical pressure the velocity remains constant.

The critical pressure in the duct p_1^* can be calculated from the isentropic relation for the pressure [431][25]

$$\frac{p_2}{p_1^*} = \left(\frac{2}{\gamma+1}\right)^{\frac{\gamma}{\gamma-1}} \tag{6.31}$$

where the indexes 1 and 2 denote the quantities in the duct and downstream of the nozzle, respectively. Here, the nozzle back pressure equals the ambient pressure $p_2 = 101.325\,\mathrm{kPa}$. Then, p_1^* is only dependent on the heat capacity ratio γ. The heat capacity ratio for air varies slightly within the temperature limits encountered here (see Table A.10), so that the critical pressure yields $p_1^* = 191.9\,\mathrm{kPa}$ at 293 K and $p_1^* = 189.1\,\mathrm{kPa}$ at 773 K.
The mass flow rate through the nozzle is given by [431]

$$\dot{m} = A_2\sqrt{2p_1\rho_1}\,\Psi\,, \tag{6.32}$$

where Ψ describes the discharge of the fluid. For duct pressures below p^* it is given by

$$p_1 < p_1^*\text{:}\quad \Psi = \sqrt{\frac{\gamma}{\gamma-1}\left[\left(\frac{p_2}{p_1}\right)^{\frac{2}{\gamma}} - \left(\frac{p_2}{p_1}\right)^{\frac{\gamma+1}{\gamma}}\right]}\,, \tag{6.33}$$

while for higher pressures

$$p_1 \geqslant p_1^*\text{:}\quad \Psi = \left(\frac{2}{\gamma+1}\right)^{\frac{1}{\gamma-1}}\sqrt{\frac{\gamma}{\gamma+1}}\,. \tag{6.34}$$

Applying the continuity equation to Equation (6.32) an expression for the duct Mach number can be found

$$M_1 = \frac{A_2}{A_1}\sqrt{\frac{2}{\gamma}}\,\Psi\,. \tag{6.35}$$

25 Commonly, the velocity upstream of the nozzle is assumed zero, so that the pressure upstream is the stagnation pressure and the pressure downstream is the critical pressure and Equation (6.31) is commonly written as $p_2^*/p_1 = \ldots$. Here, the pressure downstream of the nozzle is the ambient pressure, which remains constant, and the pressure in the duct is increased until the critical condition is reached. The notation in Equation (6.31) is adapted accordingly.

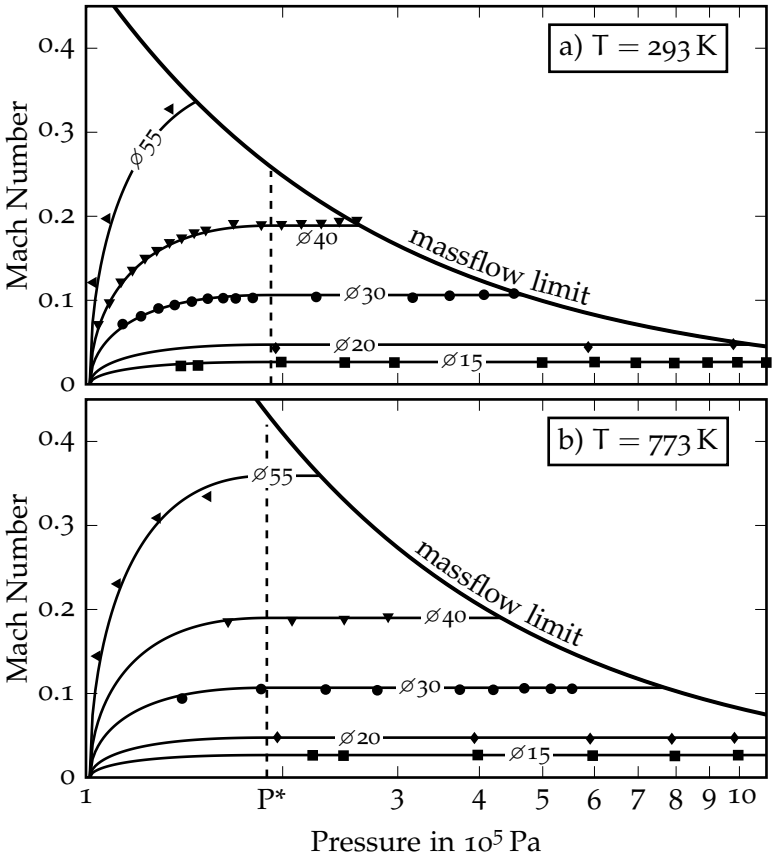

Figure 6.17: Relationship between pressure and Mach number for various nozzle diameters of the Hot Acoustic Test Rig at two temperatures. Lines: theoretical predictions; Symbols: measurement. Please note the log scaling of the pressure axis.

Table 6.1: Available nozzles and associated grazing flow Mach numbers in the Hot Acoustic Test Rig when $p_1 \geqslant p_1^*$.

Nozzle Diameter in mm	15	20	30	40	55
Mach Number	0.027	0.047	0.106	0.189	0.359

Equation (6.35) can be used to describes the Mach number characteristics of the Hot Acoustic Test Rig. This is demonstrated in Figure 6.17 for five nozzles with diameters between $\varnothing 15\,\text{mm}$ - $\varnothing 55\,\text{mm}$ and at temperatures of $293\,\text{K}$ and $773\,\text{K}$. The theoretical predictions according to Equation (6.35) and the measured values are in good agreement. The numerical values of the Mach numbers at critical condition are given in Table 6.1. Below the critical pressure the Mach number is a function of the pressure, so that a change of pressure changes the Mach number. The maximum Mach number for a given nozzle diameter remains constant with temperature. The higher temperature pushes the mass flow limit to higher pressures. However, the capacity of the air heater is limited, depending on the mass flow rate and the flow speed. The limit can be seen in the gap between the experimental values and the mass flow limit in Figure 6.17b.

The dependency of the maximum Mach number on pressure and temperature is plotted in Figure 6.18. The mass flow limit curves in Figure 6.17 are lines of constant temperature in Figure 6.18.

The dependency of the Reynolds number on the temperature is plotted in Figure 6.19 for various grazing flow Mach numbers at ambient pressure. Increasing the pressure would also increase the Reynolds number. The Reynolds number of the grazing flow is always larger than the critical Reynolds number ($Re_c = 4000$), so that the flow can be considered fully turbulent.

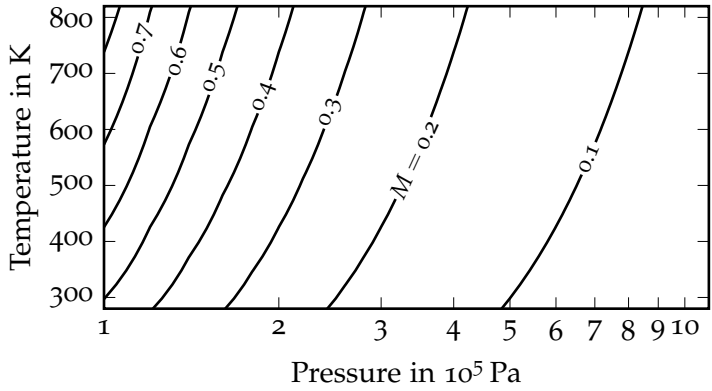

Figure 6.18: Maximum Mach number depending on pressure and temperature. Please note the log scaling of the pressure axis.

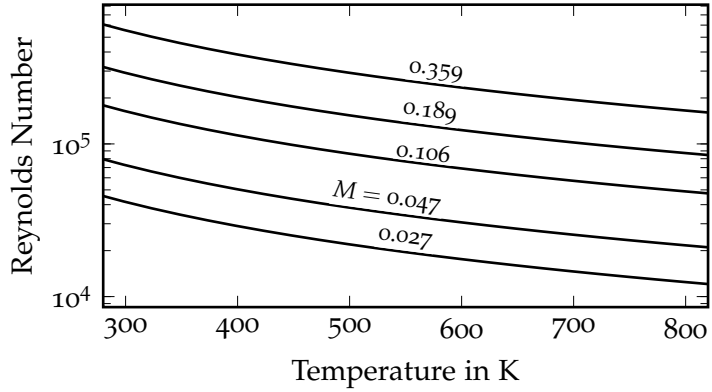

Figure 6.19: Reynolds number for various Mach numbers plotted over the temperature at $p = 101.325\,\mathrm{kPa}$.

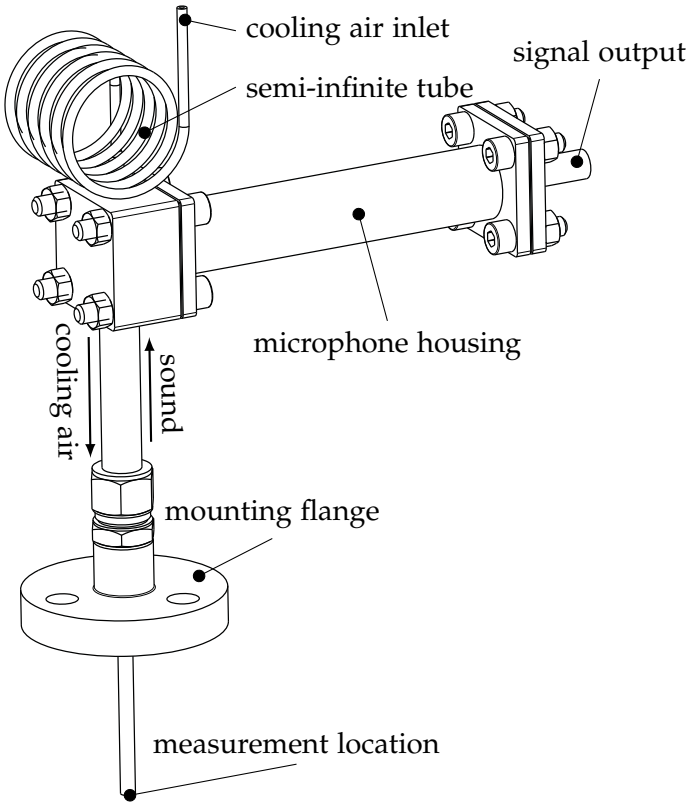

Figure 6.20: Design of the microphone probes used for acoustic measurements at the Hot Acoustic Test Rig.

6.6.3 *Microphone Probes*

Accurate acoustic measurements in high temperature flow are very challenging. Commercial products are typically based on a piezoelectric sensor. Their maximum tolerable temperature is typically around 620 K (in a very few cases the specifications go as high as 920 K). However, the sensitivity of piezoelectric pressure sensors is much lower compared to a standard condenser microphone. In order to overcome this limitation a microphone probe has been developed at DLR. The original design has been used successfully for several years, e. g. for acoustic measurements in a laboratory combustion chamber. Recently, the design has received a major upgrade to include the ability of measuring in high pressure environments of up to 2000 kPa. The microphone probes have been successfully tested in a combustion facility with respect to their safety and data reproducibility at conditions up to 1350 kPa and 1500 K.

The design of the microphone probes is shown in Figure 6.20. The probes are mounted to the test duct via a flange. The tube below the flange is inserted into the wall of the test duct, so that the end of the tube is flush with the wall. This is the measurement location where the acoustic pressure is to be recorded. The tube extends outwards with a constant diameter. After a certain length a microphone is mounted perpendicular to the tube inside a pressure-proof housing. The housing contains a standard quarter-inch condenser microphone (G.R.A.S. 40BP or 40BH) and its pre-amplifier (G.R.A.S. 26AC). The acoustic signal is transmitted from the tube to the microphone membrane via a small opening. The microphone signal is passed on through the wall with a pressure-proof wall bushing that ends in a LEMO connector.
In order to prevent reflections of sound, the tube is extended beyond the location of the microphone, following the principle of a semi-infinite tube. The overall length of this tube is about one meter which is mostly wound-up in a spiral to save space. The large

ratio between diameter and length of the tube provides sufficient viscous damping, so that the frequency range of interest is free from resonances.

A small amount of cooling air is fed through the tube, preventing hot gases from the duct to enter the tube and get into contact with the microphone membrane. A study regarding the influence of the cooling flow on the acoustic measurement was done with the initial design of the microphone probes (unpublished). At atmospheric pressure it was shown that a velocity of 4 m/s in the tube is enough to ensure the safe operation of the microphones. This corresponds to a mass flow rate of 0.054 kg/h at atmospheric conditions. The required value for the cooling flow velocity is held constant at elevated pressures, so that the mass flow rate has to be adjusted according to the change in density. A disturbance of the signal by the cooling air could only be observed for velocities beyond 30 m/s.

Each microphone probe has a characteristic transfer function which is determined by the geometric dimensions of the probe, i. e. the diameter of the tube, the distance between the measurement location and the microphone membrane, etc. The transfer function has to be considered in the analysis, correcting the signals from the transfer characteristics of the probe. While the specified geometry is identical for all probes, so should be their transfer functions. However, small variation in manufacturing and assembly require the determination of an individual transfer function for each probe.

A probe together with a microphone is forming one unit, which is only separated if a component is damaged. Instead of determining the transfer function of the probe separately, a calibration curve for the whole unit is determined. Then, the calibration curve includes the transfer function of the probe as well as the behavior of the microphone itself. Three different ways of calibration have been established:

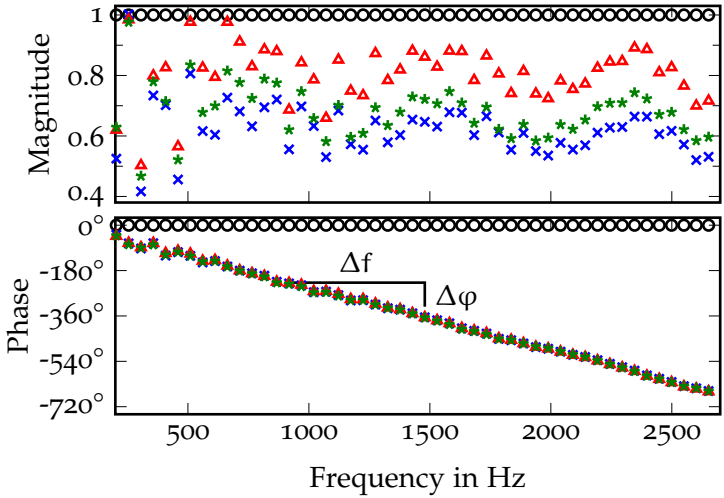

Figure 6.21: Quasi-absolute calibration curves at ambient conditions: ○ Reference, × Probe 08, △ Probe 12, * Probe 16.

1. Absolute calibration: Calibration with a pistonphon, regarding the magnitude at one frequency.

2. Quasi-absolute calibration: Calibration regarding the magnitude and phase over the complete frequency range with respect to a reference condenser microphone.

3. Relative calibration: Calibration regarding the magnitude and phase over the complete frequency range with respect to a reference microphone probe.

The absolute calibration defines the deviation of the measured signal to a reference signal supplied by a pistonphon, i. e. 124 dB at 250 Hz. The magnitude correction value, expressed as a sensitivity in V/Pa, is saved in the data acquisition system and is directly applied to the recorded data.

The two other options apply the in-duct calibration method that was described in Section 6.5.2. The quasi-absolute calibration employs a wall-flush mounted condenser microphone as ref-

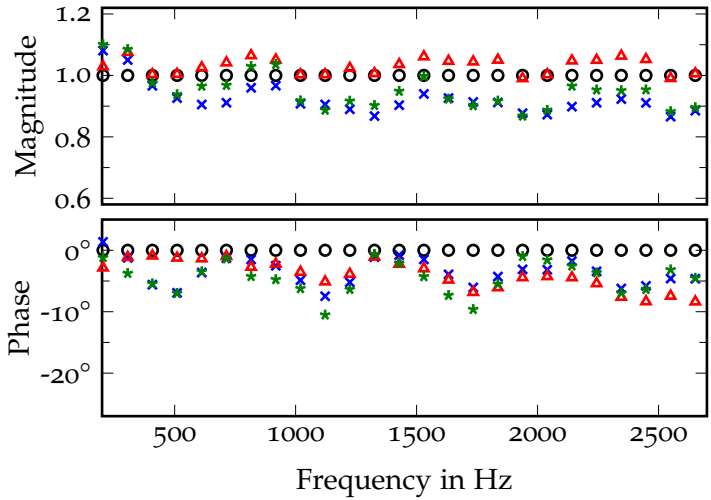

Figure 6.22: Relative calibration curves at ambient conditions: ○ Probe 04 (Reference), × Probe 08, △ Probe 12, * Probe 16.

erence. The condenser microphone is calibrated with a pistonphon, so that the results can be considered to be quasi-absolute. Plots of the magnitude and phase correction values for three exemplary microphone probes are given in Figure 6.21. The reference magnitude and phase have a constant value of unity and zero, respectively. All three microphone probes have been calibrated with a pistonphone previously, so that their magnitude correction values at 250 Hz are equal to unity. The plot shows the frequency dependency of magnitude and phase. The continuous slope of the phase reveals that there is no resonance within the frequency range. The slope itself defines the time delay of the acoustic wave traveling from the measurement location to the microphone: $\Delta t = \Delta\varphi/360°/\Delta f$. Picking two random points from the phase curve of probe 16, say (1020 Hz, -266.8°) and (2091 Hz, -512.8°), yields a time delay of $\Delta t = -6.38 \cdot 10^{-4}$ s (the negative sign indicates the delay). Assuming $c = 343.38$ m/s (at 293.15 K) gives

a distance of 219.1 mm between measurement location and microphone. This agrees very well with the actual distance of 220 mm.

The third calibration method is the relative calibration with respect to a chosen reference microphone probe. Again, the procedure is based on the in-duct calibration method described before. Figure 6.22 shows the resulting calibration curves for the same microphone probes from the previous plot. The curves look very different to Figure 6.21, but they basically contain the same information. The advantage of the third method is that it only employs microphone probes, so that the calibration can be done at the actual operating condition of the measurements. Doing so reveals the dependency of the microphone probes on temperature and pressure. The influence of temperature and pressure on microphone probe 20 is shown in Figures 6.23 and 6.24, respectively.

The calibration curves exhibit no dependency on the temperature in the duct. This is expected, as the microphone probes are flushed with cooling air of constant temperature while the duct temperature increases. The actual temperature within the probes does not change that much. The static pressure on the other hand, is the same within the probe and the duct. A strong influence on both, magnitude and phase, can be observed. The viscothermal losses within the tube are decreasing considerably at high pressure, so that the assumption of the semi-infinite tube is violated and reflections occur. This effect becomes more and more visible while the pressure increases. The reflections can be avoided by further extending the tube. However, due to the ability to provide magnitude and phase correction values for each operating condition, the pressure dependency can be handled very well.

Each of the three methods is important to characterize the behavior of the microphone probes. The quasi-absolute calibration serves as a one-time check that the design was successful (no resonances). The absolute calibration with the pistonphon equalizes the levels of all microphone probes. Furthermore, it serves as an easy way of health checking in-between measurements. However,

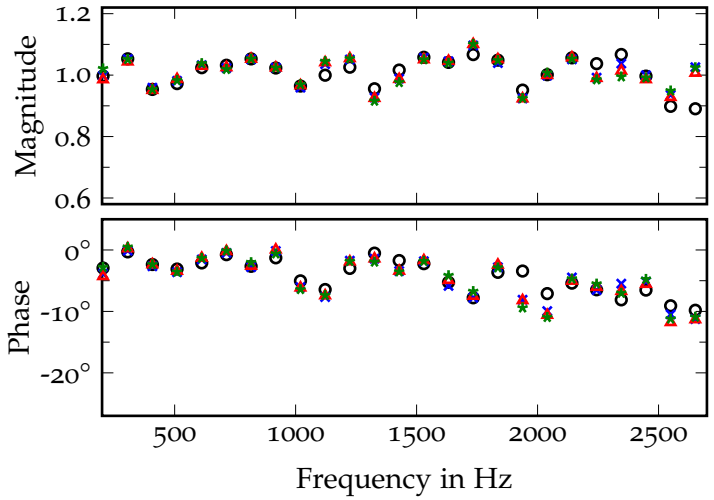

Figure 6.23: Relative calibration curves of microphone probe 12 at 200 kPa and ○ 293 K, × 423 K, △ 573 K, * 773 K.

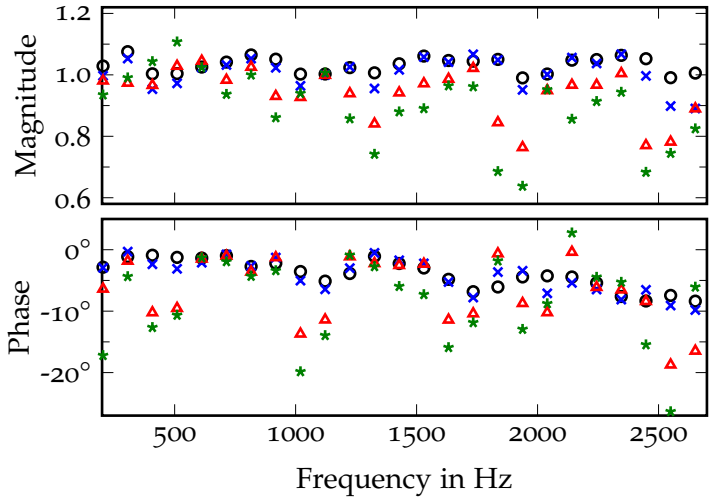

Figure 6.24: Relative calibration curves of microphone probe 12 at 293 K and ○ 101 kPa, × 200 kPa, △ 600 kPa, * 1000 kPa.

it should be noted that applying a new absolute calibration value makes any previous relative calibration invalid (the magnitude curve will have an offset). The relative calibration at operating condition is crucial for the analysis of the data. Therefore, a relative calibration is performed in regular intervals, at least at the beginning of a measurement campaign.

6.6.4 *Estimation of the Humidity*

The treatment of the acoustic losses at elevated pressure and temperature in the next section requires some knowledge about the humidity. The relevant quantity for the acoustic losses is the molar concentration of water vapor h (fraction of air molecules that are water). The air provided for the Hot Acoustic Test Rig is dried at a dew point temperature $T_d = 276.15\,\mathrm{K}$ (3 °C) at an operating pressure of 1500 kPa. The saturation pressure at the dew point temperature is calculated from Equation (5.64) and results in $p_{ws}(T_d) = 758.054\,\mathrm{Pa}$. The relative humidity in the saturated state is RH = 100 %, so that the molar concentration of water vapor is given by Equation (5.63) as $h = 0.051\,\%$. The molar concentration is determined by the operating conditions of the air dryer. The temperature in the Hot Acoustic Test Rig is always well above the dew point temperature and the pressure is always well below the saturation pressure at the respective temperature, so that the molar concentration of water vapor in the air stays constant and is independent of the operating temperature and pressure.

The relative humidity might be the more well-known quantity. It can be calculated from Equation (5.63) with $h = 0.051\,\%$, the saturation pressure at operating temperature $p_{ws}(T)$, and the operating pressure p. Its values range from 32.9 % (at 288.15 K and 1100 kPa) to 0.0002 % (at the critical temperature $T_c = 647.096\,\mathrm{K}$ and 101.325 kPa), while it is 4 % at ISA conditions (288.15 K and 101.325 kPa).

The given values of relative humidity and molar concentration of water vapor are estimates only. The uncertainties lie in the actual dew point temperature and variations in the operating pressure of the air dryer. The value of $h = 0.051\,\%$ can be regarded as a minimum estimation, as deviations in the dew point temperature are expected rather to higher temperatures than below the specified 276.15 K (3 °C) and the operating pressure of the air drier of 1500 kPa is a maximum value.

6.6.5 *Attenuation at Elevated Pressure and Temperature*

The various acoustic losses that occur when sound is propagating through a smooth, hard-walled duct with flow are discussed in Section 5.4. At ambient conditions the losses within the fluid are generally two orders of magnitude smaller than the viscothermal losses at the duct wall, so that they are usually neglected. This is common practice and reproduces the physics accurately [273, 316, 445]. However, recent measurements [277] revealed an increasing attenuation of sound at elevated pressure and temperature, which cannot be justified by the viscothermal losses at the wall alone. A rigorous review of the other loss mechanisms, i. e. the losses due to turbulent flow and the losses within the fluid, and their dependency on pressure and temperature has been presented by Lahiri et al. [278]. It was found that the molecular relaxation losses within the fluid become more important when pressure and temperature are increased from their ambient values, so that they cannot be neglected any longer.

It is assumed that the losses at the walls and the losses within the fluid are additive and that the effect of convection on the attenuation within the fluid can be accounted for by division with $1 \pm M$, then the total losses are given by

$$k^{\pm}_{\text{total}} = \omega / c^{\pm}_{\text{ph,total}} - i\alpha^{\pm}_{\text{total}} \tag{6.36a}$$

with the attenuation coefficient and phase velocity given by

$$\alpha^{\pm}_{\text{total}} = \alpha_{\text{fluid}}/(1 \pm M) + \alpha^{\pm}_{\text{turb}} \text{ and} \tag{6.36b}$$

$$c^{\pm}_{\text{ph,total}} = (c + \Delta c_{\text{ph,fluid}} + \Delta c^{\pm}_{\text{ph,turb}})(1 \pm M)\,. \tag{6.36c}$$

The total losses include the viscothermal losses within the fluid, the losses due to rotational and vibrational molecular relaxation, the viscothermal losses at the duct wall, the convective effect of the flow on the wall losses, and the absorption due to the turbulent flow boundary-layer. The respective equations for α_{fluid}, $\alpha^{\pm}_{\text{turb}}$, $\Delta c_{\text{ph,fluid}}$, and $\Delta c^{\pm}_{\text{ph,turb}}$ are given in Section 5.4.

The attenuation coefficient at elevated pressure and temperature has been determined experimentally with the Hot Acoustic Test Rig. Details of the measurements can be found in [278]. Figure 6.25 shows a comparison between the experimental data and the theoretical predictions of Equation (6.36b). The convective influence of the flow on $\alpha^{\pm}_{\text{total}}$ is small, so that only the average value $\overline{\alpha}_{\text{total}} = (\alpha^{+}_{\text{total}} + \alpha^{-}_{\text{total}})/2$ is plotted.

While there is some scatter in the experimental data, it matches the theoretical predictions rather well. Setting $h = 0.08\,\%$ for the model matches the experimental data slightly better than the estimate $h = 0.051\,\%$. This corresponds, for example, to a change of operating condition of the air dryer to 280.65 K and 1300 kPa, which is a valid assumption.

According to Equation (6.36b), the total losses are the superposition of α_{fluid} and $\alpha^{\pm}_{\text{turb}}$, which are also plotted in Figure 6.25. $\alpha^{\pm}_{\text{turb}}$ is mostly determined by the viscothermal losses at the duct wall, except at low frequencies where the losses due to the turbulent flow boundary-layer become prominent. However, the attenuation in the measured frequency range (indicated in gray) is dominated by the losses within the fluid at both operating conditions.

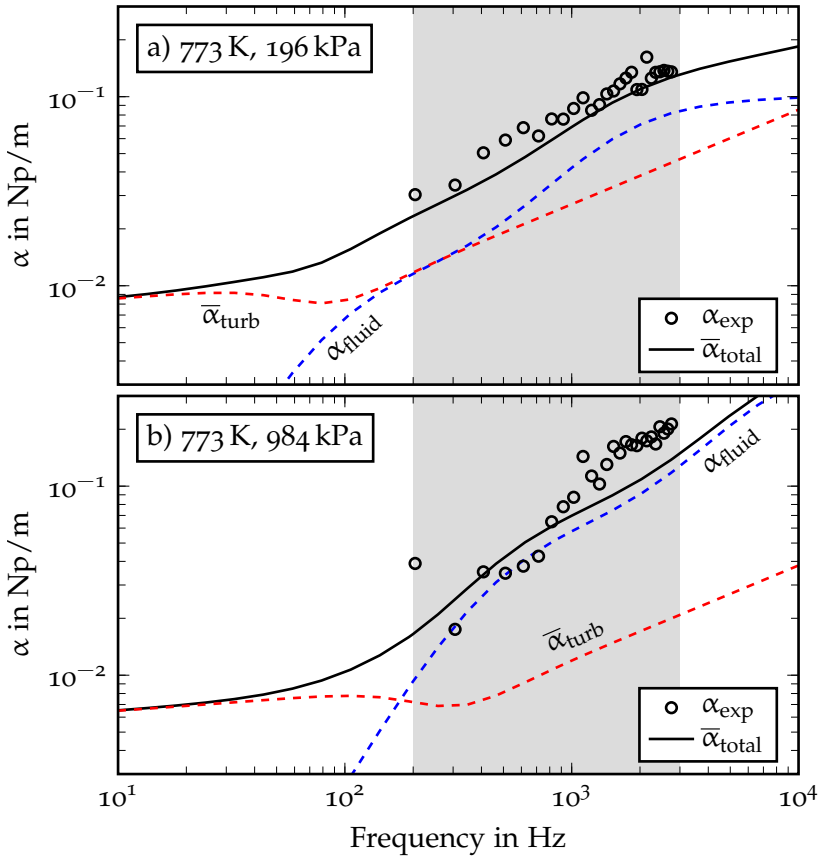

Figure 6.25: Comparison of the attenuation coefficient determined experimentally and from theoretical predictions at two elevated temperature and pressure conditions with $h = 0.08\,\%$, $M = 0.05$, and $R = 0.035\,\mathrm{m}$: a) 773 K, 196 kPa; b) 773 K, 984 kPa. The frequency range that is covered by the experiments is indicated in gray.

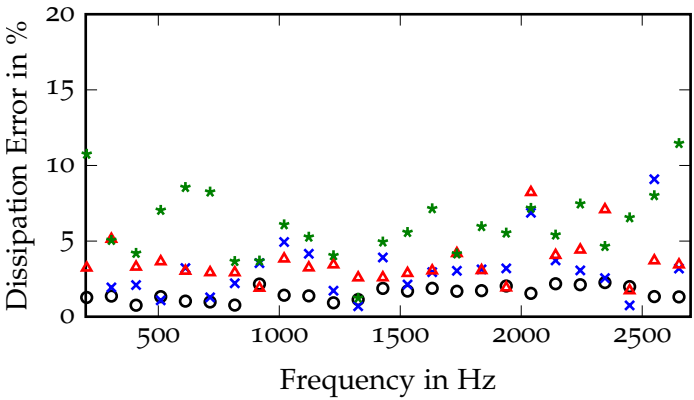

Figure 6.26: Dissipation error as a measure for the accuracy at the four extreme operating conditions: o 288 K, 101.325 kPa; × 288 K, 1100 kPa; △ 773 K, 200 kPa; * 773 K, 1100 kPa.

6.6.6 *Accuracy*

The dissipation error is plotted in Figure 6.26 for four operating conditions. At normal atmospheric temperature and pressure and without flow, the dissipation error is generally below 3 %. The error increases at elevated pressure and temperature.

7

PARAMETER STUDY

This chapter presents the results of the experimental parameter study. Each parameter is addressed individually, always including a bias flow. The text presents a selection of results of significant importance. The geometric specifications of the liner configurations are listed in Table 7.1.

7.1 SOUND PRESSURE LEVEL

The amplitude of the acoustic oscillations in a gas turbine combustor can be very high, especially when instabilities occur. This section studies the effect of high amplitudes on the dissipation of sound at perforations with and without bias flow.

Various definitions of the measured amplitude are discussed in Section 2.4.2. Here, a combination of the incident wave amplitude and the fixed reference location method is applied. The loudspeaker output is adjusted to match a nominal SPL at a reference microphone in the hard-walled duct section. The measurement is performed with this nominal SPL value. In the analysis, the incident wave amplitude is determined from a wave decomposition and used for the presentation of the data. The combination of these two methods eliminates the time consuming adjustment to match a certain SPLvalue. As a result, the actual SPL values are scattering slightly around the nominal values.

Table 7.1: Geometric specifications of the studied liner configurations. Double-skin configurations are represented by two consecutive lines, the first for the damping liner and the second for the metering liner specifications. The configurations labeled with DCXXX are measured in the Duct Acoustic Test Rig (see Section 6.5), while HCXXX indicates the Hot Acoustic Test Rig (see Section 6.6).

Config.	D	t	d	α	A_{open}	σ	L_{eff}	D_c	L_c	V
–	mm	mm	mm	deg	mm^2	%	mm	mm	mm	cm^3
DC006	140	1	1	90	286	1.1	59.5	240	60	1757
DC007	140	1	2.5	90	295	1.0	66	240	60	1757
DC008	140	1	2.5	90	1787	6.8	59.5	240	60	1757
DC009	140	1	1	90	47	0.2	66	240	60	1757
DC010	140	3	1	90	286	1.1	59.5	240	60	1703
DC011[a]	140	1	2.5	90	295	1.0	66	240	60	1757
DC012[b]	140	1	2.5	90	295	1.0	66	240	60	1757
DC013[c]	140	1	2.5	90	295	1.0	66	240	60	1757
DC014	140	1	1	90	286	1.1	59.5	162	60	280
	162	1	1	90	85	0.4	42	240	60	1446
DC015	140	1	1	90	286	1.1	59.5	192	60	780
	192	1	1	90	85	0.3	51	240	60	941
DC017	140	1	2.5	90	1787	6.8	59.5	212	60	1161
	212	1	2	90	440	1.1	59.5	240	60	556
DC018[d]	140	1	2.5	90	1787	6.8	59.5	212	60	1161
	212	1	2	90	440	1.1	59.5	240	60	556
DC019	140	1	2.5	90	1787	6.8	59.5	160	280	1164
	160	1	2	90	440	1.5	59.5	240	280	6896
DC021	140	1	2.5	90	2042	6.8	68	240	280	8201
DC022	140	1	2.5	90	2042	6.8	68	240	280	8201
DC023	140	1	2.5	90	2042	6.8	68	240	280	8201
DC024	140	1	2.5	90	2042	6.8	68	240	280	8201
HC005	70	1	2.5	90	893	7.4	54.8	130	56	515
	130	1	2	90	217	1.2	45.9	190	51	748
HC006	70	2	1.73	90	724	7.5	43.75	190	56	1347
HC007	70	2	1.73	60	719	7.3	45	190	56	1347
HC008	70	2	1.73	30	724	7.5	43.75	190	56	1347

a Same as DC007 with cross shaped orifices, see Figure 2.5g.
b Same as DC007 with both edges round, see Figure 2.6b.
c Same as DC007 with nonuniform porosity, see Figure 7.40b.
d Same as DC017 with partitioned cavity, see Figure 2.10c.

The two-source scattering matrix method, described in Chapter 6, requires two consecutive measurements to produce one data point. The reference microphone is chosen next to the liner. Depending on the excitation with speaker A or B, that is microphone 6 or 7 (referring to the notation in Figure 6.7), respectively. The discrepancy of the incident wave amplitude between these two measurements is generally below 0.5 dB. The average value is used for the presentation of the results.

The influence of the sound pressure level on the dissipation is studied at configurations DC006 and DC008. The only difference between these two liners is the orifice diameter and the resulting porosity (see Table 7.1 for specifications). The SPL is varied in the range from 100 dB to 135 dB for two bias flow velocities and four frequencies. The settings are listed in Table 7.2. There is no grazing flow present and temperature and pressure are at normal atmospheric condition.

The two liner configurations and four frequencies are chosen due to their different damping behavior. The dissipation curves of the two configurations and the corresponding bias flow settings are displayed in Figure 7.1. The frequencies are chosen by evaluating the dissipation curves: a low frequency (306 Hz), a medium frequency (816 Hz), a high frequency (1224 Hz), and the frequency of maximum dissipation for the respective configuration (DC006: 510 Hz, DC008: 1020 Hz).

Table 7.2: Parameter settings for the measurements regarding the influence of the sound pressure level.

Configuration		DC006	DC008
Sound Pressure Level	dB	100-135	100-135
Bias Flow Mach Number	–	0, 0.04	0, 0.036
Frequency	Hz	306, 510, 816, 1224	306, 816, 1020, 1224

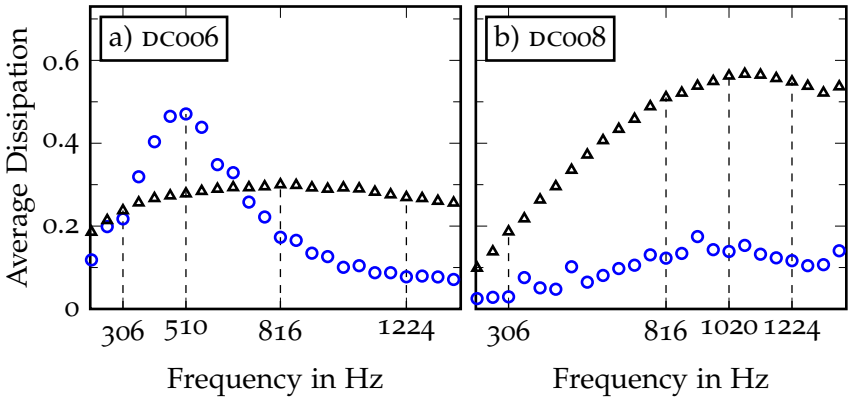

Figure 7.1: Dissipation curves of the studied configurations. a) DC006 ○ $M_B = 0$, △ $M_B = 0.036$; b) DC008 ○ $M_B = 0$, △ $M_B = 0.04$.

Results

The results of the linearity study for configuration DC008 are given in Figure 7.2. The left column, plots a) and c), shows the behavior without bias flow and the right column, plots b) and d), when a bias flow is present. The top row, plots a) and b), depicts the average dissipation. The different dissipation levels at the various frequencies and different bias flow conditions are apparent. In order to remove this distraction and concentrate on the linear/nonlinear behavior the data has been normalized with the linear dissipation value, i.e. the dissipation value from the measurement at the lowest SPL (around 100 dB). The normalized dissipation expresses the deviation from the linear dissipation in percent. It is plotted in the bottom row, plots c) and d).
In the case without bias flow the dissipation increases continuously for SPLs beyond 115 dB. This behavior is consistent for all frequencies. When a bias flow is present the dissipation remains unchanged up to the maximum SPL. As the linear regime is defined by being independent of the amplitude it can be concluded that a linear to nonlinear transition occurs at about 115 dB for the

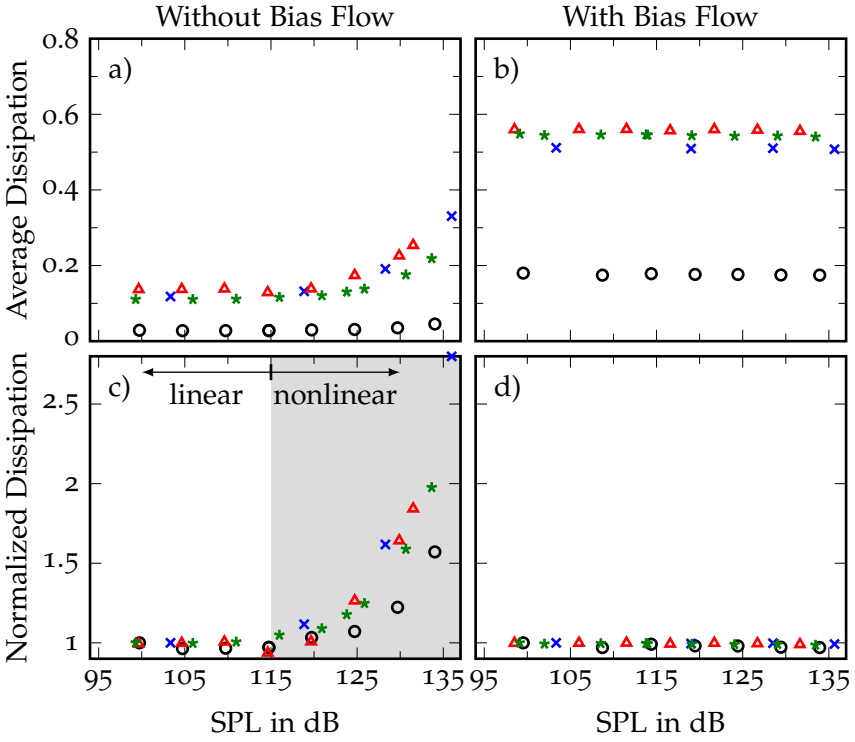

Figure 7.2: Influence of the sound pressure level on the dissipation of configuration DC008 for the frequencies ○ 306 Hz, × 816 Hz, △ 1020 Hz, and * 1224 Hz. In the bottom row the dissipation is normalized with its value at the lowest SPL.

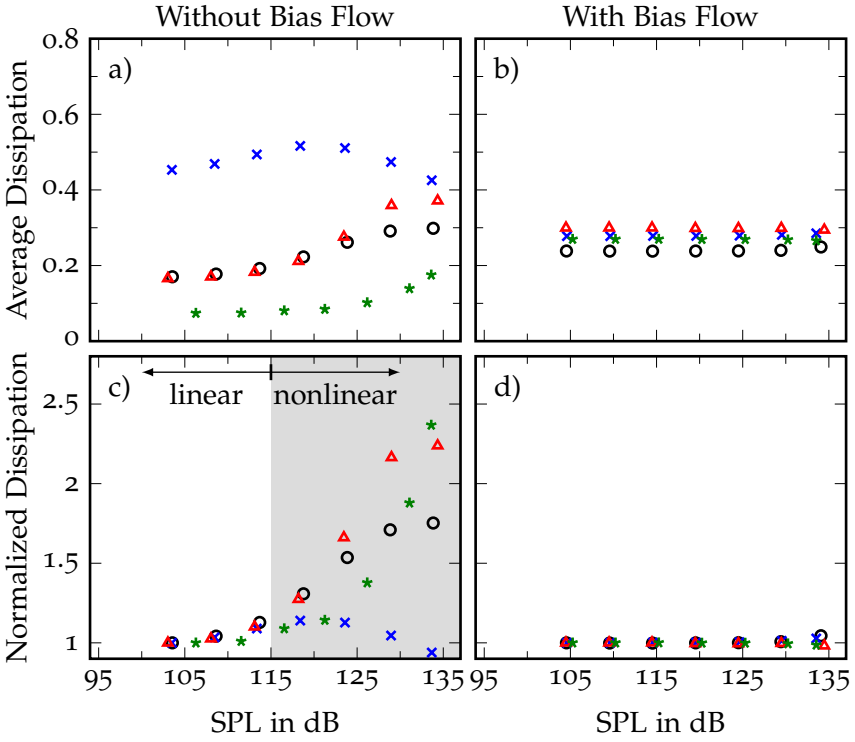

Figure 7.3: Influence of the sound pressure level on the dissipation of configuration DC006 for the frequencies ○ 306 Hz, × 510 Hz, △ 816 Hz, and * 1224 Hz. In the bottom row the dissipation is normalized with its value at the lowest SPL.

case without bias flow. When a bias flow is present, the linear regime extends over the whole range of SPLs tested in this study (up to 135 dB).

The results of configuration DC006 are presented in Figure 7.3, using an identical arrangement of the plots as in Figure 7.2. While the general outcome is very similar to the results of configuration DC008, a remarkable difference can be observed in the nonlinear regime. The nonlinear increase of dissipation reaches a maximum value at a certain sound pressure level. This is most obvious at 510 Hz with a maximum at about 120 dB. For higher SPLs the dissipation is reduced, ultimately resulting in dissipation values below that of the linear dissipation. Similarly, the dissipation curves for 306 and 816 Hz exhibit a saturation towards high SPLs. The saturation occurs for average dissipation values beyond 0.3. This could be one reason why this effect is not observed for configuration DC008, its dissipation values without bias flow stay below this limit. When the saturation occurs, it seems that the dissipation curves converge towards a common value of approximately 0.3 for high amplitudes (Figure 7.3a). This coincides with the constant dissipation value when a bias flow is present (Figure 7.3b).

Figure 7.4 shows the transition between linear and nonlinear behavior depending on the bias flow. Plotted is the average dissipation over the bias flow Mach number for a low and high sound pressure level at two frequencies. The behavior is linear when both curves agree and nonlinear if they do not. Without any flow and at low Mach numbers the behavior is dependent on the sound pressure level. Increasing the Mach number eliminates the amplitude dependency. At 510 Hz the dissipation values agree for bias flow Mach numbers beyond 0.02, while the limit is at about 0.035 at 816 Hz. However, these limits are rather vague.

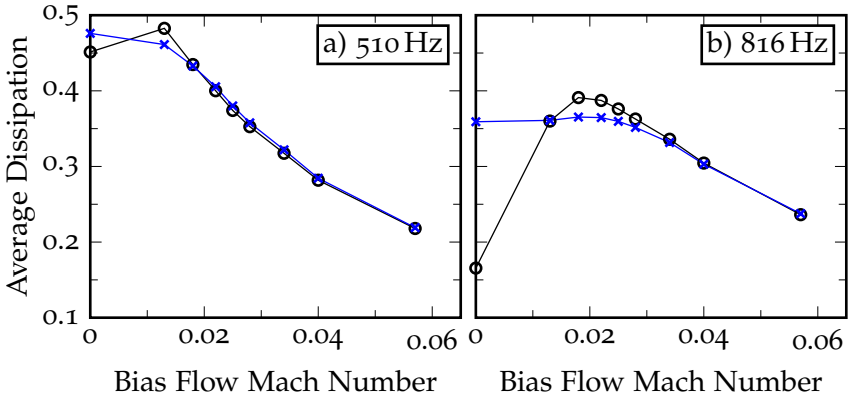

Figure 7.4: Dissipation of configuration DC006 plotted over bias flow at two frequencies a) 510 Hz and b) 816 Hz, comparing two sound pressure levels —o— 105 dB and —×— 130 dB.

Discussion

The dependence of the orifice behavior on the sound pressure level seems to be fundamentally different with or without bias flow. The nonlinear behavior of orifices without bias flow has been demonstrated and discussed in many publications [26, 58, 61, 72, 105, 123, 225, 227, 228, 243, 327, 361, 441, 473, 474, 505]. The results here suggest a transition from linear to nonlinear behavior when increasing the sound pressure level beyond $\approx$ 115 dB. This limit seems to be independent of the frequency and the orifice diameter. These results are in agreement with previous findings. For example, the same limit was found by Tran et al. [481], studying the influence of the sound pressure level on the reflection coefficient of two different perforated plates. Heuwinkel et al. [199] found a limit of 110 db at 310 Hz for a cylindrical liner configuration. Lee and Kwon [287] determine a lower limit at 102 dB[1].

1 A reason for this deviation could be that Lee and Kwon [287] use a random broadband signal, where the overall SPL should be the significant quantity

The experimental results show, that the dissipation is independent of the SPL when a bias flow is present. This behavior agrees with the findings in [40, 199, 481]. However, this conclusion might not apply generally. According to Luong et al. [308], the transition between linear and nonlinear regime takes place when flow reversal occurs. In that case, the oscillating acoustic velocity is larger than the steady bias flow velocity. Below this limit, Luong et al. [308] assume that the nonlinear effects are negligible[2]. This limit, based on theoretical assumption, is confirmed by the measurements of Rupp et al. [415, 419].

The results of the experimental study by Rupp et al. [415, 419] exhibits a similar saturation of the absorption at high amplitudes as configuration DC006 in Figure 7.3. They argue that the absolute amount of energy that can be absorbed is fixed, so that the absorption or dissipation coefficient decreases due to the increasing incident energy.

It can be concluded from the results and the discussion of the literature, that nonlinear effects are of minor importance for bias flow liners. They only become significant when flow reversal occurs, that is at very high amplitudes (of course depending on the bias flow velocity). It could be argued that the pressure amplitudes of the instability are in fact very high. This is of course correct, however, a successful liner design aims to disrupt the feedback loop between the heat-release fluctuations and the acoustic pressure fluctuations, so that an instability does not occur. Thus, the design operating point of a liner should be at much lower amplitudes.

Furthermore, flow reversal in a combustor liner leads to hot gas ingestion into the liner cavity [99, 417, 420]. This changes the absorption characteristics of the liner and, in worst case, results in overheating and failure of the structure. Thus, the velocity of

(see discussion on page 31). It is not clear which definition the 102 dB are based on.

2 Recently, Bodén and Zhou [70] showed that the nonlinear effects cannot be neglected entirely below this limit.

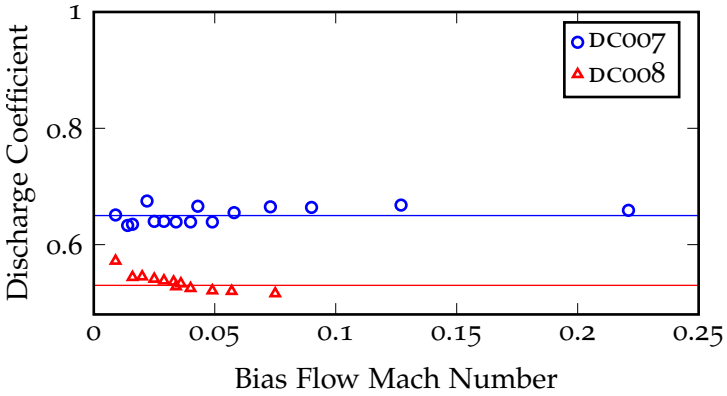

Figure 7.5: Measured values of the discharge coefficient (symbols) and average value (solid line). The data is listed in Table 7.3.

the steady bias flow must be sufficiently high, so that flow reversal does not occur. Following these presumptions, the liner is required to operate in the linear regime.

7.2 BIAS FLOW

This section discusses the general influence of the bias flow on two representative liner geometries. However, the bias flow is the main parameter of this study, so that it will be included in the discussion of each parameter in the subsequent sections.

The general influence of the bias flow is demonstrated with configurations DC007 and DC008. Their results reflect the typical behavior of the other configurations in this study. The geometric specifications are given in Table 7.1.

Table 7.3 lists the characteristic bias flow parameters of the selected test points. The mass flow rate and the pressure difference are measured, while the other quantities are calculated as described in Section 2.5.2. Please note that the maximum mass flow rate that is supported by the mass flow controller in the measurements is 100 kg/h. The test points of configuration DC008 that

Table 7.3: Measured data of the bias flow parameters of the selected test points.

DC007					DC008				
M_B	U_B	$\dot{m}_B$	ΔP_T	C_d	M_B	U_B	$\dot{m}_B$	ΔP_T	C_d
–	m/s	kg/h	%	–	–	m/s	kg/h	%	–
0.000	0.0	0.0	0.000	–	0.000	0.0	0.0	0.000	–
0.009	2.9	2.4	0.005	0.65	0.009	2.9	12.8	0.005	0.57
0.014	4.5	3.8	0.012	0.63	0.016	5.0	21.8	0.015	0.54
0.016	5.1	4.3	0.016	0.63	0.020	6.4	28.0	0.024	0.54
0.022	7.1	6.1	0.030	0.68	0.025	8.1	35.0	0.039	0.54
0.025	8.2	6.9	0.039	0.64	0.029	9.3	40.0	0.051	0.54
0.029	9.2	7.8	0.051	0.64	0.033	10.5	45.0	0.065	0.54
0.034	10.8	9.1	0.069	0.64	0.034	10.8	45.7	0.069	0.53
0.040	12.9	10.9	0.099	0.64	0.036	11.7	50.0	0.081	0.53
0.043	13.8	11.7	0.113	0.67	0.040	12.9	54.4	0.099	0.52
0.049	15.7	13.3	0.147	0.64	0.049	15.9	66.3	0.150	0.52
0.058	18.6	15.6	0.206	0.66	0.057	18.2	76.1	0.197	0.52
0.073	23.3	19.8	0.322	0.67	0.075	24.2	100.0	0.347	0.52
0.090	28.9	24.6	0.497	0.66	0.090	28.8	–	0.493	–
0.127	40.7	34.8	0.986	0.67	0.127	40.8	–	0.987	–
0.221	70.7	59.5	2.971	0.66	0.217	69.8	–	2.892	–

required a higher mass flow rate have been measured without the mass flow controller by adjusting the line pressure directly, so that mass flow data is not available here.

The discharge coefficient C_d is calculated from the pressure drop and mass flow rate according to Equation (2.14). The result is plotted in Figure 7.5. The values are rather constant over the bias flow Mach number, so that the average value is used. However, the difference between the two configurations is quite surprising. After all, the orifices have the same geometry and dimensions, just the spacing between them is changed.

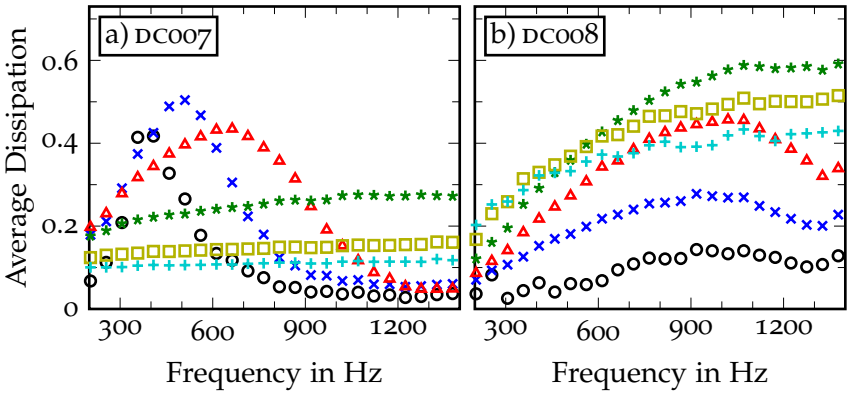

Figure 7.6: Dissipation plotted over the frequency at various bias flow Mach numbers ○ 0, × 0.016, △ 0.025, * 0.049, □ 0.090, and + 0.127 for two liner configurations a) DC007 and b) DC008.

Results

Figure 7.6 plots the dissipation coefficient over the frequency for some selected bias flow velocities. Without any bias flow, configuration DC007 exhibits a prominent dissipation maximum around 400 Hz. Introducing a bias flow and increasing its velocity shifts the dissipation maximum to higher frequencies. At the same time, the maximum level of dissipation is first increased and then reduced, while the dissipation becomes more broadband. The Mach number for maximum dissipation is around 0.016 and the optimum Mach number to achieve a good broadband damping is around 0.049.

Configuration DC008 in Figure 7.6b demonstrates different characteristics. The damping is very poor when there is no bias flow present and there is no obvious peak frequency. The flow through the liner improves the dissipation levels over a broad frequency range. The center frequency of the broadband increase of dissipation is around 1 kHz. A maximum dissipation of nearly 60 % is reached when the bias flow Mach number is around 0.049. For

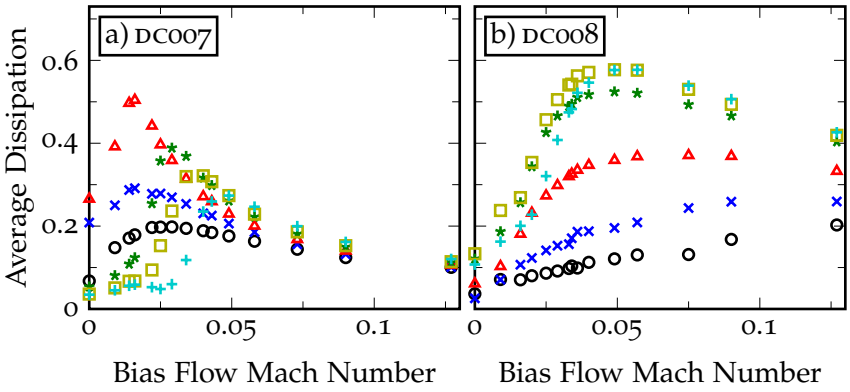

Figure 7.7: Dissipation plotted over the bias flow Mach number at various frequencies ○ 204 Hz, × 306 Hz, △ 510 Hz, * 816 Hz, □ 1020 Hz, and + 1326 Hz for two liner configurations a) DC007 and b) DC008.

higher velocities the dissipation is mainly reduced, except at the low frequency end (< 500 Hz), where it is slightly improved.

The influence of the bias flow on the dissipation becomes even more clear in Figure 7.7. Here, the dissipation coefficient is plotted over the bias flow Mach number for some selected frequencies. The dissipation increases for all frequencies when introducing a bias flow. A maximum is reached at rather small Mach numbers (0.02-0.05) and the curves converge towards a common dissipation value for high velocities. An interesting feature can be observed for configuration DC007. At high frequencies (1020 Hz and 1326 Hz) the level of dissipation is constant for very low bias flow Mach numbers and then quickly rises to its maximum value at a certain Mach number setting.

The contents of the two previous figures can be combined to produce a contour plot of the dissipation depending on both frequency and bias flow Mach number. While the previous figures only displayed a selection of the available data, the contour plot is based on 416 data values (26 frequencies and 16 bias flow Mach numbers). When necessary, the data has been smoothed with an appropriate fit. The result is shown in Figure 7.8. The limits of the

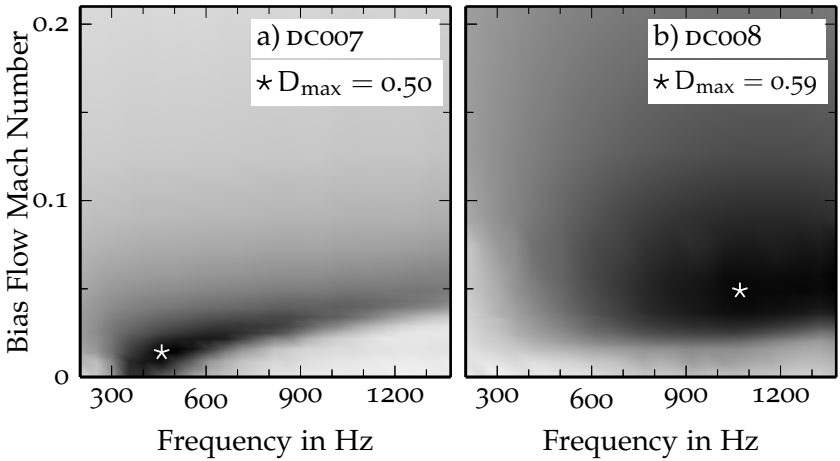

Figure 7.8: Contour plot of the average dissipation depending on frequency and bias flow Mach number for two liner configurations a) DC007 and b) DC008. The limits of the colormap are $D = 0$ (white) and $D = D_{max}$ (black). The star indicates the maximum dissipation.

black and white colormap are $D = 0$ (white) and $D = D_{max}$ (black) and distributed linearly in-between. The contour plot gives a convenient overview of the general characteristics of the two liners, where the bias flow-frequency combinations for optimum damping can easily be determined. Clearly, the two configurations have very different characteristics, as was already discussed with the previous two figures. These two examples are representative of all liner configurations that were studied within this work. Depending on their porosity they can be divided into two groups: low porosity ($\approx$ 1 %) with characteristics similar to DC007 and high porosity ($\approx$ 7 %) with characteristics similar to DC008.

Figure 7.9 enlarges a detail of Figure 7.8a. It is shown how the maximum dissipation coincides with a curve of constant Strouhal number. Obviously, the optimum combination of bias flow velocity and frequency is related via the Strouhal number. The actual value of the Strouhal number will be discussed later in Section 7.17. However, the Strouhal number dependency is that ex-

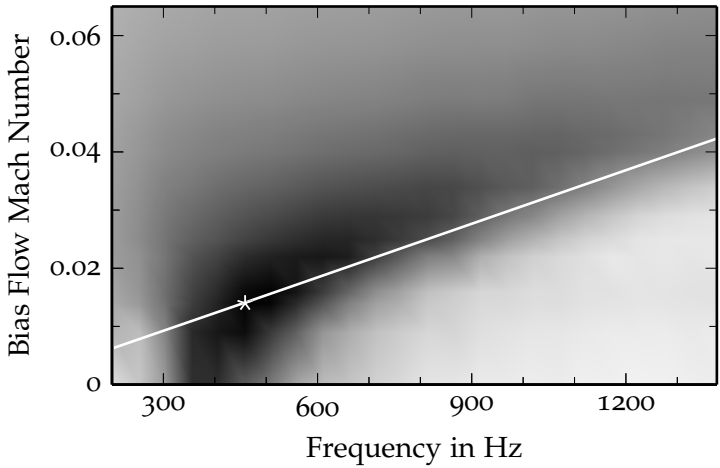

Figure 7.9: Detail of Figure 7.8a. The solid, white line represents a curve of constant Strouhal number that includes D_{max}.

plicit for configuration DC007 only and is not reproduced with configuration DC008.

Figure 7.10 compares the prediction of the models presented in Chapter 4 to the experimental results of DC007 and DC008 at various bias flow Mach numbers. The general trends of the two geometries and various bias flow Mach numbers is captured by all models. However, at intermediate bias flow Mach numbers the agreement of the models and the measurements is rather poor, i. e. in b) and d). The differences between the models are largest at the low bias flow Mach number in a). Here, EDM:Jing and TMM:Bellucci provide the best match with the experiments. At high Mach numbers, in e) and f), all models yield a similar result, which is in excellent agreement with the experimental data. Only EDM:Jing is slightly off in f).

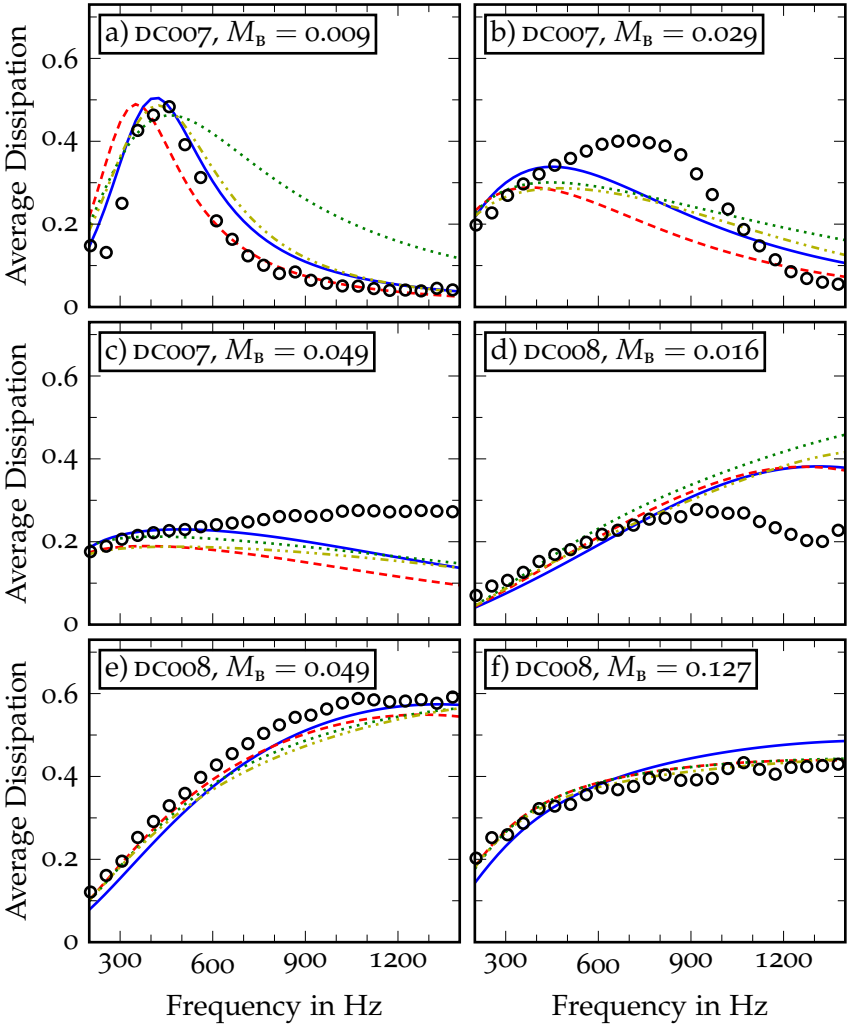

Figure 7.10: Comparison between experimental data and models for configurations DC007 and DC008 and various bias flow Mach numbers. ○ Experiment, — EDM:Jing, - - - TMM:Jing, ····· TMM:Betts, -·- TMM:Bellucci.

Discussion

The results show, that a bias flow does improve the absorption of a perforated liner compared to the same configuration without bias flow. These findings comply with the results reported in [41, 142, 161, 198, 219, 241], for example.

There exists an optimum bias flow, where the absorption is maximum. Eldredge and Dowling [142] find the optimum Mach number to be 0.015 for the liner geometry specified in Table 4.1. They derive an optimum ratio of bias flow Mach number to porosity. In order to achieve maximum absorption the liner should obey

$$\left(\frac{M_B}{\sigma}\right)_{opt} = \frac{PL/A}{2\sqrt{2}}\,. \tag{7.1}$$

Applying the equation above to configurations DC007 and DC008, where for both $PL/A = 1.46$, the optimum bias flow Mach numbers should be 0.0052 and 0.035, respectively. This is in contrast to the optimum bias flow Mach numbers revealed by the experiments: 0.016-0.049 for DC007 and 0.049 for DC008. While the results for DC008 are in the same range, the estimation for DC007 is very far off. A similar outcome was reported by Macquisten et al. [310]. They found Equation (7.1) to underestimate the optimum bias flow Mach number, especially when the number of orifice rows is low.

The two liner configurations presented here demonstrate very different characteristics. Without bias flow, configuration DC007 exhibits a typical resonance damping behavior[3]. The bias flow modifies this resonance effect until a sufficiently high bias flow velocity is reached, beyond which the bias flow effect dominates. On the other hand, no obvious resonance effect can be observed

3 At the location of the perforation, the incident wave from the duct and the reflected wave from the cavity are 180° out of phase, so that they cancel each other out.

for configuration DC008 without bias flow. Then, however, the bias flow increases the dissipation, primarily around the resonance frequency, before it leads to the typical broadband absorption. It is believed, that these two regimes correspond in some way to the high and low Strouhal number regimes observed by Scarpato et al. [430].

The resonances that are observed here are of the Helmholtz type. The resonance frequency can be estimated by (e. g. [260])

$$f_r = \frac{c}{2\pi}\sqrt{\frac{A_{open}}{Vl_{eff}}}, \tag{7.2}$$

which yields 400 Hz for DC007 and 985 Hz for DC008. This corresponds very well with the maxima observed in Figure 7.6. The dependence of the dissipation on the resonance frequency is further discussed in Section 7.11.

The models seem to provide reasonable predictions (with exceptions), when either the resonance effect or the bias flow effect dominates. The transition between both effects is not captured very well. The critical quantity during this transition seems to be the reactance, which would be responsible for shifting the resonance frequency. According to Figure 7.9, this phenomenon seems to be dependent on the Strouhal number.
It has been reported very early [319] and more recently [242, 291], for example, that the reactance drops considerably when a bias flow is introduced. This behavior can be found in the models of Jing and Bellucci, as shown in Figure 4.9. The models seem to disagree about the amount that the reactance is reduced by, as well as the Strouhal number dependency of this process. However, the development of the reactance with the Strouhal number seems to be essential to describe the behavior in the transition region.

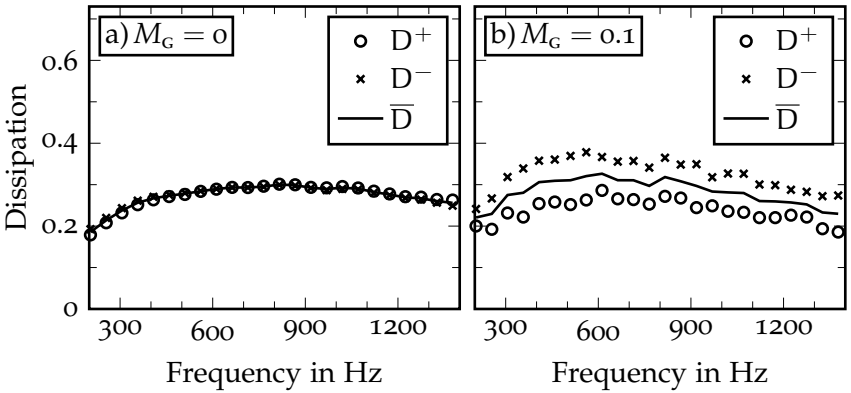

Figure 7.11: Demonstration of the influence of a grazing flow depending on the direction of sound propagation and the average dissipation for configuration DC006: a) without grazing flow, b) with grazing flow, and $M_B = 0.041$ in both plots.

7.3 GRAZING FLOW

In this section, the grazing flow is studied separately from the bias flow. However, the operation in a gas turbine combustor includes a grazing and bias flow simultaneously. This will be discussed in Section 7.4.

Results

The dissipation coefficient of a symmetric liner configuration in stationary fluid is independent of the direction of wave propagation. A grazing flow introduces an asymmetry, so that $D^+ \neq D^-$. This can be observed in Figure 7.11 by comparing two measurements of configuration DC006 with and without grazing flow. Plotted are the dissipation coefficients for sound propagating in positive and negative axial direction, D^+ and D^- respectively, and their average value $\overline{D}$. In Figure 7.11a, without grazing flow, the values are identical. Introducing a grazing flow in Figure 7.11b,

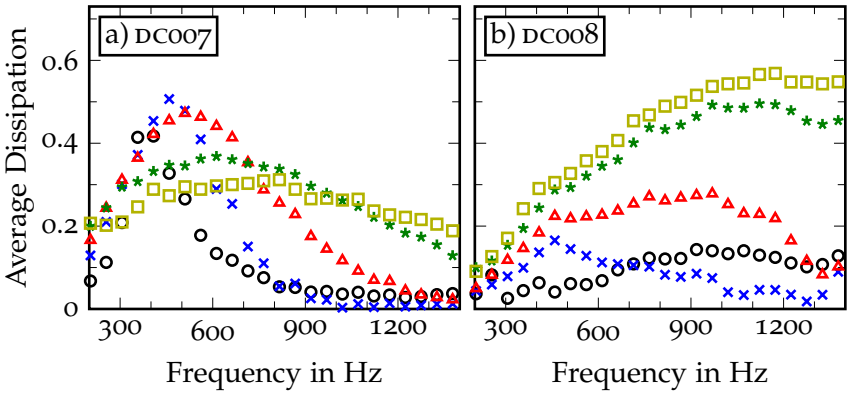

Figure 7.12: Average dissipation plotted over the frequency at various grazing flow Mach numbers ○ 0, × 0.04, △ 0.06, * 0.1, and □ 0.13 for two liner configurations a) DC007 and b) DC008 without bias flow.

the dissipation is increased for sound waves propagating against the flow and reduced when propagating in flow direction. This can be an important feature when the sound wave is mainly coming from one direction. However, for a general comparison the average dissipation coefficient is more suitable (see Section 6.4.1) and will be used here.

The influence of the grazing flow on the average dissipation is illustrated in Figure 7.12 for the two liner configurations DC007 and DC008. The average dissipation coefficient is plotted over the frequency for various grazing flow Mach numbers. Figure 7.12a displays a dissipation peak at around 400 Hz for configuration DC007 without flow. Introducing a grazing flow shifts the frequency of maximum dissipation to higher values. The peak level reaches an optimum for grazing flow Mach number of 0.04-0.06. The maximum value is reduced at higher velocities, in exchange for a more broadband absorption. Configuration DC008 Figure 7.12b experiences a general broadband increase of the dissipation with increasing grazing flow Mach number. The air supply of the DUCT-C test

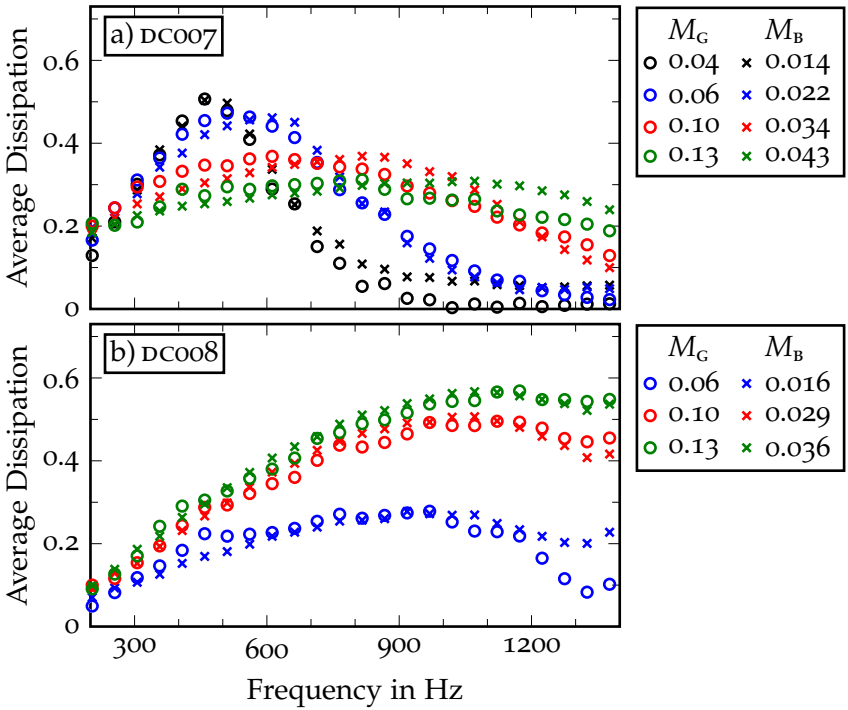

Figure 7.13: Visually matched pairs of dissipation curves comparing the effects of either grazing flow or bias flow.

rig limits the maximum grazing flow Mach number to 0.13, where maximum dissipation is achieved.

Comparing these results to Figure 7.6, where the influence of the bias flow is shown, reveals a very similar behavior of the dissipation with either grazing or bias flow. For a better comparison an attempt is made to match the curves of equal dissipation. This is done as follows: The dissipation curve for one grazing flow velocity is compared to several dissipation curves obtained by varying the bias flow velocity. The best visual match is chosen and plotted as a pair in Figure 7.13. As the curves are chosen from available data, there might exist an even better match for a bias flow velocity that has not been measured.

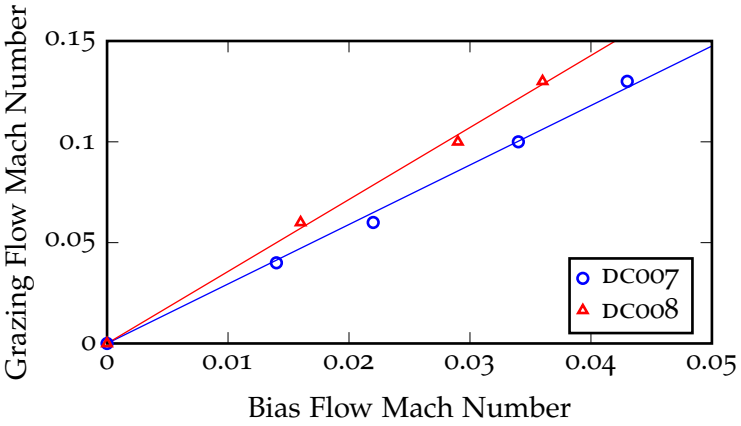

Figure 7.14: Grazing flow velocity plotted over bias flow velocity for the matching dissipation curves from Figure 7.13. The solid line is a linear fit through the measurement data and the origin.

Figure 7.13 presents the matching pairs for both liner configurations and various flow conditions. The respective grazing and bias flow Mach numbers are listed in the legend of the figure. The overall agreement is remarkable. It seems to be of no importance if the flow is passing the liner tangentially or if it is penetrating through the orifices of the liner. The effect on the dissipation seems to be the same. However, a systematic difference can be observed for configuration DC007: The frequency of maximum dissipation is slightly higher when applying a bias flow. This discrepancy cannot be fixed by finding a better matching bias flow velocity.

The legend of Figure 7.13 reveals that the grazing flow velocity needs to be significantly higher than the bias flow velocity to achieve a similar dissipation. Figure 7.14 plots the grazing flow Mach number over the bias flow Mach number of the matched pairs as they are listed in the legend of Figure 7.13. The experimental data exhibits a linear relationship between the two quantities. A linear fit, separately for configurations DC007 and DC008, yields a proportionality factor of 3 and 3.6, respectively. That means the

velocity of the grazing flow needs to be about 3.3 times higher as the bias flow velocity to achieve a similar absorption. It remains unclear if the deviation between the two configurations is a physical reality or if it is a result of the quite vague method of matching the dissipation curves, so that the proportionality factor should only be regarded as rough estimate.

Discussion

Evaluating D^+ and D^- separately reveals, that the absorption is reduced for sound traveling in grazing flow direction while it is increased by a similar amount when propagating in the opposite direction. This effect is discussed in [226, 264, 274, 321, 322, 324, 329, 349, 374, 467] and the difference between D^+ and D^- is accredited with two phenomena:

1. The velocity gradient within the flow boundary layer refracts the direction of propagation of the sound wave. While the wave normal without flow is assumed to be parallel to the wall (neglecting any acoustic boundary layer), it is refracted into the liner when propagating downstream and away from the liner when propagating upstream. This would result in an increased absorption for sound waves propagating in flow direction and a reduction against flow. This phenomenon is pronounced at higher frequencies and Tack and Lambert [467] suggest to neglect it when $k\delta \leqslant 0.1$, where δ is the thickness of the flow boundary layer.

2. The convective effect of the flow modifies the phase velocity of the wave by a factor $1 + M_G$ in flow direction and $1 - M_G$ against, increasing and reducing the wave length respectively. Thus the absorption per wave length remains constant when a grazing flow is present, while the absorption due to a liner of fixed length is reduced for waves traveling downstream and increased against flow direction [321].

Both phenomena have a converse effect on increasing and reducing the dissipation. It can be observed in Figure 7.11 that the second phenomena dominates here.

The effect of the grazing flow on the average dissipation is corresponding to the bias flow effect. In fact, similar results are achieved when $M_G \approx 3.3\, M_B$. This similarity between the influence of grazing and bias flow on the dissipation was also observed by Feder and Dean [158]. They compared the grazing flow velocity to the bias flow velocity producing the same change of resistance. Their measurements include six perforations with varying porosity (10-35 %) and two grazing flow velocities (90 and 150 m/s). The ratio of grazing to bias flow velocity is virtually independent of the porosity, but different values are obtained for the two grazing flow velocities. They arrive at ratios of approximately 8 and 5 for the low and high grazing flow velocity, respectively. Their calculation of the bias flow velocity neglects the orifice discharge coefficient. Applying a general discharge coefficient of 0.61 yields ratios of grazing to bias flow velocities of about 5 and 3, which is in good agreement with the values obtained here.
The impedance model of Bauer contains a term for the resistance due to the grazing flow and a second term for the resistance due to the bias flow (see Section 4.6). Both terms are identical, except for a factor of 3.8 between them. This corresponds very well to the experimental finding discussed above.

Judging by the similarity of the grazing flow and bias flow effects, the absorption mechanism seems to be the same, i. e. the conversion of acoustic energy into shedding vorticity. Feder and Dean suggest the following explanation of the grazing flow phenomenon [158, p. 22]: "The reason for this similarity is believed to be due to boundary layer fluctuations, induced by the grazing flow velocities, causing airflows through the specimens. The frequency of these fluctuations is believed to be low enough so that

the resulting through flows affect the acoustic characteristics of the specimens in a manner similar to steady through flows."

The results above demonstrate a throughout positive effect of the grazing flow on the acoustic performance of a perforated liner. However, it has been reported, that at certain combinations of grazing flow velocity and liner geometry, depending on the orifice Strouhal number, sound might be generated rather than absorbed (see [23, 75, 216, 321, 377], for example). This effect occurred during the measurements here for configuration DC008 at $M_G = 0.05$ and produced a dominant tone at about 1300 Hz. However, slightly changing the grazing flow velocity or introducing a bias flow suppressed the phenomena.

7.4 SIMULTANEOUS GRAZING & BIAS FLOW

The effects of grazing flow and bias flow are mostly studied separately, as was done in the two previous sections. However, when both are present simultaneously, the result might be influenced by the interaction of the two.

Results

Figure 7.15 shows dissipation curves at two bias flow velocities for varying grazing flow Mach number. In Figure 7.15a, at the low bias flow Mach number, the dissipation increases with the superposition of the grazing flow. At the faster bias flow, in Figure 7.15b, the result is unimpressed by the grazing flow.

The superposition of grazing and bias flow does not improve the dissipation beyond what can be achieved by applying either one alone. There seems to be an upper limit of dissipation which cannot be surpassed by the combination of grazing and bias flow. So, if any of the two velocities is already at an optimum (for maximum dissipation), then the other imposes only a minor or no influence on the result.

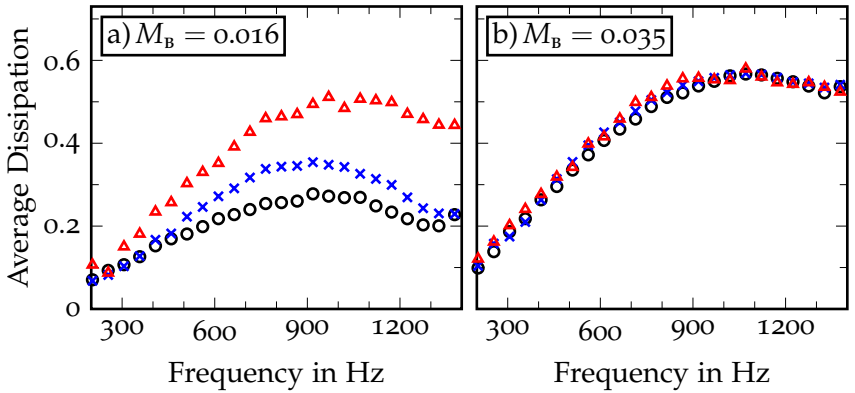

Figure 7.15: Average dissipation of configuration DC008 plotted over the frequency for varying grazing flow Mach number ○ 0, × 0.046, and △ 0.097 at two bias flow Mach numbers a) $M_B = 0.016$ and b) $M_B = 0.035$.

Discussion

The results demonstrate that the presence of a grazing flow at a bias flow liner seems to have either a beneficial effect or no effect on the absorption. At sub-optimal bias flow Mach numbers the additional grazing flow increases the dissipation, while it shows no effect when the bias flow Mach number is already optimal. Of course, higher Mach numbers ($M_G > 0.1$) might produce some adverse effects that are not observed here. However, typical combustor Mach number fall into the range studied here.

In an early experimental study Marino et al. [313][4] come to the conclusion that only the bias flow needs to be accounted for when both bias and grazing flow are present. Lewis and Garrison [300] get more specific by stating that the grazing flow has no effect

4 As mentioned in a footnote in [171, p. II-3]: "From the results of previous experiments (Reference 2) [that is [313]], it was found that, for liners subjected to simulataneous [simultaneous] flow through and past the apertures, the acoustic resistance should be computed as if only flow through were present."

when the bias flow Mach number is greater than 0.1, basing their conclusion most likely on the same experiments, i.e. [313].

Dean and Tester [118, p. 23] state, with a reference to experimental data of Rice [392], that the influence of the grazing flow can be neglected when the ratio of bias to grazing flow velocity is larger than $M_B/M_G > 0.3$. Below this limit the grazing flow dominates the resistance. Their model computes the grazing and bias flow resistance separately and then uses the large one only. It should be noted, that the given limit matches very well with the condition $M_G \approx 3.5\, M_B$ where a similar dissipation is obtained when bias or grazing flows are applied separately (see Section 7.3).

Rogers and Hersh [406] conducted a detailed study regarding the steady state resistance of a single orifice subjected to grazing flow. A bias flow simulates the acoustic flow through the orifice captured in a steady state. They define five flow regimes, representing one cycle of the acoustic oscillation: zero net flow, low outflow, high outflow, low inflow, and high inflow. They find that the grazing flow imposes a constriction to the flow through the orifice and describe this phenomena with an effective discharge coefficient based on the ratio of bias flow velocity to grazing flow velocity.

A similar approach, but applied to the acoustic resistance instead of the steady state resistance, was followed by Sun et al. [463]. They propose an effective discharge coefficient[5]

$$C_d = \frac{1}{\sqrt{c_1 + c_2/\lambda + c_3/\lambda^2}}, \tag{7.3}$$

where λ is the ratio of bias flow velocity to grazing flow velocity $\lambda = M_B/M_G$. The empirical constants for the bias-outflow case, which is considered here, are given by $c_1 = 2.1$, $c_2 = -0.332$, and $c_3 = 0.0566$. Equation (7.3) tends to $C_d = 0.69$ for high values of λ, i. e. pure bias flow. The resulting discharge coefficient is plotted

5 Please note, Eq. 8 in [463] is not correct. The correct version, corresponding to Equation (7.3), is given in Section 5 of [463].

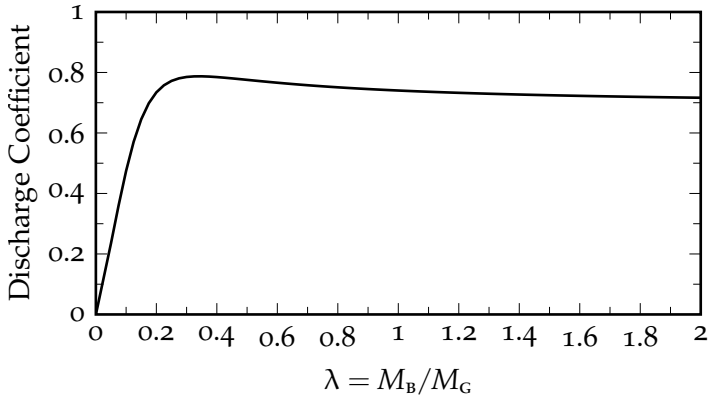

Figure 7.16: Effective discharge coefficient due to the interaction of bias and grazing flow according to Equation (7.3) [463].

in Figure 7.16. Again, the ratio of $M_B/M_G \approx 0.3$ is a characteristic value, above which the interaction between bias and grazing flow seems to be negligible.

Summarizing the suggestions of the references: The dissipation is largely independent of the grazing flow when roughly $M_B/M_G > 0.3$. The grazing flow dominates at smaller velocity ratios. This can be accounted for by applying an effective discharge coefficient to the bias flow velocity, which essentially increases the bias flow velocity. These findings generally agree with the observations made here.

7.5 POROSITY

The porosity is the combination of the two parameters orifice area and orifice spacing. However, various combinations of orifice area and orifice spacing yield the same porosity, so that the porosity is an ambiguous parameter. It is unclear, weather the porosity is sufficient to describe the acoustic characteristics of a perforation or if the orifice area and spacing are significant on their own.

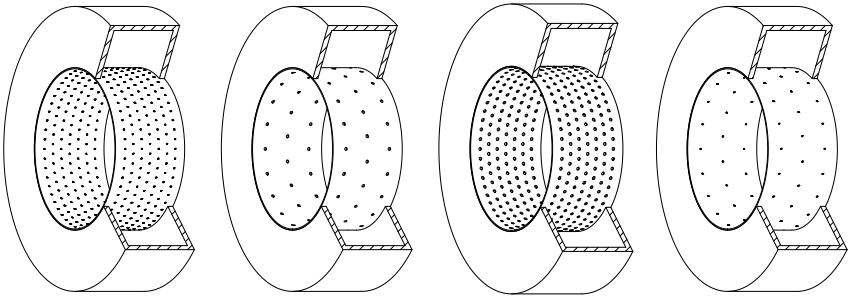

(a) DC006 (b) DC007 (c) DC008 (d) DC009

Figure 7.17: Illustration of the four configurations studied regarding the influence of porosity.

Four different liner configurations are compared. Informally they are characterized by:

1. Medium porosity by many small orifices with tight spacing,
2. medium porosity by few large orifices with loose spacing,
3. high porosity by many large orifices with tight spacing, and
4. low porosity by few small orifices with loose spacing.

The perforation parameters of these four configurations are summarized in Table 7.4, the remaining specifications are given in Table 7.1.

Table 7.4: Perforation parameters of the four configurations studied regarding the influence of porosity.

Configuration		DC006	DC007	DC008	DC009
Porosity	%	1.1	1.0	6.8	0.2
Orifice Number	–	364	60	364	60
Orifice Diameter	mm	1	2.5	2.5	1
Orifice Spacing	mm	8.5	22	8.5	22

Results

Figure 7.18 compares the four configurations at various bias flow Mach numbers. Without flow and at low Mach numbers the results of the four configurations are very different. With increasing bias flow Mach number, the curves of equal porosity align more and more, so that they become identical for $M_B \geqslant 0.049$. This is remarkable, as apart from the porosity the geometric specifications are quite different. The porosity is clearly the significant parameter at higher bias flow Mach numbers, overruling the orifice area, the orifice spacing, and the number of orifices.

At the same time it becomes obvious, that higher porosities yield an increased absorption. Again, this trend is only revealed at higher bias flow Mach numbers.

Figure 7.19 reproduces Figure 7.18d and includes the model predictions for all four porosities. While the details of each model vanish in the multitude of lines, it can be observed at a glance that all models capture the general influence of the porosity successfully.

Matching the porosity of two liners yields nearly identical results in the experiments. The models, however, show a greater variation when comparing DC006 and DC007. In order to allow a more detailed comparison, these two configurations are plotted separately in Figure 7.20. For convenience, the differences between the two configurations are indicated by filling the area between the respective curves with the associated color. It is obvious that the models do not depend on the porosity alone, but that the orifice diameter, the orifice spacing, or the number of orifices has an impact on the prediction. This is in contrast to the experimental results. However, the general agreement between the experiment and the models of these particular configurations is satisfactory at best. Especially, the broadband nature of the damping is not captured correctly.

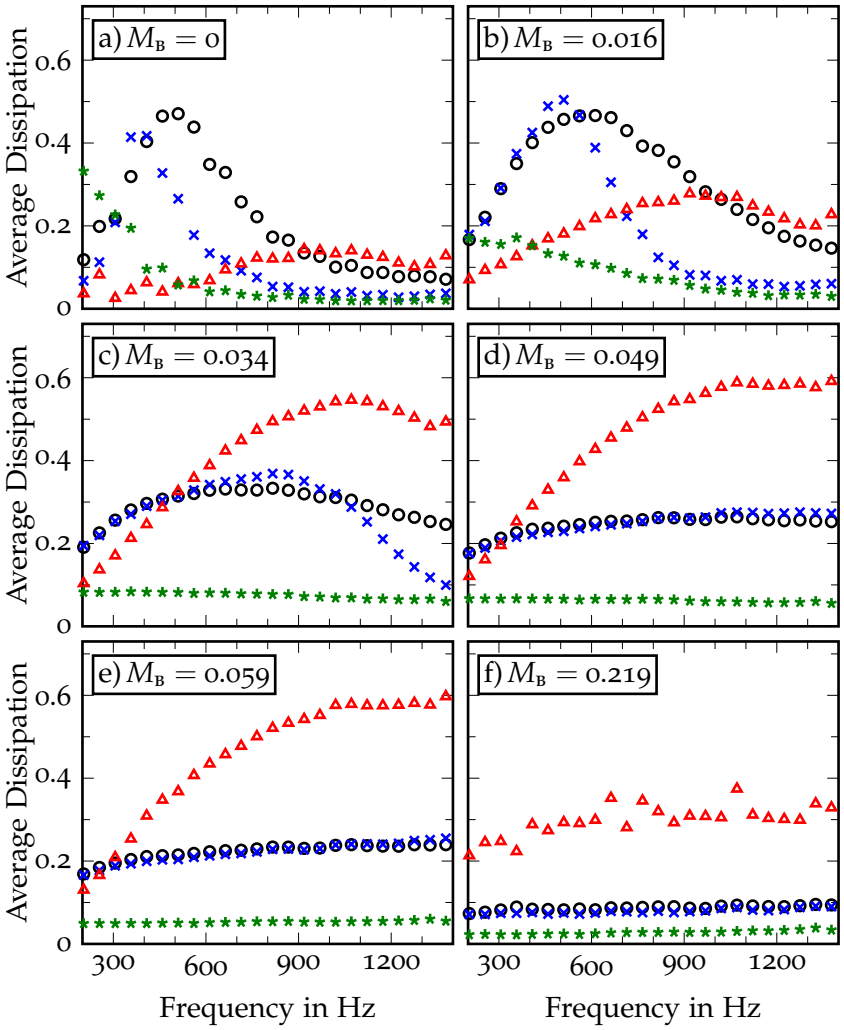

Figure 7.18: Average dissipation plotted over the frequency comparing four liner configurations with different porosities ○ 1.1 %, × 1.0 %, △ 6.8 %, and * 0.2 % at various bias flow Mach numbers.

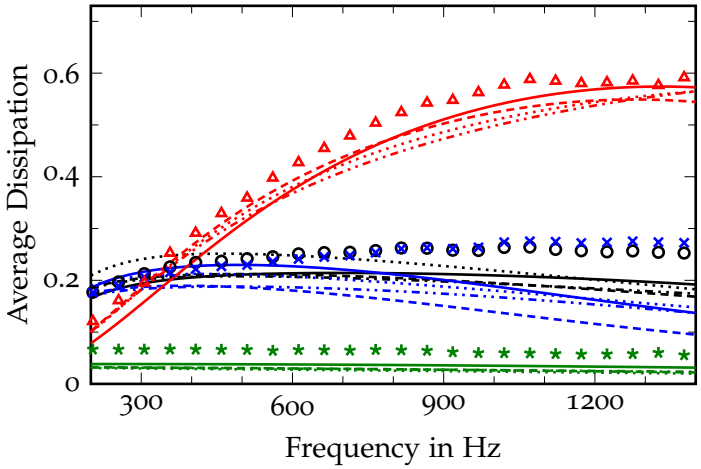

Figure 7.19: Comparison between experimental results and model predictions at $M_B = 0.049$, corresponding to Figure 7.18d. Experiment: ○ DC006; × DC007; △ DC008; ★ DC009. Models: —— EDM:Jing; - - - - TMM:Jing; ····· TMM:Betts; -·-·- TMM:Bellucci.

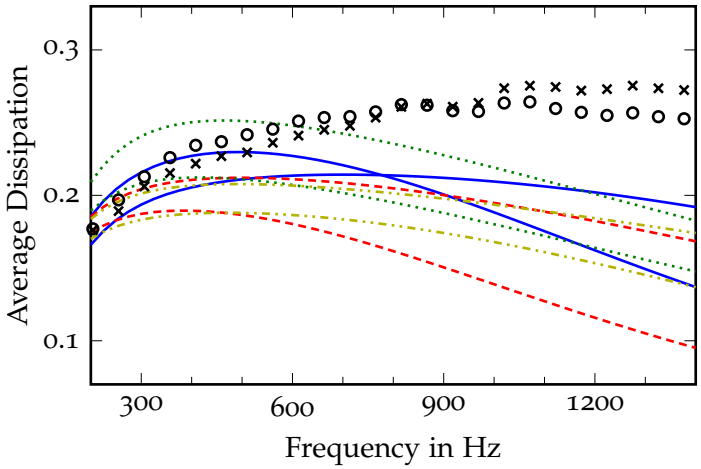

Figure 7.20: Detail of Figure 7.19, enlarging the predictions for the two configurations of similar porosity. Experiment: ○ DC006; × DC007. Models: —— EDM:Jing; - - - - TMM:Jing; ····· TMM:Betts; -·-·- TMM:Bellucci.

Discussion

It is common practice to model a single orifice only. The single orifice model is then applied to a perforation by constructing a smooth boundary condition. When dealing with impedance this is usually done by dividing the single orifice impedance by the porosity [241, 327]. In terms of conductivity that is equivalent to an effective compliance [46, 142, 219, 297, 298]. This simplification seems to give reasonable results.

It is assumed that the orifices are sufficiently far apart so that there is no interaction between them and that the wave length is large in comparison to the orifice spacing. The latter condition is commonly given by $s \ll \lambda$, but recently Bendali et al. [46] showed, that $s < \lambda/2$ would be sufficient. This requirement is typically met for the porosities and frequencies relevant in combustion chambers.

The first assumption, however, might become invalid for some realistic geometries. The usual restriction demands that the orifice diameter is much smaller than the orifice spacing, i. e. $d \ll s$. This is a rather vague limit. Melling [327] gives $\sqrt{\sigma} < 0.2$, which translates to $\sigma < 4\,\%$, as a limit where orifice interaction can be neglected. Melling [327] discusses the interaction effect: The attached masses of adjacent orifice are combined, so that the effective attached mass is reduced. A similar effect can be pictured for the resistance, which is reduced due to the loss of shear region when the oscillation through both orifices are in phase. The impedance models of Betts and Bellucci include a correction term for the interaction, but it only considers the effect on the reactance. Furthermore, the existing treatment of the interaction does not consider any bias flow, where other interaction effects than the ones considered by Melling might occur.

The porosity of DC008 is 6.8 %, so that interaction might occur. Indeed, it seems that the models which take the interaction into account, i. e. Betts and Bellucci, predict a slightly higher frequency of

maximum dissipation compared to the Jing model (cf. Figure 7.19). However, this does not improve the agreement with the experimental data. The interaction of the bias flow jets might be less important or might have a different effect on the absorption. For a further clarification, measurements with higher porosities would be required. However, typical porosities of combustor liners are rather at the lower end of the porosities encountered here, so that the interaction effect should be of minor importance.

When the absorption effect is dominated by the bias flow, the level of dissipation seems to be in some way proportional to the porosity. However, one should keep in mind, that increasing the porosity requires a higher mass flow rate, when keeping the bias flow velocity constant.

7.6 WALL THICKNESS

The influence of the wall thickness is studied by comparing configurations DC006 and DC010, where the walls are 1 mm and 3 mm thick, respectively. The full specifications are available in Table 7.1.

Results

The comparison is presented in Figure 7.21. Without any bias flow, in Figure 7.21a, the most significant difference is that the frequency of maximum absorption is shifted to lower frequencies when the liner is thicker. The peak dissipation is nearly identical for both thicknesses, but the 1 mm configuration is slightly superior at higher frequencies. This broadband advantage of the thin liner (DC006) increases at low and medium bias flow velocities. The frequency of peak dissipation is moving slightly to higher frequencies when the bias flow is increased. The frequency shift is somewhat larger for the thinner configuration. At high bias flow velocities in Figure 7.21d the results have nearly converged and an appreciable difference is observed towards high frequencies only.

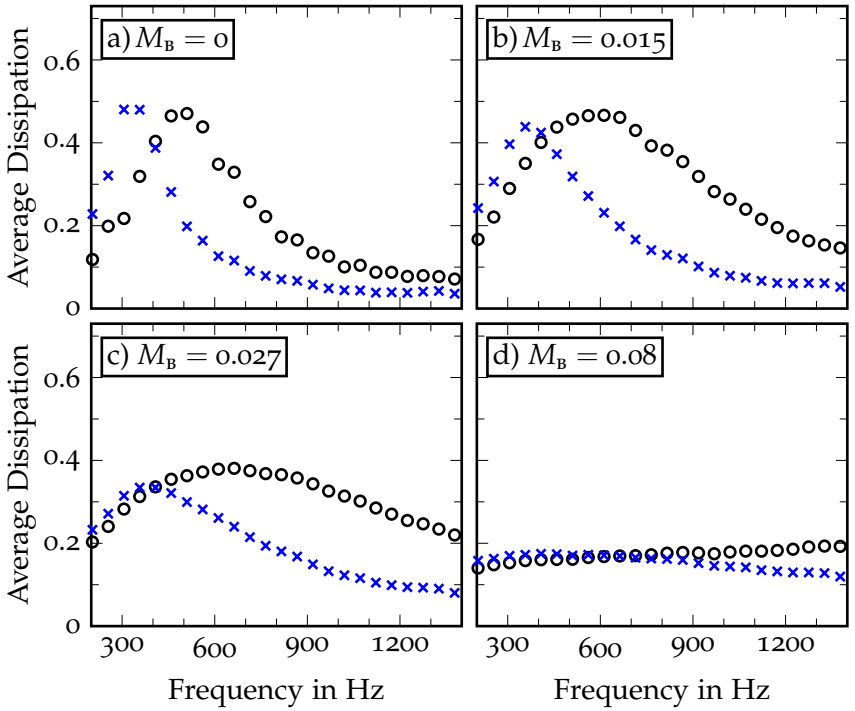

Figure 7.21: Average dissipation plotted over the frequency comparing two liner configurations with different wall thickness ○ 1 mm (DC006) and × 3 mm (DC010) at various bias flow Mach numbers.

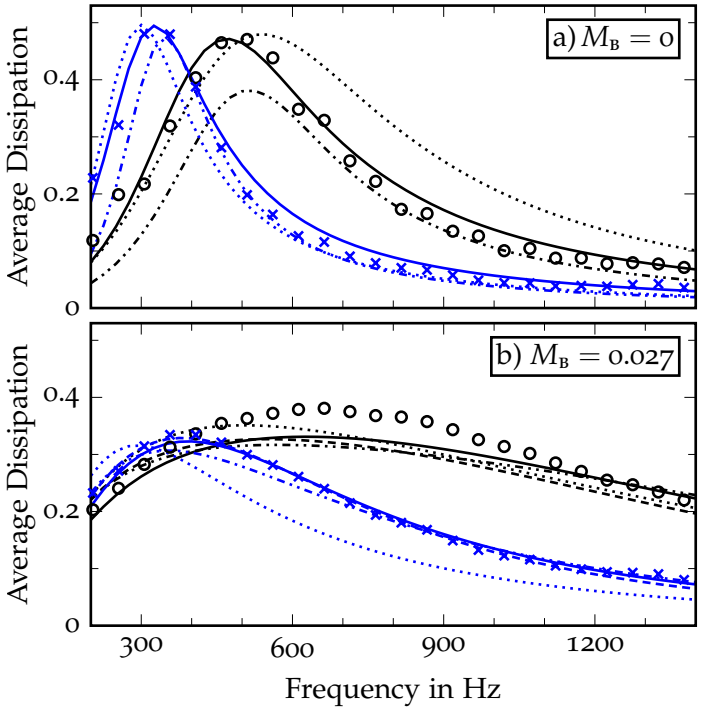

Figure 7.22: Average dissipation plotted over the frequency comparing two liner configurations with different wall thickness at various bias flow Mach numbers. Experiment: ○ DC006; × DC010. Models: —— a) TMM:Melling/b) EDM:Jing; - - - - TMM:Jing; ····· TMM:Betts; -·-·- TMM:Bellucci.

Without bias flow in Figure 7.22a the best agreement with experimental data is achieved by TMM:Melling. The other models, TMM:Betts and TMM:Bellucci, reproduce the general trend when changing the thickness, but exhibit less optimal agreement with the measurements. However, the agreement is better for DC010. The predictions follow the trend also at $M_B = 0.027$. Again, the agreement is better for the thicker configuration, while all models underpredict the dissipation for DC006.

Discussion

The wall thickness is a prominent parameter in any of the orifice models presented in Chapter 4. Without flow, the thickness effect is well understood. A longer orifice increases the mass inertance and the viscous losses. The main effects on the dissipation are the decrease of the peak frequency and the increase of the Q factor, cf. [41, 241]. Both effects are reproduced in the experimental data presented here and predicted rather accurately by TMM:Melling. Both, TMM:Betts and TMM:Bellucci, yield a better agreement with the experiments for the 3 mm wall thickness. Both models use an approximation of Equation (4.12), which seems to be suited better at this larger thickness.

When a bias flow is present the absorption characteristics of the thin wall are clearly superior with a higher peak absorption and covering a wider frequency range. This is in agreement with the experimental results of Jing and Sun [241] and Bellucci et al. [41].

7.7 ORIFICE CROSS-SECTION SHAPE

The standard orifices in this study have a circular cross-section. Now, the dissipation characteristics of a circular orifice is compared to a cross-shaped orifice with equal open area. The geometry of the cross-shaped orifice is illustrated in Figure 2.5G with the dimensions $l_1 = 1$ mm and $l_2 = 1$ mm. The characteristic spec-

Table 7.5: Orifice cross-section geometry parameters.

Configuration		DC007	DC011
Cross-Section Shape	–	circle	cross
Orifice Open Area	mm^2	4.9	5.0
Orifice Perimeter	mm	7.9	12.0
Hydraulic Diameter	mm	2.5	1.7
Jet Contraction Coefficient	–	0.65	0.69

ifications of these two configurations are given in Table 7.5. As already mentioned, the open area is kept constant for both configurations. This results in an increased perimeter length for the cross-shaped orifice and thus a reduced hydraulic diameter. The given jet contraction coefficient is the mean value taken from the measurements of various bias flow velocities.

Results

The comparison of the two cross-section geometries is presented in Figure 7.23 for four different bias flow Mach numbers. The results from these two fundamentally different geometries agree very well. Only a slight shift of the frequency of maximum dissipation can be observed at $M_B = 0.028$. It can be concluded that the actual cross-section geometry and a varying orifice perimeter is rather unimportant to the dissipation. This is found for configurations with and without bias flow.

Discussion

In the literature the influence of the cross-section shape on the acoustic properties of an orifice has only been studied for a stationary medium or including a grazing flow. The previous work is quickly reviewed here.

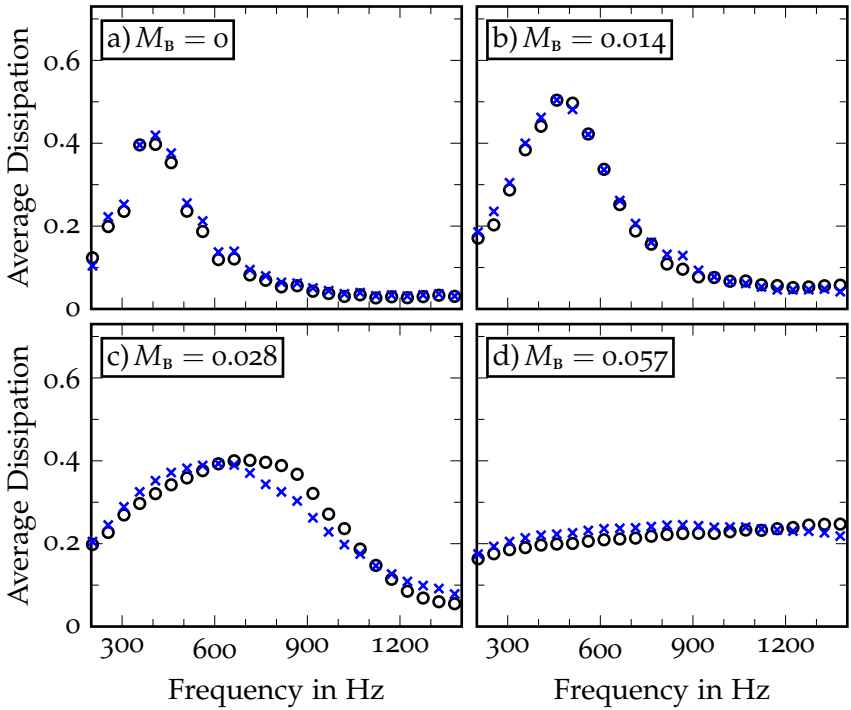

Figure 7.23: Average dissipation plotted over the frequency comparing two liner configurations with different orifice cross-section geometries ○ circular (DC007) and × cross (DC011) at various bias flow Mach numbers.

Rayleigh [385, 390] compares the theoretical conductivity of a circular orifice to that of elliptic orifices with various elongations. He states without formal proof, that the circular orifice is the shape which has a minimum conductivity. However, he finds that a moderate eccentricity of an ellipse of equal area results only in small change of the conductivity. He concludes, that the conductivity can be calculated from the area alone, so that $K_R A \approx \text{const.}$.

Ingard [225] compares the end-correction of circular and rectangular orifices. Based on his measurements he argues that the end-

correction scales with the orifice area only, confirming Rayleigh's theoretical assumption.

Morfey [336] reviews the work concerned with the influence of orifice shape on the sound transmission, which includes circular, elliptic, and rectangular cross-sections. In conclusion, he estimates the conductivity of an orifice of arbitrary shape in terms of perimeter P and area A with

$$K_R = \frac{\pi}{2} \frac{P}{\ln(P^2/A)} . \tag{7.4}$$

For a circular orifice Equation (7.4) yields $K_R \approx 3.9r$, which agrees with Rayleigh's result[6] $K_R = 4\sqrt{A/\pi} = 4r$. However, according to Morfey Equation (7.4) gives more appropriate results for very long, narrow openings, where the longest dimension remains small in comparison with the wavelength. Inserting the dimensions of the circular and cross-shaped orifices from Table 7.5 yields a slightly different conductivity of 4.85 mm and 5.61 mm, respectively. Instead, using the hydraulic diameter to calculate the conductivity of the cross-shaped orifice yields $K_R = 4.54$ mm, which matches slightly better to the circular geometry.

Chanaud [89] presents a theoretical study on geometry effects on the resonance frequency of Helmholtz resonators. Amongst other things, he studies the influence of the orifice cross-section geometry. He treats a circular, square, rectangular, and three different cross-shaped orifices, all of which have equal area. His results suggest that the orifice cross-section shape is not highly significant.

Grace et al. [181] numerically calculates the Rayleigh conductivity for a variety of orifice shapes for both one-sided and two-sided grazing flows. The cross-section geometries includes a circle, square, various triangles, and a crown[7] with equal maximum

6 Morfey treats only one side of the orifice, so this equals twice the value obtained by Rayleigh for both sides.

7 The crown is an orifice with square cross-section and triangular serrated leading or trailing edge, see Figure 2.5i.

dimension in streamwise direction. Accounting for the different open areas of the orifices, the conductivities are normalized with respect to $\sqrt{A}$. The results are found not to vary significantly with the orifice shape, where the triangular shapes produced the largest differences compared to a circular orifice.

Ahuja and Gaeta [7, 169] performed an experimental study on the effect of the orifice shape on its acoustic impedance. The cross-section geometries of the orifices are circular, square, triangular, star-shaped, and eye-shaped[8] with equivalent area. The length of the perimeter is more than doubled between the circular and star-shaped orifice. Measurements were done at low and high sound pressure levels. They find that at low incident sound amplitudes the resistance increases with the perimeter, so that orifices with shapes that are significantly different from circular yield a higher absorption. However, at higher amplitudes the resistance appears to be independent of the orifice shape. They specify an orifice velocity of 0.5 m/s as limiting value where the transition occurs.

Based on the literature, the orifice cross-section shape seems to have a minor effect on the acoustic properties in stationary medium or with grazing flow. The findings of Ahuja and Gaeta [7, 169] at high amplitudes suggest that any effect vanishes when there is a bias flow present. This is confirmed by the experimental results here. As a consequence it seems to be sufficient to match the orifice area when dealing with different cross-section geometries.

Rayleigh [385, 390] and Morfey [336] expect a more substantial change of the conductivity for a long narrow slit when compared to a circular orifice. However, no data is available that provides such a comparison.

8 This is achieved by sliding a perforation consisting of circular orifices over another identical perforation, see Figure 2.5J. Ahuja and Gaeta [7, 169] refer to this shape as stepped-oval geometry.

Table 7.6: Flow parameters of the measurements with varying orifice edge geometry, corresponding to Figure 7.24.

	DC007 (square edge)			DC012 (round edge)		
M_B^{nom}	M_B	$\dot{m}_B$	C_d	M_B	$\dot{m}_B$	C_d
–	–	kg/h	–	–	kg/h	–
0.000	0.000	0.0	–	0.000	0.0	–
0.022	0.022	6.1	0.68	0.022	7.6	0.82
0.033	0.034	9.1	0.64	0.033	11.7	0.87
0.044	0.043	11.7	0.67	0.044	15.6	0.86

7.8 ORIFICE EDGE GEOMETRY

This section presents a comparison between orifices with square edges (DC007) and round edges (DC012) as was illustrated in Figure 2.6. All remaining geometry parameters are kept constant and are listed in Table 7.1. As discussed in Section 2.5.2, the behavior of the flow through the orifice is very sensitive to the edge geometry. The flow parameters for the two geometries and four bias flow settings presented here are given in Table 7.6. The discharge coefficient C_d is closer to unity for the round geometry. Thus, keeping the bias flow Mach number constant, the mass flow needs to be increased for the rounded geometry.

Results

The comparison of both geometries is presented in Figure 7.24. Without any bias flow, in Figure 7.24a, the square edge is superior to the round edge. When a bias flow is present this finding is reversed and the dissipation of the round edge configuration is slightly better than that of the square edge. However, please keep in mind that a higher mass flow rate needs to be applied for the

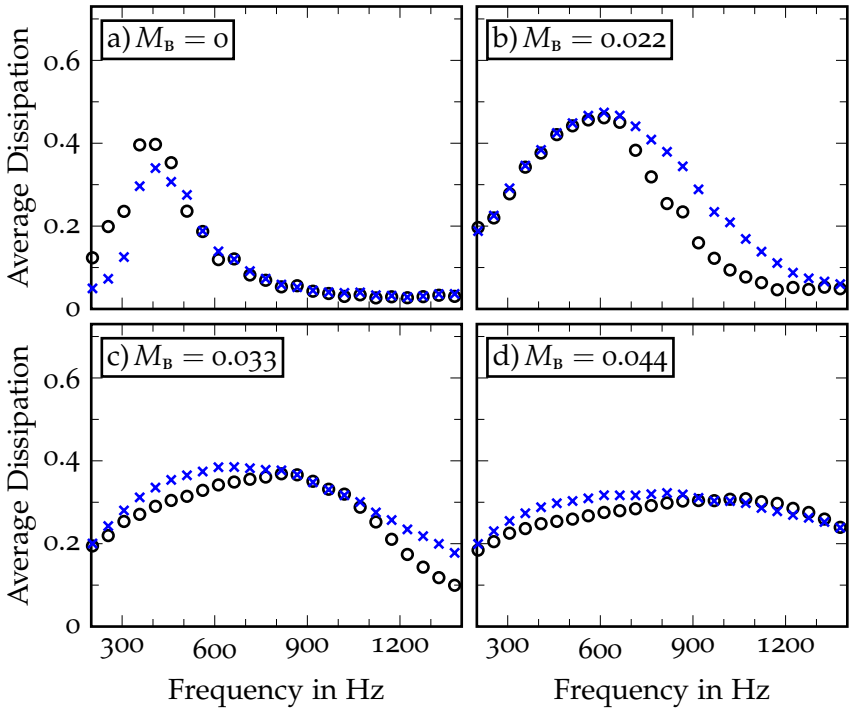

Figure 7.24: Average dissipation plotted over the frequency comparing two liner configurations with different orifice edge geometries ○ square edge (DC007) and × round edge (DC012) at various bias flow Mach numbers.

round edge configuration, which adversely affects the efficiency of the liner.

The improvements of the round edge over the square edge become more explicit when a grazing flow is present. This is demonstrated in Figure 7.25 for $M_G = 0.1$ with and without bias flow.

Discussion

The results show only minor effect of the orifice edge geometry on the dissipation. The length of the orifice is effectively reduced by

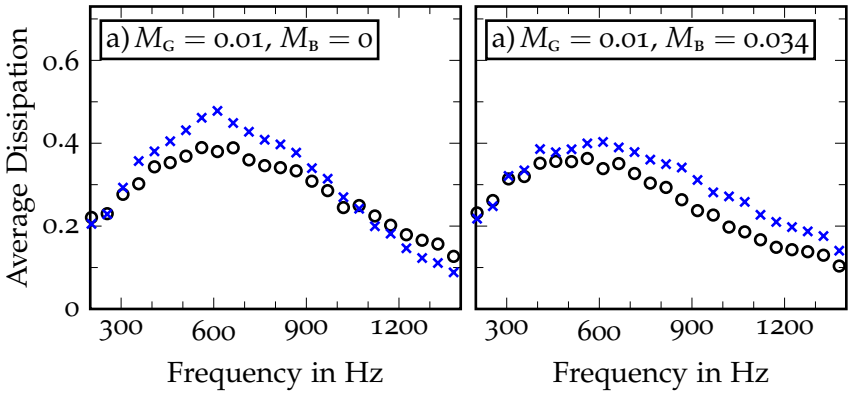

Figure 7.25: Comparison of the square-edge orifice and the round orifice at $M_G = 0.1$ without bias flow: ○ square edge (DC007) and × round edge (DC012).

rounding both edges, so that the lower absorption without flow could be attributed to reduced viscous losses within the orifice. Additionally, the smaller frequency of maximum dissipation in Figure 7.24c and d, could be a result of an increased mass reactance due to the enlarged open area at the surface.

Keller and Zauner [258] observed an increase of absorption by 55 % when rounding both edges of a Helmholtz resonator neck compared to having square edges. The neck had a length of 100 mm, a diameter of 9 mm, and the edge describes an arc of 15 mm radius over an angle of 40° (see Figure 7.6 in [258]). The improved absorption was obtained without flow as well as with a bias flow of 4 m/s. Similarly, Laudien et al. [284] improved the absorption of Helmholtz resonators and quarter-wave resonators by rounding off the edges. However, no geometric specifications of the setup is given.

These large improvements by round edges that are reported in the literature are in contrast to the findings here: While round edges are found to be superior to square edges when either bias or grazing flow is present, the improvements are rather minimal.

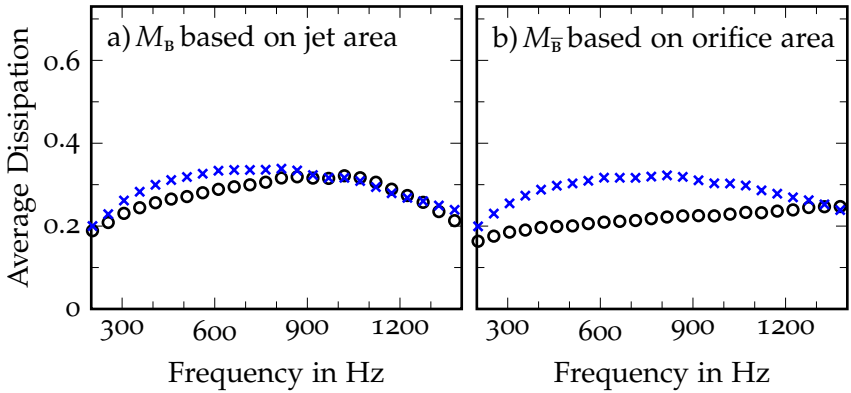

Figure 7.26: Comparison of the square-edge orifice and the rounded orifice at $M_B \approx 0.039$: a) M_B based on jet area, b) $M_{\overline{B}}$ based on orifice area.

These deviation is most probably the results of a different definition of the bias flow velocity. Keller and Zauner [258] use the orifice mean velocity and keep it constant for either square or round edge. The bias flow velocity here is based on the velocity of the contracted jet.

In order to determine which definition should be used when comparing bias flow liners, the dissipation curves for two configurations with substantially different contraction coefficients are compared. This is demonstrated in Figure 7.26. The contraction coefficients for the square-edge orifice and the rounded orifice are approximately 0.65 and 0.85, respectively. Figure 7.26a compares both configurations by matching the velocity based on the jet area, that is taking the jet contraction into account. The velocity in Figure 7.26b is based on the orifice area. The respective Mach numbers are listed in Table 7.7. The dissipation curves in Figure 7.26a are in a much better agreement than in Figure 7.26b. Similar results are found at other bias flow velocities and with other configurations, cf. Figure 7.24 or 7.18. It can be concluded that the jet velocity which includes the jet contraction is the relevant param-

Table 7.7: Flow parameters for the comparison of jet velocity and mean orifice velocity, corresponding to Figure 7.26.

	Figure 7.26a			Figure 7.26b		
	M_B	$M_{\overline{B}}$	C_d	M_B	$M_{\overline{B}}$	C_d
DC007 (o)	0.040	0.026	0.65	0.058	0.038	0.65
DC012 (×)	0.040	0.034	0.85	0.044	0.038	0.85

eter for the dissipation. This definition has been applied to the experimental data throughout this work.

A similar comparison is not provided in the literature. However, the significance of the jet velocity is supported by Ronneberger [412, Figs. 4.18 & 4.19], who finds a much better agreement of experimental data with his vorticity wave theory when using the jet velocity instead of the orifice velocity.

All models that are used here take the orifice mean velocity as an input parameter. The jet contraction is then considered in various ways. In Bauer's model a constant discharge coefficient of 0.61 is 'baked' into the expression for the bias flow. Bett's model includes the discharge coefficient as a variable parameter. The bias flow contribution in the models of Bellucci and Jing is based on Howe's model, which considers the orifice mean velocity as relevant quantity.

The bias flow through a combustor liner is controlled via the pressure difference across the liner. In that case, the jet velocity is independent of the jet contraction and depends only on the pressure difference, cf. Equation (2.10). As a consequence, the dissipation remains constant when changing the orifice edge geometry from square to round at the same pressure difference. However, the mass flow rate that is discharged through the orifice will be increased.

Table 7.8: Geometry parameters regarding the orifice angle.

Configuration		HC006	HC007	HC008
Orifice Angle	deg	90	60	30
Wall Thickness	mm	2	2	2
Orifice Length	mm	2	2.3	4

7.9 ORIFICE ANGLE

Inclining the orifices from their 90° angle results in an asymmetric behavior, so that the amount of dissipated acoustic energy depends on the direction of sound propagation relative to the inclination angle. Here, the orifices are inclined in positive x-direction, so that while reducing the inclination angle the direction of the bias flow injection aligns more and more with the grazing flow. Keeping the wall thickness constant increases the orifice length for angles other than 90°, as specified in Equation (2.1). These geometric features are listed in Table 7.8.

Results

The influence of the inclination angle on the directional performance of the liner is shown in Figure 7.27. The dissipation curves for sound propagating in positive and negative direction are compared for liners of different inclination angles. The curves for the 90° angle (no inclination) are identical, as is expected for a symmetric configuration without grazing flow. Decreasing the inclination angle increases the dissipation of sound propagating in positive x-direction, while it decreases the dissipation of sound propagating in the opposite direction. It was shown before (see Figure 7.11) that a grazing flow has the opposite effect. Looking at inclined orifices in a grazing flow environment (the right column in Figure 7.27) reveals that both effects counteract each other

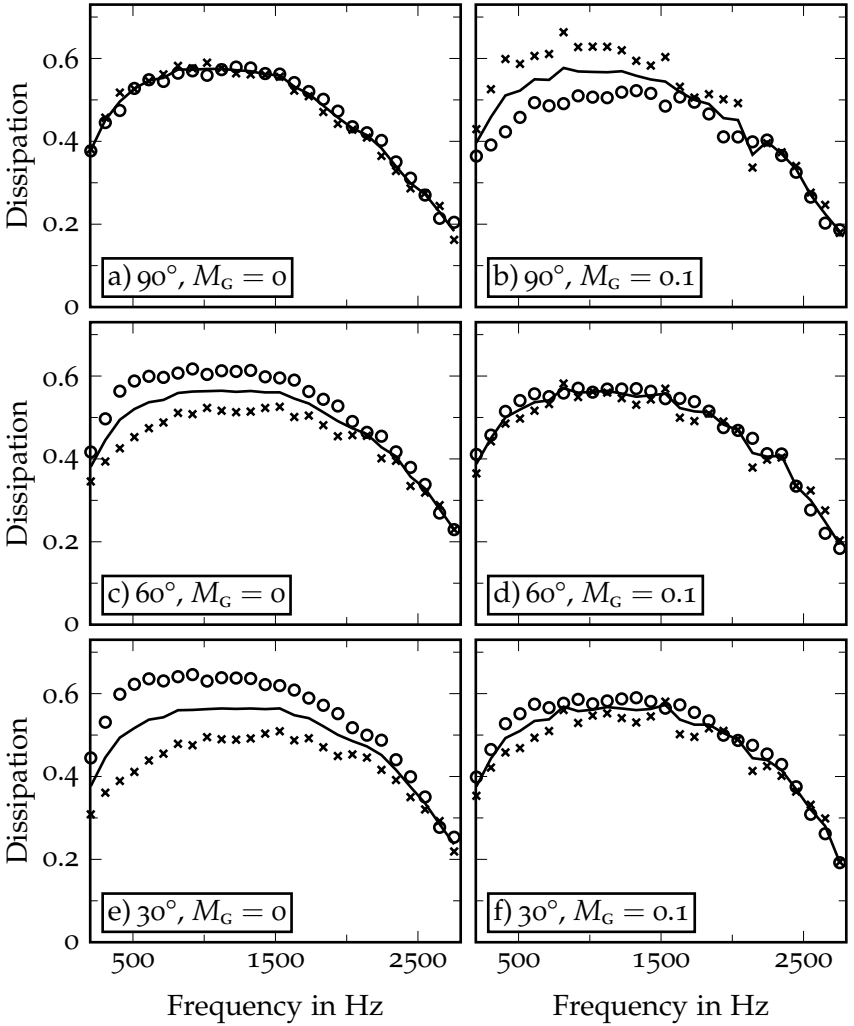

Figure 7.27: Influence of the orifice angle (top row: 90°, middle row: 60°, bottom row: 30°) on the dissipation at two grazing flow velocities (left column: $M_G = 0$, right column: $M_G = 0.1$) with a constant bias flow Mach number of 0.087. Legend: o D^+, × D^-, — $\overline{D}$

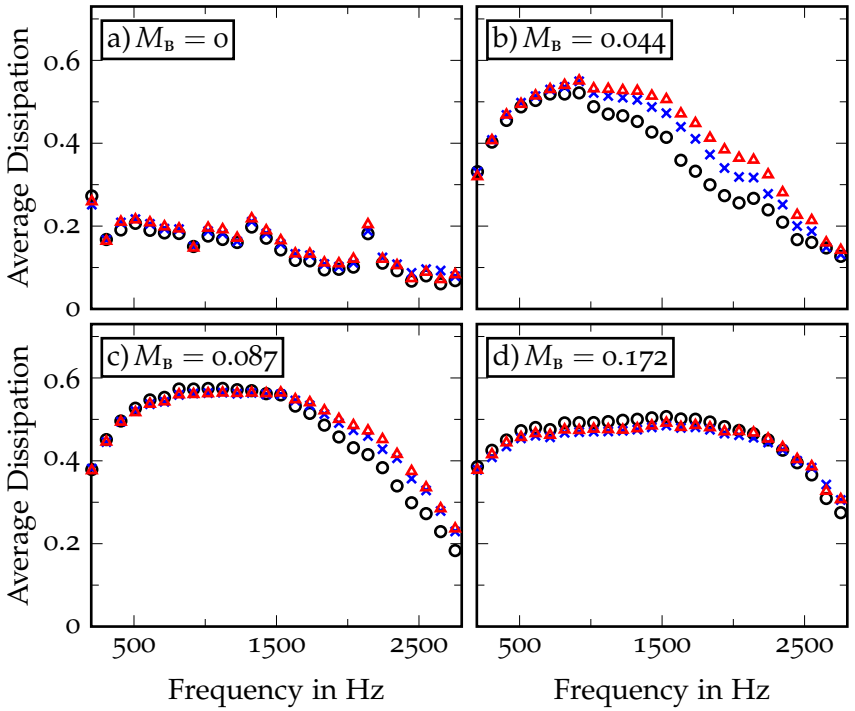

Figure 7.28: Average dissipation plotted over the frequency comparing three liner configurations with different orifice angles ○ 90°, × 60°, △ 30° at various bias flow Mach numbers.

and cancel each other out when the angle and the grazing flow is chosen properly (here around 60° and $M_G = 0.1$).

From a design point of view, the orifice angle can be used to improve the damping in positive x-direction, when the dissipation in the other direction is of minor importance, for example in an exhaust duct. For a combustor the overall damping performance, that is considering both directions of wave propagation, is essential. The overall performance is represented by the average dissipation, see Section 6.4.1. The average dissipation is already included in Figure 7.27, but the three configurations with varying angle are finally compared in Figure 7.28.

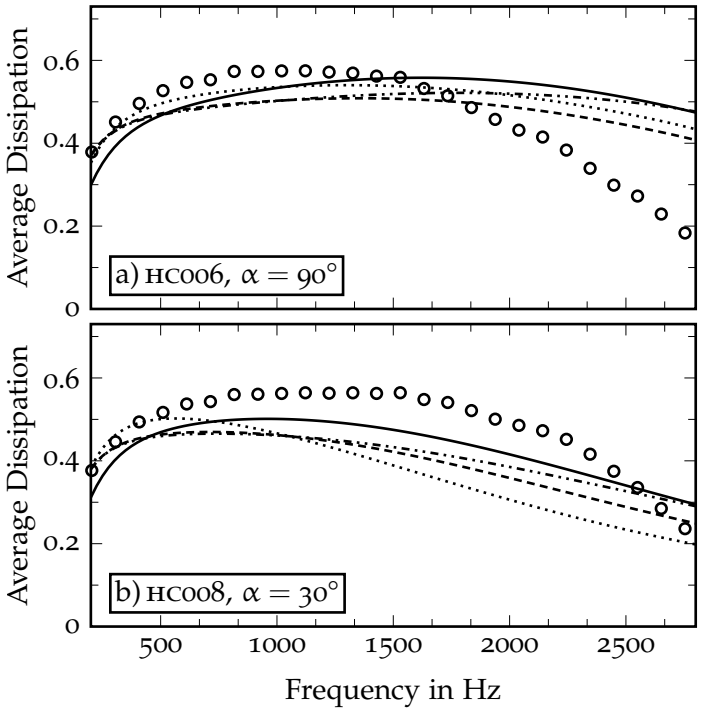

Figure 7.29: Comparison of the experimental data and the model prediction for two inclination angles at $M_B = 0.087$: a) HC006, $\alpha = 90°$; b) HC008, $\alpha = 30°$. o Experiment, —— EDM:Jing, - - - - TMM:Jing, ····· TMM:Betts, -·-·- TMM:Bellucci.

The liners are designed for bias flow operation. As shown in Figure 7.28a, their performance without bias flow is rather poor. Also, the orifice angle seems to be of no importance when looking at the average dissipation or D^+ and D^- separately (not shown here). At medium bias flow velocities, Figure 7.28b and 7.28c, smaller angles achieve a slightly better broadband dissipation. At high bias flow velocities, Figure 7.28d, there is hardly any influence of the inclination angle.

Figure 7.29 plots the model predictions for HC006 with 90° inclination angles and HC008 with 30°. The inclination angle is in-

cluded in the models by simply using the orifice length (Equation (2.1)) instead of the wall thickness. The behavior of the models is rather similar. As the angle is included by adjusting the orifice length, the predicted effect is equivalent to increasing the wall thickness and keeping the angle constant, cf. Section 7.6. The result is a reduction of the broadband absorption with increasing orifice length/decreasing angle. However, the experimental results show the opposite effect. Unfortunately, the agreement between models and experiment is poor at frequencies $> 1500\,\mathrm{Hz}$, already for the standard 90° configuration. Thus, a detailed interpretation of the model results is difficult.

Discussion

Eldredge and Dowling [142] include the inclination angle in their analysis by simply using the orifice length, instead of the wall thickness (cf. Figure 2.7b). The same approach was used by Eldredge et al. [141] and compared to data obtained from a large-eddy simulation of an inclined bias flow orifice. They found that the agreement can be further improved by considering that the actual openings of the orifice are elliptical and not circular when it is inclined, i. e. the area is slightly larger. This is taken into account by an empirical correction factor of 0.75, so that the corrected orifice length for an inclined orifice is given by

$$l = 0.75\, t / \sin\, \alpha \tag{7.5}$$

Andreini et al. [17] report that any effect of the inclination angle disappears with increasing bias flow, while the 90° orientation is slightly superior at low bias flow velocities. However, their measurements include a grazing flow which might counteract on the effect of the inclination angle as shown in Figure 7.27. They are comparing the results to EDM:Jing and yield good agreement[9].

9 Eq. (6) of [17] only includes the wall thickness and not the orifice length. However, this must be a spelling mistake as the predictions for the two con-

Here, the largest effect is found to be at higher frequencies. The data of Andreini et al. [17] is limited to frequencies below 1500 Hz.

Laurens et al. [285] present a mathematical treatment of the Rayleigh conductivity for inclined orifices in the absence of flow. They show that the effect of the orifice angle is not entirely captured by the intuitive extension of the length, as described by Equation (2.1) and applied previously [17, 141, 142, 328], but that the increased area of the elliptical openings needs to be considered as well[10]. Laurens et al. [285] derive upper and lower bounds of the Rayleigh conductivity of an inclined orifice with circular cross-section and elliptical openings[11]. They find that the empirical correction of Eldredge et al. [141] falls within these bounds, in fact it is close to the mean value of the upper and lower bounds. This good agreement is quite surprising as the bounds in [285] are derived for stationary fluid and the simulation in [141] includes a bias and grazing flow.

The effect of the orifice length alone (without inclination) was discussed in Section 7.6. While the inclination angle also increases the length, it seems to have the opposite effect on the dissipation. This hints to an additional effect that has not been accounted for in the models. As suggested in the literature, the elliptical opening should be considered as well. This can be done by applying the correction factor given by Eldredge et al. [141]. The correction factor is presumed to be dependent on the inclination angle. However, it was determined for a 30° configuration[12], which is available here as well. Anyhow, the angle of 30° doubles the length compared to the 90° configuration. Applying a correction factor

figurations produce different results when the inclination angle is the only modified parameter.

10 This was already suggested by Eldredge et al. [141], who applied an empirical correction (cf. Equation (7.5)).

11 They extend their treatment to other geometries as well, but this is the relevant configuration for gas turbine combustors.

12 Please note, that the angle in [141] is measured from the wall normal, so that 60° in [141] is equivalent to 30° here.

of 0.75 for the elliptical opening will produce a result that lies in-between the results for 30° and 90° without the correction factor, but will not surpass the 90° result. As a consequence the effect will be weakened, but not be turned around.
Section 7.6 has shown that the influence of the wall thickness disappears at high bias flow velocities. When transferring this finding to the inclined orifice, it could be proposed to keep the relevant length constant to the wall thickness and apply a correction for the increased opening area only. This would yield the desired effect for a bias flow setup.

7.10 DOUBLE-SKIN CONFIGURATION

A double-skin configuration allows to reduce the bias flow velocity of the damping liner when the total pressure drop is fixed, as it is in a combustor. The bias flow velocity through the damping liner is then determined by the open-area-ratio between damping and metering liner. The velocity through the metering liner is typically much higher.

Results

The experimental results in Figure 7.30 demonstrate this effect for two double-skin configurations. The open-area-ratio of both configurations is 0.3. Without any bias flow the dissipation curve exhibits two maxima (one maximum in Figure 7.30a is expected just beyond the plotted frequency range). The frequencies of these two maxima correspond to the Helmholtz resonances of the damping and metering liners and their associated cavities, so that each maximum can be related to the one or the other. Here, the maxima at the higher frequencies correspond to the damping liner. The peaks associated with the metering liner are eliminated when applying a damping liner bias flow of $M_B = 0.014$. At the given open-area-ratio, that corresponds to a metering liner bias flow Mach number

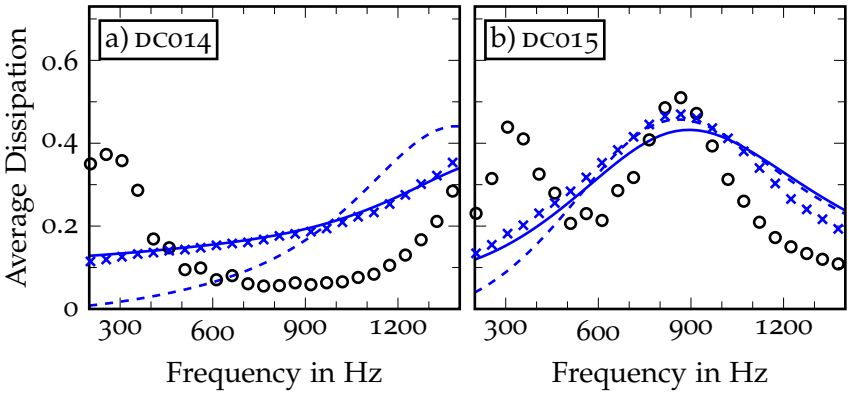

Figure 7.30: Influence of a double-skin arrangement on the dissipation with and without bias flow. Experiments: o $M_B = 0$; × $M_B = 0.014$. Prediction of EDM:Jing for $M_B = 0.014$: —— with second liner; - - - with hard wall.

of nearly 0.05. The result suggests that the influence of the metering liner can be neglected.

This conclusion can be verified with the Eldredge and Dowling method, where a second liner can be included. Predictions of EDM:Jing are also plotted in Figure 7.30 for two cases: 1. Including a second liner in the model, so that the actual geometry is reproduced, and 2. replacing the second liner with a hard wall, i. e. neglecting the second liner's influence. The prediction of DC014 is improved when accounting for the second liner. The result for DC015 is not as clear. While the inclusion of the second liner gives a better match with experiments at low frequencies, it slightly underestimates the peak level. Generally, the predictions of EDM:Jing benefit from the inclusion of the second liner. However, due to the small open-area-ratio the differences between second liner and hard wall predictions vanish when increasing the velocity further (not shown here).

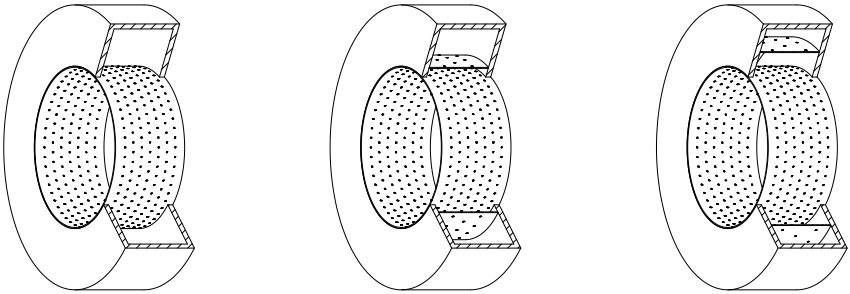

(a) DC006 (b) DC014 (c) DC015

Figure 7.31: Illustration of the configurations studied regarding the influence of the cavity volume.

Discussion

Jayatunga et al. [240] develop an impedance model for a plane double-skin configuration. Modeling a double-skin liner with bias flow demonstrates the same behavior as above: Two absorption maxima are dominant at low bias flow velocities, while the maximum associated with the outer volume disappears at high bias flow velocities. However, no details of the geometry, nor a comparable measurement are presented.

In a different setup the second liner could be implemented to improve the absorption, similar to a locally-reacting double-degree-of freedom liner. In that case the open-area-ratio between the two perforations should be close to unity, allowing for a significant effect of the second liner.

7.11 CAVITY VOLUME

The cavity volume is modified by using double-skin arrangements with various dimensions. The three configurations are illustrated in Figure 7.31. Configuration DC006 is the base configuration without metering liner, yielding a of $1757\,\mathrm{cm}^3$. The metering liner in

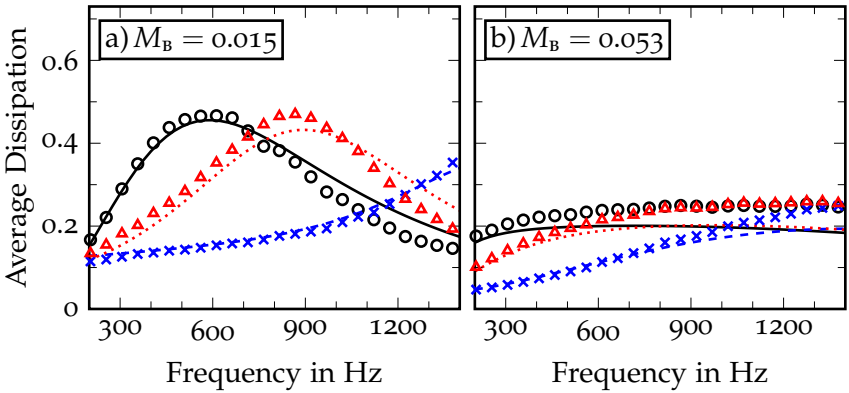

Figure 7.32: Influence of the cavity volume at two bias flow Mach numbers. Experiment: ○ DC006 (1757 cm³); × DC014 (280 cm³); △ DC015 (780 cm³). Prediction by EDM:Jing: —— DC006; - - - DC014; ····· DC015.

configurations DC014 and DC015 reduces the volume to 280 cm³ and 780 cm³, respectively. The damping liner is the same in all configurations. The geometric specifications are given in Table 7.1.

Results

The comparison of the three different volumina is plotted in Figure 7.32. The peak dissipation is shifted to higher frequencies when the volume is reduced[13]. The peak level of dissipation remains unchanged. At higher bias flow velocities, Figure 7.32b, the dissipation increases with the frequency up to the resonance frequency of the respective configuration and remains at the maximum level for higher frequencies.

Figure 7.32 also plots the predictions of EDM:Jing. The double-skin arrangements of DC014 and DC015 are accounted for in the modeling. The influence of the cavity volume is reproduced well by the model. At $M_B = 0.053$, the model consistently yields a lower dissipation than the measurements.

13 The peak of DC014 is expected just beyond the plotted frequency range.

Discussion

As discussed in Section 7.2, the frequency of maximum dissipation is related to a resonance frequency of the system. When all dimensions are much smaller than the wave length, this is typically a Helmholtz resonance. In that case, the resonance frequency is directly dependent on the cavity volume. This relationship is an obvious conclusion from Figure 7.32a. The theoretical Helmholtz resonance frequencies for the three configurations are included in Table 7.9.

The bias flow shifts the resonance frequency to higher values[14], so that the theoretical values in Table 7.9 do not exactly match with the dissipation maxima in Figure 7.32a. This is due to the decrease of the reactance by the bias flow (see discussion in Section 7.2). The reduction of the reactance seems to be a generally accepted fact, but the literature does not provide a collective opinion on the more specific behavior. While some models do not include any influence on the reactance at all, other models predict very different strengths of the phenomena (see Figure 4.9). Westervelt [491] found that the reactance ultimately becomes zero when a bias flow is present. The impedance measurements of Jing and Sun [242] demonstrate the behavior of the reactance, and in fact it is close to zero at a certain bias flow setting. However, this behavior is underestimated by the Jing model as well as the numerical model presented in [242].

Assuming the reactance becomes zero at sufficiently high bias flow velocities, this would yield a resonance frequency of infinity. In fact, at $M_B = 0.053$ in Figure 7.32b no resonance is visible. Interestingly enough, the dissipation increases with the frequency until it reaches its maxium at the theoretical no flow Helmholtz resonance and remains constant at higher frequencies. This behavior can not only be observed for the three configurations in Fig-

14 The second liner in configurations DC014 and DC015 invalidates the hard-wall assumption, so that the measured resonance frequencies are slightly higher than the theoretical ones already without flow (cf. Figure 7.30).

Table 7.9: Theoretical Helmholtz resonance frequency in Hz for a hard-walled cavity with $M_B = 0$.

	DC006	DC007	DC008	DC014	DC015	HC006
$f_r = \frac{c}{2\pi}\sqrt{\frac{A_{open}}{Vl_{eff}}}$	512	400	985	1283	768	679

ure 7.32b, but as well for configurations DC007, DC008, and DC009 in Figure 7.18d. The associated Helmholtz resonance frequencies are listed in Table 7.9.

Hughes and Dowling [219] introduce a resonance parameter[15]

$$Q = (k\,s\,\cos\,\theta)^2\,\frac{d_c}{2r}\,, \tag{7.6}$$

where θ is the incidence angle of the sound wave. For normal sound incidence, Equation (7.6) corresponds to the squared ratio of frequency to Helmholtz resonance frequency of a resonator with a neck length of zero. They use it as a non-dimensional frequency parameter for the absorption of a thin liner with normal sound incidence. They show that the peak dissipation is obtained when the resonance parameter equals unity. In agreement with Figure 7.32a they found, that the bias flow alters the resonance frequency, so that the absorption maximum moves away from unity (cf. Fig. 3 in [219]). Obviously, they were operating in the resonance controlled regime.

Applying Equation (7.6) to a grazing incidence configuration yields zero (as $\cos 90° = 0$). Neglecting the incidence angle for wave lengths much larger than any liner dimension and accounting for the finite thickness of the liner yields[16]

$$Q = k^2\frac{Vl_{eff}}{A_{open}} = \left(\frac{f}{f_r}\right)^2. \tag{7.7}$$

15 The resonance parameter Q should not be confused with the Q factor, which was introduced on page 43.

16 Please note the different volume definition compared to Equation (7.6), so that Equation (7.7) can be readily applied to a cylindrical configuration.

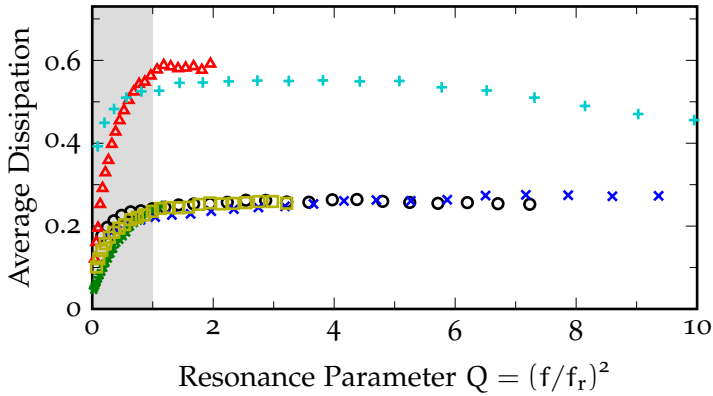

Figure 7.33: Average dissipation of various liner geometries plotted over the resonance parameter Equation (7.7). The associated resonance frequencies are listed in Table 7.9. ○ DC006, $M_B = 0.049$; × DC007, $M_B = 0.049$; △ DC008, $M_B = 0.049$; * DC014, $M_B = 0.051$; □ DC015, $M_B = 0.053$; + HC006, $M_B = 0.120$.

Figure 7.33 plots the dissipation coefficient of various liner geometries over the resonance parameter of Equation (7.7). The associate resonance frequencies are listed in Table 7.9. The bias flow Mach number for each liner was chosen, so that the dissipation is dominated by the bias flow effect. The absorption increases until $Q = 1$ (indicated by the gray background) and is largely constant for higher values of the resonance parameter. Only configuration HC006 exhibits a slight decrease of the dissipation levels for $Q > 5$.

The Helmholtz resonance frequency of the liner seems to be the lower limit of the broadband absorption of the liner, when it is operating in the bias flow regime.

7.12 PARTITIONED CAVITY

One design choice can be to divide the liner cavity into several smaller cavities. This is demonstrated in Figure 7.34. The details of the partitioned cavity are illustrated Figure 2.10c. The axial

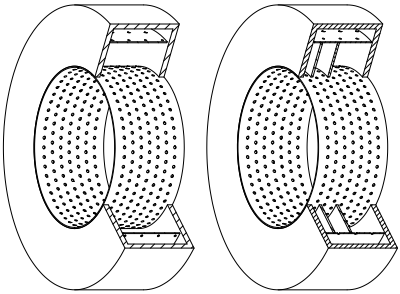

(a) DC017 (b) DC018

Figure 7.34: Illustration of the configurations studied regarding the influence of dividing the cavity into several partitions.

lengths of the three cavities are $L_{c1} = 7.25\,\text{mm}$, $L_{c2} = 14\,\text{mm}$, and $L_{c3} = 32.75\,\text{mm}$, containing one, two, and four orifice rows respectively. The open-area-ratio between metering and damping liner is kept constant for each partition, so that their damping liner bias flow velocity should be approximately the same. The two partition walls are 3 mm thick each, which slightly reduces the total volume compared to the unpartitioned configuration. The remaining specifications are given in Table 7.1.

Results

The acoustic performance of the unpartitioned and the partitioned cavity is compared in Figure 7.35. At the low bias flow Mach number the absorption is significantly increased by the partitions. It can be assumed that the resonance effect dominates and that it seems to be amplified for DC018. It can be observed that the resonance frequencies of the two configurations are slightly different. The theoretical Helmholtz resonance frequency of DC017 is at $f_r = 1211\,\text{Hz}$. In configuration DC018 the 'acoustic' volume is reduced by inserting the partition walls, yielding an average value

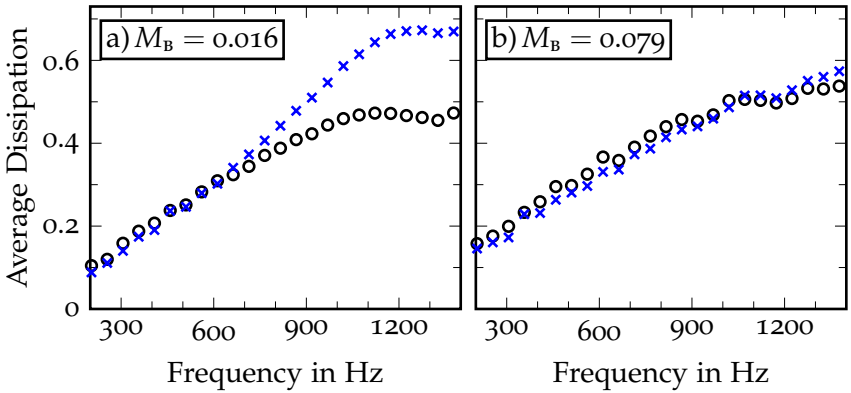

Figure 7.35: Average dissipation plotted over the frequency comparing two liner configurations with a o single large cavity (DC017) and a ×partitioned cavity (DC018) at two bias flow Mach numbers.

of $f_r = 1299\,\text{Hz}$. This difference agrees well with the experimental data.

The results at $M_B = 0.079$ are virtually identical. It can be assumed that the bias flow effect dominates the absorption characteristics. In that case, the partitions seem to have no influence.

Discussion

The cavity was partitioned in a way, that the resonance frequency was largely kept constant. In that case, the dissipation behaves as if the Q factor of the resonance was increased. This effect does increase the absorption for a small frequency range around the resonance. To broaden the frequency range at low bias flow velocities, the partitions could be tuned to respond to different resonances.

7.13 PERFORATION PLACEMENT

The position of the liner within a combuster is very important. Especially at resonance, the sound field describes a distinctive spa-

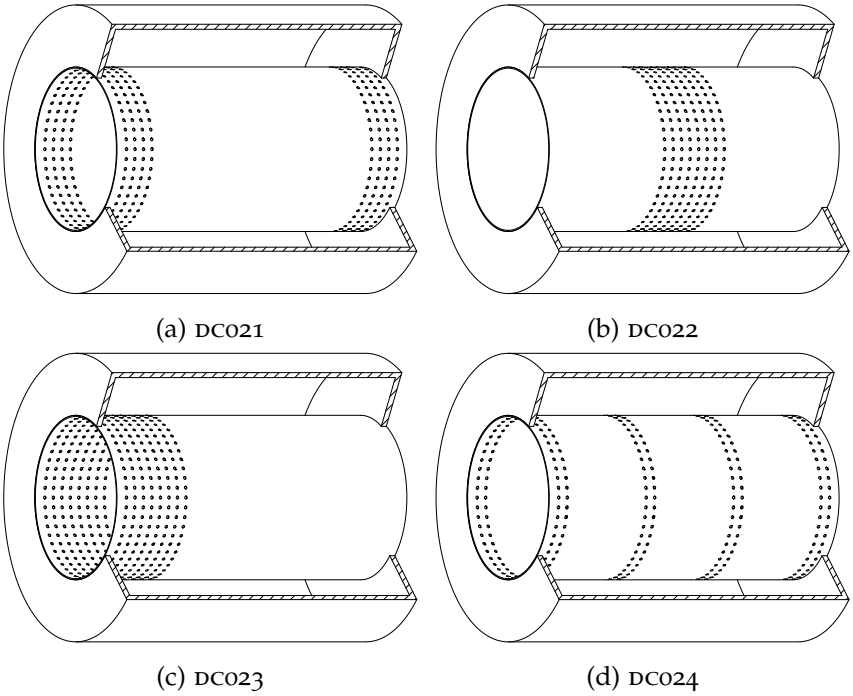

(a) DC021 (b) DC022

(c) DC023 (d) DC024

Figure 7.36: Parameter study perforation placement configurations.

tial pattern of maximum and minimum pressure fluctuations. It has been shown, that the liner is most effective when it is located at a maximum of the pressure fluctuation [501]. The position of the liner relative to the external sound field can be accounted for in the Eldredge and Dowling method. However, the position of the liner does not characterize the performance of the liner itself, but rather reflects the properties of the combustor or test rig. Here, the perforation placement relative to the internal sound field of the liner, i. e. within the liner cavity, is studied. In contrast to the position of the liner, the perforation placement can be used as a design parameter for the liner itself.

The perforation placement can only be important, when a spatial structure of the sound field does exist. This means, when look-

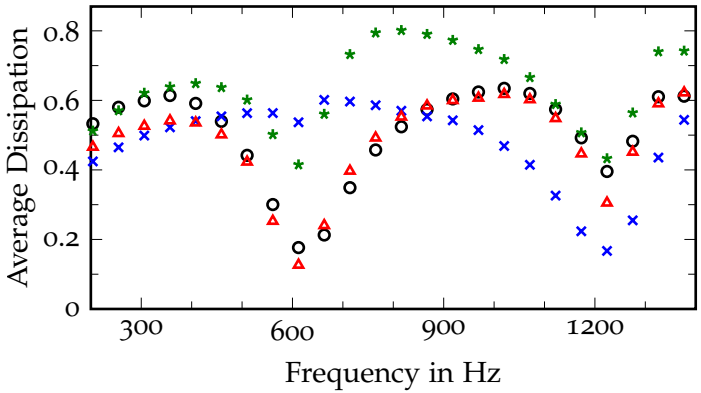

Figure 7.37: Average dissipation plotted over the frequency comparing four liner configuration with different perforation placement at $M_B = 0.049$. ○ DC021, × DC022, △ DC023, and * DC024.

ing at the placement in axial direction, that the axial dimension of the cavity should be larger than half a wave length. The configurations studied here are illustrated in Figure 7.36. With 280 mm the cavity is nearly five times longer than the previous configurations. The total amount of perforation is constant in all four configurations. The perforation is either moved axially (cf. DC022 and DC023) or split up into several segments of equal local porosity (cf. DC022, DC021, and DC024). The geometric specifications are listed in Table 7.1.

Results

The results of the four configurations are compared in Figure 7.37 where $M_B = 0.049$. The behavior is strongly dependent on the axial resonances within the cavity. Two axial resonances lie within the frequency range, that is a $\lambda/2$-resonance with $f_r = 612\,\text{Hz}$ and a λ-resonance with $f_r = 1224\,\text{Hz}$. The magnitude of the axial pressure distribution for these two resonances is illustrated in Figure 7.38. The dissipation drops to significant lower values

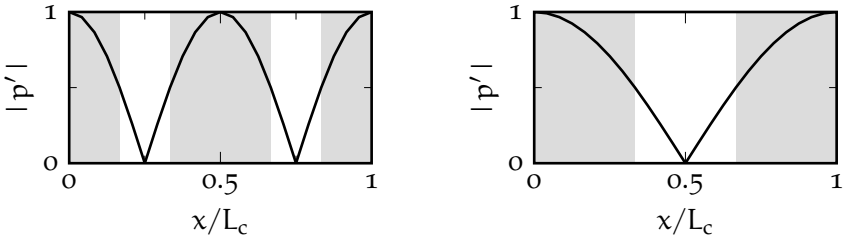

(a) $\lambda = L_c$ (b) $\lambda/2 = L_c$

Figure 7.38: Magnitude of the acoustic pressure at resonance.

at these resonance frequencies. This effect can be reduced when placing the perforation at a pressure node (indicated by the white background in Figure 7.38. For example, the perforation of configuration DC022 is located at a pressure node of the $\lambda/2$-resonance and the dissipation curve exhibits only a minor effect at that frequency.

Configuration DC024 yields much higher dissipation levels compared to the other setups. The dissipation coefficient surpasses values beyond 0.8 at frequencies around 800 Hz. The design with alternating hard wall and perforated sections seems to improve the sound absorption significantly.

The transfer matrix method allows to include hard-wall sections at both ends of the perforation, so that configurations DC022 and DC023 can be modeled without any modifications. Figure 7.39 compares the model predictions with the experimental data for these two configurations. The models predict a very similar behavior and the general agreement is good. Especially the resonance effect is reproduced quite accurately.

Discussion

The configurations in the previous sections meet the requirement that the wave length of the frequencies of interest is much longer

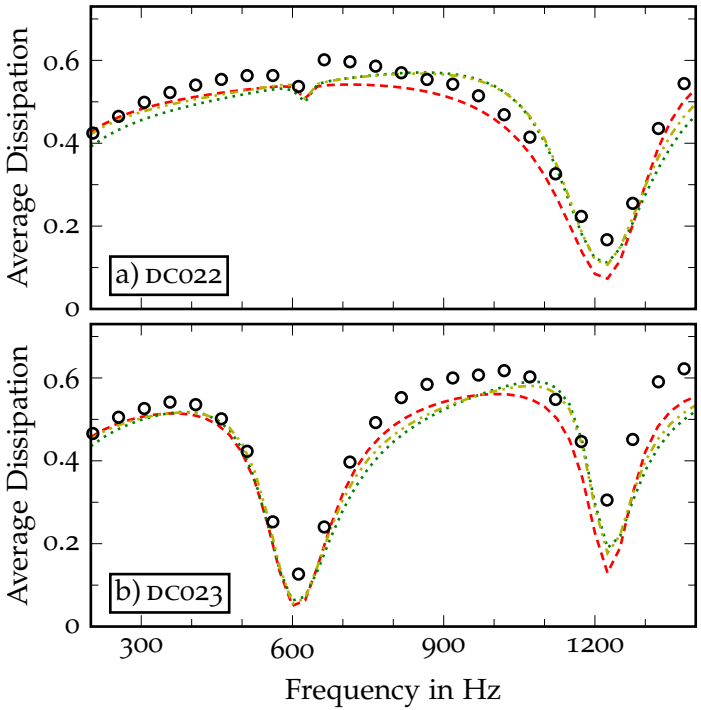

Figure 7.39: Average dissipation plotted over the frequency comparing four liner configuration with different perforation placement at $M_B = 0.049$. o Experiment, ---- TMM:Jing, ····· TMM:Betts, -·-·- TMM:Bellucci.

than the dimensions of the cavity. In that case the resonances of the system are of the Helmholtz type (see Section 7.11) and the resonance frequency is dependent on the combination of cavity volume and orifice dimensions. When the axial length of the cavity is increased beyond the wave length restriction, in fact when $L_c \geqslant \lambda/2$, the axial resonances become dominant. This transition was already observed by Davis et al. [116, p. 43]: "If the resonant chamber is itself long, the resonance becomes a length-controlled phenomenon instead of a volume controlled one [...]".

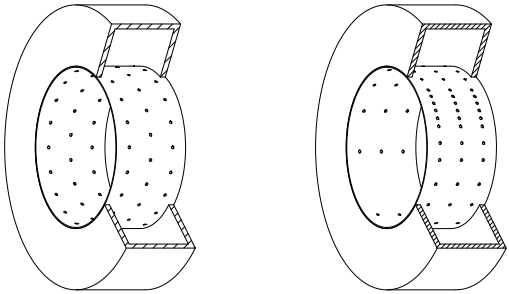

(a) uniform (DC007) (b) nonuniform (DC013)

Figure 7.40: Parameter study perforation pattern configurations.

When axial resonances do occur, then the placement of the perforation becomes crucial. Davis et al. [116] found that the perforation should be located a quarter wave length away from the hard wall. In that case, the reflection from the hard-wall is 180° out of phase with the incoming wave at the perforation, so that they cancel each other out [116, p. 16]. This condition is meet when the perforation is located at the pressure nodes of the respective resonance (cf. Figure 7.38). The same conclusion was drawn from the experimental data above.

While configuration DC024 with alternating hard-wall and perforated sections exhibits the same resonance phenomena, its absorption is generally higher compared to the other configurations. It can be assumed that portions of the sound wave are reflected at each change of the wall boundary condition, i. e. the transition from hard-wall to impedance wall and vice versa. Due to multiple reflections within the length of the liner portions of the wave pass the liner several times, yielding an increased attenuation.

7.14 PERFORATION PATTERN

The geometric characteristics of different perforation patterns are defined in Section 2.2.2. The measurements compare a uniform,

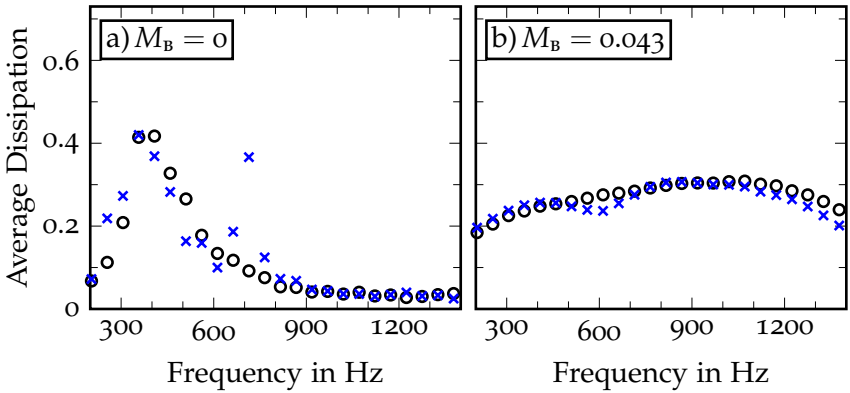

Figure 7.41: Average dissipation plotted over the frequency comparing two liner configurations with different circumferential perforation distribution ○ uniform (DC007) and × nonuniform (DC013) at two bias flow Mach numbers.

staggered perforation to a nonuniform pattern with circumferential variation of the porosity. The layout becomes more clear in Figure 7.40, where both configurations are shown. DC007 has a uniform porosity of 1 %. The local porosity of the nonuniform configuration (DC013) changes around the circumference from 3 % to 0.6 %, resulting in an overall porosity of 1 %, i. e. the ratio of total open area to total hard wall is identical to DC007. The remaining geometric specifications are given in Table 7.1.

Results

The comparison of the acoustic performance of both setups is plotted in Figure 7.41 for two bias flow Mach numbers. Without any bias flow in Figure 7.41a the results are very similar, except for an additional peak at 714 Hz produced by the nonuniform perforation. This peak is associated with the cut-on frequency of the first circumferential mode in the annular cavity. The circumferential structure of the perforation pattern resembles the spatial pattern

of the mode, so that it is excited. The theoretical cut-on frequency for a hard-walled annulus of the same geometry is at 577 Hz. This frequency is shifted to slightly higher values due to the perforated wall at the inner radius (cf. [281]).

When a bias flow is present, as shown in Figure 7.41b, the resonance effects are largely suppressed and the broadband damping due to the bias flow dominates. The absorption of both geometries is rather similar, though two weak maxima are still visible for configuration DC013.

Discussion

The only experimental data that is found in the literature regarding a variation of the perforation pattern is concerned with the perforation aspect ratio, i. e. the abandonment of a square perforation pattern for a rectangular pattern as illustrated in Figure 2.8.

Andreini et al. [17] present experimental results with two rectangular perforation patterns, varying the perforation aspect ratio from s_x/s_θ =1.24 to 1.93. Both measurements are done with simultaneous grazing and bias flow and retain a porosity of 1.82 %. The change in perforation aspect ratio did not show any influence on the dissipation.

Lee et al. [288, 289] vary the perforation aspect ratio from a nearly square configuration with s_x/s_θ =0.96 to a rectangular setup, stretched in axial direction and compressed in circumferential direction, resulting in s_x/s_θ =2.45. The porosity was kept constant at 8.4 %. Without any flow they observe an increase of the transmission loss for the rectangular arrangement. This deviation between square and rectangular pattern becomes larger at higher frequencies.

This difference is somewhat surprising. When thinking in terms of porosity and diameter (which are both kept constant), the difference would not be reproduced by any of the models. The actual orifice spacing seems to be important. The requirement for the ori-

fices to act independently without interaction is given by $d \ll s$. For a square perforation pattern this limit is associated with a certain porosity $\sigma \leqslant 4\,\%$ (see Section 7.5). Due to the distortion of the orifice grid, the porosity cannot be used as a sole indicator for the interaction anymore. The spacing between the orifices has to be evaluated in both directions separately. Translating the porosity requirement into a minimum spacing requirement yields $s_{min}/d \geqslant 4.4$.

The spacing of the nearly square pattern is 7.6 mm and 7.9 mm in axial and circumferential direction, respectively. The rectangular pattern is streched to 12 mm in axial direction and compressed to 4.9 mm in circumferential direction. The closer proximity of the orifices in circumferential direction could promote the interaction, even when the porosity is kept constant. The ratio of minimum spacing to orifice diameter is reduced from $s_{min}/d = 3$ for the square pattern to 2 for the rectangular one. Both values fall short of the required limit given above. The spacing to diameter ratios of Andreini et al. [17] are $s_{min}/d = 4.7$ and 5.9. This is larger than the ratios in Lee et al. [288, 289] and above the spacing requirement.

The increased orifice interaction could be one possible explanation for the effect observed by Lee et al. [288, 289] and their contradictory results to Andreini et al. [17]. On the other hand, one major difference between the two studies is, that the experiments of Lee et al. [288, 289] are performed without any flow, while both bias and grazing flow is present in [17].

The experiments here have shown that the perforation pattern can be designed to promote certain cavity resonances. This is achieved by resembling the spatial structure of a cavity mode with the pattern of the perforation. This adds another degree of freedom, for example for the simultaneous absorption of multiple tonal components. Naturally, this approach works only when the

resonance effect is dominant, that is without or only slow bias flow.

7.15 TEMPERATURE

The temperature in a combustion chamber is very high and little is known on the effect of high temperature on the acoustic performance of a bias flow liner. The operating conditions of a combustor liner were discussed in Section 2.1. It is not only that the temperature is very high, but there is also a significant difference in the temperatures of the bias flow and the grazing flow. The latter setup is reproduced here. The temperature of the grazing flow is increased, while the bias flow remains constant at approximately 288 K. The liner setup HC005 is a double-skin configuration (see Table 7.1 for specifications). The total pressure drop across both liners is at 3 % of the duct pressure, yielding a bias flow Mach number of 0.04 at the damping liner. The speed of sound used in the calculation of the bias flow Mach number is based on the temperature of the cold bias flow, assumed to be constant at 288 K.

Results

Figure 7.42 compares the experimental results when increasing the grazing flow temperature. The frequency where the dissipation is at maximum remains unchanged. For frequencies below 1800 Hz it can be observed that the dissipation decreases with increasing temperature. This trend is not so clear at higher frequencies, where the data is slightly more scattered.

The results for the two extreme temperature of Figure 7.42 are reproduced in Figure 7.43, comparing them to the predictions of the models. The agreement between models is good for frequencies up to 1800 Hz, except TMM:Betts which continuously underestimates the data. Generally, the models seems to predict a constant level of dissipation for both temperature setting, but a shift

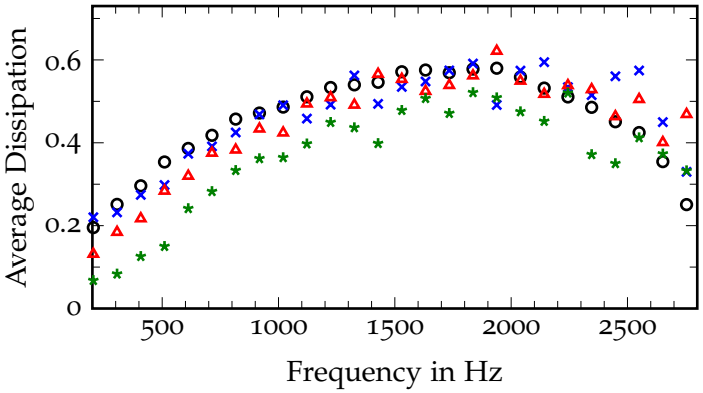

Figure 7.42: Influence of the temperature on the dissipation of configuration HC005 at 600 kPa and $M_B = 0.04$. ○ 288 K; × 423 K; △ 573 K; * 773 K.

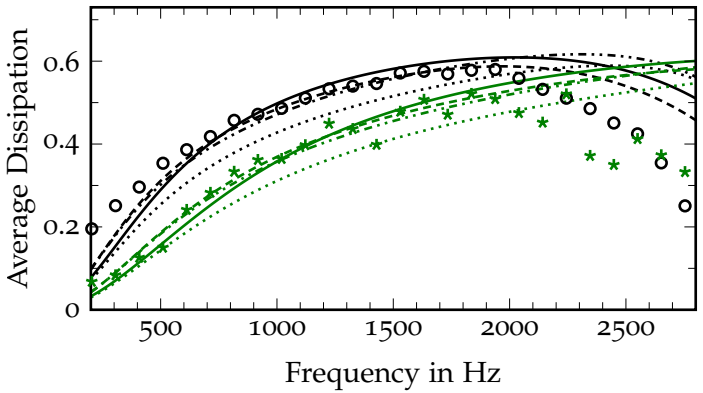

Figure 7.43: Comparison between experiment and models at different temperatures for configuration HC005 at 600 kPa and $M_B = 0.04$. Experiment: ○ 288 K; * 773 K. Models: —— EDM:Jing; - - - - TMM:Jing; ····· TMM:Betts; -·-·- TMM:Bellucci.

of the dissipation maximum to higher frequencies with increasing temperature. This is a very different behavior from what is observed by the experiments.

Discussion

Very few publications are available, that treat the influence of temperature on the acoustic properties of a liner. Their findings are summarized here.

Christie [93] studies the acoustic absorption of porous materials at high temperatures. The quantities that determine the temperature dependence are the flow resistance[17], the density of the fluid, and the speed of sound. He finds that the Delany-Bazley model[18] is capable of providing useful predictions, when the empirical constants are adjusted to the high temperature condition.

Elnady et al. [144] measure the acoustic properties of a single orifice and cavity, which they placed in an oven. The temperature is increased up to 573 K and measurements are carried out at 120 dB (linear regime) as well as at 140 dB (nonlinear regime). In the linear regime the resistance is increasing with the temperature and its maximum is shifted to higher frequencies. At 140 dB only the resonance frequency changes, while the maximum level remains constant with temperature. The reactance is reduced with higher temperatures at both sound pressure levels.
The results are compared to a standard[19] impedance model. While the reactance agrees well with the measured data, the resistance is overpredicted at higher frequencies. This mismatch occurs already for ambient temperature, so that it is not related to the temperature influence. However, the general trend when increasing the

17 It is most probably the change in viscosity of the fluid, that is responsible for the dependence of the flow resistivity.

18 The empirical Delany-Bazley model [121] describes the acoustic properties of porous materials at room temperature.

19 That means, an impedance model which was not adapted for high temperature use.

temperature is captured by the impedance model. They conclude that the temperature effect is sufficiently described by adjusting the properties of air (i. e. density, viscosity, and speed of sound) accordingly.

Rademaker et al. [380] present a series of impedance measurements of perforated, linear[20], and porous liners at varying temperatures up to 773 K and including a grazing flow with Mach numbers up to 0.4. It was found that the resistance of the perforated liner was nearly independent of the temperature, while the resistance of the linear and the porous liner is significantly increasing with the temperature. All configurations exhibit a reduction of the mass reactance with higher temperatures.

Sun et al. [462] confirm these observations regarding the impedance in a comprehensive experimental and theoretical study with metallic porous materials. Furthermore, their results show consistently, that the sound absorption is reduced when the temperature is increased.

The results can be interpreted as follows. The absorption mechanism of linear or porous liners is mainly based on viscous dissipation. The viscosity increases with the temperature (see Table A.6), so that the resistance grows accordingly. Without flow and in the linear regime, the acoustic performance of a perforated liner depends mainly on the resonance effect and only to some extent on the viscous dissipation within the orifices. However, at high sound pressure levels or in combination with either bias or grazing flow, the dominant absorption effect is due to vorticity shedding, so that the influence of viscosity is of minor importance.

The mass reactance describes the inertia of the oscillating mass and is regarded to be proportional to the wave number (see Equation (4.18), for example). Raising the temperature increases the speed of sound (see Table A.4), so that the wave number and the reactance are reduced. While this cannot be observed in the

20 Linear liners are (nearly) independent of sound pressure level and grazing flow. Commonly, this is achieved by applying a wire mesh layer on top or behind the perforated facesheet.

data of Rademaker et al. [380] it will be mentioned here for completeness, that the reactance is as well affected by the viscosity (see Equations (4.13) and (4.14)). The viscosity effect is commonly small compared to the wave number effect, but it counteracts the results, i. e. the viscosity effect increases the reactance with the temperature.

The results here present for the first time experimental data, which demonstrates the dependency of the absorption of a bias flow liner on the temperature. The main effect seems to be a slight reduction of the absorption with increasing temperature. This agrees with the results of Sun et al. [462] for a porous liner. However, the resonance frequency is not shifted to higher frequencies as reported in the literature, but remains unchanged.

A key difference between the references and the experiment here is of course the bias flow. Additionally, the bias flow is not heated, but constantly at around 288 K, while the given temperature corresponds to the mean grazing flow temperature. This approach with different bias and grazing flow temperatures reflects the conditions at a combustor liner in a gas turbine, where, however, both temperatures are at a much higher level. Here, the temperature within the cavity and the orifices of the liner is rather constant near its ambient value, which might be the reason for the rather small influence of the temperature.

The temperature dependency observed in Figure 7.42 might be of an entirely different nature. Nayfeh and Sun [350] discusses the influence of a transverse temperature gradient on the absorption of a liner. The effect can be compared to the refraction effect of a sheared grazing flow (see the discussion in Section 7.3), with the difference that it is independent of the direction of sound propagation. Nayfeh and Sun [350] come to the conclusion that "[...] cooling the duct walls leads to channeling of the sound towards the walls [...]". Their theoretical experiment yields higher attenuation when the temperature of the wall is decreased, which contradicts the findings here.

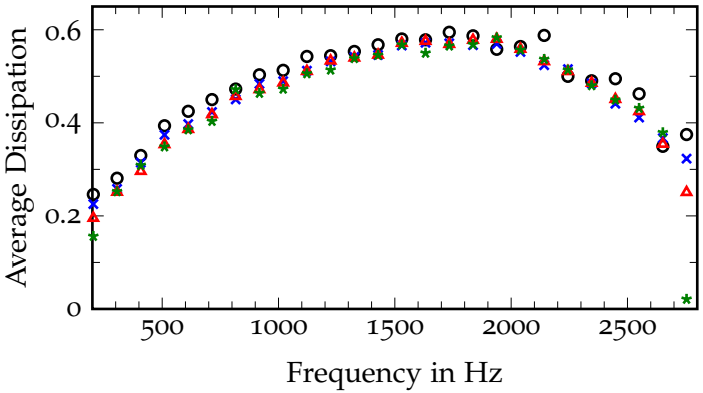

Figure 7.44: Influence of the pressure on the dissipation of configuration HC005 at 288 K and $M_B = 0.04$. ○ 101 kPa; × 200 kPa; △ 600 kPa; * 1000 kPa.

7.16 PRESSURE

The high static pressure in a combustion chamber is commonly not accounted for in experiments, theoretical studies, or simulations. Even most combustion tests are performed at atmospheric pressure conditions (e. g. [55, 310, 481]). The Hot Acoustic Test Rig allows for a controlled increase of the static pressure up to 1100 kPa, so that the influence of the pressure on the absorption of a bias flow liner can be studied. The liner configuration is again HC005 in a double-skin arrangement (see Table 7.1 for specifications). The temperature is kept at ambient. The total pressure drop across both liners is at 3 % of the duct pressure, so that the mass flow rate of the bias flow needs to be adjusted for the varying duct pressure. Doing so results in a constant bias flow Mach number of 0.04 at all operating conditions.

Results

The results of the acoustic measurements at different static pressures are compared in Figure 7.44. Tests were performed at am-

bient pressure (101 kPa), 200 kPa, 600 kPa, and 1000 kPa. The dissipation coefficient is largely unimpressed by the varying static pressure. It seems that the static pressure does not change the acoustic properties of the liner.

The same result is predicted by the models. The predictions within the pressure range of the experiments are indistinguishable, so that they are not shown here. The plot would reproduce the results at ambient conditions in Figure 7.43.

Discussion

The experimental results demonstrate, that the absorption of the bias flow liner is not at all depending on the static pressure (i. e. the density of the fluid, mainly).

Ahuja et al. [9] report about acoustic measurements of porous materials at sub-atmospheric pressures. It was observed that the absorption of porous materials is decreasing when the pressure is lowered.

In a theoretical study, Giese et al. [174] plot the maximum reachable absorption coefficient and the corresponding flow resistance of a porous ceramic tile at various pressures. The absorption coefficient remains constant while the flow resistance changes significantly. As a conclusion, the absorption is expected to change with the pressure, when the flow resistance remains constant.

Judging from the references, the acoustic properties of porous materials are indeed depending on the pressure. However, the experimental results with the bias flow liner paint a very clear picture: The absorption due to the bias flow effect is independent of the operating pressure, i. e. it is insensitive to changes in the fluid density.

7.17 STROUHAL NUMBER

The Strouhal number[21] is a dimensionless quantity relating the frequency, a characteristic length, and the flow velocity. It is oftentimes used to describe the dependency of the acoustic properties of a bias flow liner on these quantities (e. g. [70, 210, 219, 242]).

Results

The experimental results of various frequencies and bias flow velocities is plotted over the Strouhal number in Figure 7.45. In the left column the Strouhal number is based on the orifice radius $\mathrm{St} = \mathrm{kr}/M_{\overline{\mathrm{B}}}$, while it is based on the orifice length $\mathrm{St} = \mathrm{kl}/M_{\overline{\mathrm{B}}}$ in the right column. $M_{\overline{\mathrm{B}}}$ is the mean bias flow Mach number in the orifice. Each row is a different liner configuration with varying orifice radii and lengths.

Commonly, the Strouhal number is based on the orifice radius, as plotted in the left column. The Strouhal number where the dissipation is at maximum changes for the different configurations. This is indicated by the gray background. This variation is much smaller when the Strouhal number is based on the orifice length, as shown in the right column. Here, the maximum dissipation occurs in a smaller range of Strouhal numbers around unity, consistently for all configurations. In that case, it seems that the Strouhal number can be an indicator for maximum dissipation. However, the 'optimum' Strouhal number alone does not grant an optimum dissipation. The levels of dissipation measured at Strouhal numbers of unity for varying frequencies and bias flow velocities show a large diversity.

21 Named after Vincenc Strouhal (1850-1922, Czech physicist) [457].

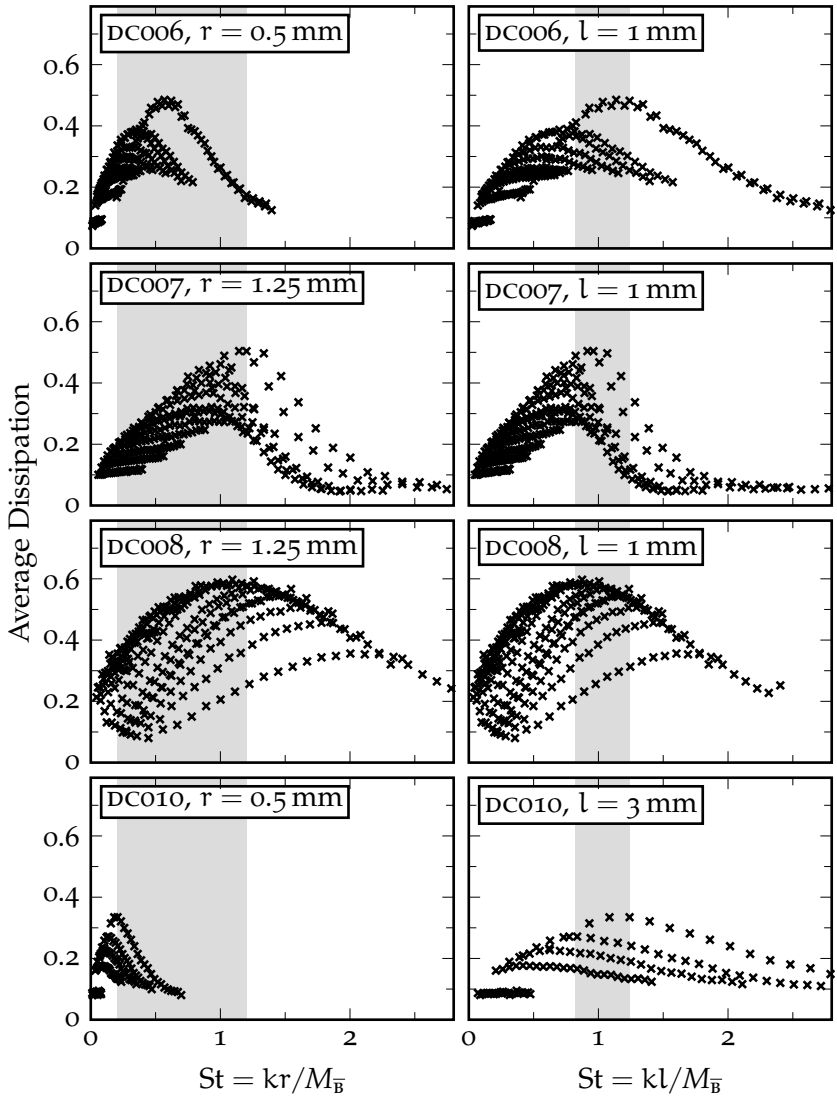

Figure 7.45: Average dissipation plotted over the Strouhal number based on the orifice diameter (on the left) and the orifice length (on the right). The gray background indicates the variation of the Strouhal number of maximum dissipation for the different configurations.

Discussion

Bodén and Zhou [70] successfully collapse their experimental data when expressing it in terms of Rayleigh conductivity and plotting it over the inverse Strouhal number. This confirms Howe's approach of using the Strouhal number as the only parameter in his model of the Rayleigh conductivity. Unfortunately, the dissipation coefficient does not have a unique relationship to the Strouhal number. However, maximum absorption can be achieved for Strouhal numbers of unity, when the Strouhal number is based on the orifice length rather than the orifice radius.

8

CONCLUDING REMARKS

This thesis provides a comprehensive experimental parameter study of bias flow liners regarding their geometric, thermodynamic, acoustic, and flow parameters. An extensive amount of available research has been collected and reviewed. The consistent database of experimental results allowed to put the existing information into perspective. The significant features of each parameter can be summarized as follows:

SOUND PRESSURE LEVEL The behavior of the liner is linear when the bias flow velocity is larger than the acoustic velocity, that is when flow reversal does not occur. A combustor liner is required to operate in the linear regime to prevent hot gas ingestion.

BIAS FLOW The bias flow was able to improve the absorption of all tested configuration, compared to the acoustic performance without flow. Two scenarios can be distinguished: The bias flow acting on the resonance effect and the pure bias flow effect. In the first case, the bias flow shifts the frequency of maximum dissipation to higher values. The bandwidth of the absorption is increased while its level is typically reduced. True broadband absorption is obtained when the bias flow effect dominates.

GRAZING FLOW The effect of the grazing flow on the acoustic properties of a perforated liner is identical to the bias flow effect. In order to achieve similar results the mean grazing flow Mach number must be a factor of ≈ 3.5 higher than the Mach number of the bias flow jets. However, at certain combinations of grazing flow velocities and liner geometries sound might be produced rather than absorbed. Due to the convective effect of the grazing flow, the absorption of sound waves traveling against flow direction is increased while it is reduced in the opposite direction.

SIMULTANEOUS GRAZING & BIAS FLOW The influence of the grazing flow can be neglected when the ratio of bias to grazing flow velocity is larger than $M_B/M_G > 0.3$. This corresponds to the condition $M_G \approx 3.5\,M_B$, where a similar dissipation is obtained when bias or grazing flows are applied separately. Below this limit the influence of the grazing flow can be accounted for by an effective discharge coefficient, which essentially increases the bias flow velocity.

POROSITY When the bias flow effect dominates the magnitude of the dissipation is directly related to the level of porosity. The individual parameters orifice area, orifice spacing, and number of orifices are unimportant. The situation is more complex without bias flow and in the transition region between resonance regime and bias flow regime.

WALL THICKNESS The wall thickness seems to be of minor significance at high bias flow velocities. A thin configuration is superior, in particular concerning the bandwidth, at low bias flow velocities.

ORIFICE CROSS-SECTION SHAPE The acoustic performance is largely independent of the orifice cross-section shape, when the

open area remains constant. However, an effect is expected for long and narrow openings.

ORIFICE EDGE GEOMETRY The velocity of the bias flow jet is very sensitive to the orifice edge geometry. The experimental data reveals that it is indeed the jet velocity and not the orifice mean velocity, which needs to be constant when comparing different setups. Complying with this rule, the orifice edge geometry exhibits only a minor influence on the absorption. The observed behavior might be the result of the effectively reduced length and the increased open area at the surface when both edges are rounded.

ORIFICE ANGLE The average dissipation is independent of the orifice angle at high bias flow velocities. At lower velocities more shallow angles result in a slightly superior bandwidth. The absorption of sound waves traveling in direction of the bias flow injection is increased, while it is reduced in the other direction. For a typical installation that counteracts the convective effect of a grazing flow.

DOUBLE-SKIN CONFIGURATION A double-skin configuration allows for a reduction of the bias flow velocity through the damping liner when a certain pressure drop needs to be met. The influence of the second liner on the acoustic performance becomes insignificant when the bias flow velocity increases.

CAVITY VOLUME In the resonance dominated regime, the frequency of maximum dissipation is associated with the Hemholtz resonance, which is inversely proportional to the cavity volume. Introducing a bias flow shifts the dissipation maximum to higher frequencies. In the bias flow regime the no flow Helmholtz resonance frequency provides a cut-off frequency, below which the absorption falls off from its broadband maximum level.

PARTITIONED CAVITY Dividing the cavity into several smaller cavities while keeping their Helmholtz resonance constant, amplifies the resonance effect. However, the partitions show no influence when the bias flow velocity is high.

PERFORATION PLACEMENT The placement of the perforation relative to the liner cavity becomes important when the cavity is longer than half an acoustic wave length. In that case, it should be preferred to place the perforation only at the pressure nodes of the axial resonance in the cavity. The experiments show that a configuration with alternating areas of hard-wall and perforation yields an improved absorption.

PERFORATION PATTERN The absorption seems largely independent of the perforation pattern. However, a nonuniform circumferential perforation distribution can be used to promote a circumferential resonance.

TEMPERATURE Increasing the temperature of the grazing flow results in a reduction of the absorption. However, in this setup the bias flow is not heated, so that this result reflects the influence of the temperature difference between grazing and bias flow, as experienced in a combustor.

PRESSURE The pressure seems to have no influence on the absorption.

STROUHAL NUMBER Maximum dissipation can be obtained at a Strouhal number of unity, when the Strouhal number is based on the orifice length rather than the orifice radius. However, a Strouhal number of unity seems to be a neccessary condition only, but is not sufficient that maximum absorption will be achieved.

Many of the parameters are becoming insignificant when the bias flow effect dominates. There seems to be a fundamentally different behavior of bias flow liners at low velocities, depending on the resonance characteristics of the liner-cavity system. If a resonance occurs without flow, then the bias flow shifts the absorption maximum to higher frequencies and broadens its frequency range. Ultimately, the bias flow suppresses the resonance effect leading to a broadband absorption, typically at a much lower level then the maximum observed due to the resonance effect. In the case without resonance, the acoustic performance of the liner is very poor without bias flow. The bias flow continuously increases the absorption until an optimum is reached, where the acoustic performance surpasses the best achievement of a resonance type liner in absorption level and frequency range. Bias flow velocities succeeding this optimum increase the broadband damping towards higher frequencies, while it reduces the level of the broadband absorption. The condition that decides which behavior will occur, i. e. if a resonance is provoked or suppressed, is not clear. Here, it seems to correlate with the porosity of the liner. The resonance effect occurs at low porosities (here around 1 %) and is absent at high porosities (here $> 6.8\,\%$).

The domination of the bias flow effect on the acoustic damping performance is mainly determined by three parameters: the bias flow velocity, the porosity, and the no flow Helmholtz resonance frequency of the liner-cavity system (assuming all dimensions are much smaller than the wave length). The Helmholtz resonance frequency is determined by the combination of the porosity, the wall thickness, and the cavity volume. It provides a cut-off frequency, below which the absorption falls off from its broadband maximum level (see Figure 7.33). The upper frequency limit of the broadband absorption is pushed to higher values while the bias flow velocity is increased, however, at the penalty of lowering the absorption level. The level of the broadband absorption is depend-

ing on the porosity and bias flow velocity. Higher porosities yield an improved absorption when keeping the velocity constant.

Models

All models capture the general trends of the experiments fairly well. It is quite surprising that the deviation between the models themselves is rather small, considering the different approaches taken. The agreement between the models and the experimental data is generally satisfactory. However, all models tend to underestimate the dissipation. The best agreement is achieved where the bias flow effect is described by Howe's theory, i. e. by Jing and Bellucci. While the Bellucci model has been extended to function as well when there is no bias flow, the Jing model is restricted to the presence of a bias flow.

The Eldredge and Dowling method (EDM) and the transfer matrix method (TMM) give largely similar results, while EDM predicts slightly higher dissipation values, which often reproduces the experimental results a bit better. Both methods have some unique features readily available. EDM provides the ability to include a second liner in a double-skin configuration. TMM allows for the simple integration of hard-wall extensions on both sides of the perforation, in the case where the perforation does not cover the entire length of the cavity.

One common problem of the models is the transition between the resonance dominated damping to the purely bias flow related regime. This transition seems to be mainly governed by the reduction of the reactance. While there is a wide variety in the models of the behavior of the reactance, none seems to capture it quite right. Recent numerical models by Jing and Sun [242] and Lee et al. [291] predict a much stronger effect on the reactance.

Outlook

The models and conclusions that have been drawn here and elsewhere are often based purely on empiricism. An enhanced physical understanding of the underlying mechanisms is needed to improve the prediction quality of the models. Recent studies by Rupp and Carrotte [415] and Heuwinkel et al. [201] and the ongoing work of Schulz et al. [436] point into this direction. They all use optical measurement techniques to capture the physical effect right at the orifice. The results of further efforts in this direction are highly anticipated.

A

PROPERTIES OF AIR

A.1 EQUATIONS OF IDEAL GAS PROPERTIES

Air at ambient conditions is commonly regarded to behave like an ideal gas, so that the properties are approximated by (e. g. [414])

$$\rho = \frac{p}{RT} \tag{A.1}$$

$$c = \sqrt{\gamma R T} \tag{A.2}$$

$$\gamma = \frac{c_p}{c_v} = 1.4 \tag{A.3}$$

$$\mu = \mu_{ref} \frac{T_{ref} + T_s}{T + T_s} \left(\frac{T}{T_{ref}} \right)^{3/2} \tag{A.4}$$

$$\kappa = \kappa_{ref} \frac{T_{ref} + T_a e^{-T_b/T_{ref}}}{T + T_a e^{-T_b/T}} \left(\frac{T}{T_{ref}} \right)^{3/2} \tag{A.5}$$

$$c_p = \frac{\gamma}{\gamma - 1} R \tag{A.6}$$

$$c_v = R/(\gamma - 1) \tag{A.7}$$

$$\nu = \mu/\rho \tag{A.8}$$

$$\chi = \kappa/(\rho c_p) \tag{A.9}$$

$$Pr = c_p \mu/\kappa \tag{A.10}$$

$$z_0 = \rho c \tag{A.11}$$

with reference quantities and constants listed in Table A.1.

Table A.1: Some reference quantities and constants. Compiled from ICAO 7488:1993 [220] and [414].

Ref. Temperature	$T_{ref} = 288.15$	K
Ref. Pressure	$p_{ref} = 1.01325 \times 10^{-5}$	Pa
Ref. Dynamic Viscosity	$\mu_{ref} = 1.7894 \times 10^{-5}$	$N\,s\,m^{-2}$
Ref. Thermal Conductivity	$\kappa_{ref} = 2.5343 \times 10^{-2}$	$W\,m^{-1}\,K^{-1}$
Specific Gas Constant	$R = 287.05287$	$J\,kg^{-1}\,K^{-1}$
Sutherland Constant	$T_s = 110.4$	K
Empirical Constant	$T_a = 245.4$	K
Empirical Constant	$T_b = 27.6$	K

A.2 IDEAL GAS VS. REAL GAS

The ideal gas assumptions reproduce the behavior of air at ambient conditions very accurately. However, real gas effects become more prominent when the density of the molecules is increased[1] or at very high temperatures[2] when polyatomic molecules might dissociate into their constituent atoms [33]. While the second effect is far beyond the temperature range encountered in this work, the first phenomenon might be of importance. Therefore, the properties of air are calculated based on the real gas equations given by Lemmon et al. [296] and Lemmon and Jacobsen [295] and compared to the ideal gas results. Table A.2 presents a comparison at ISA conditions and at the extreme condition of the Hot Acoustic Test Rig HAT. As expected, the ideal and real calculations agree very well at ambient conditions. However, at the elevated pressure and temperature condition their differences can become as large as 12 %. Motivated by this rather large discrepancy, the properties of air are calculated based on the real gas equations throughout the entire work.

1 That can either be at high pressure, low temperature, or both.

2 Batchelor [33] gives a temperature of 3000 K for oxygen and 6000 K for nitrogen.

Table A.2: Various properties of dry air at ISA conditions (at sea level: 288.15 K, 101.325 kPa) and the extreme conditions of the Hot Acoustic Test Rig (823.15 K, 1100 kPa) calculated according to ideal gas and real gas relations and their difference in percent.

			288.15 K, 101.325 kPa			823.15 K, 1100 kPa		
			ideal	real	Δ	ideal	real	Δ
ρ	10^0	kg/m^3	1.2250	1.2252	0.02 %	4.6553	4.6366	-0.40 %
c	10^2	m/s	3.4029	3.4045	0.05 %	5.7515	5.6759	-1.33 %
μ	10^{-5}	$N\,s/m^2$	1.7894	1.7962	0.38 %	3.6884	3.8147	3.31 %
ν	10^{-5}	m^2/s	1.4607	1.4660	0.36 %	0.7923	0.8227	3.70 %
κ	10^{-2}	$W/m/K$	2.5314	2.5499	0.72 %	5.8911	5.8595	-0.54 %
χ	10^{-5}	m^2/s	2.0568	2.0682	0.55 %	1.2596	1.1429	-10.21 %
Pr	10^{-1}	–	7.1018	7.0880	-0.19 %	6.2903	7.1986	12.62 %
c_p	10^3	$J/kg/K$	1.0047	1.0062	0.15 %	1.0047	1.1057	9.14 %
c_v	10^2	$J/kg/K$	7.1763	7.1763	0.00 %	7.1763	8.1741	12.21 %
γ	10^0	–	1.4000	1.4022	0.15 %	1.4000	1.3527	-3.49 %
z_0	10^2	$kg/s/m^2$	4.1686	4.1714	0.07 %	26.775	26.317	-1.74 %

A.3 TABLES OF REAL GAS PROPERTIES

The following tables for dry air are based on the real gas equations given by Lemmon et al. [296] and Lemmon and Jacobsen [295]. Each table lists a variety of pressure and temperature combinations. Some distinguished conditions are (all indicated in bold):

- ISA conditions (sea level): 288.15 K, 101.325 kPa,
- HAT extreme conditions: 823.15 K, 1100 kPa, and
- exemplary combustor conditions: 2000 K, 2000 kPa.

Table A.3: Density ρ in $kg\,m^{-3}$.

Temperature T in K	Pressure p in kPa						
	100	101.325	200	600	1000	1100	2000
273.15	1.2758	1.2928	2.5532	7.6771	12.823	14.113	25.777
288.15	1.2092	**1.2252**	2.4194	7.2700	12.135	13.353	24.353
293.15	1.1885	1.2043	2.3779	7.1439	11.922	13.119	23.914
303.15	1.1492	1.1645	2.2991	6.9045	11.519	12.673	23.085
323.15	1.0779	1.0922	2.1562	6.4715	10.790	11.870	21.595
373.15	0.9333	0.9457	1.8664	5.5965	9.3227	10.254	18.617
423.15	0.8229	0.8338	1.6454	4.9315	8.2109	9.0296	16.378
573.15	0.6075	0.6155	1.2145	3.6382	6.0547	6.6578	12.065
773.15	0.4503	0.4563	0.9003	2.6971	4.4888	4.9360	8.9456
823.15	0.4230	0.4286	0.8457	2.5334	4.2165	**4.6366**	8.4038
2000.00	0.1741	0.1764	0.3482	1.0438	1.7384	1.9119	**3.4707**

Table A.4: Speed of sound c in $m\,s^{-1}$.

Temperature T in K	Pressure p in kPa						
	100	101.325	200	600	1000	1100	2000
273.15	331.48	331.48	331.54	331.82	332.15	332.24	333.19
288.15	340.45	**340.45**	340.54	340.93	341.37	341.49	342.66
293.15	343.38	343.38	343.48	343.91	344.38	344.50	345.74
303.15	349.17	349.17	349.29	349.77	350.30	350.44	351.79
323.15	360.45	360.45	360.59	361.17	361.79	361.95	363.50
373.15	387.04	387.04	387.23	387.98	388.76	388.95	390.81
423.15	411.68	411.68	411.89	412.73	413.59	413.81	415.83
573.15	476.57	476.58	476.80	477.73	478.67	478.91	481.05
773.15	548.97	548.97	549.19	550.09	551.00	551.22	553.27
823.15	565.37	565.38	565.59	566.48	567.37	**567.59**	569.61
2000.00	863.51	863.51	863.66	864.26	864.87	865.02	**866.39**

Table A.5: Characteristic acoustic impedance $z_0 = \rho c$ in $\mathrm{kg\,s^{-1}\,m^{-2}}$.

Temperature T in K	Pressure p in kPa						
	100	101.325	200	600	1000	1100	2000
273.15	422.92	428.52	846.49	2547.4	4259.3	4689.0	8588.7
288.15	411.68	**417.14**	823.92	2478.6	4142.5	4560.0	8344.7
293.15	408.12	413.53	816.78	2456.8	4105.7	4519.4	8268.0
303.15	401.28	406.60	803.04	2415.0	4035.0	4441.2	8121.1
323.15	388.54	393.69	777.48	2337.3	3903.8	4296.5	7849.8
373.15	361.22	366.01	722.70	2171.3	3624.2	3988.2	7275.8
423.15	338.77	343.26	677.72	2035.4	3396.0	3736.6	6810.6
573.15	289.50	293.34	579.07	1738.1	2898.2	3188.4	5803.7
773.15	247.21	250.49	494.45	1483.7	2473.3	2720.8	4949.3
823.15	239.14	242.31	478.30	1435.1	2392.3	**2631.7**	4786.8
2000.00	150.35	152.34	300.70	902.10	1503.5	1653.8	**3007.0**

Table A.6: Dynamic viscosity μ in $10^{-6}\,\mathrm{kg\,m^{-1}\,s^{-1}}$.

Temperature T in K	Pressure p in kPa						
	100	101.325	200	600	1000	1100	2000
273.15	17.218	17.218	17.233	17.296	17.363	17.380	17.544
288.15	17.961	**17.962**	17.976	18.037	18.100	18.117	18.272
293.15	18.205	18.206	18.220	18.280	18.343	18.359	18.511
303.15	18.689	18.689	18.703	18.761	18.822	18.838	18.986
323.15	19.635	19.635	19.649	19.705	19.762	19.777	19.916
373.15	21.896	21.896	21.909	21.959	22.010	22.023	22.144
423.15	24.027	24.027	24.038	24.083	24.129	24.141	24.249
573.15	29.811	29.811	29.819	29.854	29.890	29.898	29.980
773.15	36.530	36.531	36.537	36.564	36.591	36.597	36.658
823.15	38.084	38.084	38.090	38.115	38.140	**38.147**	38.204
2000.00	68.068	68.068	68.071	68.081	68.092	68.094	**68.117**

Table A.7: Kinematic viscosity $\nu = \mu/\rho$ in $10^{-6}\,m^2\,s^{-1}$.

Temperature T in K	Pressure p in kPa						
	100	101.325	200	600	1000	1100	2000
273.15	13.496	13.319	6.7498	2.2530	1.3540	1.2315	0.6806
288.15	14.854	**14.660**	7.4298	2.4810	1.4916	1.3567	0.7503
293.15	15.318	15.117	7.6621	2.5588	1.5385	1.3995	0.7741
303.15	16.262	16.049	8.1349	2.7173	1.6341	1.4864	0.8224
323.15	18.215	17.977	9.1128	3.0448	1.8315	1.6661	0.9223
373.15	23.462	23.155	11.739	3.9237	2.3609	2.1479	1.1895
423.15	29.198	28.816	14.609	4.8836	2.9387	2.6735	1.4806
573.15	49.074	48.433	24.553	8.2059	4.9366	4.4908	2.4849
773.15	81.121	80.060	40.582	13.556	8.1515	7.4144	4.0979
823.15	90.038	88.862	45.042	15.045	9.0454	**8.2273**	4.5461
2000.00	390.94	385.83	195.51	65.226	39.169	35.616	**19.626**

Table A.8: Thermal conductivity κ in $10^{-3}\,W\,m^{-1}\,K^{-1}$.

Temperature T in K	Pressure p in kPa						
	100	101.325	200	600	1000	1100	2000
273.15	24.360	24.360	24.395	24.541	24.696	24.736	25.118
288.15	25.498	**25.499**	25.531	25.668	25.813	25.851	26.207
293.15	25.873	25.874	25.906	26.040	26.182	26.218	26.567
303.15	26.618	26.618	26.649	26.778	26.914	26.949	27.282
323.15	28.082	28.083	28.112	28.232	28.357	28.390	28.696
373.15	31.620	31.620	31.644	31.746	31.852	31.879	32.134
423.15	35.000	35.001	35.022	35.110	35.201	35.224	35.442
573.15	44.417	44.418	44.433	44.495	44.559	44.575	44.726
773.15	55.795	55.795	55.806	55.851	55.896	55.908	56.014
823.15	58.490	58.491	58.501	58.542	58.585	**58.595**	58.694
2000.00	114.49	114.49	114.49	114.51	114.52	114.53	**114.56**

Table A.9: Thermal diffusivity $\chi = \kappa/(\rho c_p)$ in $10^{-6} m^2 s^{-1}$.

Temperature T in K	Pressure p in kPa						
	100	101.325	200	600	1000	1100	2000
273.15	18.981	18.733	9.4801	3.1468	1.8809	1.7084	0.9331
288.15	20.956	**20.682**	10.469	3.4788	2.0814	1.8910	1.0350
293.15	21.632	21.348	10.807	3.5922	2.1499	1.9534	1.0698
303.15	23.007	22.706	11.496	3.8232	2.2894	2.0803	1.1406
323.15	25.854	25.516	12.922	4.3011	2.5777	2.3428	1.2866
373.15	33.496	33.058	16.747	5.5822	3.3499	3.0456	1.6771
423.15	41.807	41.261	20.907	6.9740	4.1881	3.8083	2.0999
573.15	69.948	69.033	34.987	11.680	7.0192	6.3837	3.5245
773.15	113.39	111.91	56.718	18.936	11.380	10.350	5.7135
823.15	125.23	123.59	62.638	20.912	12.567	**11.429**	6.3088
2000.00	525.84	518.96	262.97	87.726	52.677	47.898	**26.391**

Table A.10: Heat capacity ratio $\gamma = c_p/c_v$.

Temperature T in K	Pressure p in kPa						
	100	101.325	200	600	1000	1100	2000
273.15	1.4027	1.4027	1.4049	1.4136	1.4223	1.4245	1.4445
288.15	1.4021	**1.4022**	1.4040	1.4117	1.4193	1.4213	1.4387
293.15	1.4019	1.4020	1.4038	1.4111	1.4184	1.4203	1.4369
303.15	1.4015	1.4016	1.4032	1.4100	1.4167	1.4184	1.4337
323.15	1.4007	1.4007	1.4021	1.4079	1.4136	1.4151	1.4280
373.15	1.3979	1.3979	1.3989	1.4030	1.4070	1.4080	1.4170
423.15	1.3943	1.3943	1.3951	1.3980	1.4010	1.4017	1.4082
573.15	1.3792	1.3792	1.3795	1.3809	1.3822	1.3825	1.3855
773.15	1.3566	1.3566	1.3568	1.3574	1.3579	1.3581	1.3593
823.15	1.3516	1.3516	1.3517	1.3521	1.3526	**1.3527**	1.3538
2000.00	1.2981	1.2981	1.2981	1.2981	1.2981	1.2981	**1.2981**

Table A.11: Specific heat capacity at constant pressure c_p in $J\,kg^{-1}\,K^{-1}$.

Temperature T in K	Pressure p in kPa						
	100	101.325	200	600	1000	1100	2000
273.15	1005.9	1005.9	1007.9	1015.9	1023.9	1025.9	1044.3
288.15	1006.2	**1006.2**	1008.0	1014.9	1022.0	1023.7	1039.7
293.15	1006.4	1006.4	1008.0	1014.7	1021.5	1023.1	1038.4
303.15	1006.7	1006.7	1008.3	1014.4	1020.6	1022.2	1036.2
323.15	1007.7	1007.7	1009.0	1014.3	1019.6	1020.9	1032.8
373.15	1011.5	1011.5	1012.4	1016.2	1019.9	1020.8	1029.2
423.15	1017.4	1017.4	1018.1	1020.9	1023.7	1024.3	1030.5
573.15	1045.4	1045.4	1045.7	1047.1	1048.5	1048.8	1051.9
773.15	1092.7	1092.7	1092.9	1093.5	1094.2	1094.4	1095.9
823.15	1104.3	1104.3	1104.4	1105.0	1105.6	**1105.7**	1107.1
2000.00	1250.4	1250.4	1250.5	1250.5	1250.6	1250.6	**1250.7**

Table A.12: Specific heat capacity at constant volume c_v in $J\,kg^{-1}\,K^{-1}$.

Temperature T in K	Pressure p in kPa						
	100	101.325	200	600	1000	1100	2000
273.15	717.11	717.11	717.42	718.65	719.88	720.19	722.95
288.15	717.63	**717.63**	717.90	718.96	720.03	720.30	722.69
293.15	717.83	717.84	718.09	719.11	720.13	720.39	722.67
303.15	718.29	718.29	718.53	719.46	720.40	720.64	722.73
323.15	719.41	719.42	719.62	720.42	721.23	721.43	723.22
373.15	723.55	723.55	723.69	724.28	724.86	725.01	726.31
423.15	729.65	729.65	729.77	730.22	730.68	730.79	731.80
573.15	757.95	757.95	758.02	758.29	758.55	758.62	759.22
773.15	805.43	805.43	805.48	805.64	805.81	805.85	806.23
823.15	817.03	817.03	817.07	817.22	817.38	**817.41**	817.76
2000.00	963.33	963.33	963.34	963.38	963.42	963.44	**963.53**

Table A.13: Prandtl number $Pr = c_p \mu / \kappa$.

Temperature T in K	Pressure p in kPa						
	100	101.325	200	600	1000	1100	2000
273.15	0.7110	0.7110	0.7120	0.7160	0.7199	0.7208	0.7294
288.15	0.7088	**0.7088**	0.7097	0.7132	0.7166	0.7175	0.7249
293.15	0.7081	0.7081	0.7090	0.7123	0.7156	0.7164	0.7236
303.15	0.7068	0.7068	0.7076	0.7107	0.7138	0.7145	0.7211
323.15	0.7045	0.7046	0.7052	0.7079	0.7105	0.7112	0.7168
373.15	0.7004	0.7004	0.7009	0.7029	0.7048	0.7052	0.7093
423.15	0.6984	0.6984	0.6988	0.7003	0.7017	0.7020	0.7051
573.15	0.7016	0.7016	0.7018	0.7026	0.7033	0.7035	0.7051
773.15	0.7154	0.7154	0.7155	0.7159	0.7163	0.7164	0.7172
823.15	0.7190	0.7190	0.7191	0.7194	0.7198	**0.7199**	0.7206
2000.00	0.7435	0.7435	0.7435	0.7435	0.7436	0.7436	**0.7437**

B

SOME MATHEMATICS

B.1 RAYLEIGH CONDUCTIVITY AND IMPEDANCE

The Rayleigh conductivity

$$K_R = i\omega\rho \frac{\hat{q}}{\hat{p}_1 - \hat{p}_2} \tag{B.1}$$

with

$$\hat{q} = v' \cdot A \tag{B.2}$$

results in

$$K_R = i\omega\rho A \frac{v'}{\hat{p}_1 - \hat{p}_2} \tag{B.3}$$

The specific acoustic impedance is defined as

$$z = \frac{\hat{p}_1 - \hat{p}_2}{v'} \tag{B.4}$$

so that it is related to the Rayleigh conductivity by

$$z = \frac{i\omega\rho A}{K_R} \tag{B.5}$$

or normalized with ρc

$$\frac{z}{\rho c} = \frac{ikA}{K_R} \tag{B.6}$$

B.2 CONVERSION OF TRANSFER MATRIX INTO SCATTERING MATRIX

This section follows closely the derivation given in [217, pp. 23]. The transfer matrix $\mathbf{T}$ relates the acoustic pressure and particle velocity at the input of a system to its output:

$$\begin{bmatrix} \hat{p}_1 \\ \hat{v}_1 \end{bmatrix} = \begin{bmatrix} T_{11} & T_{12} \\ T_{21} & T_{22} \end{bmatrix} \begin{bmatrix} \hat{p}_2 \\ \hat{v}_2 \end{bmatrix} \tag{B.7}$$

Equation (B.7) can be written as

$$\hat{p}_1 = \hat{p}_2 T_{11} + \hat{v}_2 T_{12} \tag{B.8}$$

$$\hat{v}_1 = \hat{p}_2 T_{21} + \hat{v}_2 T_{22} \tag{B.9}$$

The acoustic pressure and the acoustic particle velocity at positions 1 and 2 can be given in terms of incoming and outgoing waves as

$$\hat{p}_1 = \quad \hat{p}_1^+ e^{-ikx} + \hat{p}_1^- e^{ikx}, \tag{B.10}$$

$$\hat{p}_2 = \quad \hat{p}_2^+ e^{-ikx} + \hat{p}_2^- e^{ikx}, \tag{B.11}$$

$$\hat{v}_1 = \frac{1}{z_0}(\hat{p}_1^+ e^{-ikx} - \hat{p}_1^- e^{ikx}), \text{ and} \tag{B.12}$$

$$\hat{v}_2 = \frac{1}{z_0}(\hat{p}_2^+ e^{-ikx} - \hat{p}_2^- e^{ikx}). \tag{B.13}$$

For convenience one can write

$$P_1^+ = \hat{p}_1^+ e^{-ikx},\ P_1^- = \hat{p}_1^- e^{ikx},\ P_2^+ = \hat{p}_2^+ e^{-ikx}, \text{ and } P_2^- = \hat{p}_2^- e^{ikx}.$$

Inserting Equations (B.10) to (B.13) into Equations (B.8) and (B.9) with the simplification above yields

$$P_1^+ + P_1^- = (P_2^+ + P_2^-)T_{11} \quad + (P_2^+ - P_2^-)\frac{T_{12}}{z_0}, \text{ and} \tag{B.14}$$

$$P_1^+ - P_1^- = (P_2^+ + P_2^-)z_0 T_{21} + (P_2^+ - P_2^-)T_{22}\,. \tag{B.15}$$

Introducing the substitutions

$$X^{\pm} = T_{11} \pm \frac{T_{12}}{z_0} \quad \text{and} \quad Y^{\pm} = z_0 T_{21} \pm T_{22} \,,$$

then Equations (B.14) and (B.15) yield

$$P_1^+ + P_1^- = X^+ P_2^+ + X^- P_2^- \,, \text{ and} \tag{B.16}$$

$$P_1^+ - P_1^- = Y^+ P_2^+ + Y^- P_2^- \,, \tag{B.17}$$

which can be rearranged to

$$P_1^- = \frac{X^+ - Y^+}{X^+ + Y^+} P_1^+ + \frac{X^+ Y^- - Y^+ X^-}{X^+ + Y^-} P_2^- \,, \text{ and} \tag{B.18}$$

$$P_2^+ = \frac{2}{X^+ + Y^+} P_1^+ - \frac{X^- + Y^-}{X^+ + Y^+} P_2^- \,. \tag{B.19}$$

Written in matrix form, Equations (B.18) and (B.19) result in the common expression of the scattering matrix

$$\begin{bmatrix} \hat{p}_1^- \\ \hat{p}_2^+ \end{bmatrix} = \begin{bmatrix} S_{11} & S_{12} \\ S_{21} & S_{22} \end{bmatrix} \begin{bmatrix} \hat{p}_1^+ \\ \hat{p}_2^- \end{bmatrix} \tag{B.20}$$

with the elements

$$S_{11} = \frac{X^+ - Y^+}{X^+ + Y^+} \,, \qquad S_{12} = \frac{X^+ Y^- - Y^+ X^-}{X^+ + Y^+} \,,$$

$$S_{21} = \frac{2}{X^+ + Y^+} \,, \text{ and} \quad S_{22} = -\frac{X^- + Y^-}{X^+ + Y^+} \,.$$

BIBLIOGRAPHY

[1] Åbom, M.: "Measurement of the scattering-matrix of acoustical two-ports", *Mechanical Systems and Signal Processing*, 5(2):89–104, 1991. (Cited on pages 139, 153, and 154.)

[2] Åbom, M.; Bodén, H.: "Error analysis of two-microphone measurements in ducts with flow", *Journal of the Acoustical Society of America*, 83(6):2429–2438, 1988. (Cited on pages 146 and 147.)

[3] Abramowitz, M.; Stegun, I.A.: *Handbook of mathematical functions*, Applied Mathematics Series 55, National Bureau of Standards, 1970. (Cited on pages 62 and 103.)

[4] ACARE: "European aeronautics: A vision for 2020", Report, Advisory Council for Aviation Research and Innovation in Europe, 2001. (Cited on page 4.)

[5] ACARE: "Flightpath 2050 - Europe's vision for aviation", Report, Advisory Council for Aviation Research and Innovation in Europe, 2011. (Cited on page 4.)

[6] Ahuja, K.K.; Cataldi, P.; R. J. Gaeta, J.: "Sound absorption of a 2DOF resonant liner with negative bias flow", Contractor Report NASA-CR-2000-210637, NASA, 2000. (Cited on pages 34 and 54.)

[7] Ahuja, K.K.; Gaeta, R.J.: "Active control of liner impedance by varying perforate orifice geometry", Contractor Report NASA-CR-2000-210633, NASA, 2000. (Cited on pages 17, 28, 38, and 235.)

[8] Ahuja, K.K.; Gaeta, R.J.; Agostino, M.D.: "Acoustic absorption characteristics of an orifice with a mean bias flow", Contractor Report NASA-CR-2000-210636, NASA, 2000. (Cited on pages 28, 29, 35, and 54.)

[9] Ahuja, K.K.; Gaeta, R.J.; Hsu, J.S.: "Acoustic properties and durabilitiy of liner materials at non-standard atmospheric conditions", Contractor Report NASA-CR-195010, NASA, 1994. (Cited on pages 26 and 270.)

[10] Ahuja, K.K.; R. J. Gaeta, J.; D'Agostino, M.: "High amplitude acoustic behaviour of a slit-orifice backed by a cavity", Contractor Report NASA-CR-2000-210635, NASA, 2000. (Cited on page 18.)

[11] Alfredson, R.J.; Davies, P.O.A.L.: "Performance of exhaust silencer components", *Journal of Sound and Vibration*, 15(2):175–196, 1971. (Cited on page 53.)

[12] Allam, S.; Åbom, M.: "Acoustic modelling and testing of a complex car muffler", in *International Congress on Sound and Vibration, ICSV13, 2-6 July 2006, Vienna, Austria*, 2006. (Cited on page 73.)

[13] Allam, S.; Åbom, M.: "Investigation of damping and radiation using full plane wave decomposition in ducts", *Journal of Sound and Vibration*, 292:519–534, 2006. (Cited on pages 124 and 126.)

[14] Allam, S.; Åbom, M.: "Experimental characterization of acoustic liners with extended reaction", in *14th AIAA/CEAS Aeroacoustics Conference, 5-7 May 2008, Vancouver, Canada*, AIAA-2008-3074, 2008. (Cited on pages 45, 73, and 75.)

[15] Anderson, J.D.: "Ludwig Prandtl's boundary layer", *Physics Today*, 58(1):42–48, 2005. (Cited on page 117.)

[16] Andreini, A.; Bianchini, C.; Facchini, B.; Simonetti, F.; Peschiulli, A.: "Assessment of numerical tools for the evaluation of the acoustic impedance of multi-perforated plates", in *ASME Turbo Expo 2011, 6-10 June 2011, Vancouver, Canada*, GT2011-46303, 2011. (Cited on pages 16, 19, 47, 49, 55, and 71.)

[17] Andreini, A.; Facchini, B.; Ferrari, L.; Lenzi, G.; Simonetti, F.; A.Peschiulli: "Experimental investigation of effusion liner geometries for aero-engine combustors: Evaluation of global acoustic parameters", in *ASME Turbo Expo 2012, 11-15 June 2012, Copenhagen, Denmark*, GT2012-69853, 2012. (Cited on pages 16, 19, 22, 35, 49, 50, 55, 72, 139, 245, 246, 262, and 263.)

[18] Andreini, A.; Facchini, B.; Giusti, A.; Vitale, I.; Turrini, F.: "Thermoacoustic analysis of a full annular lean burn aero-engine combustor", in *ASME Turbo Expo 2013, 3-7 June 2013, San Antonio, Texas, USA*, GT2013-94877, 2013. (Cited on pages 45, 49, 55, 73, and 75.)

[19] Andreini, A.; Facchini, B.; Picchi, A.; Tarchi, L.; Turrini, F.: "Experimental and theoretical investigation of thermal effectiveness in multiperforated plates for combustor liner effusion cooling", *Journal of Turbomachinery*, 136(9):1–13, 2014. (Cited on pages 49 and 50.)

[20] Anonymous: "Acoustic liner feasibility program", Contractor Report NASA-CR-111405, NASA, 1970. (Cited on page 44.)

[21] Armstrong, D.L.: "Acoustic grazing flow impedance using waveguide principles", Contractor Report NASA-CR-120848, NASA, 1971. (Cited on page 32.)

[22] ASTM E 1050-12: "Standard test method for impedance and absorption of acoustical materials using tube, two microphones and a digital frequency analysis system", Standard, American Society for Testing and Materials, 2012. (Cited on page 146.)

[23] Auregan, Y.; Leroux, M.: "Experimental evidence of an instability over an impedance wall in a duct with flow", *Journal of Sound and Vibration*, 317:432–439, 2008. (Cited on page 219.)

[24] Auregan, Y.; Starobinski, R.; Pagneux, V.: "Influence of grazing flow and dissipation effects on the acoustic boundary conditions at a lined wall", *Journal of the Acoustical Society of America*, 109(1):59–64, 2001. (Cited on page 32.)

[25] Avallone, E.A.; Baumeister, T.; Sadegh, A.M. (Eds.): *Marks' Standard Handbook for Mechanical Engineers*, 11th ed., McGraw Hill, New York, 2007. (Cited on pages 37 and 38.)

[26] von Barthel, F.: "Untersuchungen über nichtlineare Helmholtzresonatoren", *Frequenz*, 12(3):72–82, 1958. (Cited on pages 28, 34, 44, 45, 53, and 202.)

[27] Bartlett, M.S.: "Smoothing periodigrams from time-series with continuous spectra", *Nature*, 161:686–687, 1948. (Cited on page 140.)

[28] Bass, H.E.: "Absorption of sound by air: High temperature predictions", *Journal of the Acoustical Society of America*, 69(1):124–138, 1981. (Cited on page 130.)

[29] Bass, H.E.; Bauer, H.J.; Evans, L.B.: "Atmospheric absorption of sound: Analytical expressions", *Journal of the Acoustical Society of America*, 52(3):821–825, 1972. (Cited on pages 130 and 132.)

[30] Bass, H.E.; Sutherland, L.C.; Piercy, J.; Evans, L.: "Absorption of sound by the atmosphere", in W.P. Mason; R.N. Thurston (Eds.), *Physical Acoustics - Principles and Methods*, Vol. 17, Chap. 3, pp. 145–232, Academic Press, Orlando, FL, 1984. (Cited on pages 130, 131, 132, 133, and 134.)

[31] Bass, H.E.; Sutherland, L.C.; Zuckerwar, A.J.: "Atmospheric absorption of sound: Update", *Journal of the Acoustical Society of America*, 88:2019–2021, 1990. (Cited on page 130.)

[32] Bass, H.E.; Sutherland, L.C.; Zuckerwar, A.J.; Blackstock, D.T.; Hester, D.M.: "Atmosperic absorption of sound: Further developments", *Journal of the Acoustical Society of America*, 97(1):680–683, 1995. (Cited on pages 130 and 133.)

[33] Batchelor, G.K.: *An introduction to fluid dynamics*, Cambridge University Press, Cambridge, UK, 2000. (Cited on pages 39, 97, 98, 114, 115, and 284.)

[34] Bauer, A.B.: "Impedance theory and measurements on porous acoustic liners", *Journal of Aircraft*, 14(8):720–728, 1977. (Cited on pages 45, 67, 68, 73, 74, and 75.)

[35] Baumeister, K.J.; Rice, E.J.: "Visual study of the effect of grazing flow on the oscillatory flow in a resonator orifice", Technical Memorandum NASA-TM-X-3288, NASA, 1975. (Cited on page 50.)

[36] Beatty, R.E.: "Boundary layer attenuation of higher order modes in rectengular and circular tubes", *Journal of the Acoustical Society of America*, 22(6):850–854, 1950. (Cited on page 121.)

[37] Bechert, D.W.: "Sound absorption caused by vorticity shedding, demonstrated with a jet flow", in *5th AIAA Aeroacoustics Conference, 12-14 March 1979, Seattle, Washington*, AIAA-1979-0575, 1979. (Cited on pages 46 and 53.)

[38] Bechert, D.W.: "Sound absorption caused by vorticity shedding, demonstrated with a jet flow", *Journal of Sound and Vibration*, 70(3):389–405, 1980. (Cited on pages 6, 46, and 53.)

[39] Bechert, D.W.; Michel, U.; Pfizenmaier, E.: "Experiments on the transmission of sound through jets", in *4th AIAA Aeroacoustics Conference, 3-5 October 1977, Atlanta, Georgia*, AIAA-1977-1278, 1977. (Cited on pages 45 and 53.)

[40] Bechert, D.W.; Michel, U.; Pfizenmaier, E.: "Experiments on the transmission of sound through jets", *AIAA Journal*, 16(9):873–874, 1978. (Cited on pages 45, 53, and 203.)

[41] Bellucci, V.; Flohr, P.; Paschereit, C.O.: "Numerical and experimental study of acoustic damping generated by perforated screens", *AIAA Journal*, 42(8):1543–1549, 2004. (Cited on pages 28, 29, 35, 54, 64, 76, 77, 78, 79, 211, and 231.)

[42] Bellucci, V.; Flohr, P.; Paschereit, C.O.; Magni, F.: "On the use of Helmholtz resonators for damping acoustic pulsations in industial gas

turbines", *Journal of Engineering for Gas Turbines and Power*, 126:271–275, 2004. (Cited on pages 6, 47, 48, and 71.)

[43] Bellucci, V.; Paschereit, C.O.; Flohr, P.: "Impedance of perforated screens with bias flow", in *8th AIAA/CEAS Aeroacoustics Conference, 17-19 June 2002, Breckenridge, Colorado*, AIAA-2002-2437, 2002. (Cited on pages 54 and 76.)

[44] Bellucci, V.; Schuermans, B.; Nowak, D.; Flohr, P.; Paschereit, C.O.: "Thermoacoustic modeling of a gas turbine combustor equipped with acoustic dampers", *Journal of Turbomachinery*, 127(2):372–379, 2005. (Cited on page 80.)

[45] Beltrami, E.: "Sulle funzioni bilineari", *Giornale di Mathematiche ad Uso degli Studenti Delle Universita*, 11:98–106, 1873. (Cited on page 145.)

[46] Bendali, A.; Fares, M.; Piot, E.; Tordeaux, S.: "Methematical justification of the Rayleigh conductivity model for perforated plates in acoustics", *SIAM Journal on Applied Mathematics*, 73(1):438–459, 2013. (Cited on page 227.)

[47] Bendat, J.S.; Piersol, A.G.: *Random Data*, 4th ed., John Wiley and Sons, Hoboken, NJ, 2010. (Cited on pages 28, 141, 142, and 143.)

[48] Beranek, L.L.: *Acoustics*, Acoustical Society of America, Woodbury, NY, 1993. (Cited on page 110.)

[49] Bernoulli, D.: *Hydrodynamica, sive de viribus et motibus fluidorum commentarii (Hydrodynamics, or notes on the forces and motion of fluids)*, Johann Reinhold Dulsecker, Strasbourg, 1738. (Cited on page 39.)

[50] Bernoulli, J.: "Analysis problematis antehac porpositi, de inventione linea descensus a corpore gravi percurrendae uniformiter, sic ut temporibus aequales altitudines emetiatur: & alterius cujusdam Problematis Propositio", *Acta Eruditorum*, 9:217–219, 1690. (Cited on page 101.)

[51] Bessel, F.W.: "Analytische Auflösung der Kepler'schen Aufgabe", *Abhandlungen der Berliner Akademie (1816-17)*, pp. 49–55, 1819. (Cited on page 62.)

[52] Betts, J.F.: *Experiments and impedance modeling of liners including the effect of bias flow*, Ph.d. thesis, Virginia Polytechnic Institute and State University, 2000. (Cited on pages 27, 45, 54, 65, 68, 75, and 76.)

[53] Betts, J.F.; Follet, J.I.; Kelly, J.; Wood, H.: "An improved impedance model for perforates including the effect of bias flow", in *39th AIAA*

Aerospace Sciences Meeting & Exhibit, 8-11 January 2001, Reno, Nevada, AIAA-2001-0990, 2001. (Cited on page 54.)

[54] Betts, J.F.; Follet, J.I.; Kelly, J.J.; Thomas, R.H.: "Evaluation of an impedance model for perforates including the effect of bias flow", in *6th AIAA/CEAS Aeroacoustics Conference, 12-14 June 2000, Lahaina, Hawaii*, AIAA-2000-31118, 2000. (Cited on pages 45, 54, 65, 66, 68, 75, 76, and 79.)

[55] Bhayaraju, U.; Schmidt, J.; Kashinath, K.; Hochgreb, S.: "Effect of cooling liner on acoustic energy absorption and flame response", in *ASME Turbo Expo 2010, 14-18 June 2010, Glasgow, UK*, GT2010-22616, 2010. (Cited on pages 19, 26, 27, 35, 51, 55, and 269.)

[56] Bielak, G.; Kunze, J.G.G.; Murray, P.; Premo, J.; Kosanchick, J.; Hersh, A.; Celano, J.; Walker, B.; Yu, J.; Kwan, H.W.; Chiou, S.; Kelly, J.; Betts, J.; Follet, J.; Thomas, R.: "Advanced nacelle acoustic lining concepts development", Contractor Report NASA-CR-2002-211672, NASA, 2002. (Cited on pages 32, 45, and 54.)

[57] Bielak, G.W.; Premo, J.W.; Hersh, A.S.: "Advanced turbofan duct liner concepts", Contractor Report NASA-CR-1999-209002, NASA, 1999. (Cited on page 45.)

[58] Bies, D.A.; Wilson, O.B.: "Acoustic impedance of a helmholtz resonator at very high amplitude", *Journal of the Acoustical Society of America*, 29:711–714, 1957. (Cited on pages 28, 45, and 202.)

[59] Bird, R.B.; Stewart, W.E.; Lightfoot, E.N.: *Transport Phenomena*, 2nd ed., John Wiley & Sons, New York, 2002. (Cited on page 97.)

[60] Björck, A.: *Numerical Methods for least squares problems*, Society for Industrial and Applied Mathematics, Philadelphia, 1996. (Cited on page 147.)

[61] Blackman, A.W.: "Effect of nonlinear losses on the design of absorbers for combustion instabilities", *ARS Journal*, 30:1022–1028, 1960. (Cited on pages 28, 45, and 202.)

[62] Blackman, A.W.: "Variable pressure wave absorption for combustion chambers", Patent US2941356, United Aircraft Corporation, 1960. (Cited on page 44.)

[63] Blackman, R.B.; Tukey, J.W.: *The measurement of power spectra from the point of view of communications engineering*, Dover, New York, 1959. (Cited on page 141.)

[64] Blackstock, D.T.: *Fundamental of physical acoustics*, John Wiley & Sons, New York, 2000. (Cited on page 117.)

[65] Blasius, H.: "Das Aehnlichkeitsgesetz bei Reibungsvorgängen", *Zeitschrift des Vereins Deutscher Ingenieure*, 56(16):639–643, 1912. (Cited on page 33.)

[66] Blokhintsev, D.I.: "Acoustics of a nonhomogeneous moving medium", Technical Memorandum 1399, NACA, originally published 1946 in russian, 1956. (Cited on page 155.)

[67] Bloxsidge, G.J.; Dowling, A.P.; Langhorne, P.J.: "Reheat buzz: an acoustically coupled combustion instability. Part 2. Theory", *Journal of Fluid Mechanics*, 193:445–473, 1988. (Cited on page 5.)

[68] Bodén, H.: "Acoustic properties of perforates under high level multi-tone excitation", in *19th AIAA/CEAS Aeroacoustics Conference, 27-29 May 2013, Berlin, Germany*, AIAA-2013-2175, 2013. (Cited on page 32.)

[69] Bodén, H.; Åbom, M.: "Influence of errors on the two-microphone method for measuring acoustic properties in ducts", *Journal of the Acoustical Society of America*, 79(2):541–549, 1986. (Cited on page 146.)

[70] Bodén, H.; Zhou, L.: "Acoustic properties of an in-duct orifice subjected to bias flow and high level acoustic excitation", in *10th International Conference on Flow-Induced Vibration, 2-6 July 2012, Dublin, Ireland*, 2012. (Cited on pages 50, 55, 203, 271, and 273.)

[71] Boij, S.: "Low frequency sound absorption at sharp edges in flow ducts", in *12th International Congress on Sound and Vibration, ICSV12, 11-14 July 2005, Lisbon, Portugal*, 2005. (Cited on page 54.)

[72] Bolt, R.H.; Labate, S.; Ingard, U.: "The acoustic reactance of small circular orifices", *Journal of the Acoustical Society of America*, 21(2):94–97, 1949. (Cited on pages 28, 45, 59, 65, and 202.)

[73] Borth, W.: "Schwingungs- und Resonanzerscheinungen in den Rohrleitungen von Kolbengebläsen (Vibration and resonance phenomena in the ducts of piston blowers)", *Zeitschrift des Vereines Deutscher Ingenieure*, 60:565, 1916. (Cited on pages 43 and 53.)

[74] Brandes, M.: *Optimierung eines Meßvervahrens zur Bestimmung von akustischen Parametern im durchströmten Rohr*, Diploma thesis, Universität Göttingen, 1992. (Cited on pages 139 and 147.)

[75] Brandes, M.: *Schallverstärkung in Strömungskanälen mit resonanzartiger Wandauskleidung*, Doctoral thesis, Universität Göttingen, 1997. (Cited on page 219.)

[76] Brater, E.F.; King, H.W.: *Handbook of hydraulics*, 7th ed., McGraw Hill, Boston, 1996. (Cited on pages 36, 37, and 38.)

[77] Bronshtein, I.N.; Semendyayev, K.A.; Musiol, G.; Mülig, H.: *Handbook of Mathematics*, 5th ed., Springer, Berlin, 2007. (Cited on pages 62, 97, 100, 101, 115, and 142.)

[78] Brown, W.H.: "Anti-screech inner body", Patent US2934891, United Aircraft Corporation, 1960. (Cited on page 44.)

[79] Bruneau, A.M.; Bruneau, M.; Herzog, P.; Kergomard, J.: "Boundary layer attenuation of higher order modes in waveguides", *Journal of Sound and Vibration*, 119(1):15–27, 1987. (Cited on page 121.)

[80] Bräunling, W.J.G.: *Flugzeugtriebwerke*, 3rd ed., Springer, Berlin, 2009. (Cited on pages 2, 14, and 15.)

[81] Budoff, M.; Zorumski, W.E.: "Flow resistance of perforated plates in tangential flow", Technical Memorandum NASA-TM-X-2361, NASA, 1971. (Cited on page 32.)

[82] Busse-Gerstengarbe, S.; Bake, F.; Enghardt, L.; Jones, M.G.: "Comparative study of impedance eduction methods, Part 1: DLR tests and methodology", in *19th AIAA/CEAS Aeroacoustics Conference, 27-29 May 2013, Berlin, Germany*, AIAA-2013-2124, 2013. (Cited on pages 27, 28, and 30.)

[83] Busse-Gerstengarbe, S.; Richter, C.; Thiele, F.H.; Lahiri, C.; Enghardt, L.; Röhle, I.; Ferrante, P.; Scofano, A.: "Impedance eduction based on microphone measurements of liners under grazing flow conditions", *AIAA Journal*, 50(4):867–879, 2012. (Cited on pages 32 and 139.)

[84] Callaghan, E.E.; Bowden, D.T.: "Investigation of flow coefficient of circular, square, and elliptical orifices at high pressure ratios", Technical Note 1947, NACA, 1949. (Cited on page 38.)

[85] Camporeale, S.M.; Fortunato, B.; Mastrovito, M.: "Prediction of thermoacoustic instability in combustion chamber equipped with passive dampers", in *ASME Turbo Expo 2008, 9-13 June 2008, Berlin, Germany*, GT2008-51387, 2008. (Cited on page 6.)

[86] Campos, L.M.B.C.: "On 36 forms of the acoustic wave equation in potential flows and inhomogeneous media", *Applied Mechanics Review*, 60:149–171, 2007. (Cited on page 101.)

[87] Cataldi, P.; Ahuja, K.K.; Gaeta, R.J.: "Enhanced sound absorption through negative bias flow", in *5th AIAA/CEAS Aeroacoustics Conference, 10-12 May 1999, Bellevue, Washington*, AIAA-1999-1879, 1999. (Cited on pages 27, 34, and 54.)

[88] Cerri, G.; Giovannelli, A.; Battisti, L.; Fedrizzi, R.: "Advances in effusive cooling techniques of gas turbines", *Applied Thermal Engineering*, 27:692–698, 2007. (Cited on page 13.)

[89] Chanaud, R.C.: "Effects of geometry on the resonance frequency of Helmholtz resonators", *Journal of Sound and Vibration*, 178(3):337–348, 1994. (Cited on pages 17 and 234.)

[90] Chien, E.W.; Yu, J.: "Experimental computational study of fluid dynamics and acoustics of perforate acoustic liner", in *7th AIAA/CEAS Aeroacoustics Conference, 28-30 May 2001, Maastricht, Netherlands*, AIAA-2001-2264, 2001. (Cited on page 27.)

[91] Chisholm, H. (Ed.): *Encyclopedia Britannica - A dictonary of arts, sciences, literature and general information*, 11th ed., Encyclopedia Britannica Inc., New York, 1911. (Cited on page 37.)

[92] Cho, H.H.; Rhee, D.H.; Kim, B.G.: "Enhancement of film cooling performance using a shaped film cooling hole with compound angle injection", *JSME International Journal Series B Fluids and Thermal Engineering*, 44(1):98–110, 2001. (Cited on page 13.)

[93] Christie, D.R.A.: "Measurement of the acoustic properties of a sound absorbing material at high temperatures", *Journal of Sound and Vibration*, 46(3):347–355, 1976. (Cited on pages 26 and 266.)

[94] Chu, W.T.: "Impedance tube measurements - A comparative study of current practices", *Noise Control Engineering Journal*, 37(1):37–44, 1991. (Cited on page 147.)

[95] Chung, J.: "Rejection of flow noise using a coherence function method", *Journal of the Acoustical Society of America*, 62(2):388–395, 1977. (Cited on pages 140 and 143.)

[96] Chung, J.Y.; Blaser, D.A.: "Transfer function method of measuring induct acoustic properties, I. Theory", *Journal of the Acoustical Society of America*, 68(3):907–913, 1980. (Cited on page 146.)

[97] CLAPEYRON, B.P.E.: "Mémoire sur la puissance motrice de la chaleur (Memoir on the motive power of heat)", *Journal de l'Ecole Royale Polytechique*, 14:153–190, 1834, (english translation in: Scientific Memoirs, Selected From the Transactions of Foreign Academies of Science and Learned Societies and From Foreign Journals, 1:347-376, 1837). (Cited on page 98.)

[98] COHEN, J.M.; BANASZUK, A.: "Factors affecting the control of unstable combustors", in [305], Chap. 18, pp. 581–609, 2005. (Cited on page 6.)

[99] COSIC, B.; REICHEL, T.G.; PASCHEREIT, C.O.: "Acoustic response of a Helmholtz resonator exposed to hot-gas penetration and high amplitude oscillations", *Journal of Engineering for Gas Turbines and Power*, 134:101503, 2012. (Cited on page 203.)

[100] CRANDALL, I.B.: *Theory of vibrating systems and sound*, D. Van Nostrand, New York, 1926. (Cited on pages 59, 61, and 62.)

[101] CREMER, L.: "Über die akustische Grenzschicht vor starren Wänden", *Archiv der elektrischen Übertragung*, 2:136–139, 1948. (Cited on pages 115, 117, 118, and 121.)

[102] CULICK, F.E.C.: "Unsteady motions in combustion chambers for propulsion systems", Technical Report RTO-AG-AVT-039, NATO Research and Technology Organization, 2006. (Cited on page 5.)

[103] CUMMINGS, A.: "Sound transmission at sudden area expansions in circular ducts, with superimposed mean flow", *Journal of Sound and Vibration*, 38(1):149–155, 1975. (Cited on page 53.)

[104] CUMMINGS, A.: "High temperature effects on the radiation impedance of an unflanged duct exit", *Journal of Sound and Vibration*, 52(2):229–304, 1977. (Cited on page 26.)

[105] CUMMINGS, A.: "Acoustic nonlinearities and power losses at orifices", *AIAA Journal*, 22(6):786–792, 1984. (Cited on pages 28, 29, 45, 48, 50, 73, and 202.)

[106] CUMMINGS, A.: "The effects of grazing turbulent pip-flow on the impedance of an orifice", *Acta Acustica united with Acustica*, 61(4):233–242, 1986. (Cited on pages 32 and 67.)

[107] CUMMINGS, A.: "Transient and multiple frequency sound transmission through perforated plates at high amplitude", *Journal of the Acoustical Society of America*, 79:942–951, 1986. (Cited on pages 48, 50, and 73.)

[108] CUMMINGS, A.: "Sound propagation in narrow tubes of arbitrary cross-section", *Journal of Sound and Vibration*, 162(1):27–42, 1993. (Cited on page 121.)

[109] CUMMINGS, A.; EVERSMAN, W.: "High amplitude acoustic transmission through duct terminations: Theory", *Journal of Sound and Vibration*, 91(4):503–518, 1983. (Cited on pages 53 and 68.)

[110] DAHLQUIST, G.; BJÖRCK, A.: *Numerical Methods*, Dover, Mineola, NY, 2003. (Cited on pages 145 and 146.)

[111] D'ALEMBERT: "Recherches sur la courbe que forme une corde tenduë mise en vibration (Investigation of the curve formed by a vibrating string)", *Histoire de l'Académie des sciences et belles-lettres*, 3:214–219, 1747. (Cited on pages 100 and 109.)

[112] DASSE, J.; MENDEZ, S.; NICOUD, F.: "Large-eddy simulation of the acoustic response of a perforated plate", in *14th AIAA/CEAS Aeroacoustics Conference, 5-7 May 2008, Vancouver, Canada*, AIAA-2008-3007, 2008. (Cited on page 55.)

[113] DAVIES, P.O.A.L.: "Practical flow duct acoustics", *Journal of Sound and Vibration*, 124(1):91–115, 1988. (Cited on pages 121 and 122.)

[114] DAVIES, P.O.A.L.: "Slightly dispersive waves in pipes", *Journal of Sound and Vibration*, 132(1):169, 1989. (Cited on page 123.)

[115] DAVIES, P.O.A.L.; BHATTACHARYA, M.; COELHO, J.L.B.: "Measurement of plane wave acoustic fields in flow ducts", *Journal of Sound and Vibration*, 72(4):539–542, 1980. (Cited on pages 122 and 123.)

[116] DAVIS, D.D.; STOKES, G.M.; MOORE, D.; STEVENS, G.L.: "Theoretical and experimental investigation of mufflers with comments on engine-exhaust muffler design", Report 1192, NACA, 1954. (Cited on pages 23, 259, and 260.)

[117] DEAN, L.W.: "Coupling of Helmholtz resonators to improve acoustic liners for turbofan engines at low frequency", Contractor Report NASA-CR-134912, NASA, 1976. (Cited on page 74.)

[118] DEAN, P.D.; TESTER, B.J.: "Duct wall impedance control as an advanced concept for acoustic suppression", Contractor Report NASA-CR-134998, NASA, 1975. (Cited on pages 44, 45, 53, 67, and 221.)

[119] Deckker, B.E.L.; Chang, Y.F.: "An investigation of steady compressible flow through thick orifices", *Proceedings of the Institution of Mechanical Engineers*, 180:312–323, 1965. (Cited on page 36.)

[120] Delany, M.E.: "Sound propagation in the atmosphere: A historical review", *Acoustica*, 38:201–223, 1977. (Cited on pages 130, 131, and 132.)

[121] Delany, M.E.; Bazley, E.N.: "Acoustical properties of fibrous absorbent materials", *Applied Acoustics*, 3(2):105–116, 1970. (Cited on page 266.)

[122] Dickey, N.S.; Selamet, A.; Ciray, M.S.: "An experimental study of the impedance of perforated plates with grazing flow", *Journal of the Acoustical Society of America*, 110(5):2360–2370, 2001. (Cited on page 32.)

[123] Dickey, N.S.; Selamet, A.; Novak, J.M.: "The effect of high-amplitude sound on the attenuation of perforated tube silencers", *Journal of the Acoustical Society of America*, 108(3):1068–1081, 2000. (Cited on pages 28, 45, and 202.)

[124] Dittrich, R.T.: "Discharge coefficients for combustor-liner air-entry holes, 2 - Flush rectangular holes, step louvers, and scoops", Technical Note NACA-TN-3924, NACA, 1958. (Cited on page 38.)

[125] Dittrich, R.T.; Graves, C.C.: "Discharge coefficients for combustor-liner air-entry holes, 1 - Circular holes with parallel flow", Technical Note NACA-TN-3663, NACA, 1956. (Cited on page 38.)

[126] Dokumaci, E.: "Sound transmission in narrow pipes with superimposed uniform mean flow and acoustics modelling of automobile catalytic converters", *Journal of Sound and Vibration*, 182(5):799–808, 1995. (Cited on pages 113 and 123.)

[127] Dokumaci, E.: "A note on transmission of sound in a wide pipe with mean flow and viscothermal attenuation", *Journal of Sound and Vibration*, 208(4):653–655, 1997. (Cited on page 123.)

[128] Dokumaci, E.: "On transmission of sound in circular and rectangular narrow pipes with superimposed mean flow", *Journal of Sound and Vibration*, 210(3):375–389, 1998. (Cited on page 113.)

[129] Dowling, A.P.; Hughes, I.J.: "Sound absorption by a screen with a regular array of slits", *Journal of Sound and Vibration*, 156(3):387–405, 1992. (Cited on pages 17, 47, and 54.)

[130] Dowling, A.P.; Stow, S.R.: "Acoustic analysis of gas turbine combustors", *Journal of Propulsion and Power*, 19(5):751–764, 2003. (Cited on page 48.)

[131] Dowling, A.P.; Stow, S.R.: "Acoustic analyis of gas-turbine combustors", in [305], Chap. 13, pp. 369–414, 2005. (Cited on pages 6, 7, 47, 48, and 71.)

[132] Duhamel, M.J.M.C.: "Sur les vvibration des gaz dans des tuyaux cylindriques, coniques, etc.", *Journal de mathématiques pures et appliquées*, 14:49–110, 1849. (Cited on page 101.)

[133] Dupere, I.; Dowling, A.P.: "The absorption of sound near abrupt area axpansions", in *4th AIAA/CEAS Aeroacoustics Conference, 2-4 June 1998, Toulouse, France*, AIAA-1998-2303, 1998. (Cited on page 54.)

[134] Dupere, I.D.J.; Dowling, A.P.: "Absorption of sound near abrupt area expansions", *AIAA Journal*, 38(2):193–202, 2000. (Cited on page 54.)

[135] Dupere, I.D.J.; Dowling, A.P.: "The absorption of sound near abrupt axisymmetric area expansions", *Journal of Sound and Vibration*, 239(4):709–730, 2001. (Cited on page 54.)

[136] Dupere, I.D.J.; Dowling, A.P.: "The absorption of sound by helmholtzs resonators with and without flow", in *8th AIAA/CEAS Aeroacoustics Conference, 17-19 June 2002, Beckenridge, Colorado*, AIAA-2002-2590, 2002. (Cited on page 54.)

[137] Dupere, I.D.J.; Dowling, A.P.: "The use of helmholtz resonators in a practical combustor", *Journal of Engineering for Gas Turbines and Power*, 127:268–275, 2005. (Cited on pages 6 and 54.)

[138] Durrieu, P.; Hofmans, G.; Ajello, G.; Boot, R.; Auregan, Y.; Hirschberg, A.; Peters, M.C.A.M.: "Quasisteady aero-acoustic response of orifices", *Journal of the Acoustical Society of America*, 110(4):1859–1872, 2001. (Cited on pages 18, 54, and 139.)

[139] Efraimsson, G.; Pieper, T.; Åbom, M.; Boij, S.: "Simulation of wave scattering at an orifice by using a navier-stokes solver", in *13th AIAA/CEAS Aeroacoustics Conference, 21-23 May 2007, Rome, Italy*, AIAA-2007-3402, 2007. (Cited on page 55.)

[140] Eldredge, J.D.: "On the interaction of higher duct modes with a perforated liner system with bias flow", *Journal of Fluid Mechanics*, 510:303–331, 2004. (Cited on pages 27 and 54.)

[141] Eldredge, J.D.; Bodony, D.J.; Shoeybi, M.: "Numerical investigation of the acoustic behavior of a multi-perforated liner", in *13th AIAA/CEAS Aeroacoustics Conference 21-23 May 2007, Rome, Italy*, AIAA 2007-3683, 2007. (Cited on pages 19, 55, 245, and 246.)

[142] Eldredge, J.D.; Dowling, A.P.: "The absorption of axial acoustic waves by a perforated liner with bias flow", *Journal of Fluid Mechanics*, 485:307–335, 2003. (Cited on pages 16, 19, 25, 28, 30, 35, 47, 48, 49, 54, 71, 72, 85, 88, 156, 211, 227, 245, and 246.)

[143] Elnady, T.: *Modelling and characterization of perforates in lined ducts and mufflers*, Doctoral thesis, Kungliga Tekniska Högskolan, Stockholm, Sweden, 2004. (Cited on pages 45, 65, 66, 73, and 75.)

[144] Elnady, T.; Bodén; Kontio, T.: "Impedance of SDOF perforated liners at high temperatures", in *10th AIAA/CEAS Aeroacoustics Conference, 10-12 May 2004, Manchester, UK*, AIAA-2004-2842, 2004. (Cited on pages 26 and 266.)

[145] Elnady, T.; Bodén, H.: "On semi-empirical liner impedance modeling with grazing flow", in *9th AIAA/CEAS Aeroacoustics Conference, 12-14 May 2003, Hilton Head, South Carolina*, AIAA-2003-3304, 2003. (Cited on page 32.)

[146] Enghardt, L.: *Bestimmung akustischer Streufaktoren im durchströmten Rohr - Optimierung von Mikrofonanordung und Messprozedur*, Diploma thesis, Universität Göttingen, 1992. (Cited on pages 139 and 154.)

[147] English, E.J.: *A measurement based study of the acoustics of pipe systems with flow*, Ph.D. thesis, University of Southampton, 2010. (Cited on page 124.)

[148] Euler, L.: "Principes généraux du mouvement des fluides (general principles of the motion of fluids)", *Mémoires de l'académie des sciences de Berlin*, 11:274–315, 1757. (Cited on pages 97 and 98.)

[149] Euler, L.: "De la propagation du son (On the propagation of sound)", *Mémoires de l'académie des sciences de Berlin*, 15:185–209, 1766. (Cited on pages 100 and 109.)

[150] Euler, L.: "Supplement aux recherches sur la propagation du son (Supplement to the research on the propagation of sound)", *Mémoires de l'académie des sciences de Berlin*, 15:210–240, 1766. (Cited on page 100.)

[151] European Aviation Safety Agency: "E.012 Rolls-Royce plc. RB211 Trent 900 series engines", Engine Type Certificate Data Sheet, Issue 6, published 11 December 2013, accessed online 27 February 2014: `http://easa.europa.eu/certification/type-certificates/engines.php`. (Cited on page 3.)

[152] Evans, L.B.; Bass, H.E.; Sutherland, L.C.: "Atmospheric absorption of sound: Theoretical predictions", *Journal of the Acoustical Society of America*, 51(5):1565–1575, 1972. (Cited on pages 130 and 131.)

[153] Eversman, W.: "The effect of mach number on the tuning of an acoustic lining in a flow duct", *Journal of the Acoustical Society of America*, 48(2):425–428, 1970. (Cited on page 32.)

[154] Eversman, W.: "Effect of boundary layer on the transmission and attenuation of sound in an acoustically treated circular duct", *Journal of the Acoustical Society of America*, 49:1372–1380, 1971.

[155] Eversman, W.: "The boundary condition at an impedance wall in a non-uniform duct with potential mean flow", *Journal of Sound and Vibration*, 246(1):63–69, 2001. (Cited on page 32.)

[156] Fahy, F.: *Foundations of engineering acoustics*, Elsevier Academic Press, London, 2001. (Cited on page 61.)

[157] Farmer, G.; Brown, D.D.; Rutherford, M.E.: "Preferential multihole combustor liner", Patent US6655149, General Electric Company, 2003. (Cited on page 13.)

[158] Feder, E.; Dean, L.W.: "Analytical and experimental studies for predicting noise attenuation in acoustically treated ducts for turbofan engines", Contractor Report NASA-CR-1373, NASA, 1969. (Cited on pages 28, 29, 44, 53, and 218.)

[159] Flightglobal Insight: "Commercial engines 2013 year-end update", Special Report, published 11 December 2013, accessed online 27 February 2014: `http://www.flightglobal.com/airspace/media/reports_pdf/commercial-engines-2013-year-end-update-108241.aspx`. (Cited on page 2.)

[160] Fok, V.A.: "Teoreticheskoe issledovanie provodimosti kruglogo otverstiya v peregorodke, postavlennoi poperek truby (Theoretical study of the conductance of a circular hole in a partition across a tube)", *Doklady Akademii Nauk SSSR*, 31(9):875–882, 1941, alternatively: D. N. Rschevkin, A course of lectures on the theory of sound, Pergamon Press, London, 1963. (Cited on page 64.)

[161] Follet, J.I.; Betts, J.F.; Kelly, J.J.: "Improvements to acoustic liner broadband absorption using bias flow", in *39th Aerospace Sciences Meeting and Exhibit, 8-11 January 2001, Reno, Nevada*, AIAA-2001-0823, 2001. (Cited on pages 28, 29, 45, 54, and 211.)

[162] Follet, J.I.; Betts, J.F.; Kelly, J.J.; Thomas, R.H.: "Experimental impedance of single liner elements with bias flow", in *6th AIAA/CEAS Aeroacoustics Conference, 12-14 June 2000, Lahaina, Hawaii*, AIAA-2000-1950, 2000. (Cited on pages 27, 45, and 54.)

[163] Forecast International: "Forecast international expects power generation to fuel increasing demand for industrial gas turbines", Press Release, published 12 November 2013, accessed online 26 February 2014: `http://www.forecastinternational.com/press/release.cfm?article=272`. (Cited on page 2.)

[164] Forster, S.; Michel, U.: "Experimental investigation of the dissipation of acoustic energy in perforated walls with bias flow", in *International Colloquium on Combustion and Noise Control, 12-15 August 2003, Cranfield University, Cranfield, England*, 2003. (Cited on page 54.)

[165] Fourier, J.B.J.: *Théorie analytique de la chaleur (The analytic theory of heat)*, F. Didot, Paris, 1822. (Cited on pages 110, 115, and 141.)

[166] Fricker, N.; Roberts, C.A.: "The measurement of the acoustic radiation impedance of the open end of a thick walled tube with hot flow", *Acta Acustica united with Acustica*, 38(2):124–130, 1977. (Cited on page 26.)

[167] Fujimori, T.; Sato, S.; Minura, H.: "An automated measurement system of complex sound pressure reflection coefficients", in *InterNoise 84*, pp. 1009–1014, 1984. (Cited on page 147.)

[168] Fukumoto, Y.; Takayama, M.: "Vorticity production at the edge of a slit by sound waves in the presence of a low-mach-number bias flow", *Physics of Fluids A*, 3(12):3080–3082, 1991. (Cited on pages 18 and 54.)

[169] Gaeta, R.J.; Ahuja, K.K.: "Effect of orifice shape on acoustic impedance", in *39th AIAA Aerospace Sciences Meeting and Exhibit, 8-11 January 2001, Reno, Nevada*, AIAA-2001-0662, 2001. (Cited on pages 17 and 235.)

[170] Garrison, G.D.; Russell, P.L.; Koenig, J.W.; Schnell, A.C.: "Suppression of combustion oscillations with mechanical damping devices", Final Report PWA FR-4993, Pratt & Whitney Aircraft for NASA, 1972. (Cited on pages 44 and 53.)

[171] Garrison, G.D.; Schnell, A.C.; Baldwin, C.D.; Russell, P.R.: "Suppression of combustion oscillations with mechanical damping devices", Interim Report PWA FR-3299, Pratt & Whitney Aircraft for NASA, 1969. (Cited on pages 44, 53, 67, and 220.)

[172] Gauss, C.F.: *Theoria motus corporum coelestium in sectionibus conicis solem ambientum (Theory of the motion of the heavenly bodies moving about the sun in conic sections)*, F. Perthes and I. H. Besser, Hamburg, 1809. (Cited on page 147.)

[173] Gibbs, J.W.; Wilson, E.B.: *Vector analysis*, 2nd ed., Yale University Press, New Haven, 1929. (Cited on page 97.)

[174] Giese, F.; Ries, H.C.; Eigenbrod, C.: "On the performance of porous sound absorbent material in high temperature applications", *Journal of Engineering for Gas Turbine and Power*, 132:1–6, 2010. (Cited on pages 26 and 270.)

[175] Goldman, A.L.; Panton, R.L.: "Measurement of the acoustic impedance of an orifice under a turbulent boundary layer", *Journal of the Acoustical Society of America*, 60(6):1397–1404, 1976. (Cited on pages 32 and 67.)

[176] Goldstein, M.E.: *Aeroacoustics*, McGraw-Hill, New York, 1976. (Cited on page 99.)

[177] Goldstein, M.E.; Rice, E.: "Effect of shear on duct wall impedance", *Journal of Sound and Vibration*, 30(1):79–84, 1973. (Cited on page 32.)

[178] Goldstein, R.J.; Eckert, E.R.G.: "Effects of hole geometry and density on three-dimensional film cooling", *International Journal of Heat and Mass Transfer*, 17(5):595–607, 1974. (Cited on page 13.)

[179] Golub, G.H.; van Loan, C.F.: *Matrix Computations*, 3rd ed., John Hopkins University Press, Baltimore, 1996. (Cited on page 145.)

[180] Gordon, C.; Smith, P.W.: "Acoustic losses of a resonator with steady gas flow", *Journal of the Acoustical Society of America*, 37(2):257–267, 1965. (Cited on pages 44, 46, and 53.)

[181] Grace, S.M.; Horan, K.P.; Howe, M.S.: "The influence of shape on the rayleigh conductivity of a wall aperture in the presence of grazing flow", *Journal of Fluids and Structures*, 12:335–351, 1998. (Cited on pages 17, 67, and 234.)

[182] Greenspan, M.: "Rotational relaxation in nitrogen, oxygen, and air", *Journal of the Acoustical Society of America*, 31:155–160, 1959. (Cited on page 132.)

[183] Gritsch, M.; Schulz, A.; Wittig, S.: "Adiabatic wall effectiveness measurements of film-cooling holes with expanded exits", *Journal of Turbomachinery*, 120:549–556, 1998. (Cited on page 13.)

[184] Gritsch, M.; Schulz, A.; Wittig, S.: "Method for correlating discharge coefficients of film-cooling holes", *AIAA Journal*, 36(6):976–980, 1998. (Cited on page 38.)

[185] Gritsch, M.; Schulz, A.; Wittig, S.: "Effect of crossflows on the discharge coefficients of film cooling holes with varying angles of inclination and orientation", *Journal of Turbomachinery*, 123:781–787, 2001. (Cited on page 38.)

[186] Guess, A.W.: "Calculation of perforated plate liner parameters from specified acoustic resistance and reactance", *Journal of Sound and Vibration*, 40(1):119–137, 1975. (Cited on pages 64, 65, and 67.)

[187] Gullaud, E.; Mendez, S.; Sensiau, C.; Nicoud, F.; Pionsot, T.: "Effect of multiperforated plates on the acoustic modes in combustors", in *2nd Initiative on Advanced Combustion (INCA) Workshop, 23-24 October 2008, Rouen, France*, 2008. (Cited on page 55.)

[188] Gullaud, E.; Mendez, S.; Sensiau, C.; Wolf, P.; Nicoud, F.: "Damping effect of perforated plates on the acoustics of annular combustors", in *15th AIAA/CEAS Aeroacoustics Conference, 11-13 May 2009, Miami, Florida*, AIAA-2009-3260, 2009. (Cited on page 55.)

[189] Gysling, D.L.; Copeland, G.S.; McCormick, D.C.; Proscia, W.M.: "Combustion system damping augmentation with helmholtz resonators", *Journal of Engineering for Gas Turbines and Power*, 122:269–274, 2000. (Cited on page 6.)

[190] Harrje, D.T.; Reardon, F.H. (Eds.): *Liquid propellant rocket combustion instability*, NASA-SP-194, NASA, Washington, D.C., 1972. (Cited on page 5.)

[191] Haufe, D.; Fischer, A.; Czarske, J.; Schulz, A.; Bake, F.; Enghardt, L.: "High dynamic range measurements of acoustic particle velocity and flow velocity for the application at liners", in *19th AIAA/CEAS Aeroacoustics Conference, 27-29 May 2013, Berlin, Germany*, AIAA-2013-2053, 2013. (Cited on page 51.)

[192] Haufe, D.; Fischer, A.; Czarske, J.; Schulz, A.; Bake, F.; Enghardt, L.: "Multi-scale measurement of acoustic particle velocity and flow velocity for liner investigations", *Experiments in Fluids*, 54:1569, 2013. (Cited on page 51.)

[193] Heaviside, O.: "Electromagnetic induction and its propagation", *The Electrician*, 17:212, 1886, reprinted in: Electrical Papers Vol. 2, Section 29, p. 61-71, Macmillan & Co., 1894. (Cited on page 59.)

[194] Heidelberg, L.J.; Rice, E.J.: "Experimental evaluation of a spinning-mode acoustic-treatment design concept for aircraft inlets", Technical Paper NASA-TP-1613, NASA, 1980. (Cited on page 67.)

[195] von Helmholtz, H.: "Über den Einfluss der Reibung in der Luft auf die Schallbewegung", *Verhandlungen des Naturhistorisch-Medizinischen Vereins zu Heidelberg*, 56(17):257–260, 1863. (Cited on pages 62 and 114.)

[196] Herzfeld, K.F.; Litovitz, T.A.: *Absorption and dispersion of ultrasonic waves*, Academic Press, New York, 1959. (Cited on page 131.)

[197] Heuwinkel, C.: *Experimentelle Untersuchung der akustischen Eigenschaften perforierter Liner*, Diploma thesis, Technische Universität Berlin, 2006. (Cited on pages 54 and 161.)

[198] Heuwinkel, C.; Enghardt, L.; Röhle, I.: "Experimental investigation of the acoustic damping of perforated liners with bias flow", in *13th AIAA/CEAS Aeroacoustics Conference, 21-23 May 2007, Rome, Italy*, AIAA-2007-3525, 2007. (Cited on pages 16, 54, 139, and 211.)

[199] Heuwinkel, C.; Mühlbauer, B.; Busse, S.; Enghardt, L.; Noll, B.; Aigner, M.; Röhle, I.: "Comparison of experimental and numerical results concerning the damping of perforated liners with bias flow", in *ASME Turbo Expo 2008, 9-13 June 2008, Berlin, Germany*, GT2008-50585, 2008. (Cited on pages 28, 30, 55, 202, and 203.)

[200] Heuwinkel, C.; Pardowitz, B.; Bake, F.; Röhle, I.; Enghardt, L.: "On the excitation of a zero mass flow liner for acoustic damping", in *15th AIAA/CEAS Aeroacoustics Conference, 11-13 May 2009, Miami, FL*, AIAA-2009-3110, 2009. (Cited on pages 34 and 52.)

[201] Heuwinkel, C.; Piot, E.; Fischer, A.; Röhle, I.; Micheli, F.; Enghardt, L.; Bake, F.: "Characterization of a perforated liner by acoustic and optical measurements", in *16th AIAA/CEAS Aeroacoustics Conference, 7-9 June, Stockholm, Sweden*, AIAA-2010-3765, 2010. (Cited on pages 51, 55, and 281.)

[202] Heuwinkel, C.; Sadig, S.; Gerendás, M.; Enghardt, L.; Bake, F.: "Establishment of a high quality database for the modelling of perforated liners", in *ASME Turbo Expo 2010, 14-18 June 2010, Glasgow, UK*, GT2010-22329, 2010. (Cited on page 55.)

[203] Hofmans, G.C.J.; Boot, R.J.J.; Durrieu, P.P.J.M.; Auregan, Y.; Hirschberg, A.: "Aeroacoustics response of a slit-shaped diaphragm in a pipe at low Helmholtz number, 1: Quasi-steady results", *Journal of Sound and Vibration*, 244(1):35–56, 2001. (Cited on pages 18 and 54.)

[204] Hofmans, G.C.J.; Ranucci, M.; Ajello, G.; Auregan, Y.; Hirschberg, A.: "Aeroacoustics response of a slit-shaped diaphragm in a pipe at low Helmholtz number, 2: Unsteady results", *Journal of Sound and Vibration*, 244(1):57–77, 2001. (Cited on page 18.)

[205] Holmberg, A.; Åbom, M.; Bodén, H.: "Accurate experimental two-port analysis of flow generated sound", *Journal of Sound and Vibration*, 330:6336–6354, 2011. (Cited on page 124.)

[206] Holste, F.: *Ermittlung der aerodynamische Lärmquellen und Berechnung des abgestrahlten Schall mittels der im Nahfeld gemessenen Druckschwankungen am Beispiel eines Triebwerksmodells*, Doctoral thesis, Techische Universität Berlin, 1995, published in: Fortschritt-Berichte VDI, Series 7, No. 272, VDI, Düsseldorf, 1995. (Cited on page 101.)

[207] Howe, M.S.: "Contributions to the theory of aerodynamic sound, with application to excess jet noise and the theory of the flute", *Journal of Fluid Mechanics*, 71:625–673, 1975. (Cited on pages 47 and 100.)

[208] Howe, M.S.: "Attenuation of sound in a low mach number nozzle flow", *Journal of Fluid Mechanics*, 91(2):209–229, 1979. (Cited on pages 47 and 53.)

[209] Howe, M.S.: "The influence of grazing flow on the acoustic impedance of a cylindrical wall cavity", *Journal of Sound and Vibration*, 67(4):533–544, 1979. (Cited on pages 32 and 67.)

[210] Howe, M.S.: "On the theory of unsteady high reynolds number flow through a circular aperture", *Proceedings of the Royal Society of London*, 366:205–223, 1979. (Cited on pages 35, 47, 48, 53, 68, 69, 70, 73, 74, and 271.)

[211] Howe, M.S.: "On the absorption of sound by turbulence and other hydrodynamic flows", *Journal of Applied Mathematics*, 32:187–209, 1984. (Cited on page 126.)

[212] Howe, M.S.: "The damping of sound by wall turbulent shear layers", *Journal of the Acoustical Society of America*, 98(3):1723–1730, 1995. (Cited on pages 126, 127, and 129.)

[213] Howe, M.S.: "Influence of cross-sectional shape on the conductivity of a wall aperture in mean flow", *Journal of Sound and Vibration*, 207:601–616, 1997. (Cited on pages 17 and 18.)

[214] Howe, M.S.: *Acoustics of fluid-structure interactions*, Cambridge University Press, Cambridge, UK, 1998. (Cited on pages 35, 47, 58, 68, 69, 85, 100, 118, 126, 127, and 129.)

[215] Howe, M.S.; Scott, M.I.; Sipcic, S.R.: "The influence of tangential mean flow on the rayleigh conductivity of an aperture", *Proceedings of the Royal Society of London, Series A*, 452(1953):2303–2317, 1996. (Cited on page 32.)

[216] Hrubes, J.D.: *Flow generated noise of acoustical duct liners*, Master's thesis, Massachusetts Institute of Technology, 1977. (Cited on page 219.)

[217] Hu, Y.: *Développement de panneaux hybrides passifs/actifs pour l'acoustique (Development of hybrid passive/active acoustic panels)*, Doctoral thesis, Ecole Centrale de Lyon, 2010. (Cited on page 294.)

[218] Hudde, H.; Letens, U.: "Untersuchungen zum akustischen Meßleitungsverfahren mit festen Meßorten", *Acustica*, 56(4):258–269, 1984. (Cited on page 146.)

[219] Hughes, I.J.; Dowling, A.P.: "The absorption of sound by perforated linings", *Journal of Fluid Mechanics*, 218:299–335, 1990. (Cited on pages 25, 35, 47, 51, 54, 71, 88, 211, 227, 252, and 271.)

[220] ICAO: "Manual of the ICAO standard atmosphere", Doc 7488/3, International Civil Aviation Organization, 1993. (Cited on pages 122 and 284.)

[221] Idelchick, I.E.: *Handbook of hydraulic resistance*, 3rd ed., Jaico Publishing House, Mumbai, India, 2011. (Cited on page 38.)

[222] Igarashi, J.; Toyama, M.: "Fundamentals of acoustic silencers, Part 1: Theory and experiments of acoustic low-pass filters", Report 339, University of Tokyo, 1958. (Cited on page 80.)

[223] Imelmann, C.: *Einfluß der Strömung auf den Schalldurchgang durch Rohrmündungen (Influence of flow on the sound transmission through orifices)*, Diploma thesis, Technische Universiät Berlin, 1978. (Cited on page 53.)

[224] Imelmann, C.: "Schallabsorption in durchströmten Rohrmündungen", in *Fortschritte der Akustik, DAGA '80, München*, pp. 493–496, VDE-Verlag, Berlin, 1980. (Cited on page 53.)

[225] Ingard, U.: "On the theory and design of acoustic resonators", *Journal of the Acoustical Society of America*, 25(6):1037–1062, 1953. (Cited on pages 17, 28, 45, 59, 63, 64, 65, 74, 77, 202, and 233.)

[226] Ingard, U.: "Attenuation and regeneration of sound in ducts and jet diffusers", *Journal of the Acoustical Society of America*, 31(9):1202–1212, 1959. (Cited on pages 44, 53, and 217.)

[227] INGARD, U.; ISING, H.: "Acoustic nonlinearity of an orifice", *Journal of the Acoustical Society of America*, 42:6–17, 1967. (Cited on pages 28, 44, 45, 53, 65, 67, and 202.)

[228] INGARD, U.; LABATE, S.: "Acoustic circulation effects and the nonlinear impedance of orifices", *Journal of the Acoustical Society of America*, 22(2):211–218, 1950. (Cited on pages 28, 45, 65, and 202.)

[229] INGARD, U.; SINGHAL, V.K.: "Sound attenuation in turbulent pipe flow", *Journal of the Acoustical Society of America*, 55(3):535–538, 1974. (Cited on page 126.)

[230] INTERNATIONAL AIR TRANSPORT ASSOCIATION: "Airlines expect 31 % rise in passenger demand by 2017", Press Release 67, published 10 December 2013, accessed online 25 February 2014: `http://www.iata.org/pressroom/pr/pages/2013-12-10-01.aspx`. (Cited on page 2.)

[231] INTERNATIONAL ENERGY AGENCY: "Key world energy statistics 2013", Report, published 2013, accessed online27 February 2014: `http://www.iea.org/publications/freepublications/publication/KeyWorld2013.pdf`. (Cited on page 1.)

[232] ISO 10534-2:1998: "Acoustics - Determination of sound absorption coefficient and impedance in impedance tubes - Part 2: Transfer-function method", Standard, International Organization for Standardization, Geneva, Switzerland, 1998. (Cited on page 146.)

[233] ISO 5136:2003: "Acoustics - Determination of sound power radiated into a duct by fans and other air-moving devices - In-duct method", Standard, International Organization for Standardization, Geneva, Switzerland, 2003. (Cited on page 165.)

[234] ISO 5167-2:2003: "Measurement of fluid flow by means of pressure differential devices inserted in circular cross-section conduits running full, Part 2: Orifice plates", Standard, International Organization for Standardization, Geneva, Switzerland, 2003. (Cited on pages 19 and 36.)

[235] ISO 80000-8:2007: "Quantities and units - Part 8: Acoustics", Standard, International Organization for Standardization, Geneva, Switzerland, 2007. (Cited on page 113.)

[236] ISO 9613-1:1993: "Acoustics - Attenuation of sound during propagation outdoors - Part 1", Report, International Organization for Standardization, Geneva, Switzerland, 1993. (Cited on pages 130, 133, and 134.)

[237] Jang, S.H.; Ih, J.: "On the multiple microphone method for measuring in-duct acoustic properties in the presence of mean flow", *Journal of the Acoustical Society of America*, 103(3):1520–1526, 1998. (Cited on page 147.)

[238] Janus, M.C.; Richards, G.M.; Yip, M.J.: "Effects of ambient conditions and fuel composition on combustion stability", in *ASME Turbo Expo 1997, 2-5 June 1997, Orlando, Florida, USA*, GT1997-266, 1997. (Cited on page 5.)

[239] Jayaraman, K.; Yam, K.: "Decoupling approach to modeling perforated tube muffler components", *Journal of the Acoustical Society of America*, 69(2):390–396, 1981. (Cited on page 82.)

[240] Jayatunga, C.; Qin, Q.; Sanderson, V.; Rubini, P.; You, D.; Krebs, W.: "Absorption of normal-incedence acoustic waves by double perforated liners of industrial gas turbine combustors", in *Proceedings of ASME Turbo Expo 2012, 11-15 June 2012, Copenhagen, Denmark*, GT2012-68842, 2012. (Cited on pages 55 and 249.)

[241] Jing, X.; Sun, X.: "Experimental investigation of perforated liners with bias flow", *Journal of the Acoustical Society of America*, 106(5):2436–2441, 1999. (Cited on pages 25, 34, 47, 48, 54, 71, 72, 88, 211, 227, and 231.)

[242] Jing, X.; Sun, X.: "Effect of plate thickness on impedance of perforated plates with bias flow", *AIAA Journal*, 38(9):1573–1578, 2000. (Cited on pages 48, 54, 68, 72, 77, 93, 212, 251, 271, and 280.)

[243] Jing, X.; Sun, X.: "Sound-excited flow and acoustic nonlinearity at an orifice", *Physics of Fluids*, 14(1):268–276, 2002. (Cited on pages 28, 29, 45, and 202.)

[244] Jing, X.; Sun, X.; Wu, J.; Meng, K.: "Effect of grazing flow on the acoustic impedance of an orifice", *AIAA Journal*, 39(8):1478–1484, 2001. (Cited on pages 32 and 67.)

[245] Johnston, J.P.; Schmidt, W.E.: "Measurement of acoustic reflection from an obstruction in a pipe with flow", *Journal of the Acoustic Society of America*, 63:1455–1460, 1978. (Cited on page 146.)

[246] Jones, M.G.: "Evaluation of a multi-point method for determining acoustic impedance", *Mechanical Systems and Signal Processing*, 3(1):15–35, 1989. (Cited on page 147.)

[247] Jones, M.G.; Howerton, B.M.; Busse-Gerstengarbe, S.: "Comparative study of impedance eduction methods, Part 2: NASA tests and methodology", in *19th AIAA/CEAS Aeroacoustics Conference, 27-29 May 2013, Berlin, Germany*, AIAA-2013-2125, 2013. (Cited on pages 27 and 28.)

[248] Jones, M.G.; Watson, W.R.: "On the use of experimental methods to improve confidence in educed impedance", in *17th AIAA/CEAS Aeroacoustics Conference, 5-8 June 2011, Portland, Oregon*, AIAA-2011-2865, 2011. (Cited on page 30.)

[249] Jordan, C.: "Mémoire sur les formes bilinéaires", *Journal de Mathématiques Pures et Appliquées, Deuxiéme Série*, 19:35–54, 1874. (Cited on page 145.)

[250] Jordan, C.: "Sur la réduction des formes bilinéaires", *Comptes Rendus de l'Académie des Sciences, Paris*, 78:614–617, 1874. (Cited on page 145.)

[251] Jörg, C.; Gikadi, J.; Sattelmayer, T.: "Numerical investigation of the plane-wave reflection coefficient of an exhaust pipe at elevated temperatures using linearized Navier-Stokes equations", in *ASME Turbo Expo 2013, GT2013, 3-7 June 2013, San Antonio,Texas, USA*, GT2013-94843, 2013. (Cited on page 26.)

[252] Jörg, C.; Wagner, M.; Sattelmayer, T.: "Experimental investigation of the acoustic reflection coefficient of a modeled gas turbine impingement cooling section", in *ASME Turbo Expo 2012, 11-15 June 2012, Copenhage, Denmark*, GT2012-68916, 2012. (Cited on page 55.)

[253] Jung, I.S.; Lee, J.S.: "Effects of orientation angles on film cooling over a flat plate: Boundary layer temperature distributions and adiabatic film cooling effectiveness", *Journal of Turbomachinery*, 122:153–160, 2000. (Cited on page 13.)

[254] Kaddah, K.S.: *Discharge coefficient and jet deflection studies for combustor liner air entry holes*, Diploma thesis, Cranfield University, 1964. (Cited on page 38.)

[255] Kameier, F.: *Experimentelle Untersuchung zur Entstehung und Minderung des Blattspitzen-Wirbellärms axialer Strömungsmachinen*, Doctoral thesis, Technische Universität Berlin, 1993. (Cited on page 108.)

[256] von Kármán, T.: "Mechanische ähnlichkeit und Turbulenz", *Nachrichten von der Gesellschaft der Wissenschaften zu Göttingen (Mathematisch-Physikalische Klasse)*, pp. 58–76, 1930. (Cited on page 127.)

[257] Keefe, D.H.: "Acoustical wave propagation in cylindrical ducts: Transmission line parameter approximations for isothermal and nonisothermal boundary conditions", *Journal of the Acoustical Society of America*, 75(1):58–62, 1984. (Cited on pages 113 and 121.)

[258] Keller, J.J.; Zauner, E.: "On the use of Helmholtz resonators as sound attenuators", *Zeitschrift für angewandte Mathematik und Physik*, 46:297–327, 1995. (Cited on pages 19, 54, 78, 238, and 239.)

[259] Kim, Y.H.; Yoon, D.B.: "An experimental study on the acoustic characteristics of perforated pipe in terms of wavenumber and porosity", *Journal of Sound and Vibration*, 183(1):115–127, 1995. (Cited on page 23.)

[260] Kinsler, L.; Frey, A.; Coppens, A.; Sanders, J.: *Fundamentals of acoustics*, 4th ed., John Wiley and Sons, New York, 2000. (Cited on pages 59, 61, 63, 79, 110, and 212.)

[261] Kirchhoff, G.: "Über den Einfluss der Wärmeleitung in einem Gase auf die Schallbewegung", *Annalen der Physik und Chemie*, 210(6):177–193, 1868. (Cited on pages 62, 114, 115, 118, 120, 121, and 131.)

[262] Kirchhoff, G.: "Zur Theorie freier Flüssigkeitsstrahlen", *Journal für Mathematik*, 70:289–298, 1869. (Cited on page 37.)

[263] Knutsson, M.; Åbom, M.: "The effect of turbulence damping on acoustic wave propagation in tubes", *Journal of Sound and Vibration*, 329:4719–4739, 2010. (Cited on page 126.)

[264] Ko, S.H.: "Sound attenuation in acoustically lined circular ducts in the presence of uniform flow and shear flow", *Journal of Sound and Vibration*, 22(2):193–210, 1972. (Cited on pages 32 and 217.)

[265] Kompenhans, J.; Ronneberger, D.: "The acoustic impedance of orifices in the wall of a flow duct with a laminar or turbulent flow boundary layer", in *6th AIAA Aeroacoustics Conference, 4-6 June 1980. Hartford, Connecticut*, AIAA-80-0990, 1980.

[266] Kooi, J.W.; Sarin, S.L.: "An experimental study of the impedance of helmholtz resonator arrays under a turbulent boundary layer", in *7th AIAA Aeroacoustics Conference, 5-7 October 1981, Palo Alto, California*, AIAA-1981-1998, 1981. (Cited on pages 32 and 67.)

[267] Kooijman, G.: *Acoustical response of shear layers*, Doctoral thesis, Technische Universiteit Eindhoven, 2007. (Cited on page 18.)

[268] Kooijman, G.; Auregan, Y.; Hirschberg, A.: "Orifice impedance under grazing flow: Modal expansion approach", in *11th AIAA/CEAS Aeroacoustics Conference, 23-25 May 2005, Monterey, California*, AIAA-2005-2857, 2005. (Cited on page 32.)

[269] Kooijman, G.; Hirschberg, A.; Golliard, J.: "Acoustical response of orifices under grazing flow: Effect of boundary layer profile and edge geometry", *Journal of Sound and Vibration*, 315:849–874, 2008. (Cited on page 19.)

[270] Kovasznay, L.S.G.: "Turbulence in supersonic flow", *Journal of the Aeronautical Sciences*, 20(10):657–674, 682, 1953. (Cited on page 115.)

[271] Kraft, R.E.; Yu, J.; Kwan, H.W.: "Acoustic treatment design scaling methods, Vol. 2: Advanced treatment impedance models for high frequency ranges", Contractor Report NASA-CR-1999-209120 Vol. 2, NASA, 1999. (Cited on pages 61, 62, 65, 66, and 75.)

[272] Krebs, W.; Bethke, S.; Lepers, J.; Flohr, P.; Prade, B.; Johnson, C.; Sattinger, S.: "Thermoacoustic design tools and passive control: Siemens Power Generation approaches", in [305], Chap. 5, pp. 89–112, 2005. (Cited on page 15.)

[273] Kundt, A.: "Untersuchungen über die Schallgeschwindigkeit der Luft in Röhren", *Annalen der Physik*, 135(11):337–372, 1868. (Cited on pages 114 and 190.)

[274] Kurze, U.J.; Allen, C.H.: "Influence of flow and high sound level on the attenuation in a lined duct", *Journal of the Acoustical Society of America*, 49(5):1643–1654, 1971. (Cited on pages 32 and 217.)

[275] Kutta, W.M.: *Über die Strömung einer Flüssigkeit um in sie versenkte zylindrische Flächen und den Druck, den diese dabei erfahren*, Habilitation thesis, Technische Hochschule München, 1902. (Cited on page 46.)

[276] Kwan, H.W.; Yu, J.; Beer, B.; Armitage, D.: "Bias flow adaptive acoustic liner", in *AIAA Meeting Paper Archive 172*, AIAA-1999-1939, 1999. (Cited on pages 34, 45, and 54.)

[277] Lahiri, C.; Knobloch, K.; Bake, F.; Enghardt, L.: "Acoustic measurements of perforated liners in hot and pressurized flow", in *ASME Tubo Expo 2013, 3-7 June 2013, San Antonio, Texas, USA*, GT2013-94674, 2013. (Cited on pages 52 and 190.)

[278] Lahiri, C.; Knobloch, K.; Bake, F.; Enghardt, L.: "Attenuation of sound in wide ducts with flow at elevated pressure and temperature", *Journal of Sound and Vibration*, 333(15):3440–3458, 2014. (Cited on pages 190 and 191.)

[279] Lahiri, C.; Knobloch, K.; Sadig, S.; Bake, F.: "Influence of cavity design on the performance of hot-stream bias flow liners", in *18th AIAA/CEAS Aeroacoustics Conference, 4-6 June 2012, Colorado Springs, Colorado*, AIAA-2012-2200, 2012. (Cited on pages 16, 52, and 55.)

[280] Lahiri, C.; Pardowitz, B.; Bake, F.; Enghardt, L.: "The application of an aeroacoustic actuator in a zero mass flow liner for acoustic damping", in *17th AIAA/CEAS Aeroacoustics Conference, 05 - 08 June 2011, Portland, Oregon*, AIAA-2011-2725, 2011. (Cited on pages 34 and 52.)

[281] Lahiri, C.; Pardowitz, B.; Bake, F.; Röhle, I.; Enghardt, L.: "Excitation of a zero mass flow liner for acoustic damping", *AIAA Journal*, 49(3):513–519, 2011. (Cited on pages 32, 34, 52, and 262.)

[282] Lahiri, C.; Sadig, S.; Gerendás, M.; Enghardt, L.; Bake, F.: "Establishment of a high quality database for the acoustic modeling of perforated liners", *Journal of Engineering for Gas Turbines and Power*, 133:1–9, 2011. (Cited on pages 17, 19, 23, 25, 27, 35, 47, 48, 52, 55, 71, and 72.)

[283] Landau, L.D.; Lifshitz, E.M.: *Fluid Mechanics*, 3rd ed., Pergamon Press, Oxford, 1966. (Cited on pages 39, 114, and 115.)

[284] Laudien, E.; Pongratz, R.; Pierro, R.; Preclik, D.: "Experimental procedures aiding the design of acoustic cavities", in [497], Chap. 14, pp. 377–399, 1995. (Cited on pages 6, 19, 109, and 238.)

[285] Laurens, S.; Piot, E.; Bendali, A.; Fares, M.B.; Tordaux, S.: "Effective conditions for the reflection of an acoustic wave by low-porosity perforated plates", *Journal of Fluid Mechanics*, 743:448–480, 2014. (Cited on pages 47 and 246.)

[286] Laurens, S.; Tordeux, S.; Bendali, A.; Fares, M.; Kotiuga, P.R.: "Lower and upper bounds for the Rayleigh conductivity of a perforated plate", *ESAIM: Mathematical Modelling and Numerical Analysis*, 47(6):1691–1712, 2013. (Cited on pages 19 and 59.)

[287] Lee, D.H.; Kwon, Y.P.: "Estimation of the absorption performance of multiple layer perforated panel systems by transfer matrix method", *Journal of Sound and Vibration*, 278:847–860, 2004. (Cited on page 202.)

[288] Lee, I.: *Acoustic characteristics of perforated dissipative and hybrid silencers*, Ph.d. thesis, Ohio State University, 2005. (Cited on pages 22, 65, 262, and 263.)

[289] Lee, I.; Selamet, A.; Huff, N.T.: "Impact of perforation impedance on the transmission loss of reactive and dissipative silencers", *Journal of the Acoustical Society of America*, 120(6):3706–3713, 2006. (Cited on pages 22, 262, and 263.)

[290] Lee, S.H.; Ih, J.G.: "Emperical model of the acoustic impedance of a circular orifice in grazing mean flow", *Journal of the Acoustical Society of America*, 114(1):98–113, 2003. (Cited on pages 32, 67, and 75.)

[291] Lee, S.H.; Ih, J.G.; Peat, K.S.: "A model of acoustic impedance of perforated plates with bias flow considering the interaction effect", *Journal of Sound and Vibration*, 303:741–752, 2007. (Cited on pages 55, 68, 93, 212, and 280.)

[292] Lefebvre, A.H.; Ballal, D.R.: *Gas Turbine Combustion - Alternative Fuels and Emissions*, 3rd ed., CRC Press, Boca Raton, FL, 2010. (Cited on pages 3, 4, 12, 13, and 15.)

[293] Legendre, A.M.: *Nouvelles methodes pour la determination des orbites des cometes (New Methods for the Determination of Comet Orbits)*, F. Didot, Paris, 1805. (Cited on page 147.)

[294] Lei, L.; Zhihui, G.; Chengyu, Z.; Xiaofeng, S.: "A passive method to control combustion instabilities with perforated liner", *Chinese Journal of Aeronautics*, 23:623–630, 2010. (Cited on pages 16, 26, and 55.)

[295] Lemmon, E.W.; Jacobsen, R.T.: "Viscosity and thermal conductivity equations for nitrogen, oxygen, argon, and air", *International Journal of Thermophysics*, 25(1):21–69, 2004. (Cited on pages 284 and 285.)

[296] Lemmon, E.W.; Jacobsen, R.T.; Penoncello, S.G.; Friend, D.G.: "Thermodynamic properties of air and mixtures of nitrogen, argon, and oxygen from 60 to 2000 K at pressures to 2000 MPa", *Journal of Physical and Chemical Reference Data*, 29(3):331–385, 2000. (Cited on pages 284 and 285.)

[297] Leppington, F.G.: "The effective compliance of perforated screens", *Mathematika*, 24:199–215, 1977. (Cited on pages 47 and 227.)

[298] Leppington, F.G.; Levine, H.: "Reflexion and transmission at a plane screen with periodically arranged circular or elliptical apertures", *Journal of Fluid Mechanics*, 61(1):109–127, 1973. (Cited on page 227.)

[299] Leung, R.C.K.; So, R.M.C.; Wang, M.H.; Li, X.M.: "In-duct orifice and its effect on sound absorption", *Journal of Sound and Vibration*, 299:990–1004, 2007. (Cited on page 55.)

[300] Lewis, G.D.; Garrison, G.D.: "The role of acoustic absorbers in preventing combustion instability", in *AIAA/SAE 7th Propulsion Joint Specialist Conference,14-18 June 1971, Salt Lake City, Utah*, AIAA-1971-0699, 1971. (Cited on pages 44 and 220.)

[301] Lewis Laboratory Staff: "A summary of preliminary investigations into the characteristics of combustion screech in ducted burners", Technical Report NACA-TR-1384, National Advisory Committee for Aeronautics, 1954. (Cited on page 15.)

[302] Lichtarowicz, A.; Duggins, R.K.; Markland, E.: "Discharge coefficients for incompressible non-cavitating flow through long orifices", *Journal of Mechanical Engineering Science*, 7(2):210–219, 1965. (Cited on page 36.)

[303] Lienhard, J.H.; Lienhard, J.H.: "Velocity coefficients for free jets from sharp-edged orifices", *Journal of Fluids Engineering*, 106:13–17, 1984. (Cited on page 37.)

[304] Lieuwen, T.C.: *Unsteady Combustor Physics*, Cambridge University Press, New York, NY, 2012. (Cited on page 15.)

[305] Lieuwen, T.C.; Yang, V. (Eds.): *Combustion instabilities in gas turbine engines*, AIAA, Reston, VA, 2005. (Cited on pages 5, 7, 15, 27, 306, 309, 322, 328, and 343.)

[306] Lieuwen, T.C.; Yang, V. (Eds.): *Gas turbine emissions*, Cambridge University Press, Cambridge, UK, 2013. (Cited on page 3.)

[307] Lung, T.Y.; Doige, A.G.: "A time-averaging transient testing method for acoustic properties of piping systems and mufflers with flow", *Journal of the Acoustical Society of America*, 73:867–876, 1983. (Cited on page 154.)

[308] Luong, T.; Howe, M.S.; McGowan, R.S.: "On the Rayleigh conductivity of a bias-flow aperture", *Journal of Fluids and Structures*, 21:769–778, 2005. (Cited on pages 48, 54, 73, 74, and 203.)

[309] Lutz, O.: "Resonanzschwingungen in den Rohrleitungen von Kolbenmaschinen (Resonant oscillations in the ducts of reciprocating engines)", *Berichte aus dem Laboratorium für Verbrennungskraftmaschinen der Technischen Hochschule Stuttgart*, 3:17–110, 1934. (Cited on pages 43 and 53.)

[310] Macquisten, M.A.; Holt, A.; Whiteman, M.; Moran, A.J.; Rupp, J.: "Passive damper lp tests for controlling combustion instability", in *ASME Turbo Expo 2006, 8-11 May 2006, Barcelona, Spain*, GT2006-90874, 2006. (Cited on pages 16, 25, 26, 27, 55, 72, 211, and 269.)

[311] Maier, W.; Lutz, O.: "Resonanzerscheinungen in den Rohrleitungen von Verbrennungskraftmaschinen (Resonance phenomena in the ducts of combustion engines)", *Berichte aus dem Laboratorium für Verbrennungskraftmaschinen der Technischen Hochschule Stuttgart*, 3:1–16, 1934. (Cited on pages 43 and 53.)

[312] Malmary, C.; Carbonne, S.; Auregan, Y.; Pagneux, V.: "Acoustic impedance measurement with grazing flow", in *7th AIAA/CEAS Aeroacoustics Conference, 28-30 May 2001, Maastricht, Netherlands*, AIAA-2001-2193, 2001. (Cited on page 32.)

[313] Marino, P.A.; Bohn, N.; Russell, P.L.; Schnell, A.C.; Parson, G.L.: "A study of the suppression of combustion oscillations with mechanical damping devices", Contractor Report NASA-CR-90094, NASA, 1967. (Cited on pages 220 and 221.)

[314] Markham, J.J.; Beyer, R.T.; Lindsay, R.B.: "Absorption of sound in fluids", *Reviews of Modern Physics*, 23(4):353–411, 1951. (Cited on page 131.)

[315] Mason, V.: "Some experiments on the propagation of sound along a cylindrical duct containing flowing air", *Journal of Sound and Vibration*, 10(2):208–226, 1969. (Cited on page 103.)

[316] Mason, W.P.: "The propagation characteristics of sound tubes and acoustic filters", *Physical Review*, 31:283–295, 1928. (Cited on page 190.)

[317] Mazdeh, A.; Kashani, R.: "Distributed parameter acoustic modeling of a perforation with bias flow", in *ASME Turbo Expo 2011, 6-10 June 2001, Vancouver, Canada*, GT2011-46649, 2011. (Cited on pages 47, 51, 55, and 71.)

[318] Mazdeh, A.; Kashani, R.: "The impact of perforation geometry on acoustic damping attributes of a perforated liner with bias flow", in *ASME Turbo Expo 2012, 11-15 June 2012, Copenhagen, Denmark*, GT2012-69727, 2012. (Cited on pages 47, 51, 55, and 71.)

[319] McAuliffe, C.E.: *The influence of high speed flow on the bahavior of acoustical elements*, M.Sc. thesis, Massachusetts Institute of Technology, 1950. (Cited on pages 43, 53, and 212.)

[320] McVeigh, J.C.: "Hysteresis in the flow through an orifice", *Nature*, 212:918, 1966. (Cited on page 36.)

[321] Mechel, F.: "Schalldämpfung und schallverstärkung in luftströmungen durch absorbierend ausgekleidete Kanäle", *Acustica*, 10(3):133–148, 1960. (Cited on pages 217 and 219.)

[322] Mechel, F.: "Research on sound propagation in sound-absorbent ducts with superimposed air streams, Vol. 1", Report AMRL-TDR-62-140(1), Aerospace Medical Research Laboratories, Wright-Patterson Air Force Base, 1962. (Cited on pages 32 and 217.)

[323] MECHEL, F.: *Formulas of acoustics*, 2nd ed., Springer, Berlin, 2008. (Cited on pages 80, 81, 82, and 85.)

[324] MECHEL, F.; MERTENS, P.: "Schallausbreitung in absorbierend ausgekleideten Strömungskanälen bei hohen Windgeschwindigkeiten", *Acustica*, 13(3):154–165, 1963. (Cited on page 217.)

[325] MECHEL, F.; MERTENS, P.; SCHILZ, W.: "Interaction between air flow and airborne sound in a duct", Report AMRL-TR-65-53, Aerospace Medical Research Laboratories, Wright-Patterson Air Force Base, 1965. (Cited on pages 44 and 53.)

[326] MECHEL, F.; SCHILZ, W.; DIETZ, J.: "Akustische Impedanz einer luftdurchströmten Öffnung", *Acustica*, 15:199–206, 1965. (Cited on pages 44, 53, and 67.)

[327] MELLING, T.H.: "The acoustic impedance of perforates at medium and high sound pressure levels", *Journal of Sound and Vibration*, 29(1):1–65, 1973. (Cited on pages 28, 45, 61, 62, 63, 64, 65, 75, 77, 202, and 227.)

[328] MENDEZ, S.; ELDREDGE, J.D.: "Acoustic modeling of perforated plates with bias flow for large-eddy simulations", *Journal of Computational Physics*, 228(13):4757–4772, 2009. (Cited on pages 55 and 246.)

[329] MEYER, E.; MECHEL, F.; KURTZE, G.: "Experiments on the influence of flow on sound attenuation in absorbing ducts", *Journal of the Acoustical Society of America*, 30:165, 1958. (Cited on pages 32 and 217.)

[330] MICHALKE, A.: "On the propagation of sound generated in a pipe of circular cross-section with uniform mean flow", *Journal of Sound and Vibration*, 134(2):203–234, 1989. (Cited on page 103.)

[331] MITSUBUSHI HEAVY INDUSTRIES: "MHI achieves 1,600 °c turbine inlet temperature in test operation of world's highest thermal efficiency j-series gas turbine", Press Release No. 1435, published 26 May 2011, accessed online 27 February 2014: `http://www.mhi.co.jp/en/news/story/1105261435.html`. (Cited on pages 2 and 14.)

[332] MOERS, E.M.T.; TONON, D.; HIRSCHBERG, A.: "Sound absorption by perforated walls with bias/grazing flow: Experimental study of the influence of perforation angle", in *Acoustics 2012, 23-27 April 2012, Nantes, France*, 2012. (Cited on pages 18, 19, 34, 50, and 55.)

[333] MONGIA, H.C.; HELD, T.J.; HSIAO, G.C.; PANDALAI, R.P.: "Incorporation of combustion instability issues into design process: GE aeroderivative and

aero engine experience", in [305], Chap. 3, pp. 43–63, 2005. (Cited on pages 6 and 15.)

[334] Moore, E.H.: "On the reciprocal of the general algebraic matrix", *Bulletin of the American Mathematical Society*, 26(9):394–395, 1920. (Cited on page 145.)

[335] Morfey, C.L.: "Rotating pressure patterns in ducts: Their generation and transmission", *Journal of Sound and Vibration*, 1:60–87, 1964. (Cited on page 101.)

[336] Morfey, C.L.: "Acoustic properties of openings at low frequencies", *Journal of Sound and Vibration*, 9(3):357–366, 1969. (Cited on pages 17, 58, 234, and 235.)

[337] Morfey, C.L.: "Sound transmission and generation in ducts with flow", *Journal of Sound and Vibration*, 14(1):37–55, 1971. (Cited on page 103.)

[338] Morfey, C.L.: *Dictonary of acoustics*, Academic Press, 2001. (Cited on pages 37, 46, 61, 98, 100, 102, and 155.)

[339] Morse, P.M.: *Vibration and sound*, 2nd ed., McGraw-Hill, New York, 1948. (Cited on page 59.)

[340] Morse, P.M.; Ingard, K.U.: *Theoretical acoustics*, McGraw-Hill, New York, 1968. (Cited on pages 66, 100, 101, 111, and 118.)

[341] Mungur, P.; Whitesides, J.L.: "Influence of grazing flow on duct wall normal impedance", in *2nd AIAA Aeroacoustics Conference, 24-26 March 1975, Hampton, Virginia*, AIAA-1975-0494, 1975. (Cited on page 32.)

[342] Munjal, M.L.: "Velocity ratio-cum-transfer matrix method for the evaluation of a muffler with mean flow", *Journal of Sound and Vibration*, 39(1):105–119, 1975. (Cited on page 81.)

[343] Munjal, M.L.: *Acoustics of ducts and mufflers*, John Wiley and Sons, New York, 1987. (Cited on pages 80, 81, 82, 100, 103, 109, 110, and 111.)

[344] Munjal, M.L.; Doige, A.G.: "Theory of a two source-location method for direct experimental evaluation of the four-pole parameters of an aeroacoustic element", *Journal of Sound and Vibration*, 141(2):323–333, 1990. (Cited on page 154.)

[345] Munjal, M.L.; Rao, K.N.; Sahasrabudhe, A.D.: "Aeroacoustic analysis of perforated muffler components", *Journal of Sound and Vibration*, 114(2):173–188, 1987. (Cited on page 82.)

[346] Munt, R.M.: "The interaction of sound with a subsonic jet issuing from a semi-infinite cylindrical pipe", *Journal of Fluid Mechanics*, 83:609–640, 1977. (Cited on pages 26 and 53.)

[347] Munt, R.M.: "Acoustic transmission properties of a jet pipe with subsonic jet flow", *Journal of Sound and Vibration*, 142(3):413–436, 1990. (Cited on page 53.)

[348] Navier, C.L.M.H.: "Memoire sur les lois du mouvement des fluides", *Mémoires de l'Académie des sciences de l'Institut de France*, 6:389–440, 1822. (Cited on page 114.)

[349] Nayfeh, A.H.; Kaiser, J.E.; Telionis, D.P.: "Acoustics of aircraft engine-duct systems", *AIAA Journal*, 13(2):130–153, 1975. (Cited on page 217.)

[350] Nayfeh, A.H.; Sun, J.: "Effect of transverse velocity and temperature gradients on sound attenuation in two-dimensional ducts", *Journal of Sound and Vibration*, 34(4):505–517, 1974. (Cited on page 268.)

[351] Nealy, D.A.; Reider, S.B.; Mongia, H.C.: "Alternate cooling configurations for gas turbine combustion systems", in *Heat transfer and cooling in gas turbines*, AGARD-CP-390, Chap. 25, Advisory Group for Aerospace Research and Development, 1985. (Cited on page 13.)

[352] Neise, W.; Michel, U.: "Aerodynamic noise of turbomachines", Report DLR-IB-22314-94/B5, DLR, 1994. (Cited on page 101.)

[353] Newton, I.: *Philosophiae Naturalis Principia Mathematica*, Cantabrigiæ, Cambridge, UK, 1713. (Cited on page 36.)

[354] Nilsson, B.; Brander, O.: "The propagation of sound in cylindrical ducts with mean flow and bulk reacting lining: III. Step discontiuities", *Journal of the Institute of Mathematics and its Applications*, 27:105–131, 1981. (Cited on page 53.)

[355] Nordin, P.; Sarin, S.L.; Rademaker, E.R.: "Development of new liner technology for application in hot stream areas of aero-engines", in *10th AIAA/CEAS Aeroacoustics Conference, 10-12 May 2004, Manchester, UK*, AIAA-2004-3033, 2004. (Cited on page 26.)

[356] Norris, A.N.; Sheng, C.: "Acoustic radiation from a circular pipe with an infinite flange", *Journal of Sound and Vibration*, 135:85–93, 1989. (Cited on page 77.)

[357] Oberg, C.L.; Wong, T.L.; Ford, W.M.: "Evaluation of acoustic cavities for combustion stabilization", Contractor Report NASA-CR-115087, NASA, 1971. (Cited on pages 26 and 53.)

[358] Ohm, G.S.: *Die galvanische Kette, mathematisch bearbeitet (The galvanic circuit investigated mathematically)*, T.H. Riemann, Berlin, 1827. (Cited on page 57.)

[359] Page, N.W.; Mee, D.J.: "Wall effects on sound propagation in tubes", *Journal of Sound and Vibration*, 93(4):473–480, 1984. (Cited on page 113.)

[360] Pallek, D.: *Messung des Schalldurchgangs an Diskontinuitäten in durchströmten Kanälen*, Doctoral thesis, Universität Göttingen, 1984. (Cited on pages 19, 54, and 139.)

[361] Panton, R.L.; Goldman, A.L.: "Correlation of nonlinear orifice impedance", *Journal of the Acoustical Society of America*, 60:1390–1396, 1976. (Cited on pages 28, 45, and 202.)

[362] Paschereit, C.O.; Schuermans, B.; Polifke, W.; Mattson, O.: "Measurements of transfer matrices and source terms of premixed flames", *Journal of Engineering for Gas Turbine and Power*, 124:239–247, 2002. (Cited on page 80.)

[363] Peat, K.S.: "A numerical decoupling analysis of perforated pipe silencer elements", *Journal of Sound and Vibration*, 123(2):199–212, 1988. (Cited on pages 54, 73, and 82.)

[364] Peat, K.S.; Ih, J.G.; Lee, S.H.: "The acoustic impedance of a circular orifice in grazing mean flow: Comparison with theory", *Journal of the Acoustical Society of America*, 114(6):3076–8086, 2003. (Cited on pages 32 and 67.)

[365] Penrose, R.: "A generalized inverse for matrices", *Mathematical Proceedings of the Cambridge Philosophical Society*, 51(3):406–413, 1955. (Cited on page 145.)

[366] Peters, M.C.A.M.; Hirschberg, A.; Reijnen, A.J.; Wijnands, A.P.J.: "Damping and reflection coefficient measurements for an open pipe at low mach and low helmholtz numbers", *Journal of Fluid Mechanics*, 256:499–534, 1993. (Cited on pages 77, 122, 124, and 126.)

[367] Phillips, B.: "Effects of high-wave amplitude and mean flow on a helmholtz resonator", Technical Memorandum NASA-TM-X-1582, NASA, 1968. (Cited on page 44.)

[368] Phillips, B.; Hannum, N.P.; Russell, L.M.: "On the design of acoustic liners for rocket engines: Helmholtz resonators evaluated with a rocket combustor", Technical Note NASA-TN-D-5171, NASA, 1969. (Cited on page 44.)

[369] Pierce, A.D.: *Acoustics - An introduction to its physical principles and applications*, Acoustical Society of America, New York, 1989. (Cited on pages 60, 80, 97, 98, 99, 100, 109, 110, 115, 116, 118, 121, 130, 131, 132, 134, and 135.)

[370] Pinker, R.A.; Bryce, W.D.: "The radiation of plane-wave duct noise from a jet exhaust, statically and in flight", in *3rd AIAA Aeroacoustics Conference*, AIAA-1976-581, 1976. (Cited on page 26.)

[371] Powell, A.: "Theory of vortex sound", *Journal of the Acoustical Society of America*, 36(1):177–195, 1964. (Cited on page 47.)

[372] Prandtl, L.: "Über Flüssigkeitsbewegung bei sehr kleiner Reibung", in *Verhandlungen des III. Internationalen Mathematiker-Kongresses*, pp. 484–491, 1904. (Cited on page 117.)

[373] Premo, J.: "The application of a time-domain model to investigate the impedance of perforate liners including the effects of bias flow", in *AIAA Meeting Paper Archive 711*, AIAA-1999-1876, 1999. (Cited on pages 45, 54, and 68.)

[374] Pridmore-Brown, D.C.: "Sound propagation in a fluid flowing through an attenuating duct", *Journal of Fluid Mechanics*, 4:393–406, 1958. (Cited on pages 155 and 217.)

[375] Putnam, A.A.: *Combustion-driven oscillations in industry*, Elsevier, New York, 1971. (Cited on pages 5 and 6.)

[376] Putnam, A.A.; Dennis, W.: "A study of burner oscillations of the organ-pipe type", *Transactions of the American Society of Mechanical Engineers*, 73:15–28, 1953. (Cited on page 5.)

[377] Quinn, M.C.; Howe, M.S.: "On the production and absorption of sound by lossless liners in the presence of mean flow", *Journal of Sound and Vibration*, 97(1):1–9, 1984. (Cited on page 219.)

[378] Rademaker, E.R.; Demmenie, E.A.: "In-situ acoustic impedance measurements on air-injected liners under grazing flow", in *33rd International Congress and Exposition on Noise Control Engineering; 22-25 August 2004, Prague, Czech Republic*, NLR-TP-2004-146, 2004. (Cited on page 54.)

[379] Rademaker, E.R.; Idzenga, S.T.; Huisman, H.N.; Nijboer, R.J.; Sarin, S.L.: "A new facility for hot stream acoustic liner testing", Report NLR-TP-2003-202, NLR, 2003. (Cited on page 26.)

[380] Rademaker, E.R.; van der Wal, H.M.M.; Geurts, E.G.M.: "Hot-stream in-situ acoustic impedance measurements on various air-filled cavity and porous liners", in *16th International Congress on Sound and Vibration, ICSV16, Kraków, Poland, 5-9 July 2009*, 918, 2009. (Cited on pages 267 and 268.)

[381] Rademaker, E.R.; van der Wal, H.M.M.; Geurts, E.G.M.: "Hot-stream in-situ acoustic impedance measurements on various air-filled cavity and porous liners", Report NLR-TP-2009-142, National Aerospace Laboratory (NLR), 2011. (Cited on page 26.)

[382] Rämmal, H.; Lavrentjev, J.: "Sound refelction at an open end of a circular duct exhausting hot gas", *Journal of Noise Control Engineering*, 56(2):107–114, 2008. (Cited on page 26.)

[383] Randeberg, R.T.: *Perforated panel absorber with viscous energy dissipation enhanced by orificed design*, Doctoral thesis, Norwegian University of Science and Technology, 2000. (Cited on page 65.)

[384] Rao, K.N.; Munjal, M.L.: "Experimental evaluation of impedance of perforates with grazing flow", *Journal of Sound and Vibration*, 108(2):283–295, 1986. (Cited on page 32.)

[385] Rayleigh, J.W.S.: "On the theory of resonance", *Philosophical Transactions of the Royal Society of London*, 161:77–118, 1871. (Cited on pages 17, 57, 58, 59, 233, and 235.)

[386] Rayleigh, J.W.S.: "Notes on hydrodynamics", *Philosophical Magazine Series 5*, 2:441–447, 1876. (Cited on page 37.)

[387] Rayleigh, J.W.S.: "On waves", *Philosophical Magazine Series 5*, 1(4):257–279, 1876. (Cited on page 101.)

[388] Rayleigh, J.W.S.: "The explanation of certain acoustic phenomena", *Nature*, 18(455):319–321, 1878. (Cited on page 5.)

[389] Rayleigh, J.W.S.: "On the passage of waves through apertures in plane screens, and allied problems", *Philosophical Magazine Series 5*, 43(263):259–272, 1897. (Cited on page 17.)

[390] Rayleigh, J.W.S.: *The theory of sound, Vol. 2*, Dover, New York, 1945. (Cited on pages 5, 57, 58, 59, 120, 121, 233, and 235.)

[391] Rehman, S.F.; Eldredge, J.D.: "Numerical investigation of a bias-flow perforated liner for damping of thermoacoustic instabilities", in *ASME Turbo Expo 2007, 14-17 May 2007, Montreal, Canada*, GT2007-27319, 2007. (Cited on pages 47 and 71.)

[392] Rice, E.J.: "A model for the acoustic impedance of a perforated plate liner with muliple frequency excitation", Technical Memorandum NASA-TM-X-67950, NASA, 1971. (Cited on pages 67 and 221.)

[393] Rice, E.J.: "Spinning mode sound propagation in ducts with acoustic treatment", Technical Note NASA-TN-D-7913, NASA, 1975. (Cited on page 27.)

[394] Rice, E.J.: "A theoretical study of the acoustic impedance of orifices in the presence of a steady grazing flow", Technical Memorandum NASA-TM-X-71903, NASA, 1976. (Cited on page 74.)

[395] Richards, G.A.; Straub, D.L.; Robey, E.H.: "Passive control of combustion dynamics in stationary gas turbines", *Journal of Propulsion and Power*, 19(5):795–810, 2003. (Cited on page 6.)

[396] Richter, C.: *Liner impedance modeling in the time domain with flow*, Doctoral thesis, Technische Universität Berlin, 2009. (Cited on page 32.)

[397] Richter, K.: *Messung der akustischen Streumatrix durchströmter Lochblenden*, Diploma thesis, Universität Göttingen, 1978. (Cited on pages 53 and 139.)

[398] Richter, K.; Pallek, D.; Ronneberger, D.: "Eine Methode zur Messung akustischer Grössen in Kanälen", in *Fortschritte der Akustik, DAGA '80, München*, pp. 819–822, VDE-Verlag, Berlin, 1980.

[399] Richter, K.; Ronneberger, D.: "Schalltransmission durch Blenden und Lochbleche im Durchströmten Rohr", in *Fortschritte der Akustik, DAGA '78, Bochum*, pp. 375–378, VDE-Verlag, Berlin, 1978. (Cited on pages 53 and 139.)

[400] Rienstra, S.W.: "On the acoustic implications of vortex shedding from an exhaust pipe", *Journal of Engineering for Industry*, 103(4):378–384, 1981. (Cited on page 53.)

[401] Rienstra, S.W.: "A small strouhal number analysis for acoustic wave-jet flow-pipe interaction", *Journal of Sound and Vibration*, 86(4):539–556, 1983. (Cited on page 77.)

[402] Rienstra, S.W.: "Acoustic scattering at a hard-soft lining transition in a flow duct", *Journal of Engineering Mathematics*, 59:451–475, 2007. (Cited on page 165.)

[403] Ries, H.C.; Carlesson, M.V.; Eigenbrod, C.; Kroll, S.; Rezwan, K.: "On the performance of porous sound absorbent ceramic lining in a combustion chamber test rig", in *ASME Turbo Expo 2013, 3-7 June 2013, San Antonio, Texas, USA*, GT2013-95492, 2013. (Cited on page 26.)

[404] Rocard, Y.: *Propagation et absorption du son*, Herman, Paris, 1935. (Cited on page 131.)

[405] Rodarte, E.; Singh, G.; Miller, N.R.; Hrnjak, P.: "Sound attenuation in tubes due to visco-thermal effects", *Journal of Sound and Vibration*, 231(5):1221–1242, 2000. (Cited on page 113.)

[406] Rogers, T.; Hersh, A.S.: "The effect of grazing flow on the steady state resistance of square-edged orifices", in *2nd AIAA Aeroacoustics Conference, 24-26 March 1975, Hampton, Virginia*, AIAA-1975-0493, 1975. (Cited on pages 32, 50, and 221.)

[407] Rohde, J.E.; Richards, H.T.; Metger, G.W.: "Discharge coefficients for thick plate orifices with approach flow perpendicular and inclined to the orifice axis", Technical Note NASA-TN-D-5467, NASA, 1969. (Cited on page 38.)

[408] Rolls-Royce: *The jet engine*, 5th ed., Rolls-Royce plc, Derby, UK, 1996. (Cited on pages 12, 14, and 15.)

[409] Ronneberger, D.: "Experimentelle Untersuchungen zum akustischen Reflexionsfaktor von unstetigen Querschnittsänderungen in einem luftdurchströmten Rohr", *Acustica*, 19:222–235, 1967/68. (Cited on page 53.)

[410] Ronneberger, D.: "The acoustical impedance of holes in the wall of flow ducts", *Journal of Sound and Vibration*, 24(1):133–150, 1972. (Cited on page 17.)

[411] Ronneberger, D.: *Genaue Messung der Schalldämpfung und der Phasengeschwindigkeit in durchströmten Rohren im Hinblick auf die Wechselwirkung zwischen Schall und Turbulenz*, Habilitation thesis, Universität Göttingen, 1975. (Cited on pages 122, 123, 124, 139, and 147.)

[412] Ronneberger, D.: "Theoretische und experimentelle Untersuchung der Schallausbreitung durch Querschnittssprünge und Lochplatten in Strömungskanälen", Report, Universität Göttingen, 1987. (Cited on pages 19, 53, 54, 139, 147, 155, and 240.)

[413] Ronneberger, D.; Ahrens, C.D.: "Wall shear stress caused by small amplitude perturbations of turbulent boundary-layer flow: An experimental investigation", *Journal of Fluid Mechanics*, 83(3):433–464, 1977. (Cited on pages 123 and 126.)

[414] Rossing, T.D. (Ed.): *Springer Handbook of Acoustics*, Springer, New York, 2007. (Cited on pages 133, 135, 283, and 284.)

[415] Rupp, J.; Carrotte, J.: "Interaction between the acoustic pressure fluctuations and the unsteady flow field through circular holes", *Journal of Engineering for Gas Turbines and Power*, 132:1–9, 2010. (Cited on pages 28, 29, 49, 55, 203, and 281.)

[416] Rupp, J.; Carrotte, J.; Macquisten, M.: "The use of perforated damping liners in aero gas turbine combustion systems", in *ASME Turbo Expo 2011, 6-10 June 2011, Vancouver, Canada*, GT2011-45488, 2011. (Cited on page 55.)

[417] Rupp, J.; Carrotte, J.; Macquisten, M.: "The use of perforated damping liners in aero gas turbine combustion systems", *Journal of Engineering for Gas Turbine and Power*, 134:1–10, 2012. (Cited on pages 15, 25, 35, 47, 49, 55, 71, and 203.)

[418] Rupp, J.; Carrotte, J.; Spencer, A.: "Interaction between the acoustic pressure fluctuations and the unsteady flow filed through circular holes", in *ASME Turbo Expo 2009, June 8-12, 2009, Orlando, FL, USA*, GT2009-59263, 2009. (Cited on page 55.)

[419] Rupp, J.; Carrotte, J.; Spencer, A.: "Methodology to identify the unsteady flow field associated with the loss of acoustic energy in the vicinity of circular holes", in *ASME Turbo Expo 2010, 14-18 June 2010, Glasgow, UK*, GT2010-22178, 2010. (Cited on pages 49, 55, and 203.)

[420] Rupp, J.; Peacock, G.; Regunath, G.; Carrotte, J.: "Assessment and prediction of helmholtz resonator performance within gas turbine combustion systems", in *ASME Turbo Expo 2014, 16-20 June 2014, Düsseldorf, Germany*, GT2014-26907, 2014. (Cited on pages 55 and 203.)

[421] Salikuddin, M.; Ahuja, K.K.: "Acoustic power dissipation on radiation through duct terminations - experiments", in *7th AIAA Aeroacoustics Conference, 5-7 October 1981, Palo Alto, California*, AIAA-1981-1978, 1981. (Cited on page 53.)

[422] Salikuddin, M.; Ahuja, K.K.: "Acoustic power dissipation on radiation through duct terminations: Experiments", *Journal of Sound and Vibration*, 91(4):479–502, 1983. (Cited on page 53.)

[423] Salikuddin, M.; Brown, W.H.: "Non-linear effects in finite amplitude propagation through orifice plate and perforated plate terminations", *Journal of Sound and Vibration*, 139(3):383–405, 1990. (Cited on pages 25 and 45.)

[424] Salikuddin, M.; Syed, A.A.; Mungur, P.: "Acoustic characteristics of perforated sheets with throughflow in high itensity noise environment", in *13th AIAA Aeroacoustics Conference, 22-24 October 1990, Tallahassee, Florida*, AIAA-1990-3931, 1990. (Cited on page 54.)

[425] Salikuddin, M.; Syed, A.A.; Mungur, P.: "Acoustic characteristics of perforated sheets with throughflow in high itensity noise environment", *Journal of Sound and Vibration*, 169(2):145–177, 1994. (Cited on pages 28, 29, and 54.)

[426] Santana, L.D.; de Roeck, W.; Desmet, W.; Ferrante, P.: "Two-port indirect acoustic impedance eduction in presence of grazing flow", in *17th AIAA/CEAS Aeroacoustics Conference, 5-8 June 2011, Portland, Oregon*, AIAA-2011-2868, 2011. (Cited on page 32.)

[427] Scarpato, A.; Ducruix, S.; Schuller, T.: "A LES based sound absorption analysis with high-amplitude waves through an orifice with bias flow", in *ASME Turbo Expo 2011, 6-10 June 2011, Vancouver, Canada*, GT2011-45639, 2011. (Cited on pages 50 and 55.)

[428] Scarpato, A.; Ducruix, S.; Schuller, T.: "Optimal and off-design operations of acoustic dampers using perforated plates backed by a cavity", *Journal of Sound and Vibration*, 332:4856–4875, 2013. (Cited on pages 50, 55, and 72.)

[429] Scarpato, A.; Ducuix, S.; Schuller, T.: "A novel design method for robust acoustic dampers with perforated plates backed by a cavity operating at low and high Strouhal numbers", in *ASME Turbo Expo 2012, 11-15 June 2012, Copenhagen, Denmark*, GT2012-69249, 2012. (Cited on pages 25 and 50.)

[430] Scarpato, A.; Tran, N.; Ducruix; Schuller, T.: "Modeling the damping properties of perforated screens traversed by bias flow and backed by a cavity at low Strouhal number", *Journal of Sound and Vibration*, 331:276–290, 2012. (Cited on pages 47, 50, 55, 71, 72, and 212.)

[431] Schade, H.; Kunz, E.: *Strömungslehre*, 3rd ed., Walter de Gruyter, Berlin, 2007. (Cited on page 178.)

[432] Schlichting, H.; Gersten, K.: *Grenzschichttheorie*, 10th ed., Springer, Berlin, 2006. (Cited on pages 117 and 127.)

[433] SCHMIDT, E.: "Zur Theorie der linearen und nichtlinearen Integralgleichungen. I. Teil: Entwicklung willkürlicher Funktionen nach Systemen vorgeschriebener", *Mathematische Annalen*, 63:433–476, 1907. (Cited on page 145.)

[434] SCHMIDT, J.; BHAYARAJU, U.; KASHINATH, K.; HOCHGREB, S.: "Investigation of the effect of combustor cooling geometry on acoustic energy absorption", in *16th AIAA/CEAS Aeroacoustics Conference, 7-9 June 2010, Stockholm, Sweden*, AIAA-2010-3929, 2010. (Cited on pages 25, 51, and 55.)

[435] SCHULTZ, T.; SHEPLAK, M.; CATTAFESTA, L.N.: "Uncertainty analysis of the two-microphone method", *Journal of Sound and Vibration*, 304:91–109, 2007. (Cited on page 146.)

[436] SCHULZ, A.; BAKE, F.; ENGHARDT, L.; HAUFE, D.; FISCHER, A.; CZARSKE, J.: "Acoustic damping analysis of bias flow liners based on spectral flow characteristics", in *19th AIAA/CEAS Aeroacoustics Conference, 27-29 May 2013, Berlin, Germany*, AIAA-2013-2177, 2013. (Cited on pages 51, 55, and 281.)

[437] SEYBERT, A.F.; ROSS, D.F.: "Experimental determination of acoustic properties using a two-microphone random-excitation technique", *Journal of the Acoustical Society of America*, 61(5):1362–1370, 1977. (Cited on page 146.)

[438] SEYBERT, A.F.; SOENARKO, B.: "Error analysis of spectral estimates with application to the measurement of acoustic parameters using random sound fields in ducts", *Journal of the Acoustical Society of America*, 69(4):1190–1199, 1981. (Cited on page 146.)

[439] SIEMENS: "Trail-blazing power plant technology", Press Release, published 19 May 2011, accessed online 27 February 2014: `http://www.siemens.com/press/pool/de/pressemitteilungen/2011/fossil_power_generation/EFP201105064e.pdf`. (Cited on page 2.)

[440] SIRIGNANO, W.A.; BHATIA, R.; MOLAVI, K.: "Liquid fueled ramjet combustion instability: Acoustic and vortical interactions with burning sprays", Report, University of California, 1990. (Cited on page 5.)

[441] SIVIAN, L.J.: "Acoustic impedance of small orifices", *Journal of the Acoustical Society of America*, 7:94–101, 1935. (Cited on pages 28, 45, 63, 65, 67, and 202.)

[442] SMITH, D.; WALKER, W.J.: "Orifice flow", *Proceedings of the Institution of Mechanical Engineers*, 104(1):23–36, 1923. (Cited on page 38.)

[443] SMITH, H.: *Hydraulics - The flow of water through orifices, over weirs, and through open conduits and pipes*, John Wiley and Sons, New York, 1886. (Cited on page 38.)

[444] STAHL, B.: "Experimentelle Untersuchung zur Schallerzeugung durch die Turbulenz in einer Rohrströmung hinter einer unstetigen Querschnittserweiterung", *Acta Acoustica United with Acoustica*, 63(1):42–59, 1987. (Cited on pages 101 and 103.)

[445] STEVENS, E.H.: "Über Schallgeschwindigkeit in Luft bei gewöhnlicher und bei hoher Temperatur und in verschiedenen Dämpfen", *Annalen der Physik*, 312(2):285–320, 1902. (Cited on page 190.)

[446] STEWART, G.W.: "On the early history of the singular value decomposition", Technical Report TR-92-31 and TR-2855, University of Maryland, 1992. (Cited on page 145.)

[447] STEWART, G.W.; LINDSAY, R.B.: *Acoustics: A text on theory and applications*, Chapman & Hall, London, 1931. (Cited on page 58.)

[448] STINSON, M.R.: "The propagation of plane waves in narrow and wide circular tubes, and generalization to uniform tubes of arbitrary cross-sectional shape", *Journal of the Acoustical Society of America*, 89(2):550–558, 1991. (Cited on page 121.)

[449] STOKES, G.G.: "On the theories of the internal friction of fluids in motion, and of the equilibrium and motion of elastic solids", *Transactions of the Cambridge Philosophical Society*, 8:287–319, 1845. (Cited on pages 97, 114, and 131.)

[450] STOKES, G.G.: "An examination of the possible effect of the radiation of heat on the propagation of sound", *Philosophical Magazine Series 4*, 1:305–317, 1851. (Cited on page 131.)

[451] STOKES, G.G.: "On the effect of the internal friction of fluids on the motion of pendulums", *Transactions of the Cambridge Philosophical Society*, 9(2):8–106, 1851. (Cited on pages 62, 114, and 131.)

[452] STOW, S.R.; DOWLING, A.P.: "Thermoacoustic oscillations in an annular combustor", in *ASME Turbo Expo 2001, 4-7 June 2001, New Orleans, Louisiana, USA*, GT2001-0038, 2001. (Cited on pages 48 and 80.)

[453] STOW, S.R.; DOWLING, A.P.: "Modelling of circumferential modal coupling due to helmholtz resonators", in *ASME Turbo Expo 2003, June 16-19, 2003, Atlanta, GA, USA*, GT2003-38168, 2003.

[454] Stow, S.R.; Dowling, A.P.: "Low-order modelling of thermoacoustic limit cycles", in *ASME Turbo Expo 2004, June 14-17, 2004, Vienna, Austria*, GT2004-54245, 2004.

[455] Stow, S.R.; Dowling, A.P.: "A time-domain network model for nonlinear thermoacoustic oscillations", *Journal of Engineering for Gas Turbines and Power*, 131:1–10, 2009. (Cited on pages 48 and 80.)

[456] Streeter, V.L.: *Fluid Mechanics*, 3rd ed., McGraw-Hill, New York, 1962. (Cited on page 37.)

[457] Strouhal, V.: "Ueber eine besondere Art der Tonerregung", *Annalen der Physik und Chemie*, 5(10):216–251, 1878. (Cited on page 271.)

[458] Sullivan, J.W.: "A method for modeling perforated tube muffler components. I. Theory", *Journal of the Acoustical Society of America*, 66(3):772–778, 1979. (Cited on page 82.)

[459] Sullivan, J.W.: "A method for modeling perforated tube muffler components. II. Applications", *Journal of the Acoustical Society of America*, 66(3):779–788, 1979. (Cited on pages 44, 67, and 82.)

[460] Sullivan, J.W.; Crocker, M.J.: "Analysis of concentric-tube resonators having unpartitioned cavities", *Journal of the Acoustical Society of America*, 64(1):207–215, 1978. (Cited on page 82.)

[461] Sullivan, J.W.; Doige, A.G.: "Measurement of acoustic impedance of perforated plates in the presence of mean through flow", *Journal of the Acoustical Society of America*, 71:S78, 1982, abstract only. (Cited on page 53.)

[462] Sun, F.; Chen, H.; Wu, J.; Feng, K.: "Sound absorbing characteristics of fibrous metal materials at high temperatures", *Applied Acoustics*, 71:221–235, 2010. (Cited on pages 26, 267, and 268.)

[463] Sun, X.; Jing, X.; Zhang, H.; Shi, Y.: "Effect of grazing-bias flow interaction on acoustic impedance of perforated plates", *Journal of Sound and Vibration*, 254(3):557–573, 2002. (Cited on pages 54, 221, and 222.)

[464] Sylvester, J.J.: "A new proof that a general quadratic may be reduced to its canonical form (that is, a linear function of squares) by means of a real orthogonal substitution", *Messenger of Mathematics*, 19:1–5, 1889. (Cited on page 145.)

[465] Sylvester, J.J.: "On the reduction of a bilinear quadric of the n-th order to the form of a sum of n products by a double orthogonal substitution", *Messenger of Mathematics*, 19:42–46, 1889.

[466] Sylvester, J.J.: "Sur la réduction biorthogonale d'une forme linéo-linéaire à sa forme cannonique", *Comptes Rendus de l'Académie des Sciences, Paris*, 108:651–653, 1889. (Cited on page 145.)

[467] Tack, D.H.; Lambert, R.F.: "Influence of shear flow on sound attenuation in a lined duct", *Journal of the Acoustical Society of America*, 38(4):655–666, 1965. (Cited on pages 32 and 217.)

[468] Tam, C.K.W.; Kurbatskii, K.A.: "Microfluid dynamics and acoustics of resonant liners", *AIAA Journal*, 38(8):1331–1339, 2000. (Cited on page 18.)

[469] Tam, C.K.W.; Kurbatskii, K.A.; Ahuja, K.K.; R. J. Gaeta, J.: "A numerical and experimental investigation of the dissipation mechanisms of resonant acoustic liners", *Journal of Sound and Vibration*, 245(3):545–557, 2001. (Cited on page 18.)

[470] Tapken, U.; Enghardt, L.: "Optimization of sensor arrays for radial mode analysis in flow ducts", in *12th AIAA/CEAS Aeroacoustics Conference, 8-10 May 2006, Cambridge, Massachusetts*, AIAA-2006-2638, 2006. (Cited on pages 148 and 166.)

[471] Tapken, U.; Raitor, T.; Enghardt, L.: "Tonal noise radiation from an UHBR fan - Optimized in-duct radial mode analysis", in *15th AIAA/CEAS Aeroacoustics Conference, 11-13 May 2009, Miami, Florida*, AIAA-2009-3288, 2009. (Cited on page 148.)

[472] Tayong, R.; Leclaire, P.: "Hole interaction effects under high and medium sound intensities for micro-perforated panels design", in *10éme Congrés Francais d'Acoustique, 12-16 April 2010, Lyon, France*, 2010. (Cited on page 65.)

[473] Thurston, G.B.; Charles E. Martin, J.: "Periodic fluid flow through circular orifices", *Journal of the Acoustical Society of America*, 25(1):26–31, 1953. (Cited on pages 28, 45, and 202.)

[474] Thurston, G.B.; Logan E. Hargrove, J.; Cook, B.D.: "Nonlinear properties of circular orifices", *Journal of the Acoustical Society of America*, 29(9):992–1001, 1957. (Cited on pages 28, 45, and 202.)

[475] Tijdeman, H.: "On the propagation of sound waves in cylindrical tubes", *Journal of Sound and Vibration*, 39(1):1–33, 1975. (Cited on pages 113, 120, 121, and 122.)

[476] To, C.W.S.; Doige, A.G.: "A transient testing technique for the determination of matrix parameters of acoustic systems, I: Theory and principles", *Journal of Sound and Vibration*, 62(2):207–222, 1979. (Cited on page 154.)

[477] To, C.W.S.; Doige, A.G.: "A transient testing technique for the determination of matrix parameters of acoustic systems, II: Experimental procedures and results", *Journal of Sound and Vibration*, 62(2):223–233, 1979. (Cited on page 154.)

[478] Tonon, D.; Moers, E.M.T.; Hirschberg, A.: "Quasi-steady acoustic response of wall perforations subject to a grazing-bias flow combination", *Journal of Sound and Vibration*, 332:1654–1673, 2013. (Cited on pages 18, 19, 32, 34, 38, 50, and 55.)

[479] Tonon, T.S.; Sirignano, W.A.: "The nonlinearity of acoustic liners with flow effects", in *8th AIAA Aerospace Sciences Meeting, 19-21 January 1970, New York, NY*, AIAA-1970-0128, 1970. (Cited on pages 53 and 65.)

[480] Toulorge, T.; Roeck, W.D.; Denayer, H.; Desmet, W.: "Computational aeroacoustic characterization of different orifice geometries under grazing flow conditions", in *Proceedings of ISMA2012/USD2012*, 791, 2012. (Cited on pages 19 and 32.)

[481] Tran, N.; Ducruix, S.; Schuller, T.: "Passive control of the inlet acoustic boundary of a swirled burner at high amplitude combustion instabilities", *Journal of Engineering for Gas Turbines and Power*, 131:1–7, 2009. (Cited on pages 25, 26, 27, 28, 50, 55, 202, 203, and 269.)

[482] Tyler, J.M.; Sofrin, T.G.: "Axial flow compressor noise studies", *SAE Transaction*, 70:309–332, 1962. (Cited on pages 101, 104, and 106.)

[483] Utvik, D.H.; Blackman, A.W.; Ford, H.J.: "Evaluation of absorption liners for suppression of combustion instability in rocket engines", in *AIAA Propulsion Joint Specialist Conference, 14-18 June 1965, Colorado Springs, Colorado*, AIAA-1965-0585, 1965. (Cited on pages 44 and 53.)

[484] Utvik, D.H.; Ford, H.J.; Blackman, A.W.: "Evaluation of absorption liners for suppression of combustion instability in rocket engines", *Journal of Spacecraft and Rockets*, 3(7):1039–1045, 1966. (Cited on pages 26, 44, and 53.)

[485] Wagner, W.; Pruss, A.: "International equations for the saturation properties of ordinary water substance. Revised according to the international temperature scale of 1990.", *Journal of Physical and Chemical Reference Data*, 22(3):783–787, 1993. (Cited on page 134.)

[486] Wagner, W.; Pruss, A.: "The IAPWS formulation 1995 for the thermodynamic properties of ordinary water substance for general and scientific use", *Journal of Physical and Chemical Reference Data*, 31(2):387–535, 2002. (Cited on page 134.)

[487] Webster, A.G.: "Acoustical impedance and the theory of horns and of the phonograph", *Proceedings of the National Academy of Sciences of the United States of America*, 5(7):275–282, 1919. (Cited on page 60.)

[488] Welch, P.D.: "The use of fast fourier transform for the estimation of power spectra: a method based on time averaging over short, modified periodigrams", *IEEE Transactions on Audio and Electroacoustics*, 15(2):70–73, 1967. (Cited on page 140.)

[489] Wendoloski, J.C.: "Sound absorption by an orifice plate in a flow duct", *Journal of the Acoustical Society of America*, 104(1):122–132, 1998. (Cited on pages 47, 54, and 71.)

[490] Weng, C.; Boij, S.; Hanifi, A.: "The attenuation of sound by turbulence in internal flows", *Journal of the Acoustical Society of America*, 133:3764–3776, 2013. (Cited on page 126.)

[491] Westervelt, P.J.: *The interaction of a finite amplitude acoustic wave with small obstacles and orifices*, Ph.d. thesis, Massachusetts Institute of Technology, 1951. (Cited on pages 44, 53, and 251.)

[492] Weston, D.E.: "The theory of the propagation of plane sound waves in tubes", *Proceedings of the Physical Society, Section B*, 66:695–709, 1953. (Cited on pages 113, 120, and 121.)

[493] Weyl, H.: "Das asymptotische Verteilungsgesetz der eigenwert linearer partieller Differentialgleichungen (mit Anwendung auf der Theorie der Hohlraumstrahlung)", *Mathematische Annalen*, 71:441–479, 1912. (Cited on page 145.)

[494] Whiffen, M.C.; Ahuja, K.K.: "An improved schlieren system and some new results on acoustically excited jets", *Journal of Sound and Vibration*, 86(1):99–105, 1983. (Cited on page 54.)

[495] White, F.M.: *Viscous Fluid Flow*, 2nd ed., McGraw-Hill, New York, 1991. (Cited on pages 114, 115, and 161.)

[496] White, F.M.: *Fluid Mechanics*, 4th ed., McGraw-Hill, 1998. (Cited on page 33.)

[497] Yang, V.; Anderson, W. (Eds.): *Liquid rocket engine combustion instability*, AIAA, Reston, VA, 1995. (Cited on pages 5 and 323.)

[498] Yazaki, T.; Tashiro, Y.; Biwa, T.: "Measurements of sound propagation in narrow tubes", *Proceedings of the Royal Society A*, 463:2855–2862, 2007. (Cited on page 113.)

[499] Zeit Online: "The Energiewende", No. 47/2012, published 15 November 2012, accessed online 27 February 2014: http://www.zeit.de/2012/47/Energiewende-Deutsche-Begriffe-Englisch. (Cited on page 2.)

[500] Zhao, D.; Morgans, A.S.: "Tuned passive control of perforated liners", in *15th AIAA/CEAS Aeroacoustics Conference, 11-13 May 2009, Miami, Florida*, AIAA-2009-3406, 2009. (Cited on page 55.)

[501] Zhao, D.; Morgans, A.S.; Dowling, A.P.: "Tuned passive control of acoustic damping of perforated liners", *AIAA Journal*, 49(4):725–734, 2011. (Cited on pages 16, 55, and 256.)

[502] Zhao, H.; Sun, X.: "Active control of wall acoustic impedance", *AIAA Journal*, 37(7):825–831, 1999. (Cited on page 54.)

[503] Zhong, Z.; Zhao, D.: "Time-domain characterization of the acoustic damping of a perforated liner with bias flow", *Journal of the Acoustical Society of America*, 132(1):271–281, 2012. (Cited on page 55.)

[504] Zhou, L.; Bodén, H.: "The effect of combined high level acoustic excitation and bias flow on the acoustic properties of an in-duct orifice", in *19th AIAA/CEAS Aeroacoustics Conference, 27-29 May 2013, Berlin, Germany*, AIAA-2013-2128, 2013. (Cited on pages 50 and 55.)

[505] Zinn, B.T.: "A theoretical study of non-linear damping by helmholtz resonators", *Journal of Sound and Vibration*, 13(3):347–356, 1970. (Cited on pages 28, 45, 65, 67, 68, 74, and 202.)

[506] Zinn, B.T.; Lieuwen, T.C.: "Combustion instabilities: Basic concepts", in [305], Chap. 1, pp. 3–26, 2005. (Cited on page 5.)

[507] Zorumski, W.E.; Parrott, T.L.: "Nonlinear acoustic theory for rigid porous materials", Technical Note NASA-TN-D-6196, NASA, 1971. (Cited on page 65.)

[508] Zwikker, C.; Kosten, C.W.: *Sound absorbing materials*, Elsevier, New York, 1949. (Cited on pages 113, 122, and 123.)